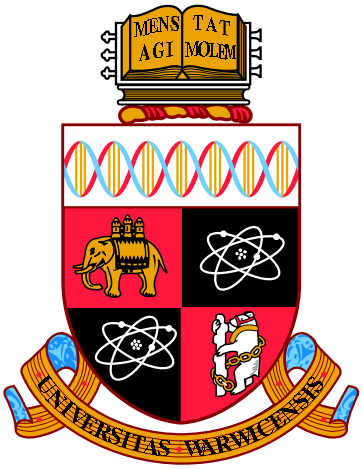

Engineering of Artificially Layered Lanthanum-based Perovskites using Pulsed Laser Deposition

by

Nessa Fereshteh Saniee

Thesis

Submitted to the University of Warwick

for the degree of

Doctor of Philosophy

Department of Physics

October 2014

THE UNIVERSITY OF WARWICK

Contents

List of Tables

List of Figures

Acknowledgments

Firstly, I would like to thank Prof. Stuart Abell, my M.Phil. supervisor, for introducing me to the subject of thin film growth and Prof. Chris McConville, my Ph.D. supervisor, for giving me the opportunity to do a Ph.D. in this very exciting field. I would also like to thank him for his continual encouragement, support and regular instruction to 'keep at it'. I would like to thank every member of Warwick Physics who have helped to make this thesis a success.

I am extremely grateful to Dr Sean McMitchell, my second supervisor, for his deep guidance and support in the final and most important year of my PhD and particularly for his patience to read my thesis word by word. I would like to thank my thesis examiner, Dr Tom Hase, who guided me through the last 6 months as my major advisor. I would also like to acknowledge Dr Tim Jackson (School of Electrical Engineering, University of Birmingham, UK) and Dr Adrian Crisan (School of Materials Engineering, University of Birmingham, UK) for allowing me to use the pulsed laser deposition system in their group.

I would like to express my deep gratitude to Dr Anna Sanchez for training me on TEM sample preparation and providing atomic resolution STEM images. Without her pedagogical inspiration, this thesis could not have been completed. I am very grateful to Steve York and Steve Hindmarsh for their technical support. I benefited greatly from training and many discussions with Dr Richard Beanland (transmission electron microscopy), Dr Neil Wilson (atomic force microscopy), and Dr Martin Lee (magnetic and electrical measurements). Next, I would like extremely thank Dr David Walker for X-ray diffraction training and helping me to analyse and understand my materials system.

I would like to thank Dr Marc Walker for providing photoelectron spectroscopy

data and running the tea club. I would also like to thank the rest of my former and present group members of various seniority; Sepehr Farahani, James Mudd, Daesung Park, Mohammed Saghir, Louise Bailey, Wojciech Linhart, Andrezej Stacel, Dr Tim Veal, and Dr Gavin Bell for their contribution to make me a better physicist with helpful conversations and explanations in the group. I appreciate the time and effort Dr Chris Burrows put for bringing various typological and grammar errors to my attention on Chapters 5 and 6 in addition to deep discussions on physics of the surface and bulk diffraction. I am very grateful to Rob Johnston for his technical support and former members of the group Dr Mukul Misra and Dr Hyunsik Kim for their help to establish the new PLD laboratory.

This thesis would not have been possible without the support of my amazing friends Catarina (whom I can trust most at any part of my life), Natalia (with whom I made the most exotic microwave food in Physics), John (the greenest house mate with continuous supply of various vegetables from our garden), Daesung (who made me feel guilty to leave the department earlier than 2 am), Nixon and Sepehr.

Had I not become a material scientist, I would have likely become a graphic designer. Therefore, please excuse the bright colouring of fancy figures in my thesis. I hope they provide occasional cheerfulness without diminishing the clarity of the physics behind them.

I heartily am thankful to my parents, Sholeh and Farhang, and especially my wonderful sister, Sarah, for their continuous encouragement and unsparing love. Last but no means least, thank you David Armstrong for giving me not only the duck but also your kindness, love and support.

Dedication

I would like to dedicate this thesis to my mother, **Sholeh Jalili Khiabani**, who is the kindest and most inspirational person I know. Without her love, support and continuous encouragement, I could not have succeeded in this Ph.D. or any stage of my life.

Declarations

I declare the content of thesis is my own work except where stated otherwise. The growth and characterisation was carried out entirely in the Physics department at the University of Warwick under the supervision of Prof. C.F. McConville, during the period of October 2009 to September 2013. The research carried out here has not been submitted, either fully or in part, for admission to a higher degree in any other academic institution. The transmission microscopy data has been taken by Dr Ana Sanchez and Dr Richard Beanland in Warwick Microscopy group. *Ex-situ* X-ray photoelectron data were carried out by Dr Marc Walker and James Mudd. Dr Hyunsik Kim carried out the magnetic and electrical measurements for the first set of samples in Chapter 4.

Work presented in this thesis but at the moment is waiting to be submitted to a refereed journal:

- The key role of oxygen content in the $LaMnO_3$ thin films: structural, magnetic and surface properties. **N. Fereshteh Saniee**, M. S. Kim, M. Walker, C. F. McConville, to be submitted to *Surf. Sci.*

- In-depth structural analysis of $LaNiO_3$ thin films: detection of Ruddlesden-Popper by grazing incidence X-ray diffraction and STEM, **N. Fereshteh Saniee**, S. R. C. McMitchell, A. M. Sanchez, T. P. A. Hase, G. R. Bell, C. F. McConville, in preparation to be submitted to *App. Phys. Lett.*

- Identification of surface octahedral distortions in short-period perovskite superlattices. **N. Fereshteh Saniee**, S. R. C. McMitchell, A. M. Sanchez, C. F. McConville, in preparation to be submitted to *Adv. Mater.*

The work presented in this thesis has been presented in the following conferences:

- Correlation between surface and bulk octahedral distortions in short period superlattices, **N. Fereshteh Saniee**, S. R. C. McMitchell, A. M. Sanchez, C. F. McConville, 5th Vacuum Symposium UK 15-16 October 2014, Coventry, UK.

- In-situ determination of the surface octahedra distortions in perovskite heterostructures, **N. Fereshteh Saniee**, S. R. C. McMitchell, A. M. Sanchez, C. F. McConville, 11th international conference on the structure of surfaces, 21-25 July 2014, University of Warwick, UK.

The work carried out by the author of this thesis during the PhD period but not presented in this thesis has been published in a refereed journal:

- Pinning effect on the band gap modulation of crystalline $BexZn_{1-x}O$ alloy films grown on Al_2O_3(0001), D. Park, J. Mudd, M. Walker, D. Seghier, A. Krupski, **N. Fereshteh Saniee**,... *Cryst. Eng. Comm.*, **16**, 2136-2143, 2014.

Work carried out during this PhD by the author but not presented in this thesis:

- Development of nanostructured anatase TiO_2 by means of pulsed laser deposition, Presentation, D. Vlachos, M. Misra, **N. Fereshteh Saniee**, D. P. Woodruff and C. F. McConville, XXVIII National Conference on Solid State Physics and Materials Science, 23-26 September 2012, University of Patras, Greece.

- Surface and bulk electronic properties of Si-doped ZnO thin films grown by pulsed laser deposition, Poster presentation, Materials Research Society, **N. Fereshteh Saniee**, T. Veal, J. S. Abell, C. F. McConville, 2011, Fall meeting, Boston, USA.

- Influence of oxygen background pressure on growth of doped ZnO thin film by PLD, Poster presentation Condensed Matter and Materials Physics, **N. Fereshteh Saniee**, J. S. Abell, C. F. McConville, 2010, University of Warwick, UK.

Abstract

With the advances made over the past two decades in microelectronics, the necessities to the fabrication of high quality materials, from semiconductors to oxides, has become increasingly stringent. To adapt to the increasing demand of new device structures, often a single material will not exhibit all the desired properties, and combining two or more materials to form artificial structures with tailored electronic and magnetic properties become essential. A deeper understanding of the relationship between physical properties of these materials and their nanostructure is therefore required. This can be achieved through atomic engineering, whereby new materials are fabricated specifically to have the desired properties, leading to new devices and applications. In this thesis the ability to fabricate high quality interfaces and superlattice structures between different lanthanum-based perovskites ($LaMO_3$ M=Ni and Mn) is demonstrated. Using a pulsed laser deposition equipped with *in-situ* reflection high-energy electron diffraction (RHEED), single unit-cell control of the deposition process could be achieved. Since the single layer thickness of the unit-cell can significantly influence the macroscopic properties of such superlattices, it is important to distinguish between the effects arising due to short periodicity and those properties from the growth of each constituent layer. Therefore detailed analysis of the layers and superlattice structures is essential to completely understand the nature of these new materials properties. Unusual magnetic properties, such as spin glass-like behaviour and an exchange bias, were observed for the $LaMnO_3$ films grown at high temperatures in lower oxygen pressure. This indicates an intrinsically inhomogeneous magnetic state in the locality of the transition. It has been shown that the crystal structure of $LaNiO_3$ is much more sensitive to the growth temperature and prone to decomposition into a secondary phase of La_2NiO_4, that is preferentially grown in the plane of the film detected by grazing-incidence angle XRD and scanning TEM. RHEED data, including strong intensity oscillations and streaky patterns, suggest that the growth of both these materials can be optimised with purely 2D growth mode, and hence making it possible to grow single unit cell layers of these materials. The resulting strong RHEED intensity oscillations and sharp XRD features indicate high quality material growth. However small variations in the growth process lead to the formation of a Ruddlesden-Popper phase. In this thesis the ability to identify the octahedral connectivity, enabled by significantly improved epitaxial growth of short-period superlattices has been shown for the first time using precise surface analysis and atomic resolution transmission electron microscope. A Jahn-Teller type distortion of the MnO_6 octahedra evolves during the deposition to reduce the symmetry by increasing the degeneracy of the energy levels leading to a $(\sqrt{2} \times \sqrt{2})R45^\circ)$ surface reconstruction. This method can be used as an emerging route to detection of the deterministic octahedral distortions by engineering potential new functionalities by identifying the phase of the terminating layer.

Abbreviations

2DEG	two dimensional electron gas
ADF	annular dark field
AFM	atomic force microscopy
BF	bright field
CMR	colossal magnetoresistance
COO	charge/orbital ordering
D-LACEBD	digital-large angle convergent electron beam diffraction
DE	double exchange
EB	exchange bias
EELS	electron energy-loss spectroscopy
EDS	energy-dispersive X-ray spectroscopy
FC	field cooling
FWHM	full-width at half-maximum
GID	grazing-incidence diffraction
HAADF	high-angle annular dark field
HRTEM	high resolution transmission electron microscopy
IMFP	inelastic mean free path
IMT	insulator-metal transition
MB	Matthews and Blakeslee
MBE	molecular beam epitaxy
MOCVD	metalorganic chemical vapour deposition
MRAM	magnetic random access memory
NNI	National Nanotechnology Initiative
PB	People and Bean
PLD	pulsed laser deposition
PPMS	physical property measurement system
PVD	physical vapour deposition
r.l.u.	reciprocal lattice units
RHEED	reflection high-energy electron diffraction
RMS	root mean square
RP	Ruddlesden-Popper
RSM	reciprocal space map

SEM	scanning electron microscopy
SQUID	superconducting quantum interference device
STEM	scanning transmission electron microscopy
STM	scanning tunnelling microscopy
$\mathbf{T_C}$	Curie temperature
$\mathbf{T_N}$	Néel temperature
TEM	transmission electron microscopy
TMO	transition metal oxide
u.c.	unit cell
UHV	ultra-high vacuum
XPS	X-ray photoelectron spectroscopy
XRD	X-ray diffraction
XRR	X-ray reflectivity
ZFC	zero-field cooling

Chapter 1

Introduction

1.1 Overview

In the past two decades, an explosive worldwide growth of research efforts has been witnessed in nanotechnology and nanoscience, in view of their tremendous potential for novel functionalities. Nanotechnology, as noted on the National Nanotechnology Initiative website (www.nano.gov), is the control and understanding of matter at dimensions of $\approx$1 to 100 nanometres (A nanometre is one billionth of a meter equivalent to $1/100,000$ the width of a human hair), where exceptional phenomena allow novel applications. A nanoscale approach has revolutionised the methods in which matter is synthesised and processed [1]. After just over a half of a century, when Richard Feyman gave his famous talk, 'There is Plenty of Room at the Bottom' [2] and he imagined a science and art of manipulating matter and creating novel structures on an atomic scale, nanotechnology is finding its way to commercial use. For instance, over 1,600 nano-enabled consumer products (identified by manufacturers) are listed on the Project on Emerging Nanotechnologies website [3] ranging from the second lightest ice axe in the world, CAMP Corsa Nanotech (featuring innovative Sandvik Nanoflex steel [4]), to germ free wireless laser mouse (IOGEAR, using titanium dioxide and silver as nano materials [5]). Clearly, the application of nanotechnology can be found in a wide spectrum of fields from medicine to physics. It has been shown that unlimited opportunities can arise from using atoms [6], molecules [7] or nanoparticles [8] as building blocks to create nano-structures and devices with emergent functionalities. In this thesis, the focus is on manipulation of matter at an atomic scale.

The observed miniaturisation trend in devices has mostly been driven by the semiconductor industry to fabricate more efficient computers in smaller sizes, even moving towards the fabrication of quantum computers [9, 10]. Recent developments in magnetic

materials have played a crucial role in the advancement of data storage and magnetic memories in information technology [11]. At present, thin film magnetic memory devices such as magnetic random access memory (MRAM) and sensors are at the heart of every computer [12]. Presently, the fast growing field of 'spintronics' has stimulated intense research activities to search for new unprecedented functionalities and novel applications [13, 14, 15].

In this context, a class of materials called 'transition metal oxides' (TMOs) possess a variety of properties that are not easily accessible in conventional semiconductors. In TMOs, the hybridisation of the *d*-orbitals of the transition metal along with the *p*-orbitals of oxygen, leads to a band gap narrowing. Such a strongly correlated system with a narrow band enhances the coupling effect between spins, charge and degrees of freedoms of the lattice as a result of orbitals overlapping and strong electronic interactions [16]. The potential significance of this electronic complexity is in the application of TMOs, where their diverse ground states can have additional orbitals and lattice degrees of freedom. These add to charge (such as semiconducting electronics) [17], or interaction of charge and spin (i.e. spintronics) [18], giving rise to colossal responses to small perturbations in the system. In addition, exotic phenomena can also be observed when competing phases of material are combined, e.g., insulating and metallic phases [19]. Among these, the colossal magnetoresistance effect (CMR) in manganites [20] and high T_C superconductivity in copper oxides [21] are some of the more impressive examples. CMR is magnetoresistance related to a magnetic phase transition from ferromagnetic to paramagnetic. The parent compound of classical CMR compounds is the perovskite $LaMnO_3$ [22]. Magnetoresistance was first observed in manganite thin films by Von Helmolt *et al.* [23] and Chahara *et al.* [24]. Efforts to reach CMR were initiated after Jin *et al.* [25] discovered very large magnetoresistance. CMR was reported in a single crystal of doped $LaMnO_3$ by Tokura group [20], where a dramatic change in the resistance by orders of magnitude was observed near the phase transition temperature in the presence of a magnetic field. The metallic state in manganites and its strong correlation with the external magnetic field comes from the mixed valence of Mn ions (Mn^{3+} and Mn^{4+}). According to the Hund's rule, the spin and charge transfer is only allowed when the core spins of Mn^{4+} are aligned with the core spins of the Mn^{3+} [26]. CMR is one the most fascinating phenomena in TMOs because of its possible application in magnetic memory devices such as MRAMs [27, 28]. Since the use of CMR effect in MRAMs is in a thin film form, much research has been carried out to achieve the best structural and physical properties.

There are other techniques used to synthesise TMOs in thin film forms over their conventional bulk preparation such as pulsed laser deposition (PLD), molecular beam

epitaxy (MBE), and metal-organic chemical vapour deposition (MOCVD). A turning point for the current developments in the field of complex oxides has been the further advancement in the instrumentation of thin film growth techniques by adding the *in-situ* surface monitoring techniques that can operate at high pressures. For instance, in a PLD system, addition of a differentially pumped reflection high energy electron diffraction (RHEED) technique [29] makes layer-by-layer growth of complex oxide heterostructures possible with atomically sharp interfaces.

In this study, $LaMnO_3$ was chosen to be synthesised using a PLD system. $LaMnO_3$ can also be a platform for coupling several degrees of freedom such as lattice, spin and charge as a model system of complex oxides in order to shed light on their rich physics. Later on in this work, $LaMnO_3$ is used as a constituent in the superlattices containing $LaMnO_3$ and $LaNiO_3$. It can be expected that interfaces between different TMOs have a profound effect on physical properties and can open a door to new and unexpected behaviour. Unpredicted two-dimensional electron gas (2DEG) at the interface between two insulating compounds [30], magnetic tunnel junctions, and devices based on the exchange bias effect [31] are some of the many examples where the critical role of the interface has been actively explored [32]. Theoretical calculations of magnetism in superlattices containing $LaNiO_3$ and $LaMnO_3$ [33] suggested that $LaNiO_3$ in the (001) orientation superlattices is almost always non-magnetic. It has also been proposed that two unit cells (u.c.) of $LaMnO_3$ separated by one monolayer of $LaNiO_3$, would carry as high a magnetic moment as 8 μ_B [34].

However, the origin of these effects cannot be truly attributed to the interfaces without preliminary understanding of the often fabrication dependent properties [35]. Underlying physics relevant to TMOs, with more focus on the manganites, will be discussed to improve understanding of the role of thin film deposition conditions such as stoichiometry, oxygen content and epitaxial strain in determination of the magnetic properties. Then, basic structures of perovskite oxides are discussed. The motivation and outline of the thesis will be the last sections.

1.2 Manganites and lattice features

TMOs show a diverse set of electronic properties such as semiconductivity, metallic conductivity and superconductivity. They can also be dielectric and Mott-Hubbard insulators [36, 37]. The diversity arises from a combination of characteristics such as geometry (i.e. crystal symmetry), quantum electrostatic and chemical properties (i.e. strong electron correlation effect, metal-to-oxygen bond length, degree of covalency or ionic bonding). In TMOs, particularly in manganites, the *d*-band occupancy not only

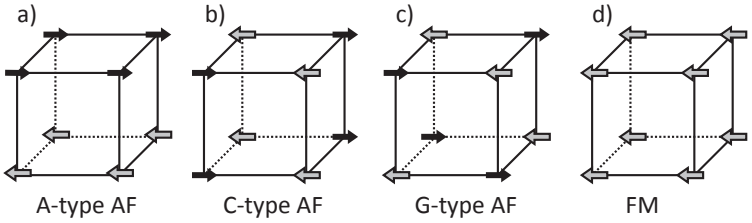

Figure 1.1: Four of the possible magnetic structures in manganites with their labels for the B-site cation in a perovskite lattice. a) A-type, b) C-type and c) G-type represent antiferromagnetic ordering and d) represents the ferromagnetic ordering. The arrows at the position of Mn ions represent the spin projections along the *z*-axis. [20].

tunes the transport properties but also the magnetic state as a result of interaction between the oxygen ligand and the manganites *d*-orbital within the crystal environment. However most of these electronic properties can qualitatively be understood by analysing the *d*-band occupation using simple models such as crystal field theory [38]. A brief description of magnetic properties in manganites is given, followed by a brief discussion of crystal field theory. Some of the exchange interactions in manganites are also introduced.

1.2.1 Magnetic ordering

Magnetic order arises in materials as a result of interactions between magnetic moments. According to the Heisenberg model the neighbouring spins of $\mathbf{S}_i$ and $\mathbf{S}_j$ are interacting with the following Hamiltonian

$$\mathscr{H} = -\sum_{ij} \boldsymbol{J}_{ij} \mathbf{S}_i . \mathbf{S}_j \tag{1.1}$$

where $\boldsymbol{J}_{ij}$ describes the spin interaction between the i-th and j-th spins and its value is called the exchange constant. The positive or negative values of the exchange constant favour parallel (ferromagnetic) or antiparallel (antiferromagnet) spin alignment, respectively. Figure 1.1 represents four of the possible magnetic structures in manganites labelled as AF for antiferromagnetic and FM for ferromagnetic. A-type, C-type and G-type represent commensurate antiferromagnetism, which are composed of the ferromagnetic planes of $\{100\}$, $\{110\}$ and $\{111\}$ when they are oppositely aligned. The last structure (from the left) represents the ferromagnetic ordering. If there is no magnetic field applied to an antiferromagnet, it has zero net magnetisation as the moments are arranged in a way so that they cancel each other out. In an antiferromagnetic system, the periodicity of the spins can be linked to the structure of the crystal. This situation of antiferromagnetic

order is described as commensurate. Conversely, it can be independent of the crystal structure which is then described as incommensurate.

1.2.2 Crystal field theory

In crystal field theory for a strongly correlated system, it is assumed that the model is purely ionic, the charge is tied to the atomic position and the local structure is only affected by interactions with the first neighbours i.e. in an octahedral coordination, the negatively charged anions (oxygen) stabilise the central cation (the transition metal Mn) by the Coulomb interaction [39]. The geometry of the central cation in the octahedral coordination is depicted in figure 1.2-a.

To understand the effect of local environments on defining the crystal energy levels of an atom, the shape of atomic orbitals is of great importance. Suppose, for the simplest case, that the central cation has one *d* electron with the quantum numbers $s = 1/2$, $l = 2$ and the degeneracy $2l + 1$. These five orbitals have the same radial parts but different associated angular wave functions. The angular dependence of *d* orbitals can be shown by the charge cloud distributions represented in figure 1.2. For the Mn^{3+} ion located in an octahedron formed by 6 neighbouring O^{2-} ions, there are electrostatic forces between the 2*p* orbital of oxygen ions and Mn 3*d* orbital. In the *d* orbital two classes of energy levels exist including the t_{2g} in which the orbitals are pointing between the x, y and z axes. The other group is the e_g orbitals pointing along these axes. In an octahedron the charge will point into six discrete points (the six oxygen ions in the corners of octahedra). To conserve energy the orbitals are no longer degenerate. The energy levels e_g are comprised of the $d_{3z^2-r^2}$ and $d_{x^2-y^2}$ levels. The d_{xz}, d_{yz} and d_{xy} are grouped together to form the t_{2g} levels. Figure 1.2-c depicts in 3D the effect of the crystal environment on the $d_{x^2-y^2}$ and d_{xy} orbitals in an octahedral symmetry. Comparing with the $d_{x^2-y^2}$ orbital, lower electrostatic energy is formed for the d_{xy} orbital since it has a lower overlap with the 2*p* oxygen orbitals as they are pointing along the x and y axes. Hence there is a lower energy configuration for t_{2g} levels than e_g levels in an octahedral crystal environment [40].

The splitting between the two energy levels is shown in figure 1.2-b by Δ. The important assumed rule about the energy splitting is that they obey a centre of gravity rule in energy that is not changed by perturbation [39]. Considering that the energy of the 4 electrons in e_g should be compensated by that of the 6 electrons in t_{2g}, Δ and the energy shift of the orbital in single *d* electron system are related such that

$$E(t_{2g}) + 2/5\Delta = E(e_g) - 3/5\Delta. \tag{1.2}$$

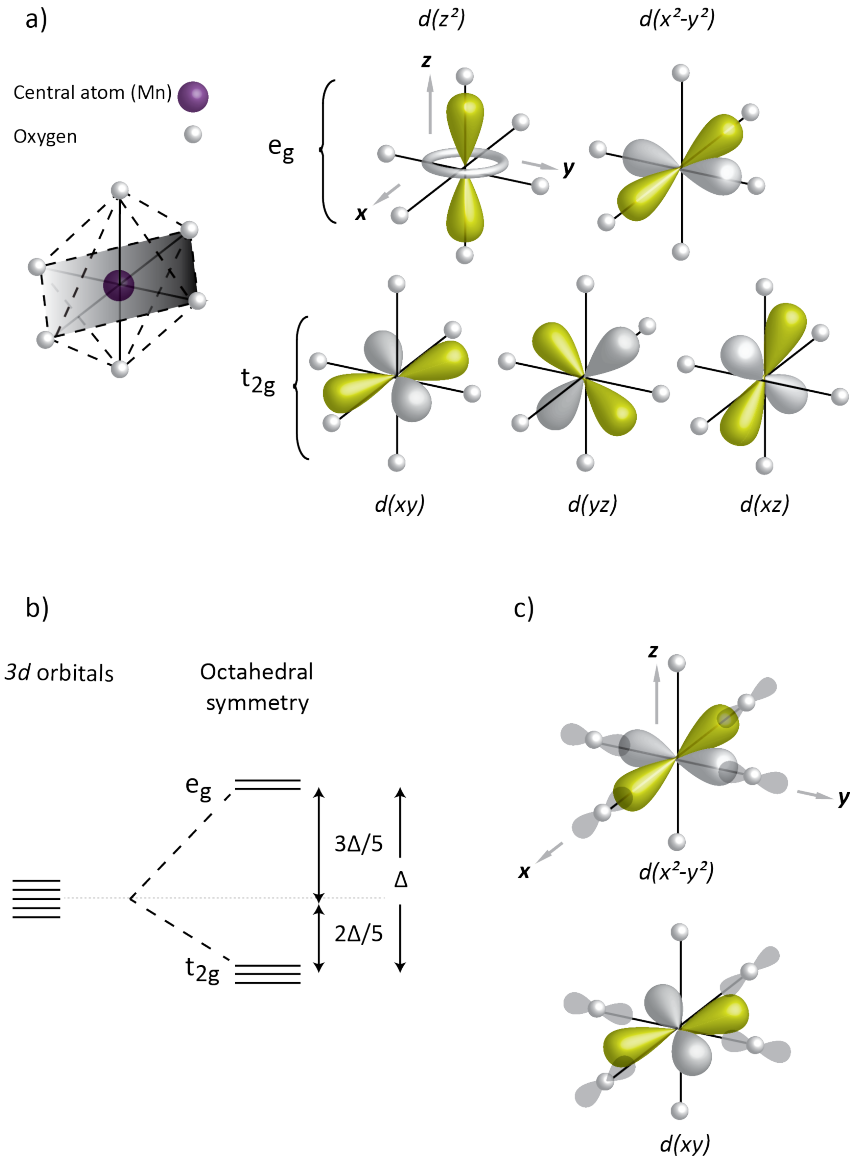

Figure 1.2: The angular distribution of the *d* orbitals. a) The $d_{x^2-y^2}$ and $d_{3z^2-r^2}$ levels are grouped together and called energy level e_g. The d_{xz}, d_{yz} and d_{xy} are grouped together to form the t_{2g} levels. b) Crystal field splitting because of the octahedral symmetry. The central atom is Mn and corner atoms are oxygen. c) The crystal field originated due to the electrostatic interactions. The $d_{x^2-y^2}$ is in higher energy levels compared to the d_{xy} orbital in an octahedral symmetry.

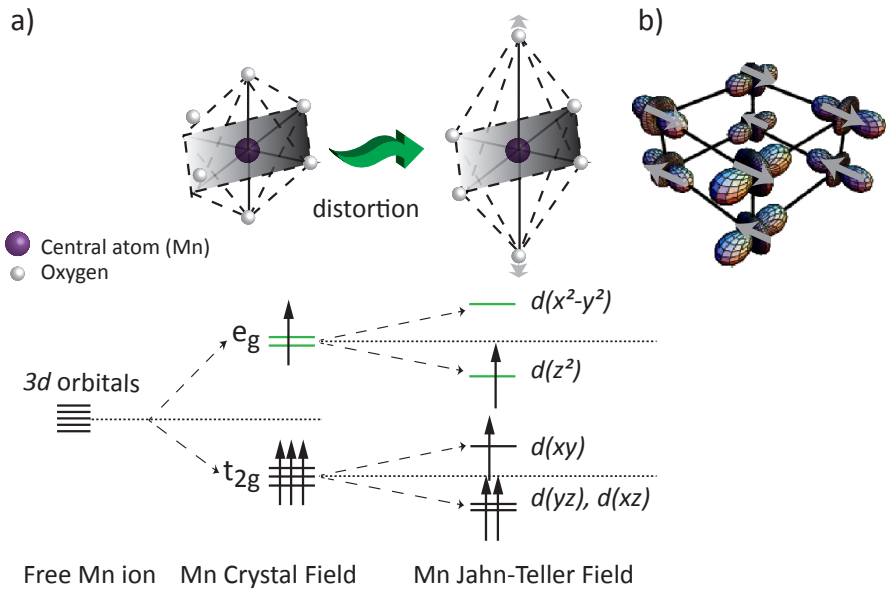

Figure 1.3: Schematic presentation of a) the 3*d* band energy levels for only one manganese ion (left), an octahedral crystal field (middle) and a JahnTeller distortion in the form of a tetragonal crystal field (right). b) The structural disorder stabilises antiferromagnetic arrangement with depicted orbital ordering (adapted from [41]).

Δ, in general, is dependent on the geometry of the crystal, the ionic repulsions, and also an effect called Jahn-Teller.

1.2.3 Jahn-Teller effect

A Mn^{3+} ion in the centre of an octahedron has four electrons in its 3*d* shell which is not fully filled. According to Hund's rule the preferred spin configuration for the system is when spins are all aligned in one direction. This will then put 3 electrons in the lower energy level (t_{2g}) and one electron in the higher energy level (e_g). In this high spin system, the total spin is S=2.

If the octahedron is distorted by straining out-of-plane (along its z-axis), and consequently a compression in the in-plane direction (x-axis and y-axis), a splitting in energy levels occurs (t_{2g} and e_g split), so that the lone electron in e_g is in the lower energy state (figure 1.3). This is known as Jahn-Teller distortion. As shown in the lower panel of figure 1.3, the distortion of the octahedra lowers the symmetry of the cubic structure in a way that the centre of gravities of the t_{2g} and e_g levels remains unchanged. Therefore, the formation of Mn^{2+} or Mn^{4+} is not favourable. However, the total electronic energy of Mn^{3+} is lowered at the expense of an elastic term, hence there

is a tendency of d^4 ions to experience the cooperative Jahn-Teller distortion. Two main proposed mechanism to explain this distortion are one-electron electron-phonon coupling [42] and many body Kugel-Khomskii superexchange [43]. At a transition temperature T_{JT}=700 K, the $3d^4$ Jahn-Teller cation exhibits a first-order cooperative orbital ordering [44] where the stabilised orbitals are $3d_{3x^2-r^2}$ and $3d_{3y^2-r^2}$. Figure 1.3-b represents the A-type antiferromagnetic structure where ferromagnetic (001) planes are coupled antiparallel. This orbital ordering in $LaMnO_3$ has been observed and confirmed by neutron scattering [45] and resonant X-ray scattering [46]. The 3 t_{2g} electrons give a localised spin $S = 3/2$ in all the manganese-oxide perovskites even where the e_g electrons are transformed to itinerant electrons of a narrow band in a mixed Mn^{3+}/Mn^{4+} valence state. However, e_g electrons remain localised in the single valence manganites [47]. Considering the position of oxygen orbitals along the coordinate axis, not any of the d_{xy}, d_{xz} and d_{yz} orbitals overlap with the O 2*p* orbitals. Therefore the only orbitals which are hybridised with O 2*p* orbitals are the e_g levels, thus, these are the only ones involved in the superexchange interactions [44].

1.2.4 Superexchange

Exchange interactions between magnetic moments results in long range magnetic ordering. Direct exchange is when the exchange occurs between neighbouring spins but if the process happens through some intermediate interactions, it is called superexchange or indirect exchange. This can be described as an indirect exchange between non-neighbouring magnetic ions via a nonmagnetic ion which is placed between the 2 magnetic ions. For example, in a system with two transition metal ions of Mn separated by an oxygen ion, if the system was perfectly ionic, each Mn *d* orbital would have one unpaired electron and oxygen would have two electrons in the *p* shell. Figure 1.4 shows that the energy of the system is lowered if the antiferromagnetic coupling occurs since both electrons in an oxygen 2*p* can freely move from oxygen ions into unoccupied Mn 3*d* orbitals.

When the Mn moments have antiferromagnetic ordering the ground state configuration is shown in figure 1.4-a which can be mixed with the excited states (figure 1.4-a' and -a"). In this way, the magnetic ions become delocalised over the Mn-O-Mn bond; therefore the kinetic energy of the system is lowered. On the other hand, if the moments on the Mn atom are ferromagnetically ordered the ground state configuration figure 1.4-b cannot be mixed with the excited states (figure 1.4-b' and b") as a result of the exclusion principle. The antiferromagnetic configuration (a) thus has lower energy than the ferromagnetic configuration (b). The magnetic ordering is typically observed by orbital ordering applied by the Goodenough-Kanamori rules [48, 49] which was later

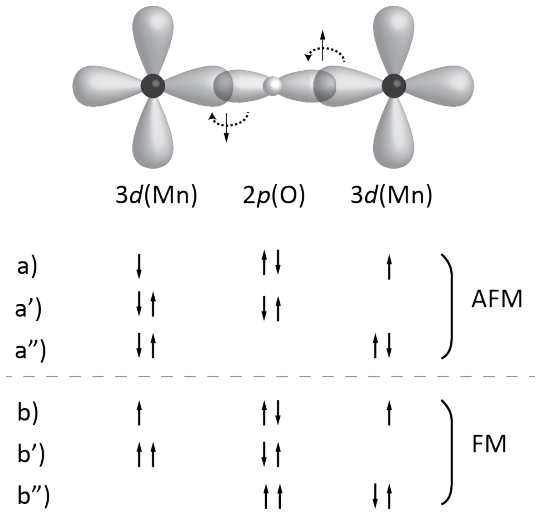

Figure 1.4: Schematically depiction of a superexchange bond in a magnetic oxide. The arrows show the spins of the 4 electrons and their distribution between oxygen and transition metal (Mn) ion with only a single unpaired electron. When the Mn moments have antiferromagnetic ordering (a, a', and a") the ground state configuration is (a) which can be mixed with the excited states (a' and a"). In this way, the magnetic ions become delocalised over the Mn-O-Mn bond; therefore the kinetic energy of the system is lowered. If the moments on the Mn atom are ferromagnetically ordered (b, b', and b") there is no possibility for the ground state (b) to be mixed with the excited states (b' and b") due to the exclusion principle.

modified by Anderson [50]. These rules expect a strong antiferromagnetic ordering when the two magnetic ions have orbital lobes of the 3*d* shells (occupied with a single electron) pointing towards each other and have a large overlap typically occurring for the M-O-M bond angle of 120-180°. On the contrary, a weak ferromagnetic ordering is expected when the singly occupied *d* orbitals have zero overlap due to the symmetry. This is mostly the case when the angle M-O-M is ≈90°. Goodenough explained the phase diagram of mixed valence manganites $La_{1-x}Ca_xMnO_3$ ($0 \leq x \leq 1$) obtained by Wollen and Koehler [51] by superexchange interaction between Mn ions. He assumed the existence of the square and coplanar hybridisation of the dsp^2 for Mn^{3+} and hybridisation of d^2sp^3 for Mn^{4+} leading to the octahedral bonding to its nearest neighbours [52]. Thus, orbital and charge ordering depend on the ratio of the Mn^{4+} to Mn^{3+} ions, and hence determine the magnetic configuration and the distortion of the crystallographic structure. $La_{1-x}Ca_xMnO_3$ exhibits a different type of antiferromagnetism from its parent material ($x = 0$ and $x = 1$). When $x = 0$, $LaMnO_3$ shows an out of plane antiferromagnetism when the in-plane Mn ions are coupled ferromagnetically due to the in-plane overlap of the d_{z^2} orbitals, known as A-type antiferromagnetism (figure 1.1). For the other

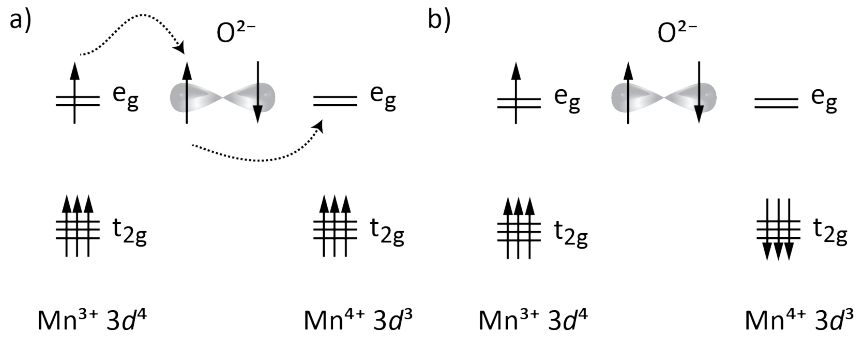

Figure 1.5: Schematic illustration of a) the double-exchange mechanism which leads to ferromagnetic coupling between Mn^{3+} and Mn^{4+} ions taking part in electron transfer only if the neighbouring atoms are ferroelectrically aligned. b) when the d^3 spins are antiparallel; there is a large energy barrier as a result of the Hund's rule interaction preventing the electron hopping.

end parent material ($x = 1$), type G antiferromagnetism is present where each Mn is antiparallel to its six near neighbours. For concentration $x = 0.3$, the compound has the highest mobility with ferromagnetic domains explained by double-exchange [44].

1.2.5 Double-exchange

In some oxides, there is the possibility to have a ferromagnetic exchange interaction due to the mixed valence of the magnetic ion. For example, perovskite manganite compounds such as $La_{1-x}Sr_xMnO_3$ ($0 \leq x \leq 1$), have both Mn^{3+} ($d^4\ t_{2g}^3 e_g^1$) and Mn^{4+} ($d^3\ t_{2g}^3$) ions as a central atom in the octahedral coordination. In this compound, the fraction of x implies the amount of Mn ions in Mn^{4+} oxidation state. In Mn 3*d*, the t_{2g} electrons are less hybridised with the oxygen 2*p*, localised due to the strong correlation effect, and stabilised by the crystal field splitting forming local spin $S = 3/2$ [20]. Such a strong correlation, indeed, affects the broad band e_g electrons which are heavily hybridised with the O 2*p* states, so they become localised in the parent Mn^{3+} compound (for $x = 0$), therefore the perovskite structure forms a Mott-insulator with antiferromagnetic arrangement. The fourth electron in e_g can be itinerant and participate in the conduction by hopping from one t_{2g}^3 core to another, figure 1.5. On the adjacent sites i and j, the electronic configurations ($d_i^4\ d_j^3$ and $d_i^3\ d_j^4$) are considered degenerate. Considering that the Hund' rule exchange coupling ($\boldsymbol{J}_H$) between the t_{2g} and e_g electrons is strong on each site (≈2 eV) [44], the electron can only hop freely if the d^3 electron spins are parallel (figure 1.5-a). However there is a large energy barrier when the d^3 spins are antiparallel as a result of the Hund's rule interaction (figure 1.5-b). In case

of misalignment of the spins by an angle θ in the adjacent sites, the effective hopping interaction (t_{ij}) can be shown by

$$t_{ij} = t^0_{ij} \cos(\theta_{ij}/2), \tag{1.3}$$

where θ_{ij} is the relative angle between the neighbouring spins [20]. The absolute magnitude of the effective hopping therefore varies as $\cos(\theta_{ij}/2)$. The interaction due to the exchange of the conduction electron is called 'double-exchange' (DE) interaction [53] and is ferromagnetic because the transfer is zero when the spins are antiparallel ($\theta_{ij} = \pi$) [11]. The e_g electron hopping can be enhanced by creating hole doping or electron-vacancy influenced by the configuration of the local spins. When θ_{ij} is zero the kinetic energy of the conduction electrons is maximised promoting the metallic ferromagnetic state. By increasing the temperature to near or above the ferromagnetic transition temperature known as Curie temperature (T_C), the orientation of the spins becomes disordered and hence the effective hopping interaction is decreased on average due to the disorder. This results in an increase in the resistivity near and above the T_C, where large magnetoresistance can be expected. The physics of CMR, however, is fascinating and far more complex that can be simply explained by the DE interactions. For further reading, there are several comprehensive review articles as great resources on this subject [22, 54, 55, 56, 57, 58]. The next section is a brief introduction to another family of TMOs, nickelates, that was studied in this thesis.

1.3 Nickelates

An interesting family of perovskites, particularly those composed of TMOs, are nickelates in the form of RENiO$_3$ (RE= rare earth). They have also been considered as a promising platform for an active area of research and have attracted attention owing to their variety of intriguing properties due to the charge transfer gap present in their band structure between the unoccupied conduction band of the Ni 3*d* and the occupied O 2*p* valence band [59, 60]. This gap is influenced by the RE radius and also the temperature, hence when they both increase, the gap starts to decrease until it disappears resulting in an insulator-metal transition (IMT) [61]. Bulk LaNiO$_3$ is the only member of this family which remains metallic at all temperatures as the size of the La ions is so large that the Ni *3d* and O *2p* orbitals overlap. However, this is not the case in ultra-thin films of LaNiO$_3$ which undergoes a IMT [62], or in heterostructures composed of thin LaNiO$_3$ layers where bulk properties are not necessarily present [63]. As an example, enhanced conductivity is observed in superlattices comprised of LaNiO$_3$-SrTiO$_3$ [64]. In recent theoretical calculations, the presence of superconductivity has been predicted in

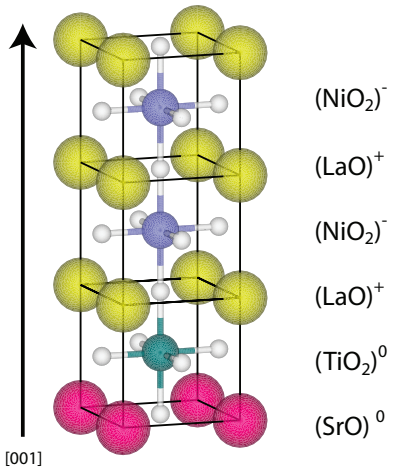

Figure 1.6: Crystal structure at the interface between $LaNiO_3$ and $SrTiO_3$ (001) direction of pseudo-cubic perovskite structure

superlattices containing one unit-cell thick layers of $LaNiO_3$ [65]. The manifestation of quantum confined magnetism in heterostructures of $LaNiO_3$ when layered with magnetic perovskites such as $LaMnO_3$ has been experimentally reported [66, 67] resulting in more efforts to find the origin of the induced magnetism in paramagnetic $LaNiO_3$ [33]. Many of these novel physical effects are associated with interfacial properties, thus the high quality controlled growth of these heterostructures is desirable to be able to design the electronic or magnetic properties by adjusting the layer thickness down to one monolayer. For example in the case of growing $LaNiO_3$ thin films on $SrTiO_3$ (001) substrates, the atomic stacking can be explained as in the following and is illustrated schematically in figure 1.6. Depending on the valence of the cation, the planes within the perovskite structure (AO or BO_2) can be charged or neutral. In the case of $SrTiO_3$ both planes of TiO_2 and SrO are neutral as titanium has valence of $4+$ and strontium $2+$. In contrast, the atomic planes of $LaNiO_3$ are charged as both lanthanum and nickel have a valence of $3+$ leading to excess charge of $+1$ for LaO plane and -1 for NiO_2 (figure 1.6). Therefore, when polar $LaNiO_3$ grows epitaxially along the (001) direction of neutral $SrTiO_3$, a polar discontinuity occurs at the interface which is not energetically stable. A similar scenario is suggested in the case of $LaAlO_3$ on TiO_2-terminated $SrTiO_3$ resulting in a 2DEG at the interface [30], however no superconductivity has been reported to the date of this work in heterostructures of $LaNiO_3$-$SrTiO_3$. Since the physical properties of perovskite oxides are closely related to their crystal structure and can be changed drastically by small distortions of the octahedral unit, the next section is devoted to a brief introduction of perovskite structures and their symmetries.

1.4 The perovskite structure-in brief

The most studied family of TMOs belongs to a family with structures known as 'perovskite' oxides, named after a Russian scientist, Aleksevich von Perovski, and was discovered by Gustav Rose (1839) from the mineral calcium titanium oxide ($CaTiO_3$). Their chemical formula is ABO_3 that contains corner sharing octahedra BO_6 where B is a transition metal cation positioned at the centre of the octahedra, surrounded by 6 oxygen atoms at each corner (figure 1.7). The whole family of perovskite compounds

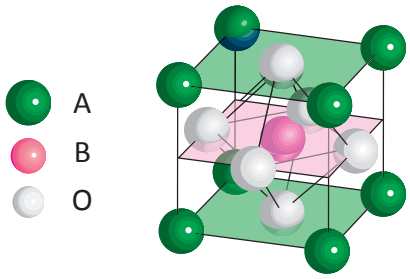

Figure 1.7: A schematic of ABO_3 perovskite structure. This is the ideal cubic $Pm\bar{3}m$ space group with the highest symmetry in the perovskite family.

can be synthesised with an extremely broad diversity of element combinations resulting to exceptionally different physical properties: Perovskites structures have the ability to accommodate both small and large cations in the B-site and A-site, respectively. Depending on the composition of the cations and their ordering they exhibit insulating or metallic behaviour. Further flexibility to host variety of cation sizes is provided by the distortion of the ideal cubic structure leading to a notable diversity in the type of magnetic ordering or structure. Finally they are known for their remarkable tolerance to vacancy formation. In general the replacement of A-site and B-site cations must follow a rule imposed by ionic radii of the compounds, put forward by Goldschmidt (1926) [68] known as the 'tolerance factor':

$$t = \frac{r_B + r_O}{\sqrt{2}\,(r_A + r_O)}, \tag{1.4}$$

where r_A, r_B and r_O are the ionic radii of the large A-site cations, small B-site cations and the anion (oxygen), respectively. The perovskite structure (ABO_3) occurs mostly at high temperature, whereas atoms are displaced by minuscule amounts at room temperature causing a small distortion of the u.c., specifically oxygen octahedron [69]. Typical perovskite-type compounds commonly show tolerance factors of between 0.78 and 1.05 [70]. The high-symmetry ideal structure of perovskites belongs to the space

group $Pm\bar{3}m$ with a basis including 5 atoms shown in figure 1.7 [70]. By changing the ionic radii of the cations, the characteristic BO_6 octahedral unit is deformed and rotated by small amounts and therefore the symmetry of the u.c. is lowered from the ideal cubic structure to tetragonal, orthorhombic, rhombohedral and monoclinic. When $t < 1$, the

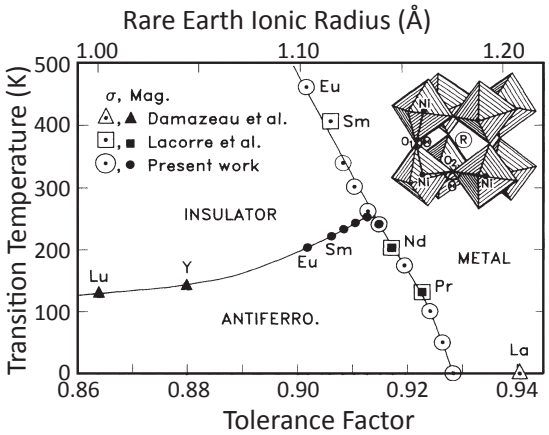

Figure 1.8: Insulator-metal-antiferromagnetic phase diagram for $RE\text{NiO}_3$ versus the tolerance factor and also to the rare earth (RE) ionic radius [61].

A-site cation is smaller than the hole linking the oxygen octahedra, therefore, the A-site cation is not able to bond with all twelve surrounding oxygen anions successfully. An excellent example to show how the tolerance factor plays a significant role in perovskite structure is the insulator-metal transition (IMT) in rare earth nickelate perovskites which is related structurally with the progress of their tolerance factor. The drop in the tolerance factor is accommodate by so-called 'buckling' of the NiO_6 which results in bending of the Ni−O−Ni bond resulting in the reduction of overlapping orbitals and promoting the insulating phase over the metallic one (figure 1.8 [60]).

1.4.1 Glazer notation

Glazer [71, 72] described and classified the changes in the symmetry of the u.c. as a result of tilting of the oxygen octahedra by giving it a notation as follows. All tilts were explained as combinations of component tilts about the three pseudocubic axes of [100], [010] and [001] where the magnitude of the tilt about each axis was shown by the letters a, b and c respectively. Wherever the octahedra were tilted equally about two axes, this was represented by repeating the suitable letter; for example aaa shows equal tilts about all three pseudocubic axes and abc shows unequal tilts about each pseudocubic axis.

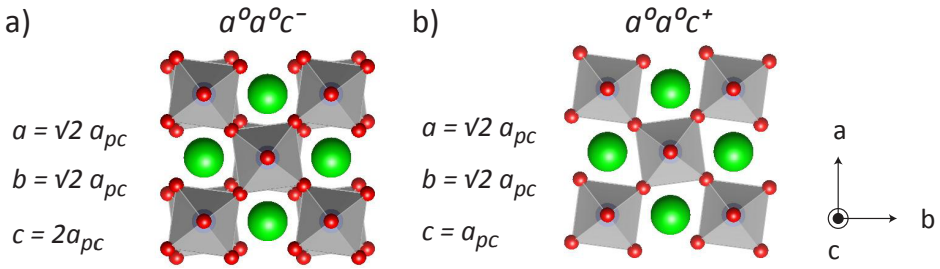

Figure 1.9: Two BO_6 octahedron tilting systems a) $a^0a^0c^-$ and b) $a^0a^0c^+$ are shown schematically. In both systems the pseudocubic (pc) lattice becomes tetragonal after the rotation about the c-axis, for the antiphase rotation the c-axis lattice parameter is doubled.

The superscript after each letter denotes to the phase of the tilting i.e., in-phase tilting is denoted with a $^+$, antiphase tilting is denoted with a $^-$ and no tilting with ^{0}. Therefore, the notation $a^0a^0c^-$ represents a perovskite with antiphase tilting only about the c pseudocubic (pc) axis whereas $a^0a^0c^+$ exhibits an in phase tilting about the c axis, as are shown in figure 1.9. Rotations of BO_6 octahedra lead to tetragonal symmetry with elongation of the in-plane lattice parameters a and b to $\sqrt{2}a_{pc}$ with no change in the out-of-plane (c-axis) for $a^0a^0c^+$ rotation. However in $a^0a^0c^-$ system where octahedral rotations along single out-of-plane axis is antiphase, the c-axis lattice parameter doubles to $2\ a_{pc}$. Howard and Stokes [73] showed that in fact only 15 distinct space groups were derived from the 23 tilting notations suggested by Glazer. 15 distinct tilt systems are shown in figure 1.10. The Glazer notation for the bulk materials used in this thesis is as follows. $SrTiO_3$ substrate ($Pm\bar{3}m$) shows no tilting of the octahedra shown by $a^0a^0a^0$. In $LaNiO_3$ t is smaller than one (t=0.95), which favours the tilting and rotation of the oxygen octahedron towards one of the A-site cations generating a rhombohedral distortion. Thus, $LaNiO_3$ has a $R\bar{3}c$ group symmetry with distinct Glazer tilt system of $a^-a^-a^-$. $LaMnO_3$ undergoes Jahn-Teller distortions with space-group symmetry of $Pnma$ or $Pbnm$ ($a^+b^-b^-$) and has an orthorhombic structure.

1.5 Motivation, aims and objectives

As stated in the overview, with further advancement in the development of nano-devices, the necessity for the fabrication of high quality materials becomes stringent. In such advanced designs, often, one single material will not exhibit the desired properties and combining multiple existing materials becomes essential. Deeper understanding

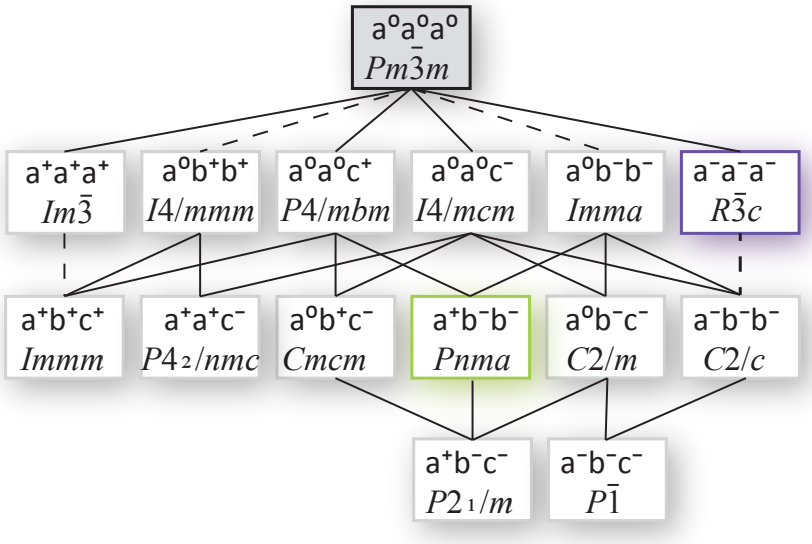

Figure 1.10: Glazer tilt system is shown with the group and sub-groups and the relation between them. The figure is reproduced from [74].

of the relationship between the physical properties of materials (such as magnetic, electronic, surface chemical properties) and their nanostructure is required which can only be achieved through atomic engineering of new materials.

There are a number of issues to be focused on concerning the optimisation of growth processes for thin films and their superlattice structures as each individual layer can have its own optimal conditions for growth, which can be different to that of the other constituents of the superlattices. When stacking different layers, the optimal growth for each of the layers relies on the interaction and the mismatch between each layer. Conversely, a complete multilayer is of interest due to its functionality and specific physical properties such as magnetic, electrical and structural properties. This highlights the fact that growth needs to be optimised for each layer but the final optimisation is defined from a material point of view and coupling of all the relevant properties.

This thesis is aimed at investigating further examples of perovskite superlattices grown by ultra-high vacuum (UHV) PLD. This system was equipped with RHEED that allowed both *in-situ* monitoring of the deposition in a layer-by-layer growth fashion and surface structural analysis. Transition metal oxide materials (TMO), specifically [RE(TM)O_3], where RE was Lanthanum (La) and the TM was either Mn or Ni, were chosen to be explored. The primary aim was to optimise the growth of an individual constituent perovskite material (e.g. $LaNiO_3$ and $LaMnO_3$), and then combine them in superlattice structures of varying periodicity i.e.: artificially layered structures with

repeating units varying from 5 u.c., down to a single u.c. (as calibrated using (RHEED). If individual layers in a heterostructure are as thin as one u.c., it is arbitrary, or perhaps meaningless, to distinguish the distinction between a superlattice of different constituents separated by interfaces and a completely new single-phase compound. Therefore these heterostructures can appropriately be called 'artificially layered' compounds. One significant difference can be identified between naturally self-ordered materials and the artificially layered superlattices; A self-ordered compound is at least at some point of its fabrication process thermodynamically in full equilibrium, whereas artificially layered compounds show a kinetically stabilised metastable state due to the high energy barrier for diffusion provided by physical vapour deposition techniques such as PLD [32]. It will be shown in this thesis that detailed *ex-situ* analysis of the microstructure of the artificially layered compound is essential to truly understand the nature of the materials properties required for devices. One of the fundamental aspects that has not been considered in the theoretical calculations is the effect of ultra-short-period superlattices on the BO_6 octahedral rotations and distortions. The mechanisms involved in the length scale of the octahedral distortion relaxation are not yet fully exploited. Two of the most often occurring symmetries in perovskite oxides are orthorhombic ($a^-a^-c^+$) and rhombohedral ($a^-a^-a^-$), and the schematic representation of them are shown in figure 1.11. The length scale and strength of the interfacial octahedral coupling between these two symmetries can be exploited in the $LaNiO_3$/$LaMnO_3$ superlattices. Indeed by using misfit strain in epitaxial growth of thin films, any of these tilting systems can be present in the perovskite heterostructures and in fact it will differ from their bulk symmetry [75].

Motivated by these open questions, a surface technique such as RHEED was combined with transmission electron microscopy to identify the characteristic octahedral rotation. Identifying the position of oxygen atoms in perovskites has been one of the main challenges in this field [75]. This study hopes to bring growth scientists' attention to consider RHEED not only as a technique to control the layer-by-layer growth but also as a tool which can monitor *in-situ* the distortion in the perovskite oxides if the electron beam is scattered from the appropriate high symmetry crystallographic direction.

In conclusion, artificially layered phases of the compounds $(LaNiO_3)_m/(LaMnO_3)_m$ were grown in thin film form that are not stable in bulk. Approaching this from a growth and structural analysis point of view highlighted the importance of comparing growth data with a detailed structural analysis. This allows for a full understanding of the growth mechanisms and structural formation that can drastically affect the physical properties. This is the first and most important step in designing novel nanoscale devices incorporating perovskite oxides. The remainder of this chapter outlines the structure of this thesis.

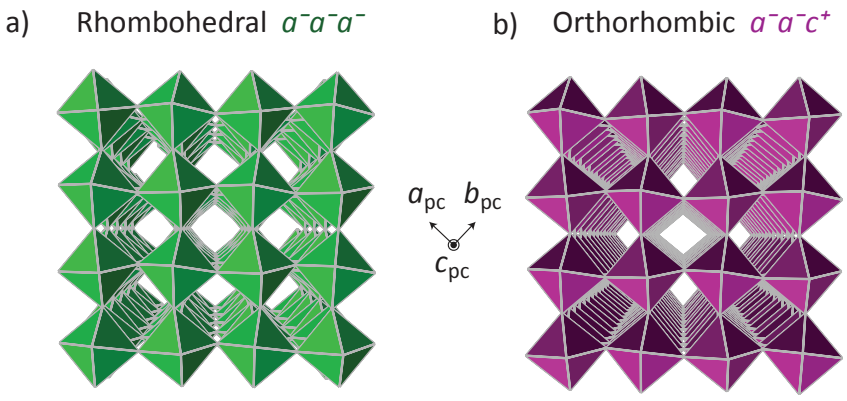

Figure 1.11: Two common tilting systems adopted for perovskite oxides a) $a^-a^-a^-$ and b) $a^-a^-c^+$, are shown schematically. Rotations about the [111] direction in cubic lattice result in the rhombohedral structure (such as $LaNiO_3$), whereas rotations about the [110] direction lead to the orthorhombic symmetry one of the most seen rotation patterns in perovskite (such as $LaMnO_3$).

1.6 Outline of the thesis

In chapter 2, the physics behind PLD is explained and relative growth thermodynamics are discussed. A detailed surface analysis and a guide on how to calibrate a RHEED system is also presented. To achieve the main aim, growth of low-dimensional oxide superlattices, the growth condition was separately optimised for each constituent and then samples were characterised using various techniques explained in detail in chapter 3 such as X-ray diffraction (XRD), atomic force microscopy (AFM), transmission electron microscopy (TEM) and others. In chapter 4, $LaMnO_3$ thin films were grown on $SrTiO_3$ (001) substrates that showed the ability to self dope by acquiring an oxygen non-stoichiometry. By varying growth temperature at two different regimes of oxygen pressure, the intrinsic ground states originated by changing the oxidisation environment during the deposition are investigated and discussed. The structural, transport, and magnetic properties of these $LaMnO_3$ thin films were characterised. A systematic correlation between the *c*-axis lattice parameter and magnetic structure was observed due to the change in the oxidation state of the Mn ion related to the crystal environment. Growth of the $LaNiO_3$ thin films were optimised in chapter 5 to achieve metallic $LaNiO_3$ with high crystallinity. $LaNiO_3$ is known to be sensitive to the oxygen environment and more likely to develops Ni^{2+} ionic state instead of the Ni^{3+} in $LaNiO_3$. Since small amount of this ionic state can affect the electronic properties, it is crucial to investigate the microstructures of the films after the growth. Small amounts of the Ruddlesden-Popper

compound La_2NiO_4 was detected both in scanning transmission microscopy (STEM) images and grazing angle in-plane X-ray diffraction.

After the growth conditions were optimised for $LaNiO_3$ thin films in chapter 5, it was important to explore the effect of dimensionality on the $LaNiO_3$ films. For this reason, in chapter 6 initially the role of surface termination on the growth and heterointerfaces that were formed are explained. Ultra-thin films of $LaNiO_3$ (e.g. 2.5 and 3 monolayers) were skilfully deposited using RHEED which was also used for the surface structure determination. Surface electronic properties of the ultra-thin films were characterised by X-ray photoelectron spectroscopy (XPS), giving an insight to the insulating state of the ultra-thin films. This knowledge and experience was a prerequisite to the deposition of artificially layered heterostructures. Chapter 7 presents a detailed study of the growth of $(((LaNiO_3)_n)/((LaMnO_3)_n))_x$ superlattices, where $n = 1$, 2 and 5 and x was varied to reach 100 monolayers thickness. Detailed surface analysis revealed a $(\sqrt{2} \times \sqrt{2})\ R45^\circ$ tetragonal arrangement due to the distortion of the MnO_6 octahedra. Finally in chapter 8, the conclusions and an overview of the results and discussions are presented with some suggestions for the direction of future work in this field.

Chapter 2

Pulsed laser deposition and reflection high energy electron diffraction

2.1 Introduction

In the past three decades pulsed laser deposition (PLD) has emerged as an important and popular deposition technique to fabricate a wide range of novel materials [76, 77, 78]. The preliminary experiments in PLD were carried out in the mid-sixties following the invention of high power lasers, but it was not popularised until the late-eighties, when it was revisited by the discovery of high-temperature superconducting films. Today PLD is being recognised as a reproducible and fast technique for device-quality oxide film growth. The technique gained such popularity due to the intrinsic versatility, flexibility, and rapidness of the method enabling the growth of a wide range of materials from metals, through binary compounds, to complex oxides. Since the laser is located outside of the deposition chamber, the growth can take place across a wide range of vacuum regimes from ambient pressure to ultra-high vacuum. The wide range of deposition pressures along with stoichiometric transfer of the materials from the target onto the substrate allow deposition of various families of materials such as semiconductors, complex oxides, nitrides, and carbides. The pulsed nature of PLD also permits deposition of heterostructures and multilayers of different compounds. In PLD, the deposition process is far from thermal equilibrium such that the ablated highly energetic particles in a low background pressure can form metastable phases. Physical proprieties such as stress, texture, electronic and magnetic properties of the films can be manipulated by changing the kinetic energy of the ablated species [79].

Reflection high-energy electron diffraction (RHEED) can be used as an *in-situ* surface structure monitoring technique especially after the invention of high-pressure RHEED which made the growth monitoring of oxides at higher pressures possible [80]. While precise control of the growth rate is possible due to oscillation of the RHEED specular spot intensity, as a result of the layer-by-layer growth, valuable information can also be obtained from the RHEED patterns about the growth and the type of surface structure. In this thesis PLD equipped with *in-situ* RHEED was used to deposit artificially layered superlattices of perovskite materials. In this chapter the basics and principles of PLD and RHEED are presented. Furthermore the factors that determine the growth quality of the films are also discussed.

2.2 Pulsed Laser Deposition

PLD is a physical vapour deposition (PVD) technique that uses a laser to ablate material from a target and subsequently grow a film on a substrate. The laser source is usually an excimer or Nd-YAG (355 nm) with a highly energetic pulsed laser beam pulse (frequencies between 0-100 Hz), which is focused onto a ceramic or single crystal target to evaporate materials in the form of a plasma plume. By changing the laser gas medium the wavelength can be varied; ranging from XeF at 351 nm, to ArF at 193 nm. One very stringent requirement to obtain well-defined interfaces is the control of growth on an atomic scale. The growth is defined initially by the adsorption of atoms (so-called adatoms) onto a surface, which is highly dependent on the deposition conditions.

In PLD the experimental setup is relatively simple and is shown schematically in figure 2.1. It consists of a laser, a vacuum chamber with required pumps, a target holder with motors for scanning, a target material (typically a sintered pellet or single crystal), a heater stage to which a substrate is mounted, and a gas inlet with a range of pressure gauges working at various vacuum regimes.

A substrate is placed opposite the target and perpendicular to the direction of the plume (figure 2.1) generated when the laser pulse(s) strike the target. Vaporisation and ionisation take place due to the interaction of photonic energy of the excimer laser beam with the target material, consequently converting photon energy to kinetic energy. The PLD plume consists of ions, electrons and highly energetic particles. The substrate is heated to promote the surface mobility and improve the crystallinity of the resulting thin films. To keep the stoichiometry constant to that of the target, deposition takes place in an oxygen atmosphere or with other gases presents as a background. The possibility to maintain a high oxygen background pressure during deposition accompanying the ability to grow stoichiometric films from a single source, is what makes PLD a favourable

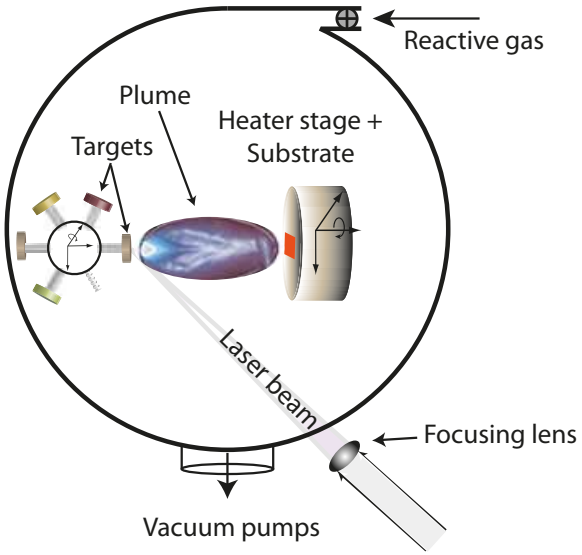

Figure 2.1: A schematic of a PLD experimental setup. The main components are: target holder, heater stage with a mounted substrate, the laser beam and a focusing lens outside of the PLD window. Heater stage has freedom to move about the marked axis.

ablation technique for complex oxides due to the stoichiometric transfer of particles.

2.2.1 Principles of PLD

A deposition chamber is back-filled typically with a reactive gas (e.g. O_2) to promote surface reactions and to conserve the stoichiometry of ablated materials. The reactive gas for the growth of complex oxides is molecular oxygen in the pressure range of from 10^{-4} to 0.5 mbar. In this way, ablated species are transferred from the target onto the heated substrate placed opposite the target while maintaining the expected stoichiometry. The substrate temperature was controlled using a radiative heater which can typically go up to 1000 °C. By tuning the kinetic energy of the adatoms in the plume and varying the substrate temperature, the growth kinetics can be optimised from the wide thermodynamic conditions available [31]. Apart from the freedom for growth manipulation and ease of setup, PLD has several other advantages compared with other epitaxial thin film deposition techniques, specifically for complex oxides. Firstly, having the energy source outside of the vacuum chamber makes PLD a versatile technique and allows work on various materials systems without concerns over cross contamination.

It is possible to use one single laser as a source of multiple chambers by guiding

the laser beam though several optical elements. It is necessary to use UV-laser compatible optics for mirrors and focussing lenses. An attenuator is placed in the beam path to accurately set the energy transmitted while the laser is running under its more stable conditions. Another important part of PLD is the materials for the laser port window in the vacuum chamber to allow transmittance of both visible light and also UV light. (such as UV-grade quartz). The viewport windows of a PLD chamber equipped with RHEED must not transmit X-rays and UV light (for the safety of the users). With *in-situ* monitoring, such as RHEED added to PLD, the quality of PLD grown thin films has been improved significantly. To better understand how to control these effects, the following sub-sections explain the nature of ablation using an excimer laser.

2.2.2 Physics behind PLD

When an excimer laser beam irradiates the surface of a solid material, the high energy photons will be absorbed effectively (3.5 to 7.9 eV corresponding to wavelengths of 351 to 157 nm). For example, the laser used in this work was a KrF laser with a photon energy of 5 eV (248 nm) [81]. As a result of the absorption of the excimer radiation an electronic transition will be induced leading to conversion of electromagnetic energy to an electronic excitation. If the excitation energy is of a similar value to the binding energy of the electrons in the materials, then the excited material will be fragmented. The remainder of the beam energy will be converted to kinetic energy in the shape of vibration or rotation modes, and will give rise to rapid heating of the target. A plume forms in front of the target, and is initially a dense vapour of ablated material originating from the target, if the energy density is sufficiently high. With additional laser energy irradiating the target, the pressure and also the temperature of this plume increases resulting in explosive evaporation and forming a plasma of ionised material. This blast wave, when combined with the low pressure background gas in the chamber, is very directional and expands normal to the target surface carrying atoms, electrons, ions, molecules, and micrometre size particulates. The last two species are not desirable and should be avoided, especially any particulates. The ablation process takes place within tens of nanoseconds (typical excimer laser pulse duration is about 10-30 ns), while absorption of the laser light into the bulk material happens in picoseconds. In this initial step, a fraction of the light is reflected (R) and the remainder is absorbed and then the intensity of the pulse decreases exponentially [81] such that;

$$I(x) = (1 - R)I_0 e^{(-\alpha x)} \tag{2.1}$$

where x is the penetration depth, I_0 is the laser intensity at the surface (where $x = 0$),

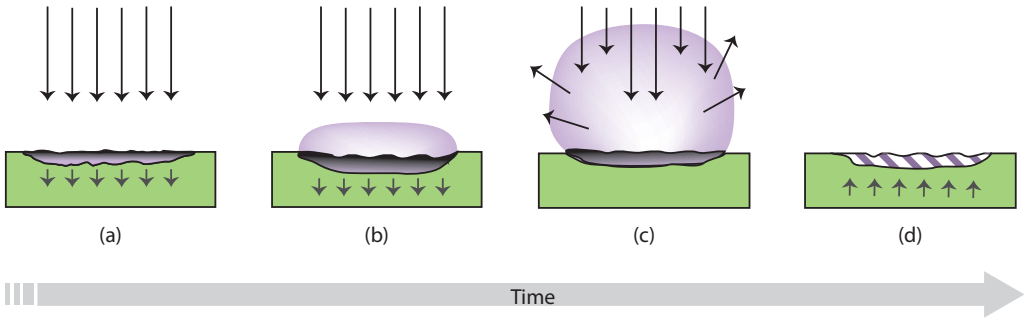

Figure 2.2: Schematic illustration of the ablation process by laser irradiation of a PLD target (green). (a) Pulsed laser (long arrows) is initially absorbed, melting and vaporisation begin (shaded area is an indication of the melted material) and the melted area propagates further into solid (short arrows show the motion of the solid-liquid interface). (b) Vaporisation continues accompanied by laser-plume interaction forming a dense vapour in front of the target. (c) Expansion of the plasma plume due to laser interaction with the dense vapour. (d) Re-solidification occurs as the solid-liquid interface recedes. The next laser pulse interacts with some or all of re-solidified region.

R is reflectance, and α is an absorption coefficient. Note that $1/\alpha$ is the absorption penetration length which is about 100 nm for a considerable number of oxide materials using an UV excimer laser [31]. Figure 2.2 illustrates schematically the process of laser-target interactions. Due to this absorption, the photonic energy will excite the electrons in target material over a picosecond timescale (figure 2.2-(a)).

The second step is the motion of the solid-liquid interface into the bulk as the heat transfers further into the target material accompanied by vaporisation. The induced rapid heating by the laser, and consequently the volume of re-solidification is related to the laser energy. The depth of this diffusion can be calculated from [31]

$$\lambda_{\text{thermal}} = 2(\alpha_{\text{thermal}}\ \Delta t)^{1/2} \tag{2.2}$$

where Δt is the duration of the laser pulse, λ_{thermal} is the thermal diffusion length and thermal diffusivity, α_{thermal}, is equivalent to

$$\alpha_{\text{thermal}} = K/\rho c, \tag{2.3}$$

where ρ is the density of mass, c is the specific heat capacity, and K is the thermal diffusivity. The increasing pressure of the dense vapour formed in front of the target, drives the ejection of material from the surface of the target (figure 2.2-(b)). The plasma plume is created as a result of multi-photon ionisation of the gaseous phase, that is

when the temperature on the target surface can go beyond the vaporisation temperature of the material. Unless using very short-length laser pulses, the ejected material will be irradiated by the remainder of the laser pulse and become ionised (figure 2.2-(c)). This will result in further excitation of the species in the plume and their ionisation. The excitation state of free electrons occurs causing emission from the plasma to be visible [31, 82]. After the laser irradiation stops, the temperature of the target will decrease and re-solidification will occur (figure 2.2-(d)). This can leave a frozen capillary wave at the surface of the re-solidified target and the next laser pulse will react with this topography (figure 2.2-(d)) [76].

To create a plume of material using a laser, it is essential to know its ablation threshold. To identify this minimum required energy density, there are two important parameters which are influenced by the transport of energy in a material: the photon diffusion depth and the heat conduction. The former is dependent on the laser pulse duration and the latter is an inherent property of the material. The strong dependency of the absorption depth on the laser wavelength should be also noted. By varying the laser spot size, the amount of target material affected by the laser varies. The ablation threshold for a defined volume of material can be estimated by [31]

$$Q_{\text{heat}} = C_S\,(T_{\text{melt}} \;-\; T) \;+\; \Delta\; H_m \;+ C_m(T_{\text{vap}} \;-\; T_{\text{melt}}) \;+\; \Delta H_{\text{vap}} \qquad (2.4)$$

where Q_{heat} is the total energy needed defined by adding the required energy to increase target temperature to its melting point where C_S is the specific heat capacity ($C_S\,(T_{\text{melt}} \;-\; T)$), added with $\Delta\; H_m$ the heat of melting, summed up with required energy for vaporisation of melted target material where C_m is the mass-specific heat capacity ($C_m(T_{\text{vap}} \;-\; T_{\text{melt}})$) and finally plus ΔH_{vap} the heat of vaporisation. Shown below are the typical characteristic of a single pulse from an excimer laser:

Length of laser pulse	Laser energy density	Energy density of a single pulse
20 ns	2 J/cm^2	10^8 W/cm^2

2.3 Thin film growth

Film growth can be influenced by several parameters such as the amount of ablated materials by each laser pulse, mobility on the surface of the substrate, gas pressure, intrinsic parameters such as the strain induced due to lattice mismatch between the substrate and the film, and compatibility between interfaces. These factors also alter the physical properties of the thin films or superlattices. This section describes the factors that will determine the growth mode of thin films.

2.3.1 Growth modes

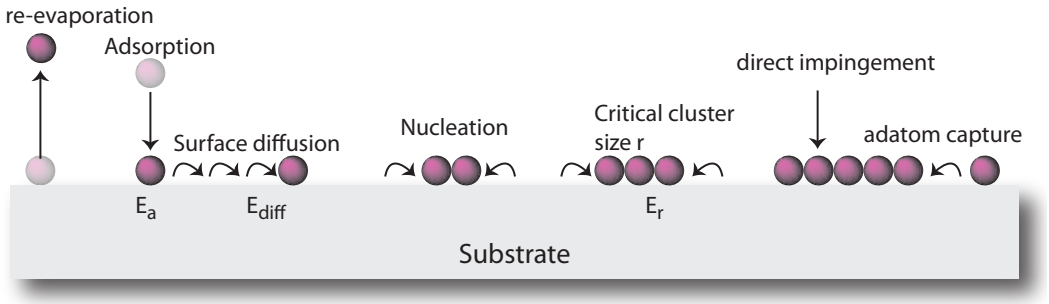

Figure 2.3: A schematic of the atomistic surface processes that can occur during layer growth. Small clusters are metastable but they begin to be stable at a critical island size r.

As the laser is fired at the target surface, the content of the plume which consists of atoms, ions, electrons and highly energetic particles, will subsequently impinge upon a heated substrate surface where they can interact freely. Following the arrival of an adatom at the surface there are several processes that can occur at the growth front which are illustrated in figure 2.3. These processes occur at a given rate defined as R_{surf}, which is given by [83]

$$R_{\text{surf}} = R_0 exp(E_a)/k_B T, \tag{2.5}$$

where R_0 is the attempt rate of the process and related to the frequency of the lattice vibration of the adatoms. This attempt rate (R_0) is exponentially dependent on the activation energy of the process (E_a), the inverse of the Boltzmann constant (k_B), and absolute temperature (T). One of the more probable situations that occurs is that the adatom is absorbed and remains on the surface. The probability of this process is known as the 'sticking coefficient' and it depends on both the arrival rate of any species and the nature of the surface. There are two categories of adsorption: physisorption which is identified by weak forces such as van der Waals' forces; and chemisorption which occurs when an atom is chemically bonded to the surface resulting in the generation of new chemical bonds at the adsorbent surface. If the substrate temperature is too high, incident atoms can re-evaporate. For epitaxial growth, it is necessary to elevate the substrate temperature to benefit from a higher diffusion rate across the surface and allow the adatoms to reach a stable nucleation site. Another possible process is multiple adatoms forming an island on the surface. Following nucleation, growth of the layer then proceeds through the chemisorption of adatoms being captured at nucleation sites. Chemisorption falls into two different categories depending on whether the growth of

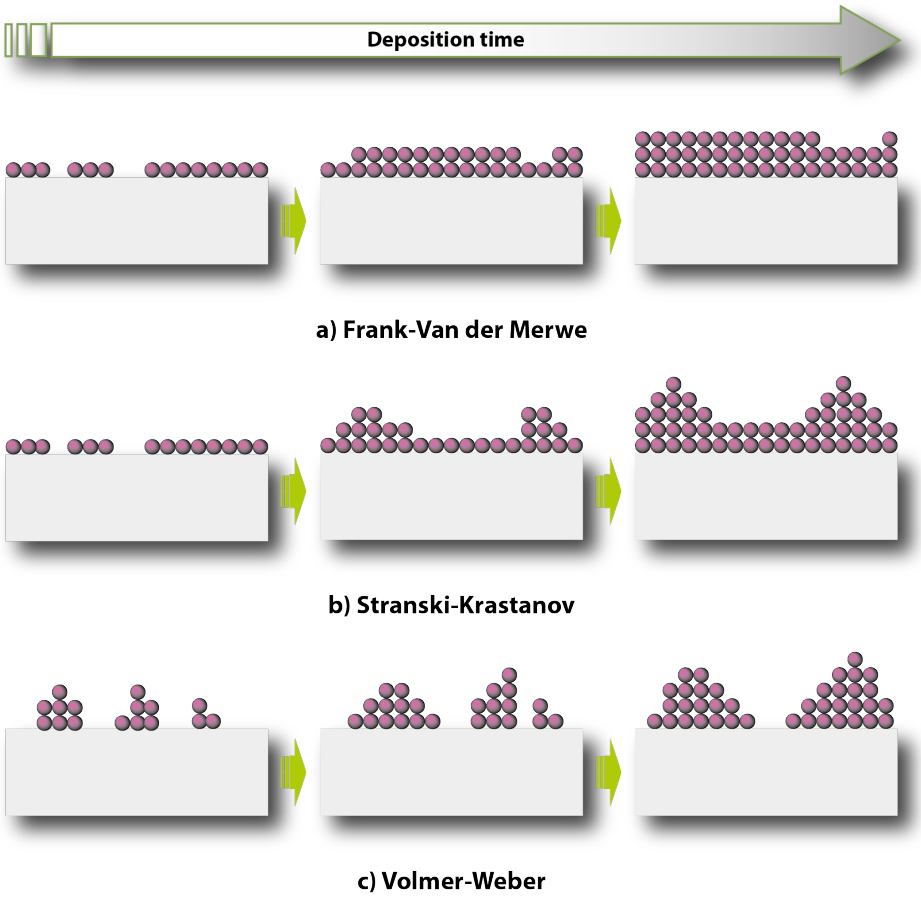

Figure 2.4: A schematic illustration of three basic growth modes possible as deposition proceeds. (a) layer by layer (Frank-Van der Merwe), (b) 2D - 3D transition (Stranski-Krastanov), (c) island / 3D growth (Volmer-Weber).

layer occurs on a substrate of the same material called 'homoepitaxy' or of different materials known as 'heteroepitaxy'.

Thin film growth is generally divided into three major modes: (a) Frank-Van der Merwe (or layer-by-layer growth); (b) Stranski-Krastanov ; and (c) the Volmer-Weber (or island growth mode). These three different growth modes are depicted schematically in figure 2.4. Figure 2.4-(a) shows the situation for an epitaxial growth when layers are formed upon the completion of the previous layer. This mode is also known as 2D growth; however, this growth mode itself is divided in to many types. Here, the smallest nuclei grow in a 2D layer, forming small islands. In this mode, the bonds between layers are stronger than that of the layer to the substrate. Once a full layer is formed, the nucleation starts for the subsequent layer with slightly weaker bonding energy to the

previous layer and this bonding strength becomes progressively weaker until the layers are bonded together with their bulk-type bond strength. The Stranski-Krastanov mode, which is shown in figure 2.4-(b), is one step away from the layer-by-layer growth as the 3D island formation starts just after the completion of a few 2D monolayers. This is attributed to the unfavourable surface energy formation of 2D plane of materials after growth of the initial monolayers. Figure 2.4-(c) represents a 3D island (Volmer-Weber) growth mode when the growth propagates in all directions instead of 2D, so 3D islands form immediately on the surface.

The growth mode of a thin film can be drastically changed by manipulation of the deposition parameters. However, variations in the growth modes can be explained by a thermodynamic model of the surface energy and nucleation processes. If this process is considered semi-quantitatively, the three growth modes mentioned above can be explained by the trade off between energy terms. Strained epitaxially grown layer can be illustrated by a hemispherical island on top of the substrate (figure 2.5). If this hemispherical island nucleates on top the previous layer, the net free energy is given by [84, 85]

$$\Delta G = \frac{2\pi r^3}{3}\Delta G_v + \pi r^2 \gamma + \Delta G_s, \tag{2.6}$$

where the net free energy (ΔG) is shown by the three different energy terms and γ is the interfacial energy. The first energy term, $\frac{2\pi r^3}{3}\Delta G_v$, shows the free volume energy for a relaxed island in regards to a strained epitaxial layer or a flat surface. In this section subscripts s, v and f denote the substrate, vapour and film respectively. The second energy term $\pi r^2\gamma$ is the interfacial energy between the relaxed island and the strained layer. The third energy term ΔG_s comes from the strain energy difference between the film layer from before and after nucleation of the island, such that [84]

$$\Delta G_s = \frac{1}{2}\left(\epsilon^2 - \underline{f}^2\right) Y h A, \tag{2.7}$$

where ϵ is the mean misfit strain as a result of the island nucleation and $\underline{f}$ is the misfit defined as

$$\underline{f} = \frac{a_0(s) - a_0(f)}{a_0(f)}, \tag{2.8}$$

where $a_0(s)$ is the lattice parameter of the substrate and $a_0(f)$ that of film. In equation 2.7, Y is the layer's Young modulus, h is defined as the epitaxial layer thickness, and A is the interface area with the island (πr^2) which is under strain. The critical radius of an island which is formed of a stable and non-dissociable nucleus (when $d\delta G/dr = 0$) is

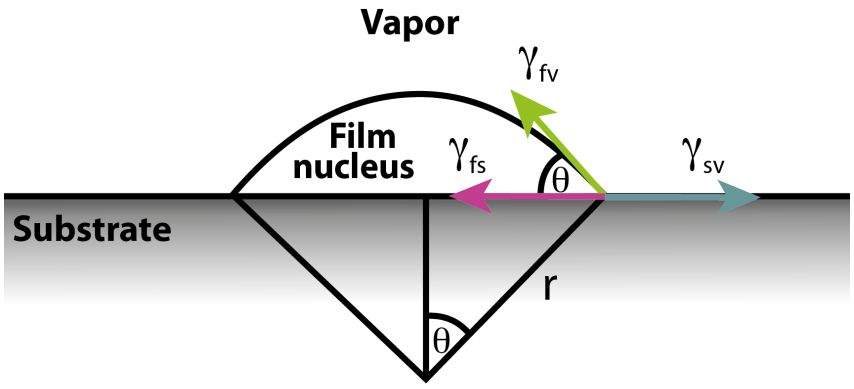

Figure 2.5: A schematic diagram of nucleation on the surface. The nucleation of a droplet from a vapour can be described as $\gamma_{sv} = \gamma_{fs} + \gamma_{fv}\cos(\theta)$ where (θ) is the wetting angle and γ is the interfacial energy.

given by [84]

$$r^* = -\frac{\left[\gamma + \frac{1}{2}\left(\epsilon^2 - \underline{f}^2\right) Y h\right]}{\Delta G_v}. \tag{2.9}$$

Hence the critical thickness for the onset of Stranski-Krastanov growth (when $r^* = 0$) is calculated to be

$$h^* = -\frac{2\gamma}{\left(\epsilon^2 - \underline{f}^2\right) Y}. \tag{2.10}$$

Two possible scenarios exist in epitaxial growth as a result of compressive strain and these are shown schematically in figure 2.6. Below the critical thickness, the deposited layer can accommodate the induced strain by increasing its c-axis lattice parameter (only if c is out-of-plane). In the second situation film, the strain is relaxed by introducing a misfit dislocation. The atomistic nucleation model can help to understand the process of growth from vapour phase using Young's equation and capillary theory [86]. The nucleation of a droplet from a vapour can be described as shown in figure 2.5 [31]. Taking into account the conservation of mechanical equilibrium for components of tensions which are parallel to the interface between the two phases, Young's equation can be written as

$$\gamma_{sv} = \gamma_{fs} + \gamma_{fv}\cos(\theta) \tag{2.11}$$

where (θ) is the wetting angle, and γ is the interfacial energy. According to Young's equation the three mentioned growth mode can be explained. In the situation of 3D island growth mode, $\theta > 0$ so $\gamma_{sv} < (\gamma_{fs} + \gamma_{fv})$. This can result in an island growth mode if the surface tension of the film material is greater than that of the substrate

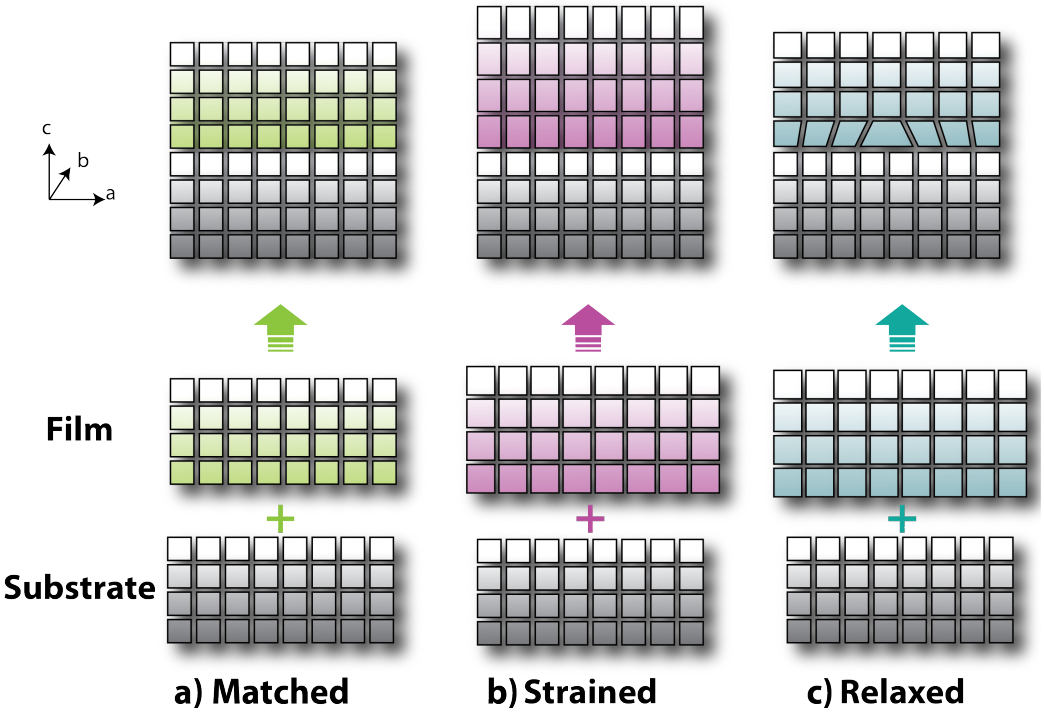

Figure 2.6: A schematic of heteroepitaxial growth of thin films. a) A matched epitaxial growth when the substrate and lattice have the same in-plane lattice parameter. b) The film and the substrate do not have the same lattice parameter but because of the epitaxial growth, the film layer is strained to the substrate and is matched in-plane but elongated out-of-plane. c) The lattice mismatch is too large therefore the system is relaxed by introducing misfit dislocations.

material, when γ_{fs} is negligible. It should be noted that here misfit strain (equation 2.7) in the system has not been taken into account and can broaden the regime of the island growth mode. This is observed mostly in metal on ceramics deposition systems [31]. When the film material wets the substrate ($\theta \sim 0$) equation 2.11 becomes

$$\gamma_{sv} \geqslant (\gamma_{fs} + \gamma_{fv}). \tag{2.12}$$

In addition to the impact of misfit strain and interface chemistry [87], the values of surface energies for complex oxides vary significantly in the literature making the prediction of the growth mode difficult. However, high quality layer-by-layer growth mostly requires a minimum difference between the surface energies of the film and the substrate (noting wetting occurs only if $\gamma_{sv} \geqslant \gamma_{fs} + \gamma_{fv}$) and the lattice parameters are matched as closely as possible, since the layer can only accommodate small amounts of misfit strain. The Stranski-Krastanov growth mode is somewhere between the other

two growth modes; initially equation 2.12 is satisfied but as a result of misfit strain energy above the critical thickness, a transition from the layer-by-layer growth to island growth happens. This thickness can be calculated using equation 2.10. It should be noted here that in equation 2.12 it is assumed that the growth (substrate) temperature and, consequently the mobility, is high enough for the growth to occur.

2.3.2 Effects of deposition conditions on the growth

In section 2.3.1, the intrinsic properties that affect the growth mode were discussed such as lattice mismatch and surface energies. However, as already stated, the growth processes in PLD is far from thermal equilibrium, and therefore is determined not only by thermodynamics, but is dominated by kinetics. The growth kinetics is determined by the deposition conditions which are of great importance and need to be carefully selected to achieve heteroepitaxial layer-by-layer growth. Important growth parameters for the deposition process are given in table 2.1. Many of these parameters have been investigated for the deposition of $LaMnO_3$ and $LaNiO_3$ thin films, although some of these parameters were expected to be similar regardless of the material used, such as laser spot size and shape.

Table 2.1: Typical values for the deposition parameters used in this thesis.

Deposition parameters:	Typical values	
Compounds	$LaMnO_3$	$LaNiO_3$
Target type	sintered pellet	sintered pellet
Background gas	O_2	O_2
Background gas pressure (mbar)	10^{-4}-10^{-2}	10^{-2}
Substrate temperature (°C)	600-750	600-750
Spot size (mm^2)	2.16	2.16
Shape of spot	rectangular	rectangular
laser fluence (J/cm^2)	1.5-2	1.5-2

These parameters are interlinked with the special features of PLD such as the relatively high kinetic energy of deposited particles, the comparably high deposition rates, and high supersaturation during the deposition pulse.

Tunable kinetic energy of deposited species

The ablated species in the plasma plume of PLD are either charged or neutral. The highest kinetic energy found belongs to the charged particles (up to 250 eV). These energies are high enough to create defects in the growing thin film. A background gas can be used to moderate the plume energies through inelastic collisions to less than 1 eV. Considering the strong detrimental impact of deviations away from stoichiometry in complex oxide thin films, precise control and understanding of how deposition parameters such as oxygen background pressure, laser fluence and substrate temperature affect the plume dynamics is one of the key challenges in oxide growth [88]. The ion flux in the laser-induced plasma revealed exponential losses as a function of propagation distance and background gas pressure using fast-time plasma diagnostics by ion probes [89]. Compared to a vacuum, the plume propagation is progressively slowed down by increasing the oxygen pressure. At low pressures, from $\sim 10^{-6}$ to $\sim 10^{-3}$ mbar, the plume front expands freely in an elliptical gas cloud, similar to an adiabatic vacuum plume expansion, with the front velocity of $\sim 1 \times 10^6$ cm/s [90]. One possible explanation for this mechanism is based on the pressure gradients of the plume acting as a piston, moving from the dense vapour into the low pressure background gas or vacuum to reduce the kinetic energy of the plume species [91]. By increasing the pressure to $\sim$ 0.1 mbar, the plume initially expands at early times (less than 1 μs), but then gradually slows down as a result of collisions with the cold gas molecules until a visible shock-wave structure forms which propagates according to the shock or drag model [89, 90].

Prior to deposition, due to these changes in expansion dynamics, the scattering effect on the ablated species by the gas molecules causes composition fluctuations. This can have stronger influence on lighter species [92]. To conserve the composition of complex oxides during PLD growth, a critical fluence has to be exceeded. It should be noted that the fluence threshold to ignite the ablation differs from the stoichiometric threshold. For example, the stoichiometric threshold for deposition of YBCO is reported to be 1 J/cm^2 [93] while the ablation threshold is 0.27 J/cm^2 [94] for the same set-up. The laser fluence defines the primary energy of the ablated species and the amount of material to be ablated through the temperature of the plasma, and hence the gradient in velocity during plume expansion [95]. In earlier studies, establishing a meaningful correlation between PLD parameters and plume dynamics were carried out, however, the effect of substrate temperature on the plume dynamics was rarely considered. A particularly interesting impact of increasing the deposition temperature is the decrease in the background gas density encountered by the ablated species moving towards the substrate. For example, in the case of $La_{0.7}Sr_{0.3}MnO_3$, the species arrived at T $\approx$ 300 °C had kinetic energy of $\approx$ 0.03 - 0.05 eV while at T $\approx$ 800-900 °C this raised

to $\approx$ 0.2 - 0.3 eV [96].

High deposition rates

The deposition parameters can be used to manipulate the total amount of material deposited per pulse of the laser, alter the surface mobility, and adjust the duration in which the adatoms can be relocated to reach nucleation sites in-between the pulse intervals [97, 98, 99]. There is a balance between these processes, which affects the growth mode. The amount of material in each pulse can be controlled by varying the background gas pressure, laser fluence, and laser spot size on the target. Controlling the size and shape of the plume using the above parameters, leads to control of the amount of material which reaches the substrate, which depends on the substrate position in respect to the target. There is a difference between deposition rate within each laser pulse and average deposition rate. The average deposition rates used in this thesis were between 0.1 to 0.01 u.c. per laser pulse. For example, for a laser frequency of 5 Hz and for lanthanum-based perovskite materials with in-plane lattice parameter of $\sim$ 4 Å, the actual deposition rate is between 2 to 0.2 Å/s. Considering that deposition occurs only when the laser is 'on' (in the order of 1 ms [100]), the deposition rate is about 10 Å/s which is an order of magnitude higher than what is reported for perovskite oxide growth by rf sputtering (100 nm per hour).

Supersaturation and growth

The mass transport at the surface is dominated by the substrate temperature, although oxygen partial pressure and laser energy also affect the growth by changing the kinetic energies of the ablated species. Epitaxial growth is more likely to be obtained at elevated temperatures because higher surface mobility favours 2D layer-by-layer growth through decreasing the probability of second layer nucleation. However, it also increases the chances of interface blurring and desorption. The ablation plume is affected by laser parameters such as: energy fluence (defined as delivered energy per unit area) which affects the stoichiometric transfer; laser spot size and shape on the target - which affect the amount of material deposition and the homogeneity; and the laser pulse frequency that controls the deposition rate and supersaturation. While higher deposition rates favour 3D growth, higher supersaturation favours 2D growth. Both background pressure and laser parameters should be adjusted in a way that no highly energetic bombardment of the surface occurs during deposition to avoid defect formation and residual stress in the films. In the case for most of the complex oxides, but more extensively in studies of high T_C superconductors, the stoichiometric transfer usually occurs when the edge of

the visible plume is touching the substrate.

By reducing the amount of material, which reaches the substrate, 3D island growth can be prevented, which increases the probability of layer-by-layer growth, as there is enough time for the arrived materials to reach a stable nucleation site. Substrate temperature influences the mobilities of the species directly, so the movement of adatoms is promoted; this results in the decrease in the possibility of 3D island formation. Although it should be noted there is trade-off between the deposition rate and the growth temperature as re-evaporation may occur [101]. Laser frequency plays an important role for determination of the growth mode as it controls the interval between each pulse and hence the time that adatoms have to find low energy sites at the 2D island edges. One of the main differences between PLD and the other growth techniques is the ability to promote high supersaturation using high laser frequencies (beyond 10 Hz [102]). Small islands are formed in this case, making the formation of second layer islands less probable. There should be a balance between the amount of material deposited and the laser frequency to ensure there is enough time for settlement of a layer before the next pulse brings more material. Growth modes can be monitored using an *in-situ* electron diffraction such RHEED. The next section explains the theory of RHEED and how it can be applied to monitor the growth in real time.

2.3.3 Effect of target on the deposition

One of the main advantages of PLD is known to be the stoichiometric transfer of the target composition to the growing film due to the extremely high heating rate of the target surface as a result of the pulsed laser irradiation. This will benefit from congruent evaporation of the target material regardless of the evaporating point of the constituent compounds of the target materials. However, this aspect of the PLD has been overlooked and non-stoichiometric films have been repeatedly reported for perovskite materials grown by PLD from a stoichiometric target [76]. Stoichiometry control is one of the main fundamental problems in perovskite oxide film growth and it has recently been highlighted in the studies on the growth of epitaxial $SrTiO_3$ [103]. Only under a small PLD growth conditions (target, laser and oxygen pressure) window can a stoichiometric $SrTiO_3$ thin film (cation stoichiometric) be synthesised from a stoichiometric target. Regardless of the non-stoichiometric transfer of the cations during ablation, strong RHEED intensity oscillations and layer-by-layer (2D) growth mode have been observed [104, 105]. Although the fundamental perovskite structure of $SrTiO_3$ stays intact for the stoichiometric variations up to 20 percent, even 1 percent deviation can cause remarkable changes in the transport properties of $SrTiO_3$ [104, 105, 106]. Further complexities arise when ablating perovskite oxide films with a rhombohedral or

orthorhombic crystal structure, as off-stoichiometric cation transfer gives rise to local strain fields that change the angle of the characteristic B-O-B bond and hence introduce distortions in the oxygen octahedral that determine the occupancy of the *d*-orbital and the magnetic ordering in numerous perovskite oxide heterostructures [107, 108]. Due to the complexities mentioned above, starting with a stoichiometric target is the priority in the successful growth of perovskite TMOs.

Apart from typical growth parameters, there are other factors affecting the stoichiometric transfer related to the characteristics of the target such as target morphology, phase structure, and density. This section emphasizes the role of such parameters on the growth of the high-quality complex oxide thin films. To understand the physics of material transfer in PLD, the first step is to recognise the complicated nature of the chemical reactions that occur when material is ablated by laser irradiation, the chemical reactions between the plume and the reactive background gas, and the final reactions between the arrived materials and the surface of the substrate at elevated temperature. To identify the role of the target characteristics on these complex gas phenomena, it is important to determine the properties of the target such as composition, density, crystalline phase, etc. since they all directly affect the composition of the growing film.

Targets are usually sintered pellets fabricated from the mixture of component metal oxides. The sintering can be done for the purpose of solid-state reactions or just for mechanical improvement of the ceramic pellet. Targets made for the first reason are called 'fully reacted' and the sintering temperature is well above 600 °C. The sintering temperature is critical and should be chosen with great care due to the possibility of the formation of unfavourable structural phases, or alteration in the stoichiometry by losing volatile components. The second type of targets is named a 'pressed oxide' meaning that the component metal powder oxides are still present. A pressed oxide target is more favourable in some materials as the lower sintering temperature (below 600 °C) used, means it is less likely that unfavourable crystallographic phases form [76]. The surface of the target is irradiated prior each deposition for 2 purposes, one removing any contamination and second to make the surface of the target stoichiometric. As a result of pre-ablation processes, a steady state composition at the surface is formed which can differ from that of the bulk target. For example, in the $LaNiO_3$ perovskite compounds, an unfavourable phase exists that belongs to the Ruddlesden-Popper family. In chapter 5, it is shown that a commercially pressed perovskite $LaNiO_3$ target possessed less than a few percent of the perovskite phase and over 95 % of the Ruddlesden-Popper phase. Consequently, the Ruddlesden-Popper phase was also detected in the film grown by PLD.

2.4 Reflection high-energy electron diffraction

RHEED is an electron diffraction technique used for the determination of surface properties. In RHEED, electrons with energies in the range of 15 to 45 keV impinge upon the surface of a solid at grazing angles of between 1 to 5°. The diffracted beams are then projected onto a phosphor screen, which is equipped with a CCD camera for data collection. The system layout of the PLD chamber, including the differentially pumped RHEED setup, is shown schematically in figure 2.7. The geometry of the setup prevents any interference with the plume of the laser beam, enabling *in-situ* monitoring of the deposition process. An initial problem with RHEED in PLD systems was the difference between background pressure in which RHEED could be used and the high oxygen pressure used in oxide film growth. At first poorly oxygenated films were compensated by combining oxygen pulse sources with laser pulses in the chamber [109]. This required extra equipment and electronics and in general was a complicated synchronisation process. The unique idea of differential pumping was a turning point in the development of PLD [29]. Using differential pumping ensured that the electron gun stayed in a lower background pressure. Electrons travel mostly in a partially sealed tube at lower pressure than the growth chamber and consequently deposition at a desirable oxygen background became achievable. This also improved the lifetime of the filament. Using differential pumping, a maximum pressure of around 0.1 mbar in the deposition chamber was achievable for *in-situ* RHEED investigations. As is highlighted in figure 2.7 via two stages of deflection (both x and y axes), the electron beam position can be adjusted ± 7 degrees through the aperture. A typical RHEED system consists of a filament, deflection coils, aperture, fluorescent screen, a shutter, view point and two separate pumping systems. By adding this powerful, surface sensitive technique, various physical surface properties of thin films and heterostructures can be analysed such as periodicity and surface morphology, in-plane lattice parameters and surface reconstruction orientation. Growth modes such as layer-by-layer or 3D island can also be extracted from recorded diffraction patterns and beam intensity oscillations [110], these are discussed in greater detail in the following sections. For the beam to be diffracted, electrons need to be scattered elastically and coherently. The energy (Equation 2.13) of the final diffracted electrons during elastic scattering (E_f) must be conserved and is equal to that of the incident electron beam (E_i), such that

$$|E_f| = |E_i|. \tag{2.13}$$

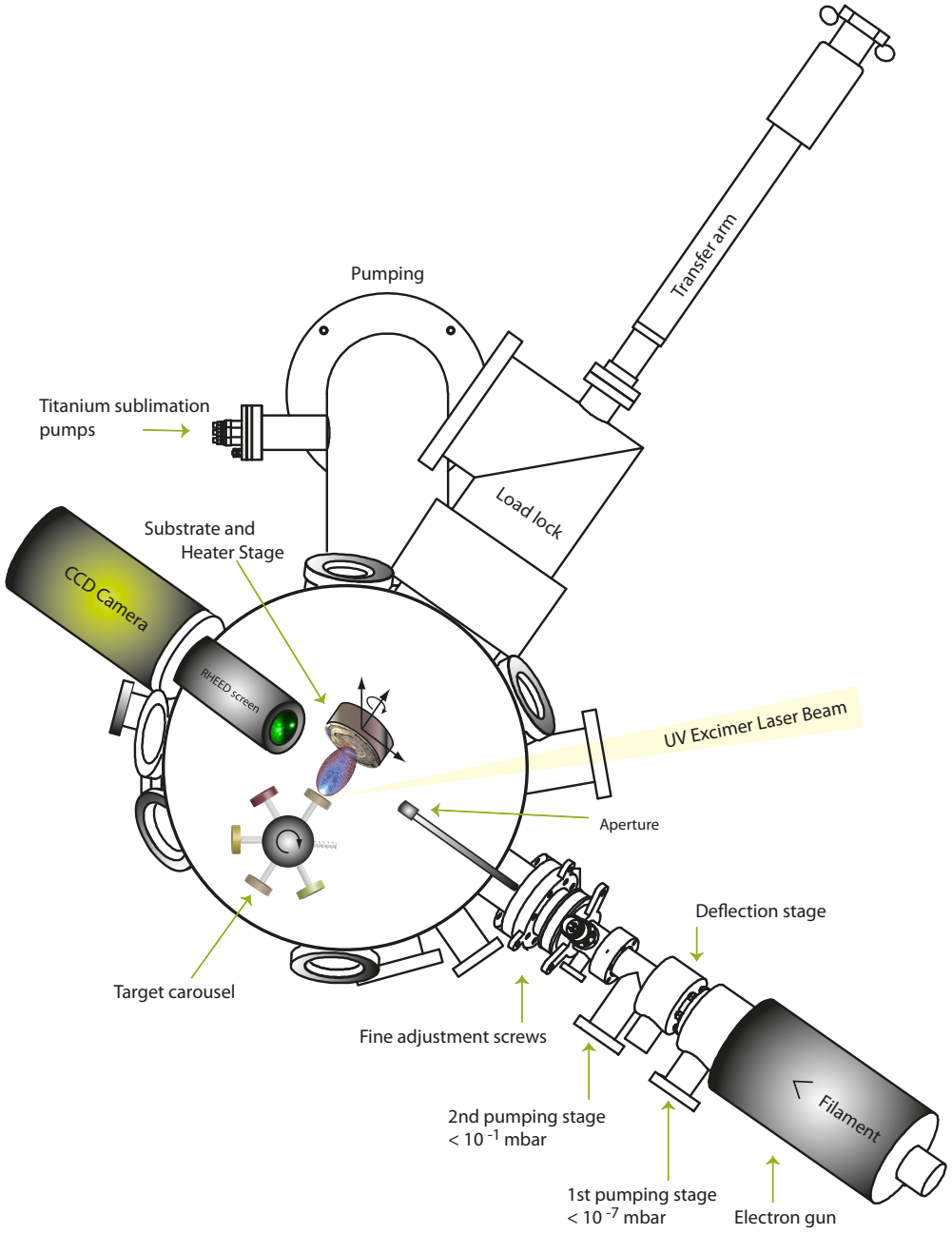

Figure 2.7: A schematic top view of PLD chamber equipped with *in-situ* RHEED setup including an electron gun with differential pumping setup. Main components are: target stage, heater stage, RHEED screen, RHEED gun, UV laser beam, load lock chamber, transfer arm, and TSP. The differential pumping includes: adjustment screws, deflection stage, two pumping stages, and electron gun.

The energy of an electron E_e is related to $|k^2|$ and is given by

$$E_e = \frac{\hbar^2 k^2}{2m_e} \tag{2.14}$$

where $k = 2\pi/\lambda$ is the wave vector of the beam with a wavelength of λ and m_e is the electron mass [111]. It is possible to estimate λ disregarding relativistic mass corrections (for E of less than 50 keV the relativistic effect can be neglected) [110], and so

$$\lambda = \sqrt{\frac{150.4}{E}} \tag{2.15}$$

when λ is in Å and E is in eV. In the system used in this thesis, the beam energy was 30 keV resulting in an electron wavelength of ∼0.07 Å. A monolayer is typically an order of magnitude larger in size than this wavelength (for cubic perovskites it is about two orders of magnitude). By using a grazing angle of incidence and exit, the overall scattering angle can be kept small while obtaining a large enough elastic scattering cross-section. However, it is the relatively short inelastic mean free path of the scattered electrons that ensures that scattering only occurs from the first few atomic layers of the surface. This makes RHEED more sensitive to surface roughness on an atomic scale than other surface electron diffraction techniques e.g. low energy electron diffraction (LEED) [112]. In X-ray diffraction (discussed in section 3.3.1), it is assumed that scattering is kinematic, however, this is not the case in RHEED as the electrons do not interact weakly with the crystal. The kinematic approach was used only to assist in understanding the physical phenomena in RHEED and qualitative analysis to some extent [80].
To obey conservation of energy, as was shown in Equation 2.13,

$$\left|\boldsymbol{k_f}^2\right| = \left|\boldsymbol{k_i}^2\right| \tag{2.16}$$

which implies that the incident and final wave vectors have to be of the same magnitude such that

$$|\boldsymbol{k_f}| = |\boldsymbol{k_i}| \tag{2.17}$$

where $\boldsymbol{k_f}$ and $\boldsymbol{k_i}$ are the final and incident wave vectors of an electron, respectively. The diffraction pattern can be observed when the value of $\boldsymbol{k_f}$ and $\boldsymbol{k_i}$ vary only by a discrete amount equal to a reciprocal lattice vector, $\boldsymbol{G_{ijk}}$, of the crystal [111] and so

$$\boldsymbol{k_f} = \boldsymbol{k_i} + \boldsymbol{G_{ijk}}. \tag{2.18}$$

Equations 2.17 and 2.18 result in the Laue diffraction condition

$$2\boldsymbol{k_i}.\boldsymbol{G_{ijk}} + |\boldsymbol{G_{ijk}}|^2 = 0 \tag{2.19}$$

These conditions can graphically be illustrated using the surface of a sphere of constant wave vector (a side view projection of this sphere in 2D is shown in figure 2.8 and a side, top and 3D view are shown in figure 2.9) known as Ewald sphere. A 2D projection of the intersection of a 3D reciprocal lattice with this sphere is a circle with a radius equal to wave vector k_i that ends on the origin of the reciprocal lattice (figure 2.8-(a)) with a radius equal to $|\boldsymbol{k_i}|$. Diffraction features appear when equations 2.17-2.19 are satisfied, this is equivalent to the intersection of reciprocal lattice points with the Ewald sphere.

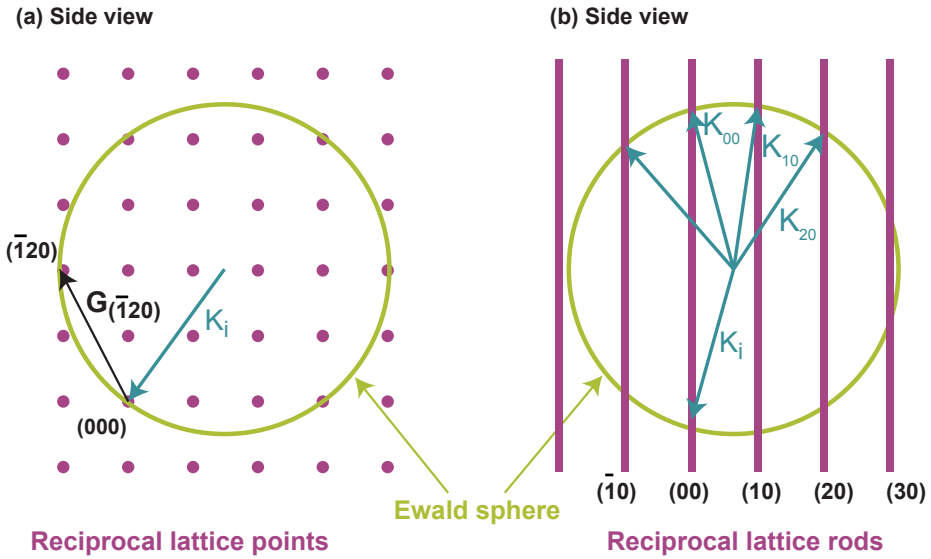

Figure 2.8: Side view projection of Ewald sphere construction shown for (a) a bulk (3D) periodic structure, the radius of the Ewald sphere is shown as $|\boldsymbol{k_i}|$. The $\boldsymbol{k_i}$ vector terminates on the (000) point of the lattice. (b) Surface (2D) representation of the Ewald sphere reconstruction.

In equation 2.18 the reciprocal lattice $\boldsymbol{G_{ijk}}$ is defined as

$$\boldsymbol{G_{ijk}} = i\boldsymbol{a_1^*} + j\boldsymbol{a_2^*} + k\boldsymbol{a_3^*} \tag{2.20}$$

where $\boldsymbol{a_1^*}$, $\boldsymbol{a_2^*}$ and $\boldsymbol{a_3^*}$ are reciprocal lattice vectors with i, j and k being integers. These are described as

$$\boldsymbol{a}_1^* = 2\pi \frac{\boldsymbol{a}_2 \wedge \boldsymbol{a}_3}{\boldsymbol{a}_1 \cdot \boldsymbol{a}_2 \wedge \boldsymbol{a}_3} \tag{2.21}$$

$$\boldsymbol{a}_2^* = 2\pi \frac{\boldsymbol{a}_3 \wedge \boldsymbol{a}_1}{\boldsymbol{a}_2 \cdot \boldsymbol{a}_3 \wedge \boldsymbol{a}_1} \tag{2.22}$$

$$\boldsymbol{a}_3^* = 2\pi \frac{\boldsymbol{a}_1 \wedge \boldsymbol{a}_2}{\boldsymbol{a}_3 \cdot \boldsymbol{a}_1 \wedge \boldsymbol{a}_2}. \tag{2.23}$$

For the 3D case, the Laue diffraction condition is obeyed when the Ewald sphere intersects with reciprocal lattice points. A similar effect is observed in RHEED for surfaces that are rough with micro-structures. If the islands are thin enough for the beam to be diffracted without being attenuated (dependent on the inelastic mean free path), then a grid-like diffraction pattern is observed. This condition is illustrated in figure 2.8-(a) and will be discussed more in detail in section 2.4.3-(figure 2.16-(b)). For surface diffraction from a smooth surface, as is shown in figure 2.8-(b), the reciprocal lattice vector $\boldsymbol{G_{ijk}}$ is converted to $\boldsymbol{G_{ij}}$ due to the loss of periodicity perpendicular to the surface (i.e. along the k direction), so to relax the momentum conservation it becomes $\boldsymbol{G_{ij}}$. The diffraction condition is met for a 2D lattice given by Laue condition with

$$\boldsymbol{k_f^{\parallel}} = \boldsymbol{k_i^{\parallel}} + \boldsymbol{G_{ij}}, \tag{2.24}$$

where the superscript $^{\parallel}$ shows that the direction of scattered wavevectors components are parallel to the surface plane.

Due to the relaxation of momentum conservation normal to the surface plane, the 2D reciprocal lattice of the surface is instead shown by infinitely long thin rods of reciprocal lattice points. To view a surface in reciprocal space in a phenomenological way, it can be imagined as if the plane of the crystal has been expanded infinitely in the direction along one of its axes. This will result in reduced lattice point spacing in reciprocal space, so lattice points become closer until they transform into rods. Figure 2.9 shows three different views of a 2D lattice in reciprocal space. Equations 2.17-2.19 are satisfied when a reciprocal lattice rod intersect the Ewald sphere. The diffraction spots lie on concentric rings termed 'Laue zones' in scattering from a 2D surface. As a result of variation in surface crystallinity, for instance surface disorder, angular divergence of the electron beam ($\Delta\theta_f$), surface lattice vibrations, fluctuation in the beam energy and to some extent the crystal temperature, reciprocal lattice rods have a finite thickness of 'W' (figure 2.9) resulting in observation of 'streaks' in RHEED patterns. A 'spotty' diffraction pattern can be achieved from a perfectly smooth crystal surface, in an ideal condition with monochromated incident electron beam and at low temperature [112].

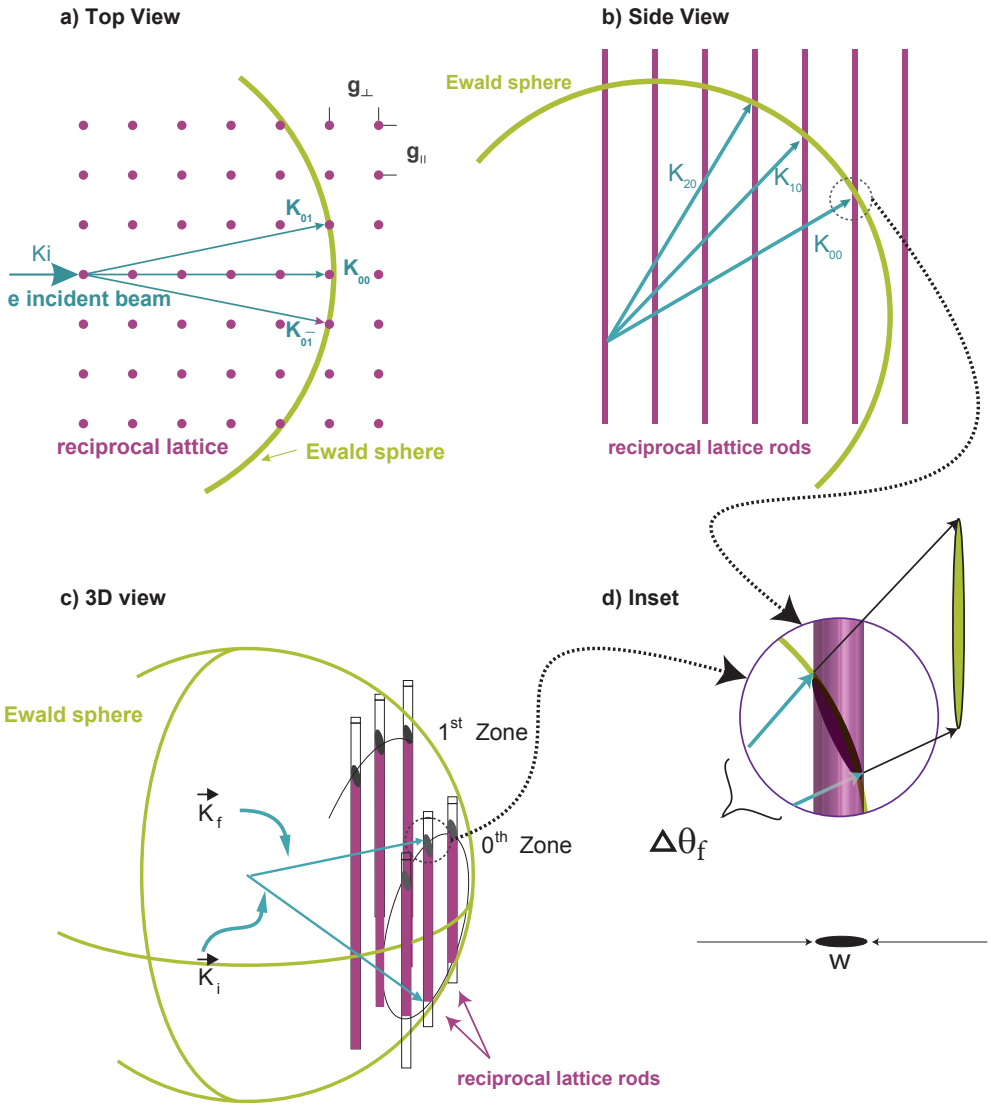

Figure 2.9: Side view (a), top view (b) and 3D illustration of a periodic surface with cubic lattice in reciprocal space showing the intersection of lattice rods with the Ewald sphere. In the 3D illustration the inset shows a zoomed-in intersection of a lattice rod with the Ewald sphere. Angular divergence of the electron beam ($\Delta\theta_f$), in conjunction with other factors such as surface lattice vibrations, variation in the beam energy and to some extent the crystal temperature gives a finite thickness of 'W' to the reciprocal lattice rods resulting in observation of 'streaks' in RHEED patterns instead of spots.

2.4.1 RHEED: determination of surface periodicity

Before discussing the use of RHEED in defining surface properties, it is worth briefly discussing the concept of surface reconstructions.

2.4.1.1 Surface reconstructions

In the early 20^{th} century, with the first X-ray diffraction experiments, the study of bulk crystal structures was established. Hence, from a simple unit cell, bulk properties could be predicted, with defects (such as dislocations and vacancies) being averaged out. However, the surface of a crystal is a significant defect and the change in periodicity may cause a relaxation of the surface at the bulk termination. This change happens when the free energy of the surface is too large to preserve the bulk structure. It is frequently seen in metal crystals that the atoms relax perpendicular to the surface to minimise this free energy [113]. The substrate material used throughout this thesis, $SrTiO_3$ (001), has a number of different surface reconstructions and terminations. There are applications of these reconstructions from the photo catalysis industry [114] to engineering of nano-structured thin films [115]. $SrTiO_3$ is the archetypal perovskite, and considering its popularity among thin film scientists as a substrate, a better understanding of the surface structure is important. Using a diverse range of surface analysis techniques such as scanning tunnelling microscopy (STM) and surface diffraction tools such as LEED and RHEED, a number of different possible reconstructions were reported for $SrTiO_3$(100) such as (1×1), (2×1), (2×2), c(4×2), c(4×4), and c(6×2) [116].

Wood Notation

Wood notation is a convenient method of describing these changes in the periodicity of the surface. The notation specifies a rotation angle and a ratio between the reconstructed surface and the bulk structure as

$$X\ \{hkl\}\ -\ (p\ \times\ q)\ R\ (\theta)^{\circ}\ -\ A. \tag{2.25}$$

This represents an adsorbate A on the $\{hkl\}$ surface plane of substrate element (can be alloys or compounds as well) X. The unit mesh rotation is given by θ and the primitive translation vectors are $|a'| = p\,|a|$, $|b'| = q\,|b|$ [112].

2.4.1.2 Interpretation of RHEED patterns

The crystallinity of the top few atomic layers of the crystal can be studied by RHEED due to elastically scattered electrons (as was discussed in detail in the previous

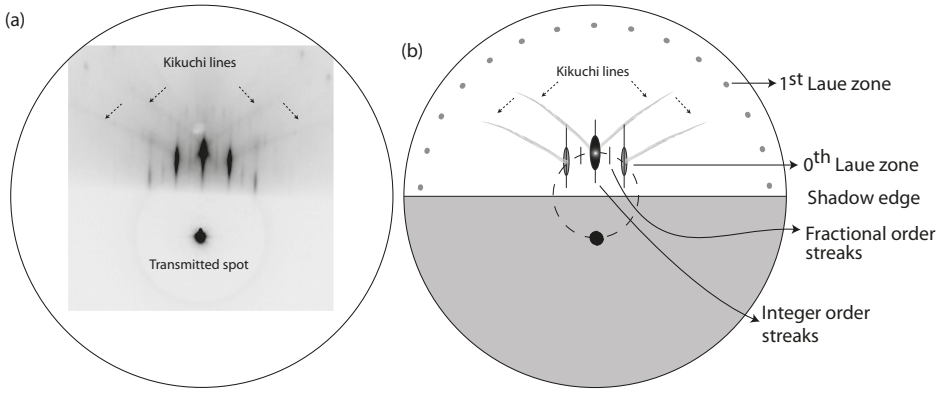

Figure 2.10: (a) RHEED image captured of $(LaNiO_3)_2/(LaMnO_3)_2$ superlattice thin film when the final layer was $LaMnO_3$ on the (100) surface of a $SrTiO_3$ single crystal substrate, with the electron beam oriented along the <110> direction showing a surface reconstruction $(\sqrt{2} \times \sqrt{2})$R45°. (b) A schematic illustration of the RHEED pattern showing features such as different Laue zones, as well as fractional and integer order streaks.

section), however, the electrons can also be inelastically scattered from a crystal. The contribution of inelastic scattering in RHEED is considerably less than electron diffraction in transmission electron microscopy (TEM) owing to the grazing geometry. Some electrons in RHEED will be travelling inside the crystal with an angle, that may satisfy the Bragg diffraction conditions for other planes, so this leads to secondary elastically scattering and the appearance of Kikuchi lines [117]. In TEM, also in RHEED in a certain degree, Kikuchi lines can be used to find the orientation of the crystal as they arise from the bulk periodicity [118].

Figure 2.10 shows a colour-inverted RHEED pattern of a $(LaNiO_3)_2/(LaMnO_3)_2$ when the final two monolayers were $LaMnO_3$ on TiO_2-terminated $SrTiO_3$ (001) single crystal substrate, with the electron beam was oriented along the <110> direction. The terminated layer was found to be MnO_2 and appeared as $(\sqrt{2} \times \sqrt{2})$ R45° reflections. Figure 2.10-(b), is a schematic highlighting some typical features of RHEED patterns such as the zeroth and first Laue zones, in addition to the fractional and integer order streaks lying on these concentric rings. Kikuchi lines are indicated by dotted arrows in both images.

The diffraction pattern observed in RHEED is due to the surface reciprocal rods crossing the Ewald sphere, this is when the integer streaks are raised from the bulk-like structure, however the fractional streaks originate from the intersection of fractional rods with larger periodicity with the Ewald sphere. So the periodicity of a bulk-like surface termination is shown as (1×1) in Wood notation [112], and fractional streaks are

present if the periodicity of the surface in real space is larger than the bulk periodicity. The integer streaks are typically brighter in intensity and can be used as a reference since they contain bulk information. For instance, fractional streaks placed halfway between integers in reciprocal space are an indication of two times larger surface periodicity.

2.4.1.3 Lattice parameter calculations from RHEED pattern

In the field of complex oxide thin films, RHEED patterns have been mostly discussed qualitatively by simply observing the pattern and its change over time during deposition. Although this is of help for extracting information about the growth quality on an atomic scale, RHEED patterns also contain detailed information about the surface crystallinity and it is possible to extract quantitative information about the surface crystallographic arrangement [119]. Typical geometry of the RHEED setup for surface diffraction is illustrated in figure 2.11. The electron beam with an incident angle of θ_i and azimuthal angle of ϕ_i is scattered with a diffraction angle of θ_f and azimuthal angle of ϕ_f. Diffracted spots/streaks are projected onto a phosphor screen located at a distance R_S away from the substrate resulting in a streak separation of S. This spacing can be used to determine the in-plane lattice parameters of the crystal. The projection of the diffracted beam can be calculated from the polar co-ordination rectilinear (k_{s_i} when $i = x, y, z$) of the wave vector $\boldsymbol{k_o}$ [80]:

$$k_{s_x} = |\boldsymbol{k_o}| \left(\cos\theta_f \cos\phi_f - \cos\theta_i \cos\phi_i\right) \tag{2.26}$$

$$k_{s_y} = |\boldsymbol{k_o}| \left(\cos\theta_f \sin\phi_f - \cos\theta_i \sin\phi_i\right) \tag{2.27}$$

(for small angles: $k_{s_y} \approx |\boldsymbol{k_o}| \left(\sin\phi_f - \sin\phi_i\right)$) and so using the small angle approximation we find that

$$k_{s_z} = |\boldsymbol{k_o}| \left(\sin\theta_f + \sin\theta_i\right) \approx |\boldsymbol{k_o}| \left(\theta_f - \theta_i\right). \tag{2.28}$$

It can be seen from figure 2.11-(a) that k_{s_x} and k_{s_y} are lying on the surface plane and k_{s_z} is in the direction normal to the surface. Equations 2.26-2.28 can be simplified for the incident beam in the x direction of the surface plane, such that the azimuthal angle ϕ_f is equal to zero. Based on Bragg's law, the lattice parameter parallel to the incident beam direction d_x can be determined as following

$$\frac{n}{d_x} = \frac{1}{\lambda}\left(\cos\theta_f - \cos\theta_i\right). \tag{2.29}$$

This is valid when the intersection of the Ewald sphere and the lattice rods are on $(h0)$ and the azimuthal angle of diffracted beam is equal to zero. As for the other in-plane lattice parameter normal to the direction of incident beam from equation 2.27, d_y is

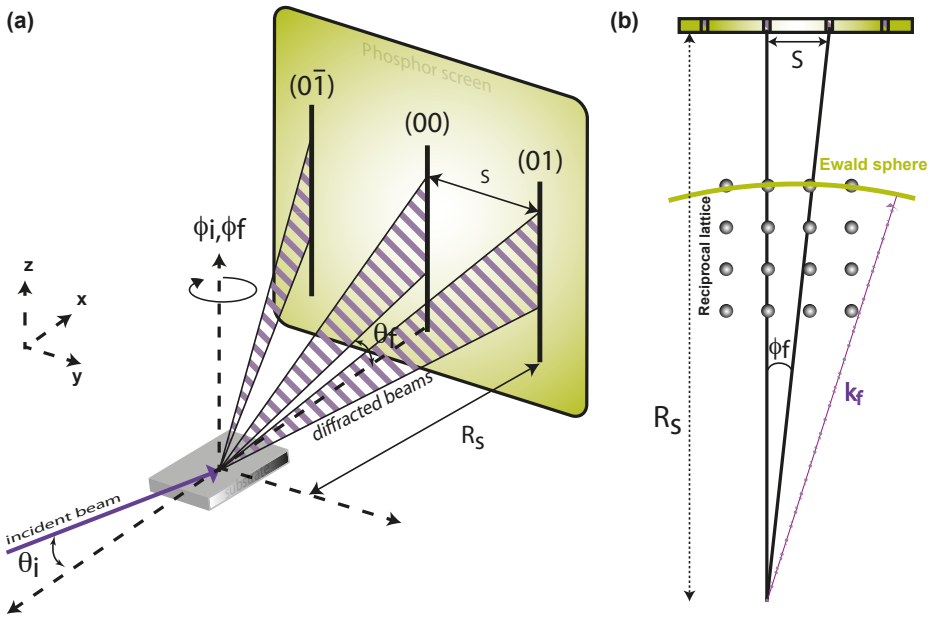

Figure 2.11: Schematic of the typical RHEED geometry. The electron beam path is shown as it impinges on the surface with grazing incident and azimuthal angles of θ_i and ϕ_i, and it will be diffracted through θ_f and ϕ_f angles. The diffraction streaks or spots will be projected onto a phosphor screen placed at a distance of R_S to the substrate, where they are evenly spaced at the distance of S from each other. Figure adapted from [120].

given by,

$$\frac{n}{d_y} = \frac{1}{\lambda}\left(\cos\theta_f \sin\phi_f\right) \tag{2.30}$$

For values of n being a reflection order, the relevant angles can be determined from the phosphor-screen to substrate distance of R_S, assuming the small angle approximations. The top view of the RHEED setup is shown schematically in figure 2.11-(b). The reciprocal lattice spacing a'_y in the y direction is related, to ϕ_f the angle between two adjacent reciprocal lattice rods, and assuming the small angles approximation, as

$$\tan\phi_f \;=\; \phi_f \;=\; \frac{a'_y}{\boldsymbol{k_f}}. \tag{2.31}$$

From figure 2.11-(b), the relation between the phosphor-screen to substrate distance R_S and the reciprocal lattice spacing can be determined by

$$\frac{a'_y}{\boldsymbol{k_f}} \;=\; \frac{S}{R_S}. \tag{2.32}$$

The inverse of the reciprocal spacing is related to the real lattice parameter by

$$a_y = \frac{2\pi}{a'_y} \tag{2.33}$$

and so from equations 2.32 and 2.33

$$a_y = \frac{2\pi\ R_S}{S\ \boldsymbol{k_f}} \tag{2.34}$$

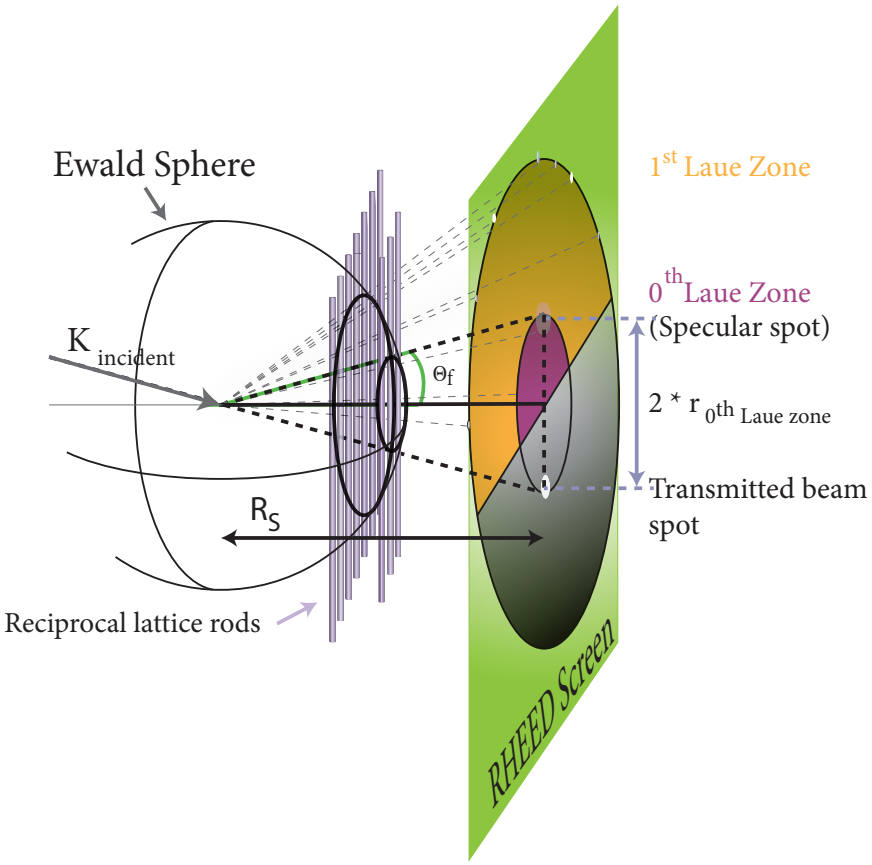

Figure 2.12: 3D view and RHEED screen projection of a cubic lattice in reciprocal space. The distance between the specular spot and transmitted spot is equal to diameter of zeroth Laue zone and related to the diffraction angle θ_f by tangential relation with R_S.

The variations in observed patterns were interpreted qualitatively in this thesis to study the quality of growth. The streak spacing is also used for in-plane lattice parameter determination. Because the radius of the Ewald sphere is large compared to the lattice parameter of complex oxides, the only diffracted spots observed on the phosphor screen were the zeroth Laue zone and occasionally the first Laue zone. The

Table 2.2: RHEED streaks spacing calculated for high symmetry $SrTiO_3$ substrate orientations

Direction	Real spacing Å	Reciprocal spacing ($Å^{-1}$)	Streaks spacing (mm)
<100>	3.905(1)	1.609(1)	1.9(1)
<110>	2.761(1)	2.275(1)	2.7(1)

zeroth order Laue circle showed the intersection of the $(0k)$ rod with the Ewald sphere. The straight-through beam occurred as a result of the partially blocked incident electron beam. The specular spot is never forbidden, unlike other diffraction spots, because it is lying on the same reciprocal lattice rod as the incident electron beam (k_i) and has the majority of the reflected intensity. The radius of the Ewald sphere for the RHEED system used in this thesis was 8.9(1) $\times$ $10^{11}m^{-1}$ for a beam energy of 30 keV. This is larger than the reciprocal lattice spacing of complex oxides by approximately two orders of magnitude. This is shown graphically in figure 2.12 indicating that only a few sets of intersections between the Ewald sphere and reciprocal rods can be projected onto the screen. In-plane lattice spacing can be calculated from high symmetry directions. For a cubic lattice an azimuthal rotation of 45° was necessary to observe both of the <100> and <110> directions.

Knowing the substrate to phosphor-screen distance R_S in the PLD chamber (169±5 mm), the streak spacing can be calculated from equations 2.32, 2.33 and 2.34. Table 2.2 contains the calculated in-plane lattice spacings. The accuracy in determining the reflection angles, due to relative errors, was about 5 to 10%, reflected in the substrate-to-screen distance (R_S). Also the substrates used were either 5 $\times$ 5 mm^2 or 10×10 mm^2 in size, and this adds $\pm$ 2.5 mm or ±5 mm to the errors in calculation of R_S. A solution to this large error was to calibrate the measurements to the single crystal substrate which has a known in-plane lattice parameters i.e., a_{SrTiO_3}=3.905(1) Å. It was possible to work out the incident angle and so convert the pixels from RHEED images to millimetres.

Additional information can be determined from RHEED patterns knowing the incident beam angle. This was obtained knowing the geometry of RHEED and certain dimensions as shown in figure 2.12. Based on the separation of the specular reflection and transmitted spot where both lie on the zeroth Laue zone, such that $\theta_i = \theta_f$ [110, 121], and hence,

$$r_{0^{\text{th}}\ \text{laue zone}} \;=\; R_S\ \tan\theta_i \tag{2.35}$$

where $r_{\ 0^{\text{th}}\ \text{Laue zone}}$ is the radius of zeroth Laue zone and is defined by half of the spacing between transmitted and reflected spot ratio of RHEED and if the incident and diffracted beam angle are equal for the zeroth Laue zone and (10) reciprocal rod.

Table 2.3: Values of dimensions in RHEED images for $SrTiO_3$ substrate impinged under an electron beam of 30 keV at various incident beam angles.

Image	Screen (mm)	0-Laue zone R (mm)	Incident angle θ_i (°)
a	6.65	3.2	1.6
b	6.65	6.1	3.2
c	6.65	8.2	4.2
d	6.65	10.2	5.2

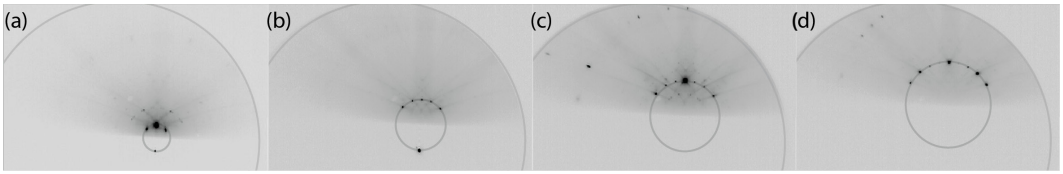

Figure 2.13: Series of RHEED patterns of $SrTiO_3$ single crystal substrate at room temperature at different incident angles (RHEED filament was at 30 keV and 1.55 A filament current). Incident beam angle, θ_i, has been increased from image (a) to (d) by tilting the heater stage. Zeroth Laue zone is highlighted by grey circle and the diameter of this circle in pixels was used to calculate the numbers in table 2.3. The shadow of the RHEED screen is highlighted with large grey circle. This diameter in pixels was associated to the real dimension of RHEED phosphor-screen in mm and used as a reference for the in-plane lattice parameter calculations.

Figure 2.13 shows the effect of the change in the angle of incident beam θ_i on the diffraction pattern of $SrTiO_3$ (001) substrate with the beam oriented along $<100>$ direction. To change the angle of incidence of the beam, the sample heater was tilted and from equation 2.35, the incident angle was calculated from the radius of the zeroth Laue zone. Table 2.3 shows the radius of zeroth Laue zone on the phosphor screen measured in mm and the calculated incident angle for each image in figure 2.13.

2.4.2 RHEED oscillations

The dependence of the intensity of the specular reflection on the film coverage is key to monitoring growth by RHEED. The intensity of the specular reflection of the beam was recorded from the RHEED pattern (RHEED-Vision STAIB, GmbH [122]) as a function of growth time. The intensity oscillations of the RHEED diffraction spots during the growth process arise due to the dependence of the specular spot intensity to the step density at the surface and are purely an effect arising from the scattering of electrons from the steps, kinks and islands at the surface. In layer-by-layer growth mode, the growth is such that one intensity oscillation is equivalent to the deposition of one monolayer.

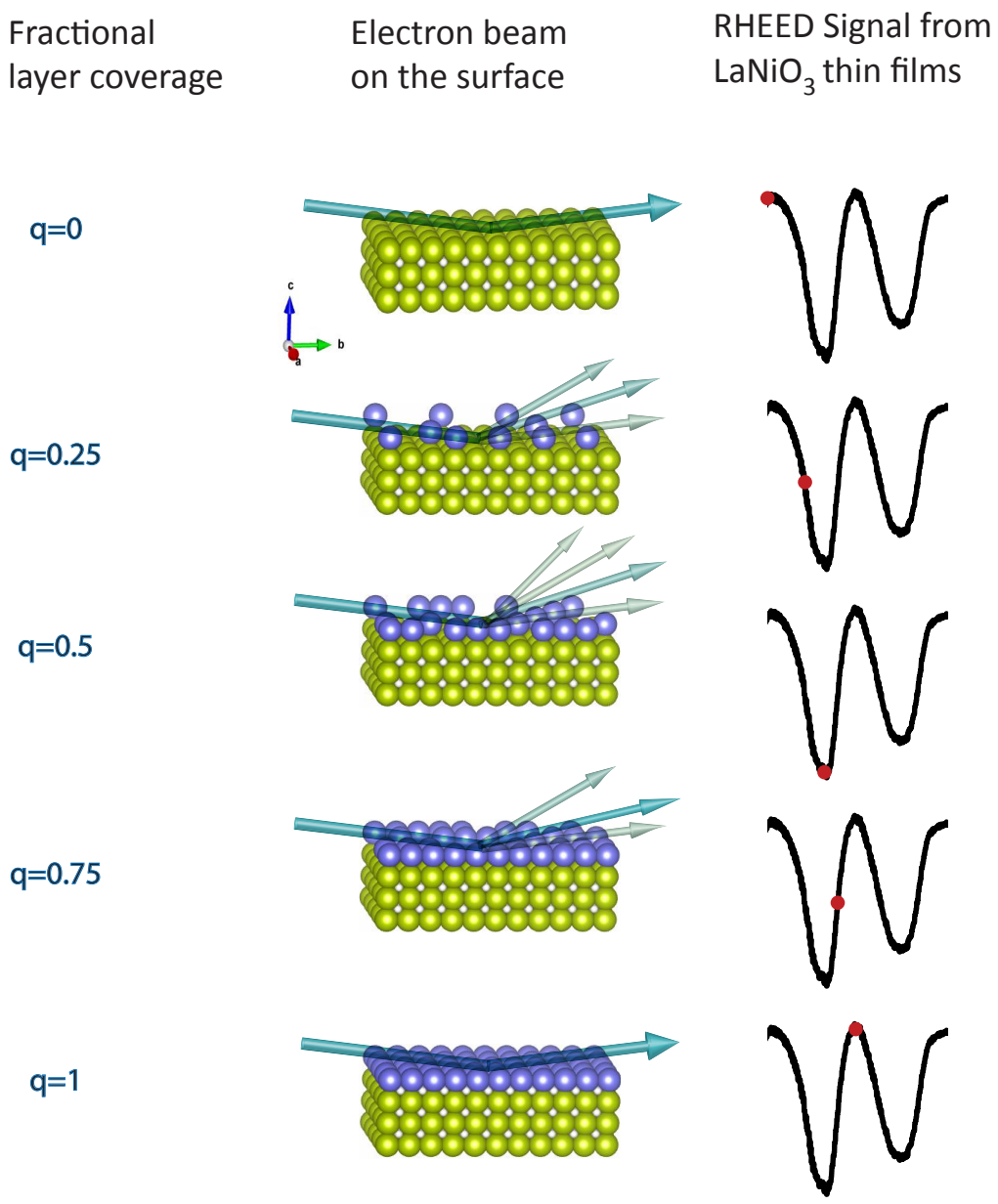

Figure 2.14: Completion of one single layer on top of a smooth surface in 2D growth mode is demonstrated. The graph on the right hand side is real data from growth of $LaNiO_3$ thin films. The coverage factor corresponds to five continuous stages of growth in order to grow one unit cell of $LaNiO_3$ on $SrTiO_3$ substrate.

Starting the growth from a smooth surface leads to the greatest intensity of the specular spot. In this process the surface undergoes cyclic periods of roughening and smoothing caused by nucleation, growth and coalescence in the completion of layers. This variation in roughness is due to the different coverage. Bearing in mind that electrons of energy 30 keV have a wavelength of 0.07 Å, considerably smaller than the thickness of the layer which it is around 4 Å, they are scattered easily by the step edges on the surface, hence the specular intensity drops. The red dot in figure 2.14 on the intensity oscillation shows the instant in the deposition and the corresponding coverage factor of it is shown by θ. Five points in the deposition of one monolayer were chosen to be illustrated schematically at quarter monolayer intervals for continuous growth of one unit cell of a $LaNiO_3$ thin film on (100) $SrTiO_3$ substrate. While the higher intensity streaks or

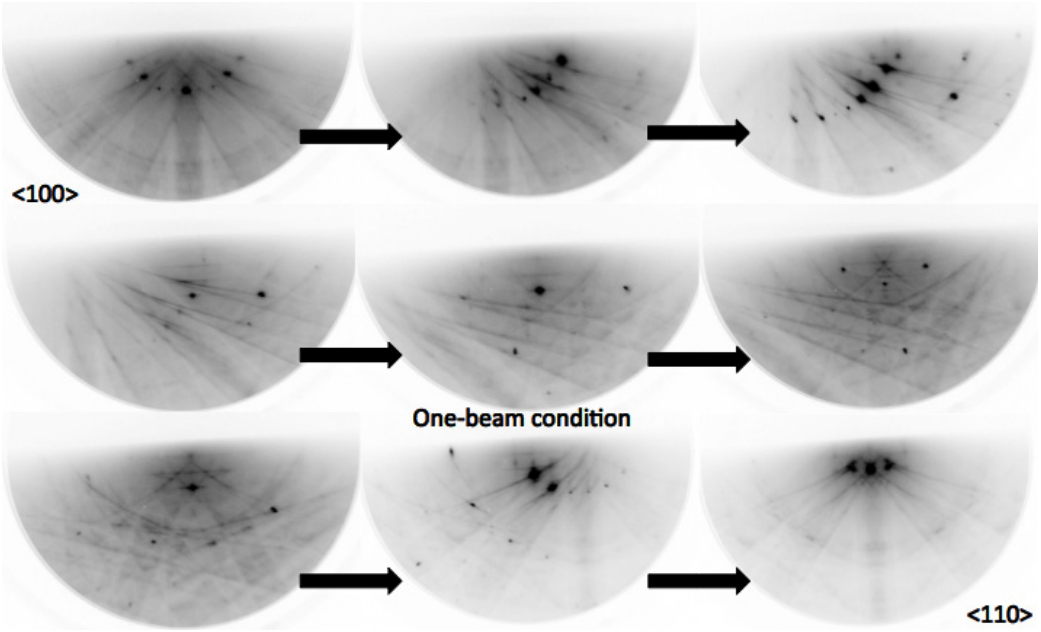

Figure 2.15: So called one-beam condition for oscillations monitoring of the RHEED specular intensity is achieved by azimuthally rotating the $SrTiO_3$ substrate from <100> to <110> orientation. The RHEED images are taken from [123] with his permission.

spots are appealing for monitoring as they are coming from elastically scattered electrons; there are extra high intensity features due to the intersection of Kikuchi lines with high symmetry direction streaks. These phenomenon can affect the intensity measured during the growth of a film and should be avoided as they can interfere with the intensity oscillation measurements. The 'one-beam condition' solves this problem by rotating the sample azimuthally and moving it away from high symmetry directions. Hence the oscillations during the growth are associated only with the oscillations of intensity

arising from completion of one monolayer. In this condition, the reflected component is the dominant component of intensity, hence is the best condition for RHEED intensity measurements as it minimises the convolution of intensities arising from Kikuchi lines and the other reflections. Figure 2.15 shows how to achieve the one-beam condition by rotating the $SrTiO_3$ substrate azimuthally from the <100> to <110> orientation.

2.4.3 RHEED patterns of different surface crystallinity

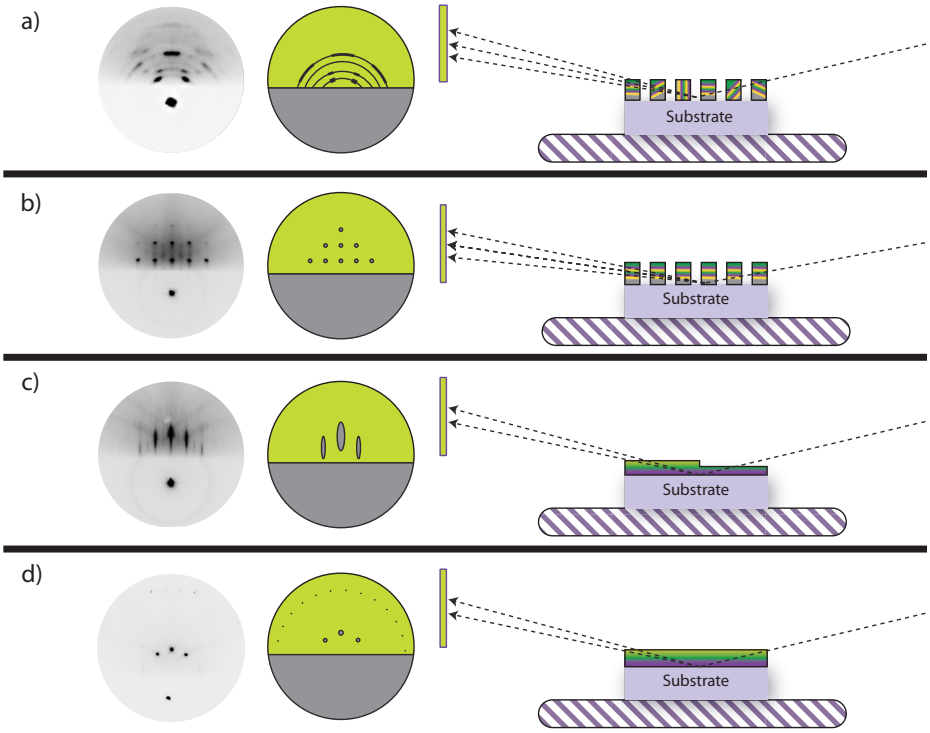

Figure 2.16: Schematic illustration of four various types of surface crystal structure with schematic and colour-inverted RHEED patterns (a) Polycrystalline nature of the crystal gives rise to a ring type pattern similar to powder diffraction rings through the transmission diffraction of different plane orientations. (b) A three dimensional surface of a single crystal showing bulk type transmission diffraction spots. (c) A smooth surface of a single crystal. (d) Atomically smooth two dimensional surface of a single crystal with minimal defects with terraces width larger than transfer width (figure adapted from [121]) with his permission.

RHEED is highly sensitive to the surface features and roughness. An important factor here is the 'transfer width' which can be defined as the largest distance in which the detection of interference is possible [124, 125]. Figure 2.16 shows four surface types and their expected inverted RHEED images. In the case of a two dimensional smooth

surface, diffraction spots will lie on concentric Laue circles. Sharp diffraction spots can be seen only if the terrace width is larger than that of the beam transfer width, as shown in figure 2.16-(d). However, if the terrace width is comparable to the interference width, this leads to the 'streaky type' pattern illustrated in figure 2.16-(c).The transfer width is related to the RHEED geometry and also the width of step terraces (for typical substrates below 500 nm) of the surface when the transfer width is typically around a few thousands Å [125]. The streaks arise when the neighbour terraces have different heights and this changes the path length. Although the terraces are atomically smooth, the phase difference causes the streaks.

By increasing the surface roughness (i.e. with a 3D island growth mode; see section 2.3.1), the possibility of transmission of the electron beam through islands increases. In this case the surface lattice rods become lattice points similar to the bulk-type structure, this leads to 3D diffraction spots which are positioned on a grid-type pattern as demonstrated in figure 2.16-(b). In this case, the kinetic energy of the electrons used in RHEED (30 keV) leads to an inelastic mean free path that is comparable to the island size, resulting in 3D, rather than 2D diffraction pattern. For example, the calculated Inelastic mean free path for rare earth transition metal oxides is between 35 to 40 nm [126]. It is difficult to determine the bulk crystal structure using RHEED as extraction of quantitative data from this type of pattern is non-trivial due to the complex origin and uncertainty in the type and size of islands. As can be seen in figure 2.16-(a), the diffraction pattern looks different when the surface roughness increases dramatically and polycrystalline islands (textured materials) are present on the surface. However, if the thin film is textured a preferred orientation can be observed, For example, if preferentially textured along the c-axis, areas of higher intensity can be seen along Laue zone circles consists of concentric rings due to rotational nature of the disorder in polycrystalline thin films and each ring can be attributed to certain plane in the polycrystal [125].

2.5 Summary

PLD was introduced in this chapter as an excellent deposition technique with the aid of *in-situ* technique such as RHEED to grow complex oxides. Different types of growth were explained. The relation between the film growth and several characteristic parameters of PLD was discussed such as the amount of ablated materials by each laser pulse, mobility on the surface of the substrate, gas pressure, intrinsic parameters such as the strain induced due to lattice mismatch between the substrate and the film, and compatibility between interfaces. In summary, RHEED and surface science related to it was explained. It can be concluded that, UHV-PLD equipped with RHEED is an excellent

technique for growth control on the atomic scale as it gives real-time feedback. The creation of artificially layered structures with unit-cell control is possible by observing and counting RHEED intensity oscillations as each oscillation corresponds to completion of one monolayer. Furthermore, RHEED intensity envelopes bring insight into growth mode transitions i.e., layer-by-layer growth to the 3D island growth mode.

Chapter 3

System setup and analysis tools

The pulsed laser deposition (PLD) system used in the course of this research was commissioned, partially assembled and tested as part of this work. Since the commissioning of the system in 2010, the PLD laboratory has undergone many minor redesigns and adjustments including the assembly of the closed laser path with the relevant optics to guide the laser beam safely to the deposition chamber. The following sections cover a brief introduction to this UHV deposition-analysis cluster, followed by the growth process and related calibrations.

3.1 System overview, design and elements

The PLD-RHEED system with *in-situ* X-ray photoemission spectroscopy (XPS) and STM system consisted of an external Excimer laser source in addition to two UHV chambers with independent pumping systems but connected by a gate valve in the middle and a transfer arm to allow *in-situ* sample transfer. This UHV cluster was a collaboration between Omicron GmbH and Twente Solid State Technologies (TSST). The system setup is illustrated both with a photo of the actual laboratory in figure 3.1 and a plan view schematic of the system drawings in figure 3.2. There were two ways of loading samples into the system; first via the load-lock chamber attached to the PLD chamber or secondly via a small load-lock placed after the gate valve which separated the PLD chamber from the analysis chamber. *In-situ* sample transfer was possible even if the pressure of the two chambers varied by 2 orders of magnitude due to the small diameter of the transfer line. The main UHV chamber was the PLD in which the samples were grown whilst being monitored by RHEED (described in detail in section 2.4).

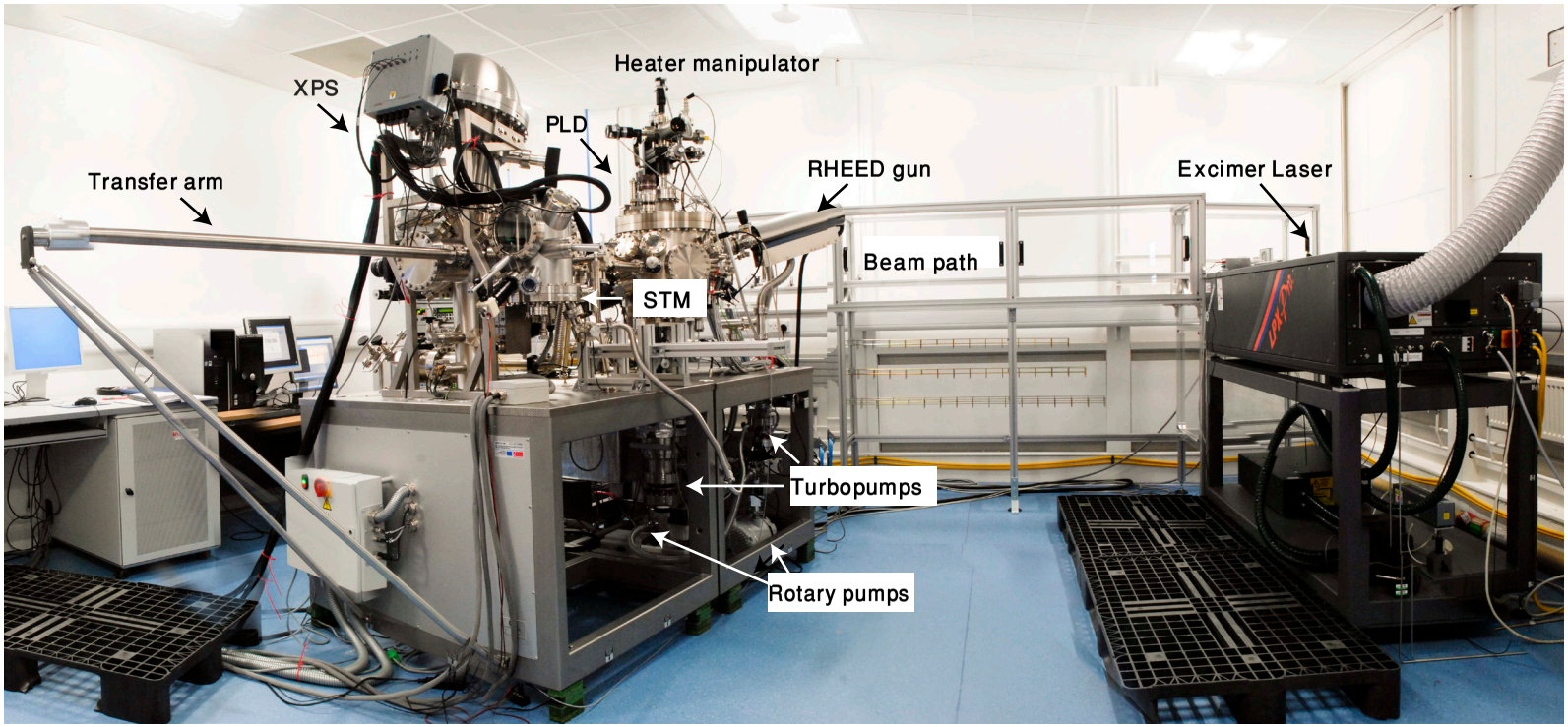

Figure 3.1: Photo of the PLD-RHEED with XPS-STM laboratory. On the right hand side is the KrF laser with gas container equipped with sensitive sensors to fluorine gas with extractors to the roof of the laboratory. The path between the laser and the PLD chamber is fully closed with UV-opaque windows. On the left hand side, there are the UHV control towers and computers in addition to the PLD chamber and analysis chamber. The pumping system is located under the benches including turbomolecular, ion and rotary pumps. There were two ways of loading samples into the system; first via the load-lock chamber attached to the PLD chamber or secondly via a small load-lock placed after the gate valve which separated the PLD chamber from analysis chamber. *in-situ* sample transfer was possible even if the pressure of the two chambers varied by 2 orders of magnitude due to the small diameter of the transfer line. The main UHV chamber was the PLD in which the samples were grown whilst being monitored by RHEED (described in detail in section 2.4).

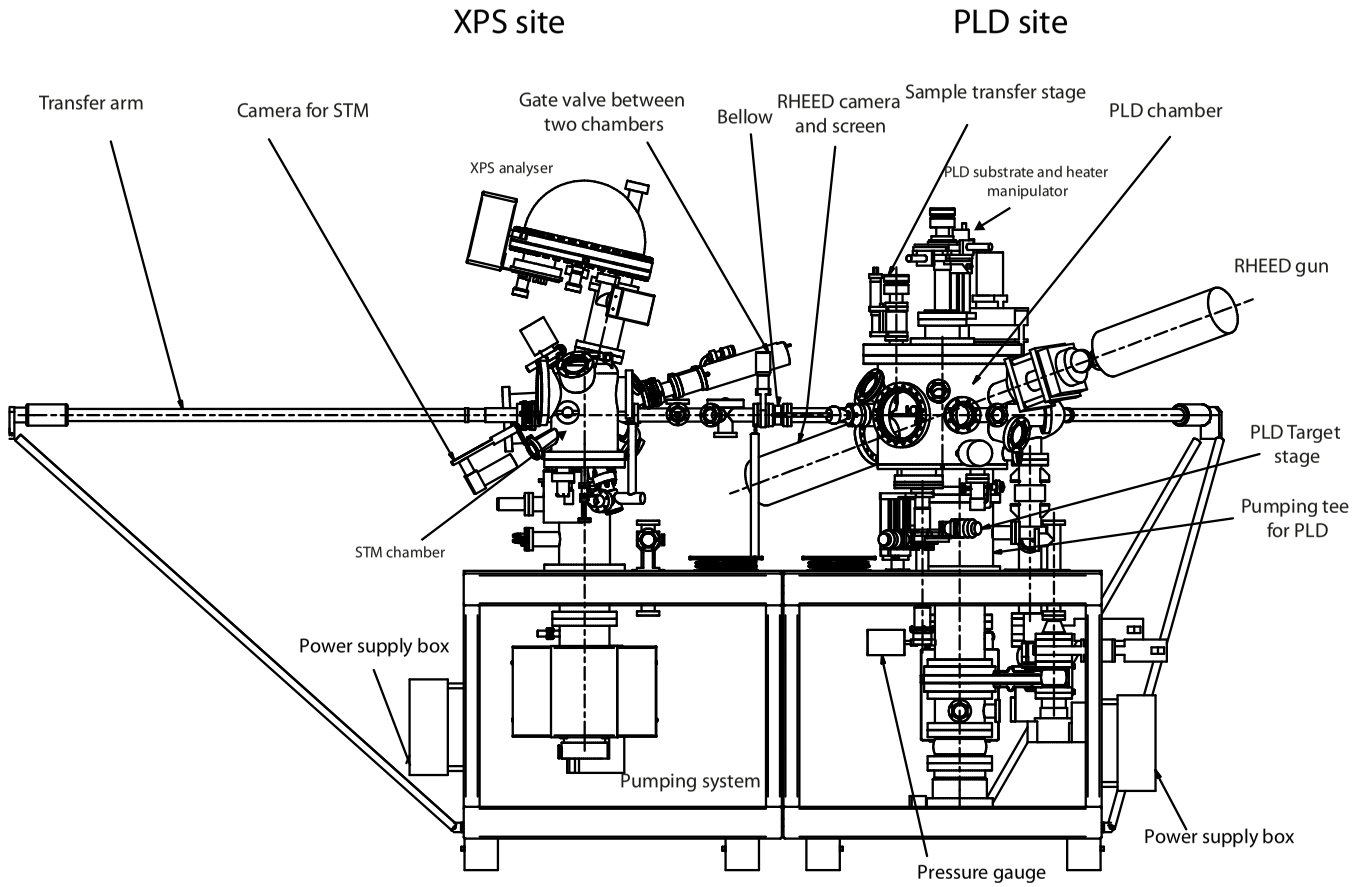

Figure 3.2: Side view plan of the system showing the vacuum components and two sites of PLD equipped with the RHEED system and XPS site with XPS/STM chamber.

The *in-situ* transfer only took place when the XPS analysis was performed immediately after the growth of the oxide thin films. The load-lock chamber attached to the PLD is also used for inserting and removing the target carousel. The system is fully controlled by computer and associated software designed by TSST. A double differentially pumped RHEED system was attached to the PLD chamber which consisted of a filament, deflection coils, aperture, fluorescent screen, a shutter, viewpoint and two separate pumping systems. The geometry of the RHEED setup attached to PLD chamber was shown previously in figure 2.1. The RHEED gun was pumped to a pressure of less than 5 $\times 10^{-4}$ mbar. The electron gun was pumped differentially to allow RHEED operation up to a maximum pressure of $\sim$ 0.1 mbar in the deposition chamber with *in-situ* RHEED investigation. To reduce the pressure to UHV in the vacuum chamber a range of equipment and pumping systems are required. Mechanical rotary pumps are used for the first stage of pumping, reducing the pressure from atmospheric pressure to a medium vacuum of 10^{-3} mbar. Rotary pumps remove gas particles by compression through repeatedly decreasing and increasing of the pumped volume and then transferring it to the atmosphere.

For the transition from the medium to high vacuum regime, a rotary pump alone is not sufficient and there is a need for further types of pumps which do not work based on the viscous flow of gases. The dominant pump used to achieve high and ultra-high vacuum in the surface analysis chambers are turbomolecular pumps (turbopumps). These pumps also work by compressing gas through a directed momentum transfer to gas molecules due to periodic collisions of particles with the surface of turbine blades. The alloyed blades are spun continuously and rapidly, up to 80 krpm, and the backing rotary or scroll pump transfers the exhaust to the atmosphere. This keeps the turbo pump in its most efficient molecular, or transition flow, regime [128]. Titanium sublimation pumps (TSP) and ion pumps are both oil-free getter-type pumps. Titanium as so many other metals, including zirconium, niobium and aluminium becomes a getter surface to trap active gases. In a titanium sublimation pump, the titanium filament takes advantage of relatively low sublimation temperature of titanium and sublimates it to cover the surrounding area and surfaces. The sublimed titanium reacts with gas molecules, becomes inactive, and thus periodic refreshing the titanium layer should take place [128].

The latter capture pump, the ion pump, consists of several Penning cells. Each cell has parallel cylindrical plates as an anode and uses an active metal (titanium) as the cathode. The pump is operated by applying a high voltage of between 3 and 7 kV to the cathode with a magnetic field of 0.1 to 0.2 T applied parallel to the anode plates. Emitted electrons will be trapped in a potential well with a circular path to prevent their immediate arrived at the anode. This maximises the ionising collision probability with gas

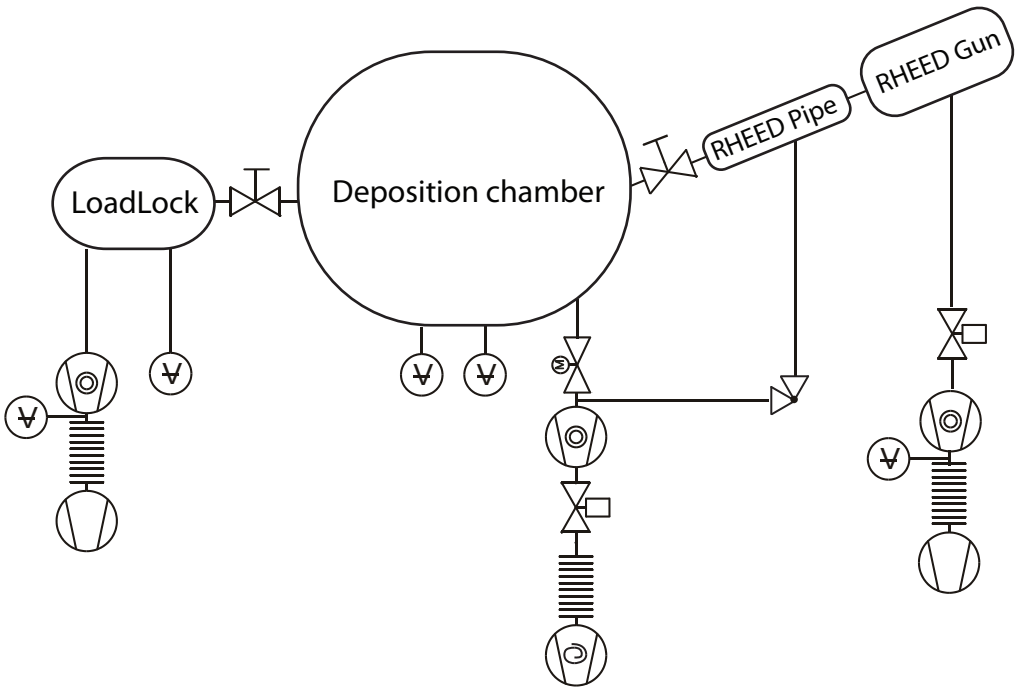

Symbol	Definition
	Vacuum measurement, vacuum gauge head
	Vacuum pump general
	Turbomolecular pump
	Scroll pump
	Flexible connection (e.g. bellows, flexible tubing)
	Hydraulic or pneumatic operation (gate valve)
	Electric motor operation (gate valve)
	Manual operation (gate valve)
	Right angle valve

Figure 3.3: A schematic diagram of the ultra-high vacuum pump system of a PLD chamber. The vacuum symbols are explained in the table. These symbols are used universally in vacuum technology [127].

molecules by increasing the traveling time of electrons in a spiral path. After collision, the ionised gas molecules are accelerated towards the cathode, and sputter away the titanium on the adjacent walls of the pump. The total number of molecules, thus, decreases resulting in a reduction of vacuum pressure. Since the number of ionisation events is approximately related to the ion current and ion current drops when pressure decreases, this allows ion pumps to be used as pressure gauges [128]. To increase desorption and diffusion rates of atmospheric gases from internal surfaces, the whole chamber should be 'baked out' periodically. The baking process involves heating the whole chamber up to 150 °C, after removing sensitive or non-bakeable connections from the system, while the chamber is under continuous pumping to remove desorbed gas molecules. Upon cooling, after degassing the components such as filaments (i.e. Bayard-Alpert ion gauge), eventually the lowest possible UHV pressure is achieved. A schematic diagram of the ultra-high vacuum pump system of a PLD chamber is shown in figure 3.3.

3.1.1 KrF Excimer laser

The laser used for deposition in this work was a Lambda Physik LPX*Pro* 210, from Coherent GmbH. The term Excimer comes from 'excited dimer' which refers to the excited diatomic molecules that acted as the lasing medium [81]. Using Krypton Fluoride (KrF) as the active lasing medium gives an output at a wavelength of 248 nm. This wavelength provides the high photon energy required in PLD to initiate the laser ablation. The high output energy required should be of the order of several J/cm^2 over an area of a few mm^2. The LPX*Pro* 210 has a maximum repetition rate of 100 Hz (can be varied from 1 to 100 Hz), nominal pulse energy of 1000 mJ and maximum average power of 65 W. The divergence of Excimer laser light is 1 mrad vertically and 3 mrad horizontally with a non-Gaussian beam profile in one direction. The pulse duration was 25 ns for this laser. For the work described here the repetition rate was kept constant at 5 Hz while the other deposition conditions were varied to find an optimal set of growth parameters.

Energy modes of the laser and energy attenuation

There are two factors that affect the output energy of an Excimer laser: the age of the laser gas and the operational high voltage (the charging voltage). The pulse energy of the laser reduces when the gas used in the laser tube ages. As the laser gas ages, the voltage should be increased to compensate for the loss in energy. The laser in this work is set to use premix gas cylinder (10 litre pre-mix of 0.12% F_2, 2.3% He, 3.03% Kr and the rest Ne gas). The laser was running under 'no gas replacement' mode

meaning there were no gas actions at the time of the operation.

There are two fundamental operational energy modes of the LPX*Pro*, The 'high voltage (HV) constant' mode and 'energy constant' mode. The former is when HV is set to certain value while the energy decreases over time due to the laser gas deterioration. The latter implies that the laser adjusts the high voltage to keep the energy constant at a pre-set value. The laser during this work was operated in HV constant mode. The reason for this was the lack of accuracy in the internal energy meter of the laser resulting in significant variations in pulse-to-pulse energy. The energy was measured after the projection lens using a head-sensor in conjunction with Coherent energy meter. The accuracy of the energy reading was 0.1 mJ. Since the pulse-to-pulse energy is more stable at higher operating voltages an attenuator was used to access lower energies whilst keeping the energy output stable. This also allowed access to a larger parameter space for optimisation. The attenuator was placed just after the exit point of the laser was a MicroLas attenuator from Coherent GmbH.

3.1.2 Optical elements for the laser path

Figure 3.4 illustrates how the laser beam was guided into the PLD chamber using a suitable arrangement of Excimer laser compatible mirrors and lenses. The distance between the laser and chamber was $\sim$4 m, which allows imaging of the aperture onto the target to obtain various spot sizes. Using a 'periscope' type mirrors arrangement, the height difference between the chamber laser window and the laser exit aperture was adjusted. To attain a well-defined spot shape and improved energy profile by cutting off the in-homogenous part of the low-intensity beam, a rectangular shape aperture was placed before the lens to restrict the beam image and to be able to adjust the demagnification factor by changing its place relative to the lens position. The dimensions of the aperture were 2.1 ± 0.1 $\times$ 18.0 ± 0.1 mm^2 which allowed at least $\sim$80 $\%$ transmission of the high intensity area of the beam.

The image of the aperture was projected onto the target surface using a lens. The lens in this setup was a UV Grade Fused Silica (50 mm in diameter with 500 mm focal length). The demagnification is important since the thin film quality is greatly affected by laser energy density, or fluence, on the target. In setting up the optics for PLD, it is not recommended to focus the beam directly on the target surface by putting the target in the focal length of the lens as this will lead to an in-homogenous distribution of energy density and interference effects [129]. As shown schematically in figure 3.5, it is necessary to place the target slightly off focus where the beam profile is imaged on the surface of the target sharply to achieve clean ablation [129]. To achieve the desired demagnification, there are a few parameters to adjust such as the target-lens distance

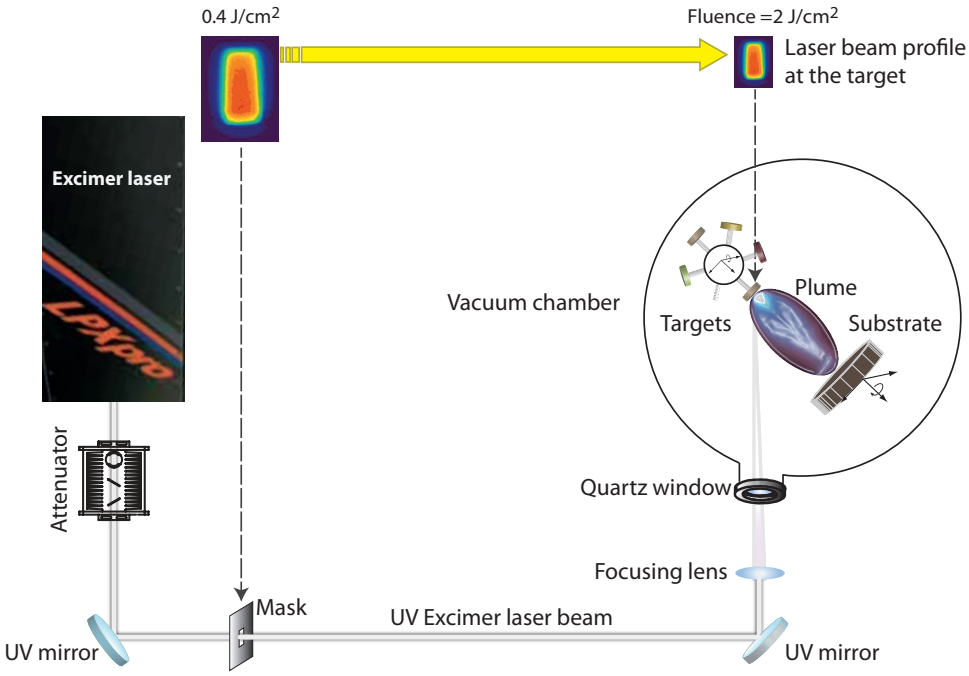

Figure 3.4: Schematic of the PLD optical arrangement with UV Excimer laser 248 nm. The long beam path allows varying the demagnification and focusing the beam onto the surface of the target as required. The energy fluence of 2 J/cm^2 was achieved by focusing the mask image onto the target.

(d_t) and the aperture-lens distance (d_m) knowing the focal length of the lens (f) and the demagnification factor is defined as d_t/d_m. The arrangement of mirrors is illustrated schematically in figure 3.4. Projection lens and also the target surface is shown with respect to the laser beam (at 45°) in this PLD setup. It should be noted that this angle affects the projection of the image onto the target surface and expands it by a factor of $\sqrt{2}$ in the width of the beam spot.

$$E_F = \frac{E}{\sqrt{2}A} \tag{3.1}$$

where E_F is the on-target energy density (fluence), E is the measured energy of the laser beam after the aperture and A is the demagnified area. It is important to note excessive demagnification of the spot can result in reduction of thin film quality and growth rate. There is a trade-off when choosing the beam spot size as the plume becomes less directional [129] when decreasing the beam spot size on the target surface. The consequences of the in-homogenous distribution of energy density on the target can lead to incongruent melting and splashing effect combined with micrometre size particulates

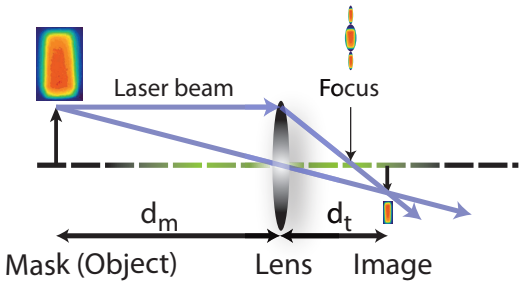

Figure 3.5: An illustration of the imaging system using a single projection lens for an Excimer laser. The Laser beam focusing is compared with laser beam imaging (coloured rectangular image is a near field measured beam profile for a KrF laser).

reaching the substrate [76]. Based on equation 3.1, four various demagnification places for the aperture and the lens were calculated and are presented in table 3.1.

Demagnification	d_t (cm)	d_m (cm)	Spot height (mm)	Spot width (mm)
1/5	64.0	320	3.6	0.6
1/4	67.4	269.6	4.5	0.8
1/3	72.5	217.5	6	1
1/2	82.0	160	9	1.5

Table 3.1: For laser beam imaging calibration, four different places of the aperture and projection lens were determined to achieve various spot sizes. It should be noted by placing the aperture and focusing lens, a flat-top image was projected onto the surface of the target for homogenous ablations.

3.2 Deposition setup

For *in-situ* characterisation i.e., XPS and STM, the substrate holder had to be compatible with *in-situ* transfer. The traditional substrate holder was not suitable for this work and was redesigned. The new design was a combination of the old stage with an additional Omicron sample plate. Figure 3.6 shows the evolution of the substrate holder from the original design to the *in-situ* transferable custom-design. The heater assembly had 5 degrees of freedom allowing for full translational movement, as well as tilt and azimuthal rotation for RHEED study and sample transfer. A silver paste was used as an adhesive to glue the substrate onto the sample plate due to its good thermal contact and stability at high temperatures.

Omicron plates were cleaned by mechanical polishing using grinding papers and

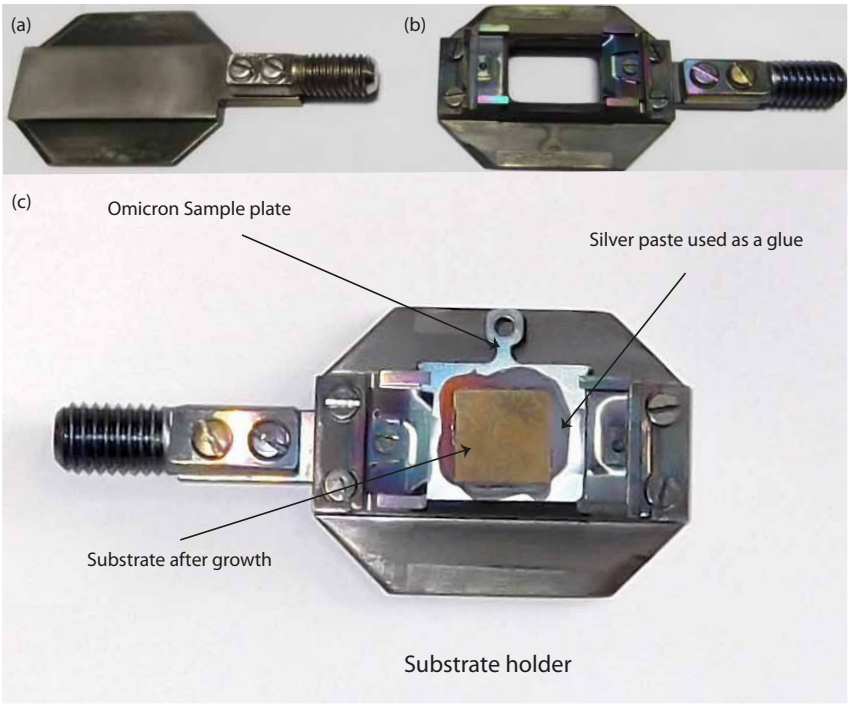

Figure 3.6: Image (a) the original holder which did not allow for *in-situ* sample transfer (b) the new design with screws to hold an Omicron sample plate (c) an image showing substrate holder with a sample attached to it after the growth.

subsequently cleaned ultrasonically using Acetone and isopropyl alcohol (IPA). A selection of single crystal substrates were studied initially by X-ray diffraction to examine their quality and were selected for final growth based on their rocking curve full width half maximum (FWHM). If not treated to achieve single termination, they were cleaned in an ultrasonic bath for 10 minutes in acetone and were transferred to IPA to avoid any residue from the acetone, and then placed in the ultrasonic bath for a further 10 minutes. Substrates were blown dried immediately after the IPA bath using a nitrogen gun. Using silver paste, the substrate was then attached to the sample plate (figure 3.6-c)). The contact between heater and substrate should be homogeneous to avoid any temperature gradient across the substrate during the growth. Once the substrate was attached, it was placed on a hot plate at 200 °C for 1 hour. Then it was blown dried again with nitrogen gas and transferred to the PLD load-lock mounting the Omicron plate onto the substrate holder. For reproducible thin film growth, the target surface was polished, because the surface alteration of the target after irradiation with several thousand pulses affects the surface morphology of the target changing the angular distribution of energetic species [130]. Gentle and even polishing using grinding paper and IPA was performed.

3.2.1 Laser ablation

To clean the area of deposition before ablation, an *in-situ* pre-ablation process was carried out with the shutter covering the substrate surface. Targets were pre-ablated in the presence of oxygen for 1000 pulses at 5 Hz prior to deposition. Pre-ablation ensured any surface contaminants adsorbed in the polishing process were removed. After completion of pre-ablation, the chamber was pumped to its base pressure. Before starting the deposition, the RHEED settings were optimised to produce a well-defined diffraction pattern of the substrate. The electrons can be focused, accelerated, and deflected in 2 orthogonal directions via the electronic and magnetic optics. There were 6 parameters in RHEED be optimised: 1) beam energy, 2) filament current, 3) focus, 4) grid, 5) X-deflection, and 6) Y-deflection. The RHEED voltage was gradually increased until it reached 30 keV which was the maximum energy achievable in our system. It was used to reduce electron scattering in ambient gas. The attenuation of the electron beam intensity occurs due to the lower mean free path of electrons in an ambient gas such that [131]

$$\frac{I}{I_0} = \exp\left(-\frac{l}{L_E}\right), \tag{3.2}$$

and L_E is the mean free path defined by

$$L_E = \frac{1}{\sigma_T n}, \tag{3.3}$$

where σ_T is total cross-section for scattering and n is the molecular density given by

$$n = \frac{P}{k_B T}, \tag{3.4}$$

where P is the ambient gas pressure, k_B is Boltzmann's constant, and T is the absolute temperature. The cross-section of the scattering σ_T depends on the energy of the electrons. The filament current controlled the temperature of the filament and hence the maximum emission current. The maximum current of 1.55 A was used to prevent burning out the filament. The focus and grid settings were adjusted simultaneously since more sharply defined diffraction patterns can be achieved at the expense of decreased intensity. The beam divergence and the position of the focus were defined by the focus value, while the grid was used to limit the beam diameter and consequently the beam current leading to a more steadily collimated beam. An ideal beam spot of a small round circle with a well-defined edge was achieved before bringing the substrate into the beam. The X-deflection and Y-deflection were then used to move the beam. The two sets of X and Y deflection units were used to deflect the beam in a horizontal and a vertical

plane, such that, the electron beam was guided through the pinhole at the end of the RHEED differential pumping tube and impinged on the surface of the substrate. The substrate can be tilted and also moved back and forward in the direction normal to the surface plane to adjust the sample position on the optical axis (figure 3.4). The sample was rotated azimuthally to capture several RHEED images for post-growth lattice parameter analysis. Next, the shutter was opened for heating in order to prevent any redeposition of material from the shutter surface onto the substrate. The sample was heated to the growth temperature at a rate of 20 °C/min. The chamber was filled with the desired oxygen background after the substrate temperature had reached 400 °C to prevent excess oxygen vacancies in the $SrTiO_3$ substrate as a result of annealing in UHV. The actual surface temperature of the substrate was verified using a pyrometer and the heater output was adjusted to stabilise the sample to the correct temperature. Once the required temperature was stabilised, the heater power supply was kept at a constant current to prevent any deflection of the electrons by any magnetic field produced by fluctuations in the heater current. For similar reasons, the main gate valve of the PLD chamber was set at a fixed position. For all the films grown, the (000) reflection was monitored. A line profile of the (000) specular spot was observed to adjust the angle of incidence, and hence optimise the FWHM of the specular peak using the X- and Y-deflection in conjunction with the focus and grid circuits of the RHEED. The number of pulses for the deposition was set at the start of the growth run, depending on the desired thickness. A different approach was followed for multilayer growth depending on the thickness of the bilayer which is discussed in detail for each superlattice in chapter 7. The following section explains the experimental techniques used after the deposition to characterise the resulting thin films.

3.3 Analysis tools

In this section the theory and principles of the experimental techniques used after the growth of thin films are explained. A wide range of techniques have been used for the analysis of the grown samples including high resolution X-ray diffraction (HR-XRD), transmission electron microscopy (TEM), atomic force microscopy (AFM), X-ray photoemission spectroscopy (XPS), magnetic measurements using superconducting quantum interference device (SQUID), and transport measurements using a physical properties measurement system (PPMS). A brief description of these characterisation techniques are given with the underlying basic principles explained.

3.3.1 High resolution X-ray diffraction (HR-XRD)

While electron scattering from the near surface region leads to diffraction of the beam in RHEED, in X-ray diffraction (XRD) photons are scattered coherently from core electrons in the bulk of a material. Diffraction peaks occur if the path length of the scattered photons between two scattering points is an integer multiple of the wavelength of the photons. This was suggested by Bragg and can be expressed mathematically as

$$n\lambda \ = 2d\sin(\theta) \tag{3.5}$$

where n is an integer, λ is the wavelength of the incident X-ray beam, d is the spacing between adjacent atomic parallel planes with Miller indices h, k and l, and θ is the angle of incidence between the X-ray beam and lattice planes of the crystal (known as the Bragg angle). For diffraction to occur, λ needs to be smaller or equivalent to the lattice spacing (of the order of Angstroms). In equation 3.5, n is referred as the 'order' of diffraction. For example a 'second order' reflection in a cubic lattice will be labelled as (002) and the corresponding planes have a d spacing equal to half that of the (001) planes.

This dependence of equation 3.5 on λ is not desirable when comparing two diffraction datasets collected using various photon energies (e.g. between a lab source and a synchrotron). This dependence can be removed by rewriting Bragg's law based on the scattering vector, $\boldsymbol{Q}$, of the scattered photons, allowing the transformation of the collected data from angular space to reciprocal space. This transformation is depicted graphically in figure 3.7 which amounts to the following mathematical relationship through geometry [132]

$$\mathbf{Q} = \begin{pmatrix} Q_x \\ Q_y \\ Q_z \end{pmatrix} = \begin{pmatrix} \frac{2\pi}{\lambda}(\sin\alpha_i + \sin\alpha_f) \\ 0 \\ \frac{2\pi}{\lambda}(\cos\alpha_f - \cos\alpha_i)) \end{pmatrix} \tag{3.6a}$$

where $\dfrac{2\pi}{\lambda}$ is the magnitude of $|\boldsymbol{k}|$, the wave vector of the scattered photons, α_i and α_f are the incident and final (outgoing) angles measured with respect to the surface of the sample or lattice plane. On the diffractometer the angle ω is defined as the circle that the sample rotates in with respect to the incident beam and the detector angle is given by 2θ. These angles are related to α_i and α_f by

$$\alpha_i + \alpha_f = 2\theta \ \text{ and } \ \omega = \alpha_i, \tag{3.6b}$$

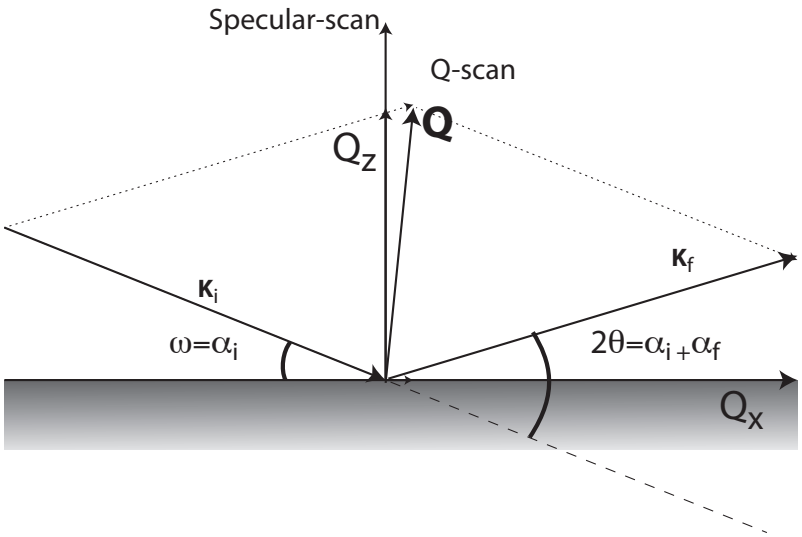

Figure 3.7: Graphic depiction of the scattering vector for an angle dispersive set-up. α_i and α_f are the incident and final (outgoing) angles. The angle ω is defined as the circle that the sample rotates in with respect to the incident beam and the detector angle is given by 2θ.[132].

so,

$$\mathbf{Q} = \begin{pmatrix} \frac{2\pi}{\lambda}(\sin\omega + \sin(2\theta - \omega)) \\ 0 \\ \frac{2\pi}{\lambda}(\cos(2\theta - \omega) - \cos\omega) \end{pmatrix}. \tag{3.6c}$$

In the case of symmetric diffraction, where $\alpha_i = \alpha_f$ equation 3.6c simply reduces to shown as

$$|\mathbf{Q}| = Q_z = \frac{4\pi}{\lambda}\sin(\omega). \tag{3.7}$$

Equation 3.7 can be substituted into Bragg's law (equation 3.5) to yield

$$d \;=\; \frac{2\pi}{|\mathbf{Q}|}. \tag{3.8}$$

This convention is useful as all families of parallel planes are evenly spaced in $\mathbf{Q}$-space and the diffracted peak positions are independent of the experimental set-up. This also simplifies lattice parameter calculations. The majority of the XRD data presented were taken from a Panalytical X'Pert Pro MRD. The source in this diffractometer was copper ($K_{\alpha 1}$ ($\lambda = 1.5406(1)$ Å)) operating at 40 kV /45 mA. To have a high intensity monochromatic beam, a hybrid Ge crystal was used at the source in addition to divergence slits to collimate the beam. There are five degrees of freedom in this set-up including

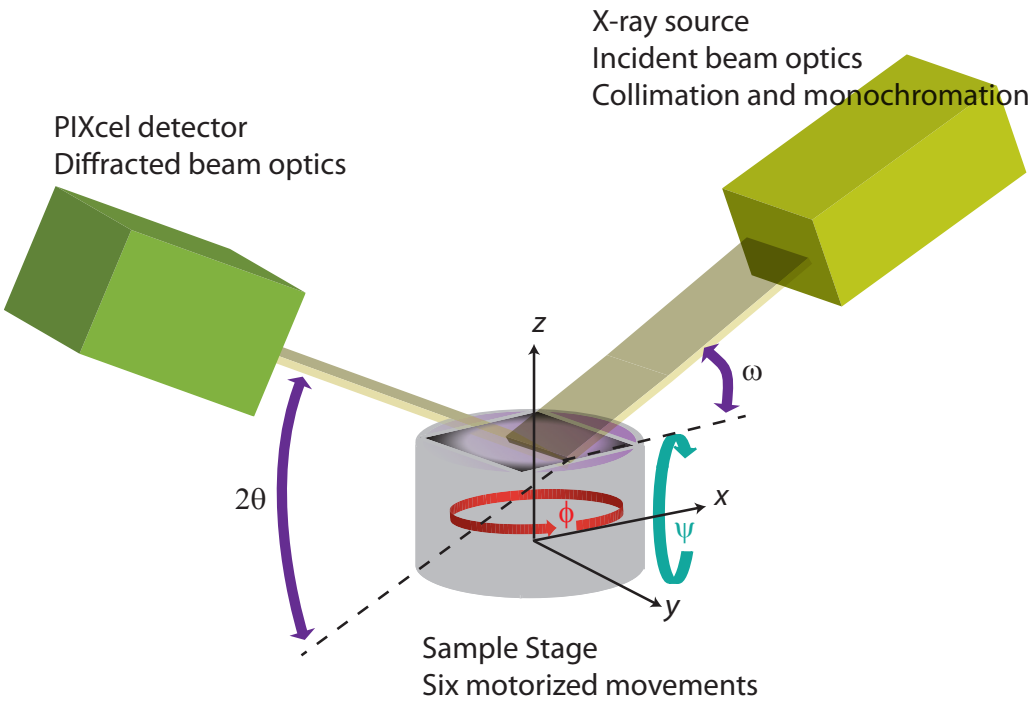

Figure 3.8: Schematic of a double axis high resolution XRD instrument. The six motorized movements of the MRD cradle are shown. The angle Ψ is also known as 'tilt' angle when Φ is azimuthal rotation. x, y and z are translational axis.

the sample stage x, y, and z which corresponds to the sample position, the rotation and also the tilt of the sample stage, phi (Φ) and psi(Ψ), respectively. Figure 4.4 is a schematic of XRD set-up showing the angles in which the sample stage can be rotated. These rotations were used to optimise the intensity of the diffraction peak (from the (002) plane of the $SrTiO_3$ substrate).

3.3.2 Transmission electron microscopy (TEM)

In order to allow the transmission of electrons in TEM, very thin (with thickness of 100 nm or less) specimens and electrons with very short wavelengths ($\sim$ 0.003 nm) are used. This very short wavelength results in a significant improvement in the resolution of the microscope (0.075 nm point resolution at 200 kV). Furthermore, the transmitted electrons not only can be used as a real space probe of the sample, but also as a reciprocal space probe using their diffraction pattern providing finer detail of the specimen's structure. High magnification images can give insight into the quality of heterostructures and reveal nanoscopic defects in a crystal. Interfaces between multi-

layers can also be examined by TEM and compositional analysis can be obtained by monitoring the energy loss of the electrons as a result of their interaction with specific elements. A schematic representation of a typical TEM column is shown in figure 3.9. Electrons are generated using an electron gun, shown at the top most part of the schematic, by thermionic emission from a heated filament. Electrons are then accelerated through the column using a voltage of 200 kV, towards a grounded anode. In order to prevent fluctuations in the beam intensity, and to prevent its interactions with the medium, the microscope column is water-cooled and kept under high vacuum (below 10^{-7} mbar). In order to correct for spherical aberrations induced by in homogeneities in the magnetic lenses, which would otherwise limit the resolving power of the microscope, spherical aberration correctors, C_S, are used [133, 134, 135, 136]. TEM can be operated under two different measuring modes: imaging and diffraction. When working in the diffraction mode, a selective area diffraction aperture is placed before the intermediate lenses, which allows the diffraction pattern to be measured from a specific area on the specimen.

The contrast in a TEM image arises from four main effects: differing atomic density (e.g. the differing contrast between La and Mn atoms), increasing the atomic number (Z) results in variations in the electron scattering intensity; variations in the specimen's thickness, which will attenuate the transmitted electron intensity; differing atomic planes due to the strain or defects in the crystal; and the selective diffraction condition due to the tilt of the specimen with respect to the incident electrons. Low-resolution defect studies were carried out by 'diffraction contrast' arising from scattering of electrons by different planes of the crystal satisfying the Bragg condition, forming a diffraction pattern. When operating in the diffraction mode, the scattered electrons are split into reflections in the focal plane of the objective lenses and the intermediate lenses are adjusted to focus the rays of individual diffraction conditions, which correspond to specific crystallographic planes, onto a single focal point. The resultant diffraction spots are then magnified using the projector lenses to resolve the diffraction pattern on the phosphor screen. Tilting the sample results in the diffraction of electrons form certain planes in a crystal. The [000] spot, comparable to that of the specular spot in RHEED, is a 'straight-through' beam and is always present. When the sample is tilted such that, either, only the [000] spot or the [000] and another spot are visible, the condition is called the 'bright field' (BF) or 'two beam diffraction' condition, respectively. Any kind of anomaly within that crystal plane will lead to an electron intensity subtraction. If the image is formed by excluding the [000] spot, it is called 'dark field imaging' (DF). By tilting the specimen onto a zone axis, such that the interference of several diffracted beams (instead of individual beams) can be measured, high resolution TEM (HRTEM)

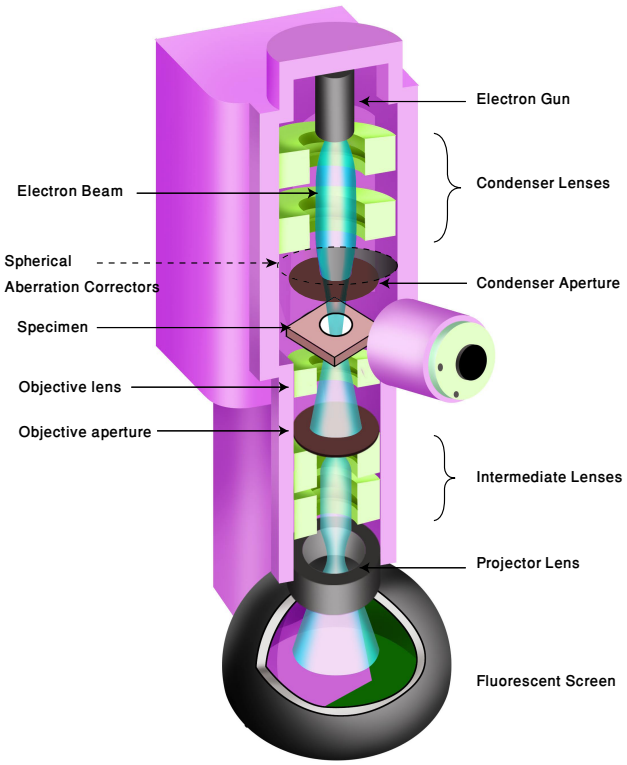

Figure 3.9: Schematic representation of a typical transmission electron microscope. Between the condenser lenses and condenser aperture is where the spherical aberration correctors are placed and also the beam deflectors. (adapted from [137])

images can be obtained. A scanning coil can also be used to raster the beam across the sample (scanning transmission electron microscopy (STEM) figure 3.10), and allows microanalysis on specific areas of the specimen. The inner cone (∼70 mrad) of the transmitted electrons, containing all of the Bragg diffracted electrons, are deflected onto an electron energy loss spectrometer (EELS) and energy of the X-ray light, generated by the electron beam incident on the sample, are detected by an energy dispersive X-ray (EDX) detector. This provides compositional analysis of the layers in the superlattice.

In high resolution HAADF-STEM, scattering from individual columns of atoms is detected. The angle of the inner cone in HAADF is made large (∼ 70 mrad) so that no Bragg diffracted electrons can be collected. The outer cone of HAADF is made as large as possible (∼ 150 mrad). The images are formed from elastically scattered electrons which have passed very close to the nucleus of atoms. The HAADF atomic resolution image shown in figure 3.10 is acquired from a perovskite thin film of $LaNiO_3$. The HAADF signal is very sensitive to the atomic number Z, the specimen thickness, and also

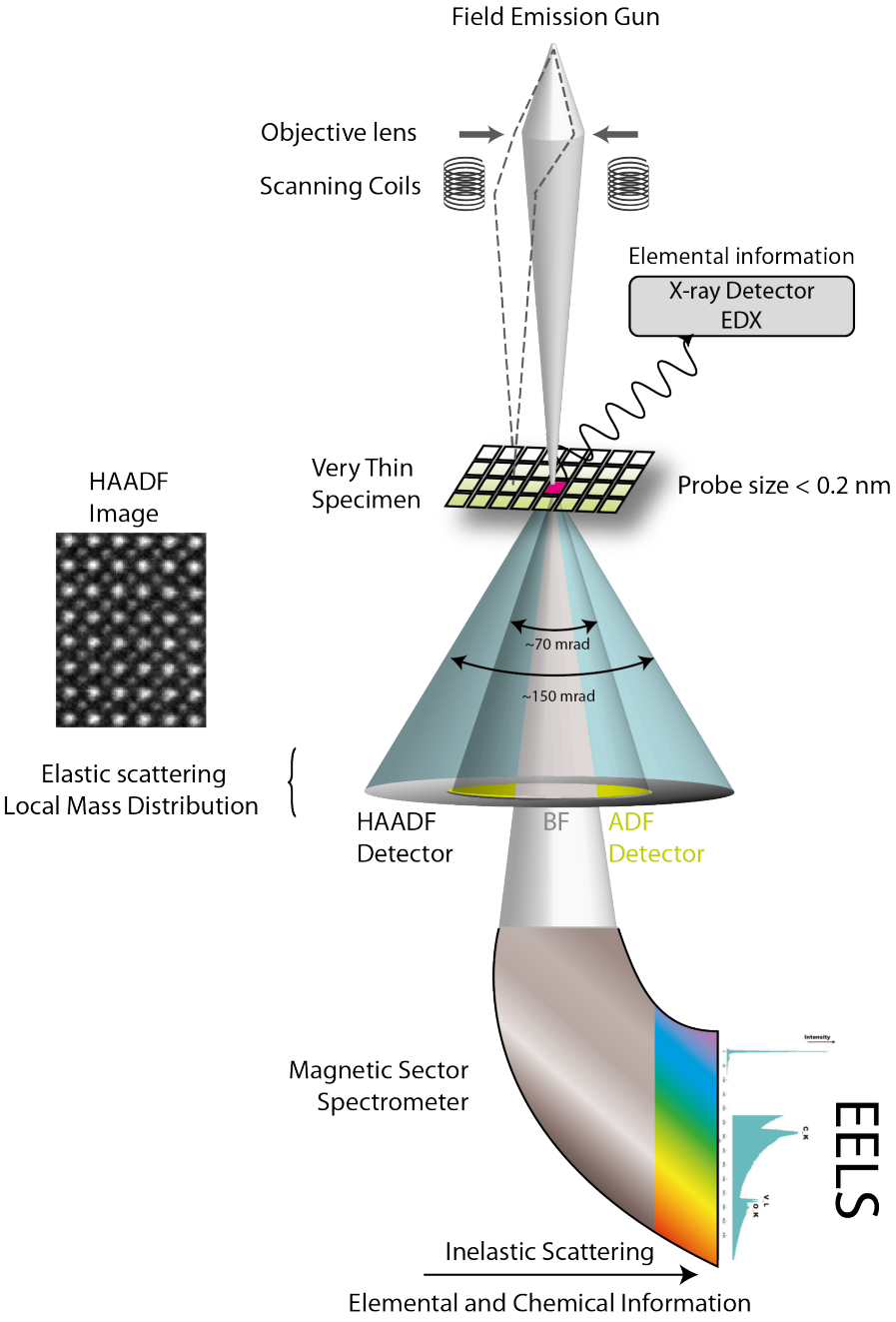

Figure 3.10: Schematic of a STEM equipped with EELS and EDX. There are three different detectors within a STEM: BF detector is located in the so-called near-axis position; ADF detector is situated around the BF detector. HAADF detector is placed as wide as possible around the ADF detector, but above the projection chamber.

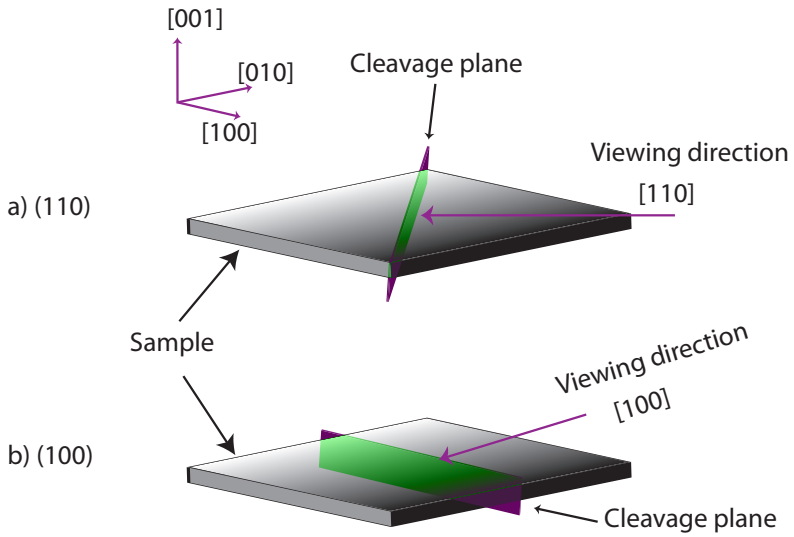

Figure 3.11: Schematic illustration of cleaving orientation for preparation of ⟨110⟩ and ⟨100⟩ TEM samples

density. High magnification images can give insight into the quality of heterostructures and reveal nanoscopic defects in a crystal. It is shown schematically in figure 3.10 that the bright field detector is located in the so-called near-axis position and the annular dark field (ADF) detector is situated around the BF detector. The acceptance angle of each detector is determined by the chosen camera length and also the detector's dimensions. the high-angle annular dark field (HAADF) detector is placed as wide as possible around ADF detector but above the projection chamber.

3.3.2.1 Cross section TEM specimen preparation

In order to acquire high quality transmission electron images, specimen preparation is of great importance. Specifically for TEM measurements, it is necessary to prepare samples that are electron transparent and limit the probability of multiple scattering events, which generally requires samples only a few hundred of nanometres thick. There are many ways to prepare such a thin sample and the methodology often must be modified on a system-by-system basis. For the majority of the work presented within this thesis, a modified 'rapid TEM sample preparation' [138] was used. In order to improve the accuracy of the cleaving, the sample was initially back thinned by mechanical grinding. To control the thickness during the grinding the sample was mounted face down on a microscope slide, using wax as glue. The sample was then roughly ground down to a

thickness of approximately 100 μm using a P800 SiC abrasive paper and then polished with a finer SiC abrasive paper (p2400). Samples could be cleaved directly along the $\langle 100 \rangle$ direction by making a mark on the edge of the thin film using a fine point diamond scribe. Afterwards the tweezers were used as a wedge then, using the groove created by the diamond scribe, a gentle force was applied.

For non-standard orientations such as [110] it was necessary to cleave the thin films in such a way that the view within the microscope would be along one of the $\langle 110 \rangle$ directions. As all the substrates used have a square shape of either 5 $\times$ 5 mm^2 or 10 $\times$ 10 mm^2, the sample were cut diagonally by the diamond saw into two or more pieces. Figure 3.11 illustrates schematically the way these viewing orientations were determined and cut along the cleavage plane by a diamond saw. The pieces cut by diamond saw must be flattened cross-sectionally, which was performed by adhering the two halves back to face using epoxy glue. This glued sandwich was then mounted between various (500, 300 and 100 μm see figure 3.12) thicknesses of microscopic slides, which not only offer a guide for grinding the sample down to a specific thickness (as above), but also to provide structural support. The thinned sample was then cross sectional polished using progressively finer abrasive papers (P800, P1200, P2400 and P4000), resulting in a polished orthogonal sandwich with a square cross-section of 100 by 100 μm^2 (figure 3.12).

The one-side polished or accurately cleaved sandwiched samples are then glued on their polished side to a TEM slot grid (which is a ring typically made of copper or molybdenum with dimensions 0.4 $\times$ 2 mm, 3.0 mm O.D.) along with two Si or $SrTiO_3$ pieces, which have been similarly back-thinned to a thickness of 100 μm, which provide structural support to the sandwich during grinding and ion milling. The thickness of the sample was monitored during this step with optical microscopy, by measuring the displacement in the focal point of the microscope between focussing on the TEM grid and on the top of the sample (note that, in order to correct for gradients on the sample formed by uneven grinding, opposite sides of the sandwich were measured using this process). To provide finer control of the grinding, a 'jig' (shown in figure 3.13) was created by mounting a microscope slide on the end of a cylindrical metal bar with a diameter of 2 cm; the sandwich and three back-thinned silicon slices (to provide levelling for the grinding) are then mounted onto the microscopic slide. As $SrTiO_3$ is relatively brittle it must be ground along the desired crystallographic direction until the sandwich sample is level with its supports to avoid fracturing and, once level, the sample is ground orthogonal to the desired crystallographic direction. Progressively finer abrasive grinding papers were used, and before moving to these finer grades, the sample was cleaned by ultrasonic cleaning in IPA. Below 30 μm the sample can no longer be safely ground

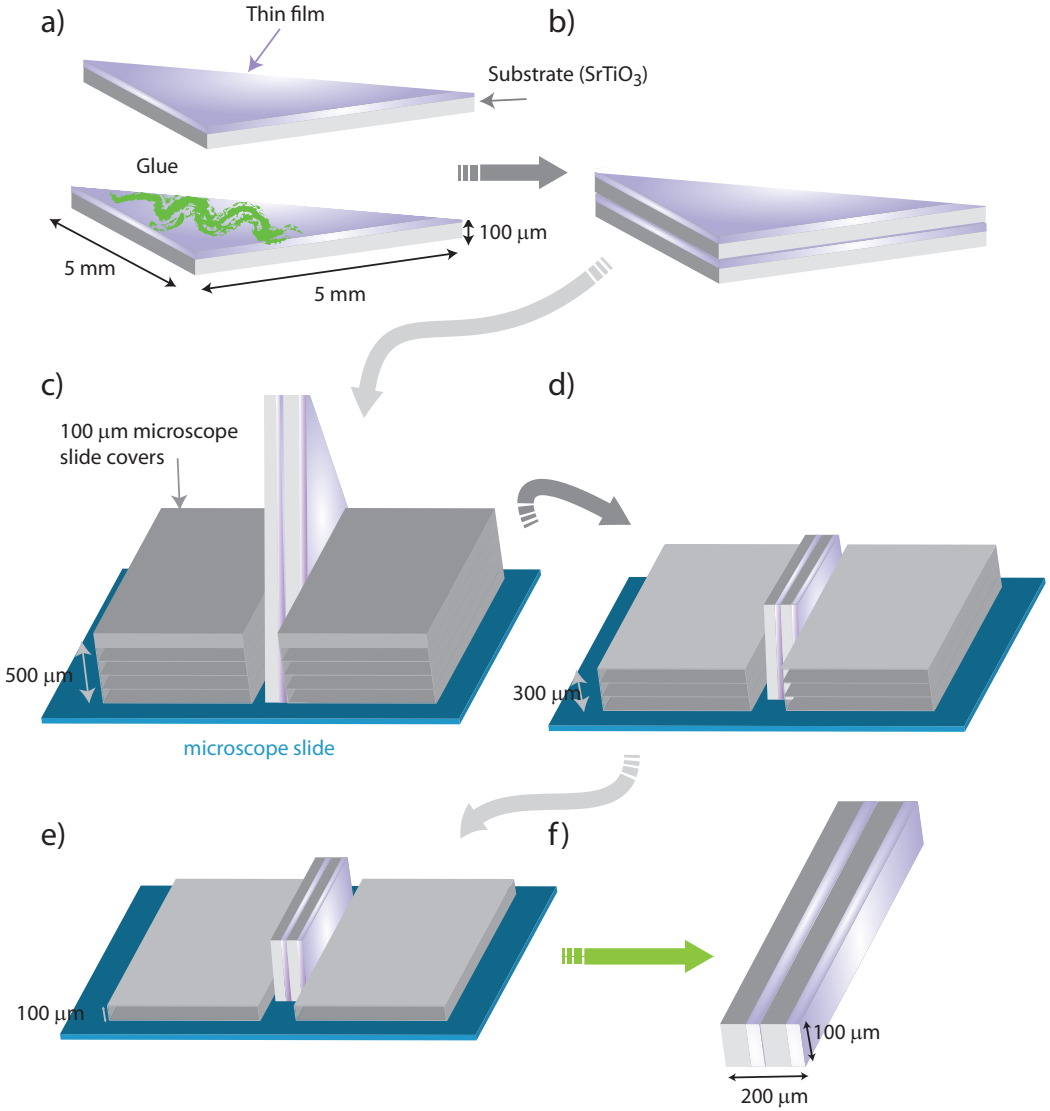

Figure 3.12: The initial process of rapid TEM preparation modified for perovskite substrate $SrTiO_3$ for <110> orientation. a) The sample (which was initially back-thinned to 100 μm) was cut diagonally and then glued back-to-face. b) Depending on the glue curing instructions, the sandwich is allowed to be set. c) Cross-section of the sandwich needs to be polished finely before being placed on the TEM grid. To facilitate controlled grinding, the supporting microscope glass slides of known thickness ($\approx$100 μm) were used starting from 5 glued microscope slides (500 μm block). d) To thin the sample further, 300 μm blocks were used as the support. e) Final grinding step before mounting the sandwich on the TEM grid is using a single microscope slide. Finer grinding papers should be used at this stage for the final finish. f) This process results in a sandwich with cross-section diameters of 200 μm $\times$ 100 μm.

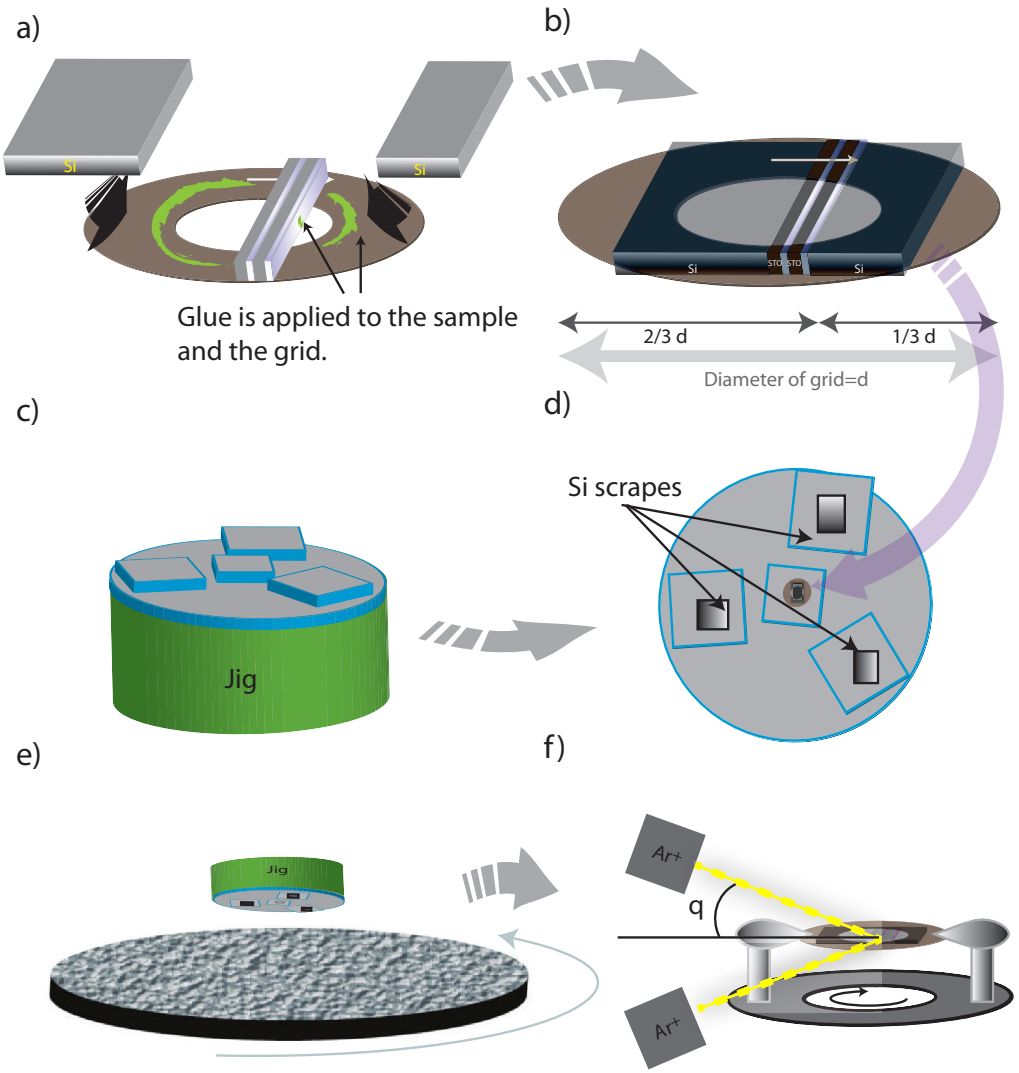

Figure 3.13: Final process of rapid TEM preparation of cross-section. a) Prior to mounting the back-thinned sandwich, a fine arrow was made by a diamond scriber for the interface identification (where the thin film is buried). A thin layer of glue was applied for mounting the sample on a 3 mm TEM-grid. To support the sample, two Si pieces were inserted on the sides. b) The first interface was placed at 2/3 of the diameter of the TEM-grid c) For more controlled polishing, a so-called 'jig' was created made of a 2 cm metal rod with glass microscope slide pieces on top. d) The grid was mounted in the middle, and then was accompanied by three Si pieces to level the grinding. e) The sandwich assembly was then ground down with similar method as back-thinning. The thickness of the sample was checked regularly using an optical microscope until it reached 30 μm. f) Sample was placed in an argon-ion mill until a hole appeared at the interface to ensure that the electron transparency is achieved.

using mechanically means, and instead is argon-ion milled and a Gatan Precision Ion Polishing System (PIPS) was used. The Gatan PIP system has an incident beam above and below the sample, whose incidence angle can be varied. The sample is rotated during ion milling to improve the homogeneity of the sample thickness. Within the ion mill the sample is bombarded with argon ions, accelerated with a voltage of 6 kV, until a hole appeared in the region of interest. This hole guarantees the presence of areas that are suitably thin for use in the TEM, and once observed the accelerating voltage is decreased to 3 kV for several minutes and then to 2 kV for final polishing to prevent Ion beam-induced amorphisation. After this process is complete, the sample is ready to be mounted into the TEM.

3.3.3 X-ray photoelectron spectroscopy

Whilst XRD and RHEED can give valuable information concerning the bulk and surface crystal structure, as well as the flatness of the interface and surface, no chemical composition data can be provided by these techniques. X-ray photoelectron spectroscopy (XPS) is a non-destructive surface sensitive technique which allows detailed quantification of electronic and chemical states of the first few atomic layers of a sample. XPS can be used for elemental and chemical identification of the surface allowing determination of the surface composition.

XPS is based on the photoelectric effect, which was first explained by Einstein [139]. In XPS, the surface of the material is irradiated by X-rays and surface atoms which absorb photons with energy greater than the sum of the electron binding energy and the work function of the sample will emit electrons (photoelectrons) due to energy transfer from the photons to the core level electrons. The process of photoemission can then be summarised as follows: the excited electron is promoted to a higher unoccupied energy state; next the photoelectrons propagate into the sample surface (where elastic and inelastic scattering may occur); finally, the electron will be transmitted into the vacuum [140, 141]. The energy of this emitted photoelectron is characteristic of the atom from which it this emitted since core level electrons do not participate in bonding and their energy is, to some extent independent on the environment [142]. By measuring the kinetic energy of the photoelectrons, the binding energy can be calculated as

$$E_B \;=\; h\nu \;-\; E_K \tag{3.9}$$

where E_B is the binding energy, $h\nu$ is the energy of the X-ray photons, and E_K is the kinetic energy. This is a rather simplified situation and to achieve accurate information on the binding energy of the material the analyser needs to be calibrated by measuring a

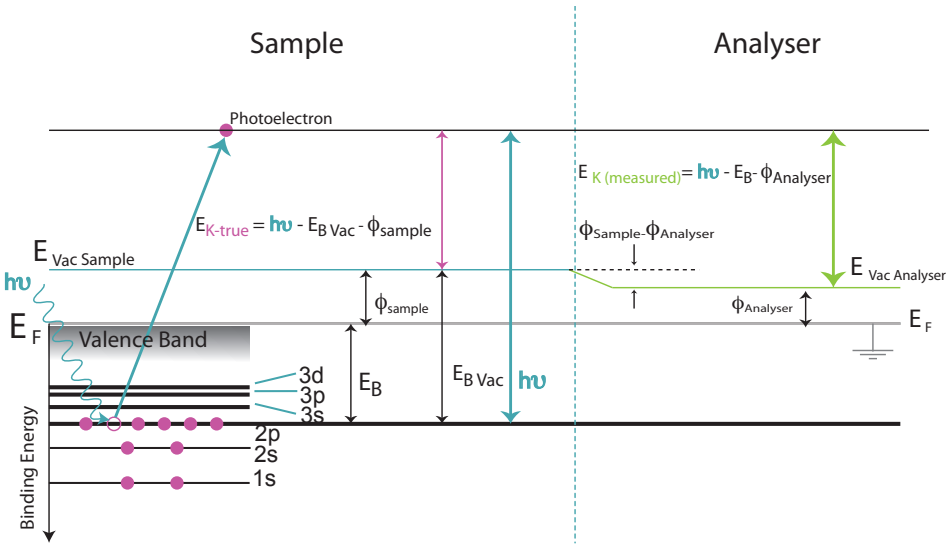

Figure 3.14: Schematic of X-ray photoelectron spectroscopy with the energy level diagram. Left) An X-ray beam with energy of $h\nu$ impinges on the surface of an electrically conducting sample which shares a ground with the electron energy analyser (spectrometer). The Fermi level of the sample and analyser are aligned such that E_B can be referenced to the E_F. Right) The measured kinetic energy ($E_{K\text{measured}}$) leads to determination of E_B without knowing the ϕ_{Sample}, but there is essential to know the ϕ_{Analyser}.

metallic sample that shares a ground potential with the analyser. This is because E_B is referenced to the Fermi level whilst the measured E_K is generally referenced to the vacuum level. There is a difference between the sum of E_B and E_K and the X-ray energy known as the 'work function' which is related to the Fermi level (E_F) and vacuum level (E_{Vac}) by [143]

$$\phi = E_F - E_{\text{Vac}}. \tag{3.10}$$

Here ϕ is the work function and defined as the minimum required energy for an electron to be ejected from the highest occupied state into the vacuum. Thus, the Einstein equation (equation 3.11) becomes

$$E_B = h\nu - E_K - \phi_{\text{Analyser}}. \tag{3.11}$$

The true value of E_K ($E_{K\ \text{true}}$) is compared to the one measured by the electron energy analyser ($E_{K\ \text{measured}}$), shown schematically in figure 3.14. Thus, an analyser for detecting photoelectrons can be calibrated by measuring a well-defined core orbital from a clean, grounded-standard metal (e.g. the Au $4f_{7/2}$ at a binding energy of 83.96 eV).

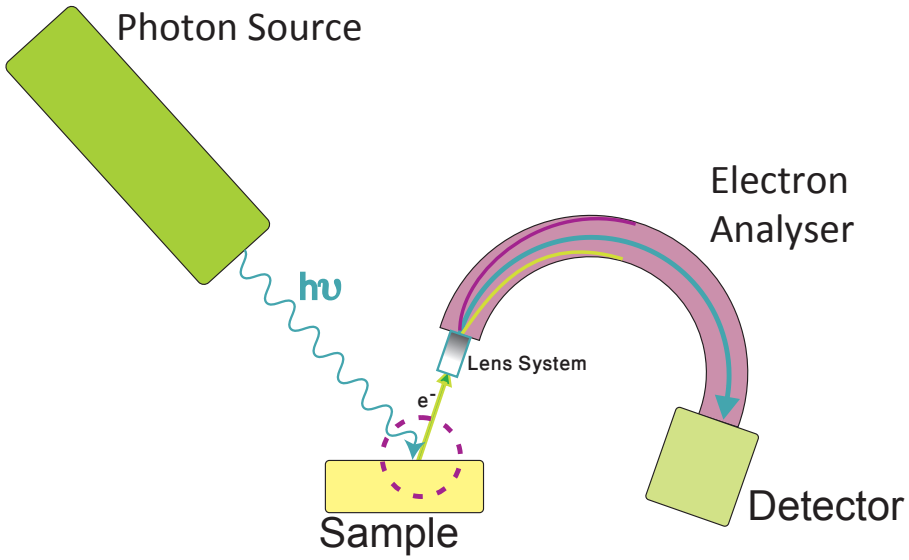

Figure 3.15: Schematic of typical X-ray photoelectron spectroscopy setup including the photon source (X-ray source), lens system and a hemispherical electron analyser to detect energy of the ejected electrons from the surface of a sample.

In this way there is no need to measure the sample's work function ϕ_{Sample}.
In XPS spectra, higher oxidation states are related to higher E_B due to the more powerful Coulomb interactions. It should be noted that the relaxation can affect the measured E_B significantly and not necessary due to changes in the chemical environment, however, by fitting the measured core level spectra it is possible to analyse reliably the chemical environment surrounding the atom, as well as the type of bonding that it is taking part in. This provides, not only an elemental fingerprint of the species at the surface, but a chemical one as well. The typical source of X-rays used in XPS is the K_α emission from aluminium (K_α=1486.58 eV) or magnesium (K_α=1253.56 eV) anodes obtained from a cathode X-ray tube. Two different types of cathode X-ray tubes were used in this work: *ex-situ* measurements were performed using a monochromatic XPS system and *in-situ* measurements were performed using a non-monochromatic XPS system with a flood gun for measuring non-conducting substrates. The recorded spectra were obtained by varying the detected E_K and measuring the intensity of the photoelectrons. In this thesis the elemental ratios or atomic percentages were of importance and knowing the instrumental constants and settings, elemental rates were determined using CasaXPS [144].

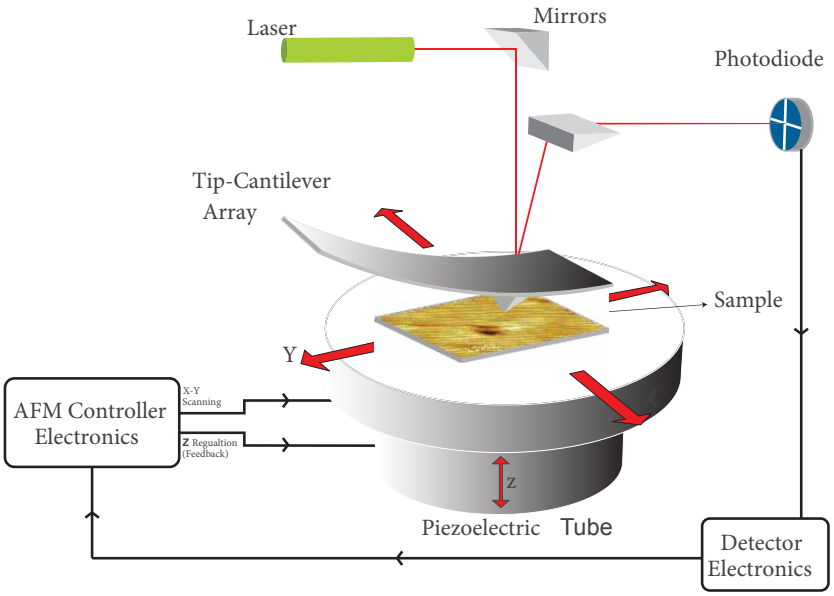

Figure 3.16: A schematic diagram of an atomic force microscope

3.3.4 Atomic force microscopy

Atomic force microscopy (AFM) was developed to image insulating surfaces. A sharp tip is brought close to a surface in atmospheric pressure while the sample is scanned, resulting in height resolution of $\sim$ 1Å and lateral resolution of better than 100 Å. AFM is particularly useful when studying insulating oxide surfaces. The tip is atomically sharp with 10 to 25 nm width at the top, which is placed at the end of a soft cantilever. When the tip is brought close to the surface (typically a few Å), the tip deflects away from the zero position of the cantilever due to any forces on the tip. This deflection can be monitored by several methods. One of the most commonly used is a laser light reflected from the back of the cantilever, onto a four-quadrant position sensitive photodiode (PSPD) as illustrated in figure 3.16. In figure 3.16 a schematic of an AFM setup is also shown including a piezoelectric scanner which controls the relative motion between the tip and the sample surface. Tip deflection (both vertically and laterally) is due to the change in the interaction between the tip and the surface of the sample when the tip is scanning over the sample. A 3D topological map is produced when the reflection movement of the laser spot is deflected on the PSPD [145].

There are two basic modes of AFM: contact mode and tapping mode. In contact mode, the tip is brought into contact with the surface physically. A feedback loop was used to maintain the deflection constant while the surface was scanned. Tapping mode

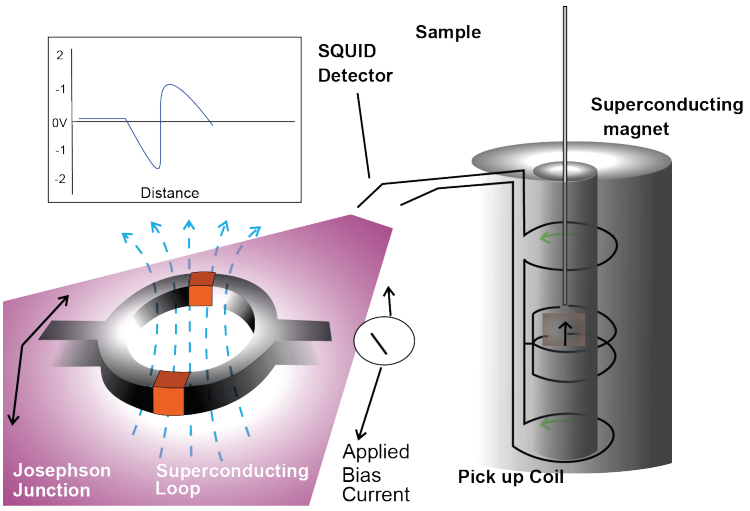

Figure 3.17: A schematic diagram of the SQUID magnetometer showing the Josephson junctions and the pick-up coils.

AFM runs under a dynamic mode in which the cantilever is vibrated at just above its resonant frequency while the tip is maintained at a constant distance from the surface. Any force on the tip results in altering the frequency of oscillation, so by maintaining constant amplitude through a feedback loop the topographic map of the sample can be obtained. The cantilever resonance is monitored by its phase, amplitude, and frequency and their variation due to the interaction forces between the tip and sample. Tapping mode works at large amplitudes ($\sim$ above 800 nm). In order to reach the sample the cantilever oscillates until it comes into contact with the surface [146]. In this thesis tapping mode AFM was used to provide a topography map of the surface. The height images are used to provide the root-mean-squared (RMS) roughness of the sample. The RMS value is an indication to the average density of surface features while high roughness gives the height of features. The images were processed using the Gwyddion software [147].

3.3.5 Magnetic measurements

A superconducting quantum interference device (SQUID) was used for bulk magnetic measurements due to its sensitivity to small magnetic fields which is ideal when monitoring slight changes in the magnetic behaviour of thin films while changing the temperature of the sample and magnetic field.

The SQUID magnetometer consists of a superconducting ring with two thin insulating layers called 'Josephson junctions' and it is attached to pick-up coils placed

inside the superconducting magnet (figure 3.17). The sample is held in a desirable orientation relative to the applied field using non-magnetic Tufnol holders (for thin films mostly in-plane magnetic measurement were carried out) which is then placed between the pick-up coils by mounting it at the end of a non-magnetic rod. Liquid nitrogen and liquid helium are used for temperature dependent measurements and also to cool the magnet down. The sample is slowly moved (typically in 32 steps) inside the detection coils within its working distance (≈4cm) while a magnetic field was applied. The generated magnetic flux passing through the pick-up coils changes as the sample is moved inducing a current within the coils via electromagnetic induction.

The pick-up coils are connected to the SQUID where the change in the magnetic flux as a function of the sample position is detected since the SQUID voltage output is strictly proportional to the current picked up by the coils. Therefore the raw data only contains the sample position and the SQUID voltage. The best fit to the voltage-to-position response is found using [148]

$$f(Z) = A + BZ + C(2[R^2 + (Z+D)^2]^{-3/2} - [R^2 + (\Lambda + (Z+D)^2)]^{-3/2} - [R^2 + (-\Lambda + D)^2]^{-3/2}), \tag{3.12}$$

where $f(Z)$ is the raw SQUID voltage at as a function of the position of the sample (Z). The constants in this equation are R the longitudinal radius equal to 0.97 cm and Λ, the longitudinal coil separation equal to 1.519 cm. The fit parameters A, B, C and D are a constant offset voltage, a linear background, the magnitude of the dipole moment, and the vertical shift of the sample, respectively.

The magnetic moment is then calculated from the amplitude of C. The voltage dipole is then converted to the electromagnetic units (emu) by measuring a Pd sample with known magnetic susceptibility and mass. Examples of the voltage-to-position response are shown in the panel a and b of figure 3.18 alongside the fit using equation 3.12 with the values of the fit shown in table 3.2. To fit the data from the magnetic thin films grown on a diamagnetic substrate additional concern must be addressed especially when the thin film signal is comparable to the diamagnetic signal produced by the substrate. The automatic background subtraction option in a magnetic property measurement system allows the point-by-point data subtraction to remove the contribution of the signal from the substrate therefore generating the thin film response which is then fit by equation 3.12. The substrate must be measured using identical condition such as the location of the sample mounting. Raw data should be collected from the substrate only. Then the thin film grown on the substrate should be measured when care is taken to mount the sample at the exact position. The raw data for both sets of data is converted to scaled

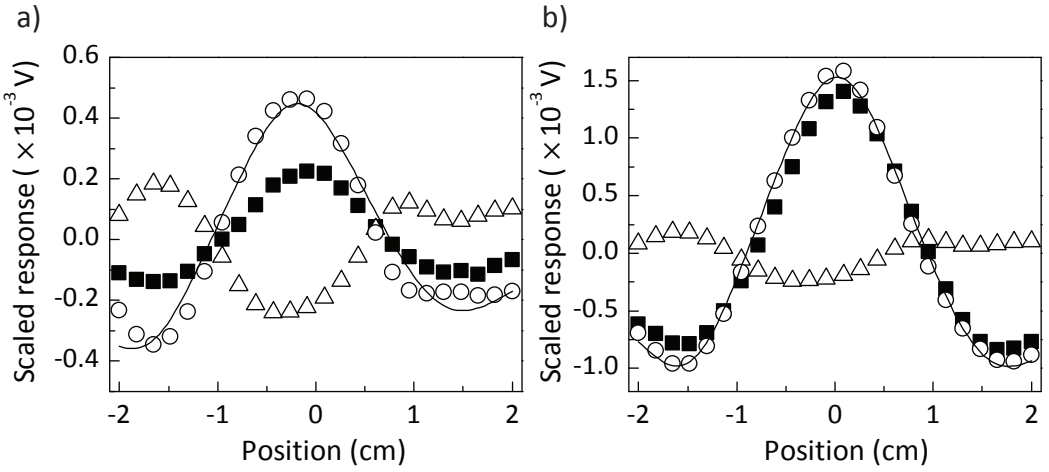

Figure 3.18: Data representative of the standard background subtraction of the raw SQUID data file for a) sample with magnetic response comparable to the diamagnetic response from the substrate b) sample with magnetic response higher than that of the diamagnetic response. All voltages shown are scaled. The squares are the response of the sample. The triangles are previously recorded scaled voltage response of the diamagnetic substrate ($SrTiO_3$). The circles represent the point-by-point subtracted data. The lines are the best computer generated fit using equation 3.12 which is then used to generate the sample moment.

voltage response and by using the built-in background subtraction function in SQUID they simply are subtracted point-by-point. In figure 3.18 there are 3 set of data shown. The squares represent the measured scaled response voltage of the thin film sample; the triangles represent the scaled voltage respond to previously collected data from the substrate while the circles are the simply point-by-point subtracted data attributed to the thin film only. The lines show the fit using the equation 3.12 to determine the value of C, which is then divided by a correction factor of 0.9125 to give the thin film moment in units of emu.

In panel a of figure 3.18, it can be seen that the diamagnetic response of the

Table 3.2: Typical values for the deposition parameters used in this thesis.

Parameters:	Values		
	Figure 3.18-a	Figure 3.18-b	Units
A	-9(1) $\times 10^{-5}$	-3.3(1) $\times 10^{-4}$	V
B	3(1) $\times 10^{-5}$	-2.7(9) $\times 10^{-5}$	V/cm
C	3.3(1) $\times 10^{-2}$	1.13(1) $\times 10^{-3}$	V
D	1.9(2) $\times 10^{-1}$	-0.34(7)$\times 10^{-1}$	cm

substrate has a signal response on the same order of magnitude as the thin film sample. after point-by-point subtraction the shape of the response signal is not ideal therefore the fit is not ideal and small changes in the positioning of the substrate during measurements can alter the generated subtracted thin film response significantly. On the other hand in the panel b of figure 3.18, it can be seen that the sample signal has a higher response than that of the substrate, therefore the subtracted scaled voltage can be fit properly with smaller errors on the values of A, B, D and specifically C (shown in table 3.2). If the automatic fit is not good then the process can take place manually by choosing the part of the signal with ideal shape and centring the signals manually.

A Quantum Design MPMS-XL was used which was able to apply magnetic fields up to $\pm$7 T. Typical measurements of magnetisation versus field (M-H) and the field-cooling magnetisation versus temperature (M-T) were carried out. The important values obtained from the hysteresis loops were the coercive field and the saturation magnetisation (M_{sat}). The second type of measurements, were zero field cooling (ZFC) and field cooling (FC) M-T. The ZFC measurements were carried out when the sample was cooled from room temperature to the minimum temperature before applying any magnetic field. In FC, sample was cooled down while a field of 2 kOe was applied. Due to variations in the nature of the magnetic ordering, different responses can be observed for these two measurements.

3.3.6 Transport measurements

A Quantum Design Physical Property Measurement System (PPMS) was used to measure the resistivity of samples using a standard four-point probe configuration over a temperature range of 3 - 300 K. As is shown schematically in figure 3.19 four electric contacts of silver wire were attached to the surface of the sample using silver epoxy. L is the separation between the inner contacts where A is the cross-sectional area (thickness

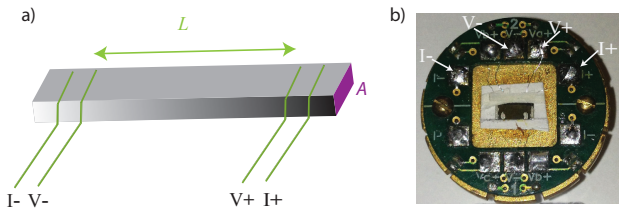

Figure 3.19: A four-point probe technique sample contacts configuration a) schematic configuration of the contacts b) a mounted sample on a PPMS holder. A is the sample cross-section area and L is the separation length between the voltage probes.

of the thin film). The resistivity ρ of the sample can be determined as

$$\rho = R \frac{L}{A} \quad \text{and} \quad R = \frac{V}{I}, \tag{3.13}$$

where I is the measured current for the applied Voltage of V in the sample with thickness of A and separation length of L between the voltage probes.

3.4 Summary

System set up for the Warwick UHV-PLD equipped with RHEED was introduced and explained in detail. Analysis tools used during this work were explained in detail and it is clear that in order to optimise the growth of functional oxides, the structural techniques such as XRD and TEM should be used along with the surface characterisation techniques such as AFM and XPS to verify the quality and stoichiometry of the thin films. Furthermore, to probe the functionalities electrical measurement and magnetic properties can be done by PPMS and SQUID, respectively. Experimental implication arising for magnetic properties as a result of the nature of the samples being in a thin film form was also explained with appropriate solutions.

Chapter 4

$LaMnO_3$ thin films on $SrTiO_3$: structure, magnetic and surface properties

$LaMnO_3$ thin films were grown on $SrTiO_3$ (001) substrates using PLD. By varying the growth temperature at two different regimes of oxygen pressure the ability to self dope by acquiring an oxygen non-stoichiometry (cation deficiency) has been studied. The structural, transport, and magnetic properties of $LaMnO_3$ thin films have been characterised to understand their intrinsic ground states originated by changing the oxidisation environment during deposition.

4.1 Introduction

The perovskite $LaMnO_3$ has recently attracted renewed attention as a building block of multilayered heterostructures. In its bulk form $LaMnO_3$ is an A-type antiferromagnetic insulator which can become a ferromagnetic metal by hole doping (substituting La with alkali materials such as Ca or Sr) [23, 24, 25]. The magnetic properties can be explained by the double exchange (DE) interaction between the Mn^{3+} and Mn^{4+} ions [53]. The bulk insulating antiferromagnetic phase, however, appeared to exist only in a very narrow oxygen content region reported by Hotta *et al.* [149] based on parameters defined by the electron phonon coupling and the antiferromagnetic coupling. In the parent compound, $LaMnO_3$, the cation deficiency gives rise to self-doping of the system without requiring synthesis of divalent ion substituted compounds creating mixed valence of Mn^{3+} and Mn^{4+} [150].

$LaMnO_3$, similar to any perovskite structure, can accept vacancies on any of the atomic sites, except it cannot incorporate interstitial ions. Thus, reported $LaMnO_{3+\delta}$ compounds are in reality cation deficient. It has been reported that any change in the La:Mn ratio, induced by oxygen non-stoichiometry, leads to ferromagnetic behaviour in $LaMnO_3$ [151]. In point of fact, thin films of $LaMnO_3$ on $SrTiO_3$ are experimentally reported to show ferromagnetic behaviour [152]. A new ferromagnetic orbital ordering by modification of the relative strength of the competing exchange interactions was suggested [153] due to the change in the lattice parameters induced by epitaxial strain [154]. $LaMnO_3$ is also an interesting material for manganite based heterostructures where epitaxial strain or electron coupling can lead to charge reconstruction (i.e. $LaMnO_3$-$SrMnO_3$ [155, 156], $LaMnO_3$-$SrTiO_3$ [108]) and recently reported $LaNiO_3$-$LaMnO_3$ superlattices [66]. It is necessary to study the effect of stoichiometry, defects or strain on $LaMnO_3$ films to be able to distinguish between the arising physical properties from the interfacial effects and growth-related effects. The main challenge, in fact, remains the difficulty in controlling and examining the oxygen content in thin films. Choi *et al.* [157] reported that the insulating antiferromagnetic phase of $LaMnO_3$ can be recovered by post-growth annealing. However, post annealing is not applicable when growing superlattice systems.

This chapter presents growth of $LaMnO_3$ thin film, where the oxygen content was varied during deposition by changing the growth temperature (T_g) at two different regimes of oxygen partial pressure (p_{O_2}). Unfortunately the oxygen content cannot be measured in thin films, such that the value of δ remains unidentified in these films. However the oxygen content can be altered during deposition by knowing that more oxygen can be absorbed at lower T_g and also at higher p_{O_2}. The physical properties originated by changing the oxidisation environment during deposition are investigated and discussed.

4.2 Crystal and magnetic structure of $LaMnO_3$

Bulk crystalline $LaMnO_3$ compound has a crystal structure proved to be isostructural with $GdFeO_3$ which is a distorted orthorhombic perovskite structure. This structure is composed of a 3D network of corner-connected MnO_6 octahedra where a Mn ion is in the middle of the octahedron. 8 octahedra next to each other form a cube with the La atom in the middle surrounded by 12 oxygen ions. If the ionic radius of A-site cation (La) is smaller than the cavity made by the oxygen atoms, the volume can be reduced by rotation of the octahedra with respect to each other and hence the bond lengths with oxygen become inequivalent. The lattice parameter of $LaMnO_3$ is almost cubic, which

makes the structure refinement arduous.

The space group $Pnma$ was first reported for $LaMnO_3$ by Elemans *et al.* [159] with lattice parameters of a= 5.655 Å, b= 7.722 Å, c= 5.528 Å [160]. The distorted orthorhombic structure contains a pseudocubic perovskite structure with lattice parameter of $a \sim \sqrt{2}a_{pc}$, $b \sim 2a_{pc}$ and $c \sim \sqrt{2}a_{pc}$ where a_{pc} is the lattice parameter of the pseudocubic. Evidently in $LaMnO_3$ with space group $Pnma$, the spin ordering consisted of ferromagnetic ac planes with spins in adjacent planes coupled antiferromagnetically [161]. The antiferromagnetism in bulk $LaMnO_3$ is explicitly related to the 3*d* shell of the Mn atom and the Jahn-Teller effect. According to the Jahn-Teller theorem [162] electrons are no longer degenerate in the electronic configuration $3d^4$ in an octahedral crystal field leading to a locally distorted octahedral coordination. As a result of lifting the degeneracy, a splitting in energy levels t_{2g} and e_g occurs such that the lone electron in the e_g orbital is in the lower energy state occupying the z^2-like e_g orbitals in the ac plane of the crystal [161]. An in-plane checkerboard-type pattern is formed since the z^2 orbitals are parallel to $a + c$ and $a - c$ vectors alternatingly. The proposed orbital ordering results in alternating short and long Mn-O bond lengths with orbitals being perpendicular and parallel to them respectively [52, 159]. Figure 4.1 shows the A-type antiferromagnetic bond and orbital ordering in the bulk stoichiometric $LaMnO_3$ lattice. In this schematic electron-spin configuration, Mn ion has an empty orbital pointing towards

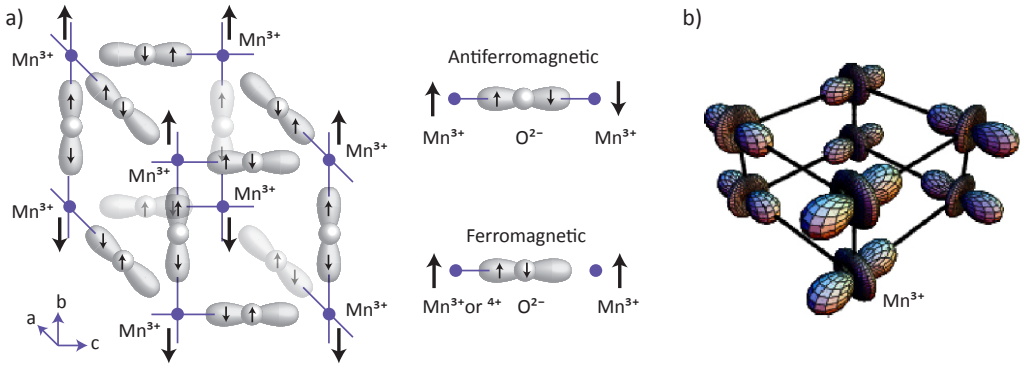

Figure 4.1: a) A-type antiferromagnetic lattice of $LaMnO_3$. Spins are aligned with ferromagnetic coupling in the ac plane and antiferromagnetic coupling of planes along b. Electron-spin configurations, in this schematic, are shown in the middle. Mn ion has an empty orbital pointing towards the O^{-2} 2*p* orbital if it is connected with a line. Figure adapted from [52]. b) Orbital ordering stabilised due to the structural distortions in $LaMnO_3$. The Jahn-Teller distortions lead to alternating long and short Mn-O bond lengths in the ac basal plane of $LaMnO_3$, with intermediate bonds along the b-axis (figure from [158].

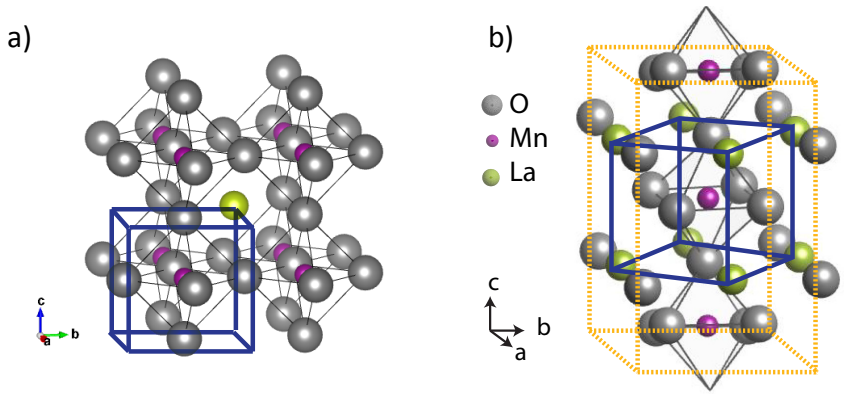

Figure 4.2: a) Cubic perovskite structure without distortion symmetry $Pm\bar{3}m$. b) A distorted orthorhombic $Pbnm$ $LaMnO_3$ structure with the Jahn-Teller cooperative distortion. In this schematic, the ionic radius is shown.

the O^{-2} $2p$ orbital if it is connected with a line. Checkerboard pattern orbital ordering as a result of the Jahn-Teller distortions is shown figure 4.1-b. When $LaMnO_3$ is grown on $SrTiO_3$ (001), a cell deformation occurs as a result of the compressive epitaxial strain leading to an elongation in the out-of-plane direction.

The space group $Pbnm$ is preferably used over $Pnma$ in physics community. This is more convenient since the b-axis is the quantisation axis in $LaMnO_3$ and also the doubled axis. The transformation is such that a, b, and c axis in $Pnma$ become b, c and a in $Pbnm$ [163]. The $LaMnO_3$ structural refinement in the space group $Pbnm$ yields lattice parameters $a \sim \sqrt{2}a_{pc}$, $b \sim \sqrt{2}a_{pc}$ and $c \sim 2a_{pc}$. An undistorted ideal perovskite structure is shown as well as the orthorhombic $LaMnO_3$ $Pbnm$ (yellow line) in figure 4.2. The pseudocubic perovskite subcell is highlighted with blue line in both panels a and b.

4.2.1 Stoichiometry ambiguities

Self-doping can rapidly change the magnetic and electronic properties of $LaMnO_3$ compounds due to the La:Mn unbalancing and/or oxygen non-stoichiometry. Consequently, it is important to discuss how oxidation of Mn ion is influenced by the La:Mn ratio and/or the oxygen content of the film. In a work by Wolcyrz *et al.* [164], 3 powder samples with the La:Mn ratios (La:Mn=r) of $r < 1$, $r = 1$, and $r > 1$ were studied where the stoichiometry and valance state of the Mn ions are refined by neutron diffraction and iodometric titration. Their work can be summarised as follows for these 3 cases. The

average valence of the Mn x is given by:

$$(1) \quad r < 1 \quad \mathrm{La}_r^{3+}\mathrm{Mn}^{x+}\mathrm{O}_3^{2-} \rightarrow 3r + x - 6 = 0 \rightarrow x = 6 - 3r, \tag{4.1a}$$

$$(2) \quad r = 1 \quad \mathrm{La}^{3+}\mathrm{Mn}^{3+}\mathrm{O}_3^{2-}, \tag{4.1b}$$

$$(3) \quad r > 1 \quad \mathrm{La}^{3+}\mathrm{Mn}_{1/r}^{x+}\mathrm{O}_3^{2-} \rightarrow 3 + x/r - 6 = 0 \rightarrow x = 3r. \tag{4.1c}$$

In situation (1), La vacancies are present and all other sites are occupied (i.e. Mn and O), and thus, to conserve the charge neutrality Mn^{3+} is partially oxidised to Mn^{4+}. According to (1), the amount of Mn^{4+} ions is 3 times that of the La vacancies. Ref. [164] reported a substitution of La sites with Mn ions for the sample with $r = 0.91$. They suggested that the oxygen sites were fully occupied as a result of a high temperature annealing (1270 K), whereas 16% of A-site La vacancies were occupied with B-site Mn cations allowing a reduction in the Mn valence.

Situation (2) suggests that the Mn valence in the stoichiometric LaMnO_3 should be equal to 3+. However, the Mn valence of 3.5 was reported in ref. [164] which was related to the presence of oxygen excess. In a closed-packed crystallographic system such as perovskite structure, accommodating an oxygen excess as oxygen interstitial is very difficult since all the possible interstitial sites (tetrahedral and octahedral) are surrounded by positively charged La ions and negatively charged Oxygen ions [165]. An oxygen excess is thus possible only through the formation of simultaneous A-site and B-site cation vacancies (i.e. Shottkey defects) [166, 167]. Such a composition is typically shown by $\mathrm{LaMnO}_{3+\delta}$ that can be better expressed as $\mathrm{La}_{(1-\epsilon)}\mathrm{Mn}_{(1-\epsilon)}\mathrm{O}_3$ with $\epsilon = \delta/(3+\delta)$ [168], or

$$\mathrm{La}^{3+}\mathrm{Mn}_{1-2\delta}^{3+}\mathrm{Mn}_{2\delta}^{4+}\mathrm{O}_{3+\delta} = (\mathrm{La}_{1-\epsilon}^{3+}[]_\epsilon)(\mathrm{Mn}_{1-7\epsilon}^{3+}\mathrm{Mn}_{6\epsilon}^{4+}[]_\epsilon)\mathrm{O}_3^{2-}. \tag{4.2}$$

where the fraction of Mn^{4+} over the total is $6\epsilon/(1-\epsilon)$ leading to 1/3 Mn^{4+} for ϵ values as small as 0.05 [169]. This explains the observed high valence of Mn suggesting that 50% of Mn^{3+} is converted to Mn^{4+} in the sample in ref. [164]. When $r > 1$ (situation 3 in 4.1), only Mn vacancies are present if other site are fully occupied. Ref. [164] found that the sample with $r = 1.1$ contains some oxygen excess after annealing at 1070 K equal to 62% of the Mn deficiencies. It is unlikely that La occupies the Mn site since the MnO_6 octahedra cannot accommodate La with its large ionic radius. The valence of Mn increases when sample contains oxygen excess such

$$\mathrm{La}^{3+}\mathrm{Mn}_{1/r}^{x+}\mathrm{O}_{3+\delta}^{2-} \rightarrow 3 + x/r - 6 - 2\delta = 0 \rightarrow x = 3r + 2\delta \tag{4.3}$$

where δ is the oxygen excess more likely resulted from simultaneous La and Mn vacan-

cies [164]. Whilst the oxygen stoichiometry for $LaMnO_{3+\delta}$ (oxygen excess case) has been investigated by many groups, the oxygen deficient $LaMnO_{3-\delta}$ compound has been less explored [170, 171]. It has been reported that $LaMnO_3$ can accommodate oxygen vacancies that is common to many transition metal oxides leading to a substoichiometric oxygen content of $LaMnO_{3-\delta}$ up to $\delta \leq 0.25$ [170, 172]. The charge distribution in this compound is shown by

$$La^{3+}Mn^{3+}_{1-2\delta}Mn^{2+}_{2\delta}O_{3-\delta} \tag{4.4}$$

where δ corresponds to oxygen vacancies resulting in a lower oxidisation state of the Mn valence. In the discussion above, changes in the physical properties of $LaMnO_3$ compounds were associated with the oxygen non-stoichiometry leading to cation deficiencies, whereas in thin films, observed experimental results cannot be only related to the nonstoichiometry since epitaxial strain affects the crystal lattice that is closely related to the electronic properties in these strongly correlated compounds.

4.2.2 Thin film versus bulk

Ferromagnetic behaviour has been reported for thin films of $LaMnO_3$ on $SrTiO_3$ by several groups [35, 150, 152, 169, 173]. This was explained by the modification of the relative strength of the competing exchange interactions as a result of the change in the lattice parameters, which was induced by epitaxial strain [154]. The ferromagnetic behaviour is mediated by the DE interactions between Mn^{3+} and Mn^{4+} ions [150]. An increase in the Curie temperature was reported by Gupta *et al.* [150] for PLD-grown thin films from 115 K for $LaMnO_3$ to 240 K for $La_{0.75}MnO_3$. The limit of self doping in $LaMnO_3$ thin film is reported to be higher than that of the bulk. Joy *et al.* [174] reported a limit of $r = 0.875$ for self doping of the sintered powder samples annealed at 1200 °C. They reported the formation of Mn_3O_4 impurities for samples with lower La:Mn ratio r lower than 0.875 when annealed above 1000 °C. Clearly the doping limit is affected by the epitaxial stabilisation and hence a larger number of vacancies are allowed within the perovskite structure. Further increase of the T_C was achieved by annealing the films at 850 °C after the deposition i.e. T_C=300 K for the $La_{0.75}MnO_3$ sample.

An interesting behaviour was reported for La:Mn ratio larger than one, where T_C was rapidly reduced regardless of a similar number of the Mn^{4+} ions in the samples [175]. Mn deficiency in the samples of $r > 1$ results into an increase in the number of Mn^{4+} ions, however simultaneously a number of Mn-O-Mn bonds are broken therefore the strength of the DE interactions is reduced [175]. Reduction in oxygen in general decreases the strength of any type of magnetic interactions due to the reduction in the total number of Mn-O-Mn bonds. Epitaxial strain may allow further substitution

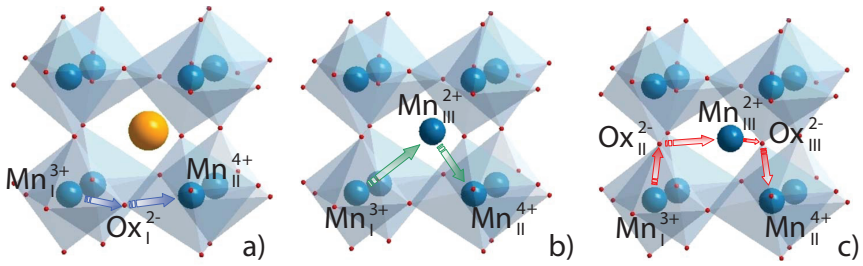

Figure 4.3: a) DE interaction between the Mn^{3+}-Mn^{4+} states in conventional manganites b) possible direct hopping between Mn^{2+} and Mn^{3+} in the A-site Mn^{2+} substituted manganites via intervening Mn^{2+} ion and c) suggested multiple DE hopping mechanisms between Mn^{2+}, Mn^{3+} and Mn^{4+} ions (figure taken from [26]).

of the Mn ion at the A-site cations and stabilisation of structures with lower r [176]. It was shown in the La deficient $La_xMnO_{3-\delta}$ thin films grown by MBE that partial substitution of the Mn ions at the A-site (La site) is actually possible. Multiple exchange interactions were suggested mediated by Mn^{2+} ion at the La site contributing in the transport mechanisms [26]. Figure 4.3 compares the possible hopping mechanisms for a) conventional manganites and b) a direct hopping path promoted by smaller tolerance factor as a result of A-site Mn substitution and c) a new multiple DE mechanism. Another aspect of epitaxial strain in manganite thin films is the effect of substrate like $SrTiO_3$ that is also a TMO. One of the controversial interface effects seen in thin film manganite is the change in the magnetic properties of $La_{2/3}Ca_{1/3}MnO_3$ and $La_{2/3}Sr_{1/3}MnO_3$ near the interface of a $SrTiO_3$ substrate. This adverse effect has been subjected to many interpretations due to the technological importance of these compounds in spin injectors or spin valves [177, 178]. Among these popular explanations are chemical/ electronic phase separation related to the interface induced structural inhomogeneities [179, 180], substrate homogeneous strain, and orbital reconstruction of the e_g electrons causing C-type antiferromagnetism [181]. Lepetit *et al.* [177] proposed a model explaining that microscopic mechanisms are controlling the interactions of epitaxially grown manganites at the interface near $SrTiO_3$ substrates. A summary of their model is as follows. (1) It is known that in epitaxial growth, the substrate affects the in-plane lattice parameter of the film so it matches that of the substrate ($a, b_{\text{film}} = a, b_{\text{substrate}}$). Because this constraint is related to the bond elongation, it is associated with one of the strongest vibrational modes [182], and hence, relaxes gradually as the thickness increases (100 nm $\sim$250 u.c. on $SrTiO_3$ substrate [179]). (2) Imposed symmetry by $SrTiO_3$ impacts the in-plane symmetry of the film. This constraint is governing the bond angles and is associated with the relatively weak vibrational modes in manganites, in particular the ones with the

lowest frequencies such as octahedra tilting. It thus can be expected to relax after a few u.c. of the film. (3) The transition metal of the substrate interacts at the interface with that of the film affecting the electronic properties of the interface giving rise to possible charge delocalisation. This implies that within the first few monolayers (6 to 8 ML) the exchange interactions are modified due to an elongation of the c-axis lattice parameter, favouring the z^2 type orbitals and hence reducing the double exchange interactions that are more dominant for in-plane *d* orbital ($d_{x^2-y^2}$). The transport and T_C of the film is therefore reduced leading to a so-called 'dead layer'. An unexpected exchange bias effect (EB) was also reported in a single film of (La,Sr)MnO_3 as a result a large epitaxial strain [183]. The exchange coupling was reported to be between the spin-glass $LaSrMnO_4$ layer formed at the interface and the ferromagnetic $LaSrMnO_3$ film. Very recently, an unexpected EB effect was observed in the single layer of oxygen deficient $LaMnO_3$ films [184] due to the vertical electronic phase separation. The EB was attributed to the exchange coupling between antiferromagnetic $LaMnO_3$ in the furthest part and ferromagnetic $LaMnO_{3-\delta}$ in the upper part of the film where the DE interactions were mediated via Mn^{2+} and Mn^{3+} ions.

Until now stoichiometry has been discussed in terms of the ratio of La:Mn. In this study XPS was used to identify the cation ratio and all films were found to be La deficient at the surface (composition analysis were performed on the *ex-situ* spectra). However, XPS is a surface technique and only gives information about the composition of the top few monolayers therefore the true compositions of the whole films are unknown and these result cannot be compared with the literature based on the La:Mn ratio. However the deposition conditions used in PLD is compared with the reports on $LaMnO_3$ films grown by PLD. XPS results were used to understand the magnetic nature of the top most layer in $LaMnO_3$ films in this study.

4.3 Growth conditions

$LaMnO_3$ epitaxial thin films were deposited on single crystal $SrTiO_3$ (001) substrates by PLD using the methodology explained in detail in section 3.2. The target was a sintered pellet of stoichiometric $LaMnO_3$ which was fabricated commercially. Typical deposition parameters for growth of $LaMnO_3$ are summarised in table 4.1. The number of pulses was kept constant at 4000. Thin films were deposited under two different p_{O_2} of 1×10^{-2} mbar and 1×10^{-4} mbar, while the substrate temperature was increased from 600 to 750 °C. The growth was monitored by observing the RHEED specular spot. All the films were cooled at a rate of 20 °C/min to room temperature under the deposition pressure. θ-2θ XRD scans were recorded using a Panalytical X'Pert PRO MRD

Table 4.1: Deposition parameters used for growth of $LaMnO_3$.

Deposition parameters:	Typical values
Compounds	$LaMnO_3$
Background gas	O_2
Background gas pressure (mbar)	0.01-0.0001
Growth temperature (T_g) (°C)	600-750
Spot size (mm^2)	2.16
Shape of spot	rectangular
Target type	sintered pellet
Laser fluence (J/cm^2)	1.5-2

instrument. The structural properties of the films change significantly when increasing the T_g. Film thickness has been kept constant at about 70 nm for the films based on the RHEED oscillations. ZFC and FC temperature dependent magnetisation (M(T)) were measured by SQUID. All magnetic data were corrected for the signal from the substrate. Transport properties of the film at different temperatures were characterised using a conventional four-point probe technique (PPMS). Surface composition and chemical state was probed by an *in-situ* Mg-source non-monochromated XPS as well as an *ex-situ* Al-source monochromated XPS.

4.4 Structural properties: the role of oxygen content

$LaMnO_3$ thin films were deposited by PLD, a technique that easily allows changing the oxygen content of the film by varying the oxygen background pressure and/or the growth temperature (i.e. the substrate temperature). Stoichiometric $LaMnO_3$ has an orthorhombic lattice structure and would experience compressive strain if grown on $SrTiO_3$. However, this is not the case for non-stoichiometric $LaMnO_3$ possessing $R\bar{3}C$ symmetry with pseudocubic lattice of about 3.90 Å (for $0.9< r <1$ La deficient $LaMnO_3$) [164]. Therefore the strain effect on the non-stoichiometric $LaMnO_3$ is negligible. To study the effect of reducing the oxygen content on the structural properties of $LaMnO_3$ films, XRD θ-2θ scans were measured and are shown in figure 4.4 converted to reciprocal lattice units (r.l.u.) relative to the lattice unit of $SrTiO_3$. A clear (002) $LaMnO_3$ peak indicates that the films are of high crystallinity, however they seem relatively weak as a shoulder of the prominent substrate $SrTiO_3$ (002) reflection. Remarkably, under both pressures, the (002) reflections in figure 4.4-a and b shift towards lower angles as T_g increases from 600 to 750 °C. An increase in the out-of-plane lattice constant can be observed in both pressure regimes when the deposition temperature increases. This shift is indicative of an increase in lattice constant which has been plotted against T_g

in figure 4.5-a. The c-axis values were determined by fitting the film peak by a Voigt function. Figure 4.5-b shows an example of fitted data for the film grown in 10^{-4} mbar and T_g=750 °C. The error bars are calculated from the standard error of the fitted data (main peak position x_c). When the (002) peak of the film was close to the $SrTiO_3$ (002) reflection, the substrate peak was fitted first with a Pseudo-Voigt function then the film peak was fitted considering the substrate contribution.

Figure 4.5-a shows that, the c-axis lattice parameter increases continuously when reducing the oxygen content of the films. Films grown in 1×10^{-4} mbar oxygen partial pressure (p_{O_2}) show an increase in out-of-plane lattice parameter compared to that of those deposited in 1×10^{-2} mbar p_{O_2} at the same temperature. The change in lattice parameter can be an indication of the valence state of the Mn ion which is strongly related to the oxidation state (i.e. oxygen vacancies). An exchange of larger ion Mn^{2+} to Mn^{3+} and then to smaller Mn^{4+} is suggested as a possible explanation of the c-axis lattice parameter dependence on oxygen content (Mn^{2+}= 0.83 Å, Mn^{3+}= 0.65 Å and Mn^{4+}= 0.53 Å [185]). Similar expansion of the out-of-plane lattice has previously been reported for $LaMnO_3$ thin films [35, 184, 186].

Reciprocal space mapping around the $SrTiO_3$ (114) reflection was performed to quantify in-plane strain for the $LaMnO_3$ film grown at 750 °C and under 10^{-4} mbar oxygen pressure. This scan is depicted in panel c of figure 4.5. The data show that the film was coherently strained to the substrate since both the substrate peak and the film peak are matched in Q parallel, and thus share the same in-plane lattice parameter which is 3.905 Å for $SrTiO_3$. Considering this the volume of the film is related directly to the c-axis lattice parameter. It can be argued that the film with the highest oxygen content has the smallest volume ($LaMnO_{3+\delta}$), which has a mixture of Mn^{4+} and Mn^{3+}. Raising the deposition temperature, the oxygen content is reduced in the film, preventing the formation of Mn^{4+} ions. By further reducing the oxygen content (increasing the deposition temperature or reducing oxygen pressure) near oxygen stoichiometric $LaMnO_3$ can be synthesised. Under low oxygen pressures and high substrate temperatures there is a possibility that $LaMnO_{3-\delta}$ forms in which case, films show oxygen vacancies and thus the formation of Mn^{2+}. This scenario requires further experiments such as X-ray absorption spectroscopy to find a foot print of Mn^{2+} in Mn L_3 and L_2 or O K absorption edges [173]. The shift in the $L3$ peak towards lower energies indicates, that the Mn ion has lower oxidisation states when decreasing the p_{O_2} [184]. The mixture of Mn^{3+} and Mn^{4+} gives rise to DE interactions that favours metallic conductivity, whereas stoichiometric $LaMnO_3$ is an antiferromagnetic insulator. Thus, the oxygen content in the film can be examined directly from resistivity measurements: a better oxygen stoichiometry is expected for films that are insulating.

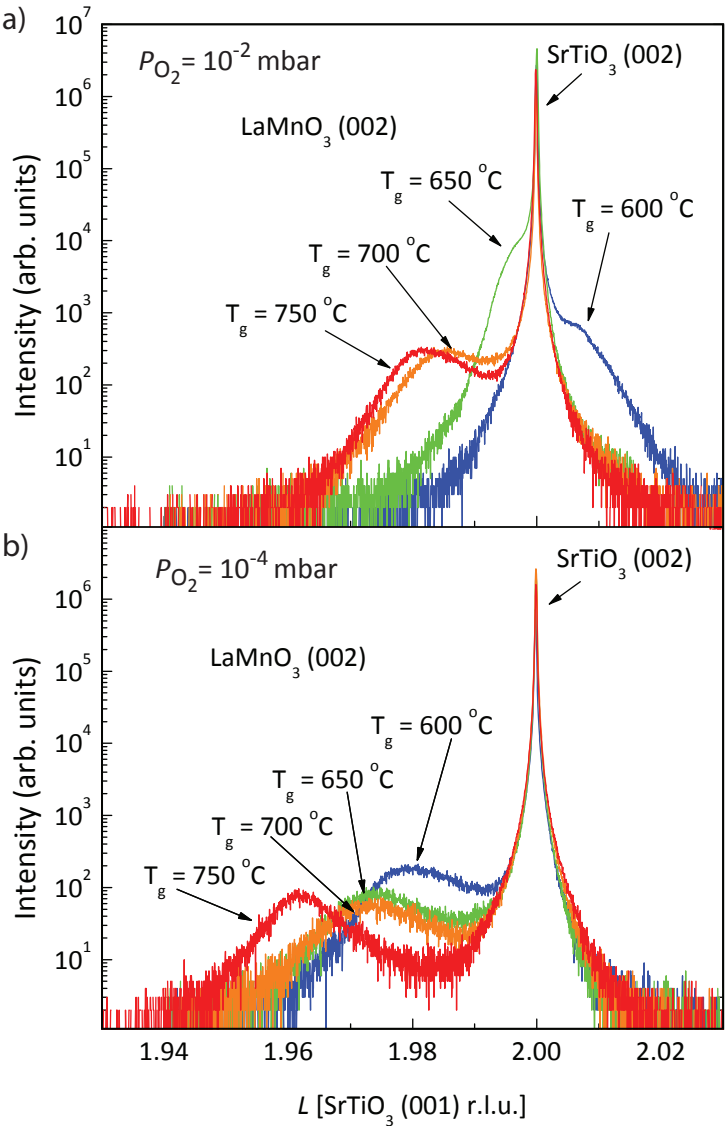

Figure 4.4: An expanded view of XRD patterns along (00L) scan around the (002) peak of $LaMnO_3$ films (≈70 nm thick) on $SrTiO_3$ substrate. Thin films were grown under a) 1×10^{-2} mbar and b) 1×10^{-4} mbar background pressure at substrate temperature ranging from 600 to 750 °C. x-axis is in the reciprocal lattice units (r.l.u.) of $SrTiO_3$.

4.5 Transport properties

Zero field resistivity as a function of temperature was measured for all films (range 10 to 300 K). The results are displayed in figure 4.6. The data are only shown for the film grown under high oxygen pressure and the film grown at 600 °C under 10^{-4} mbar pressure. The rest of the films grown in low oxygen pressure (10^{-4} mbar) were highly

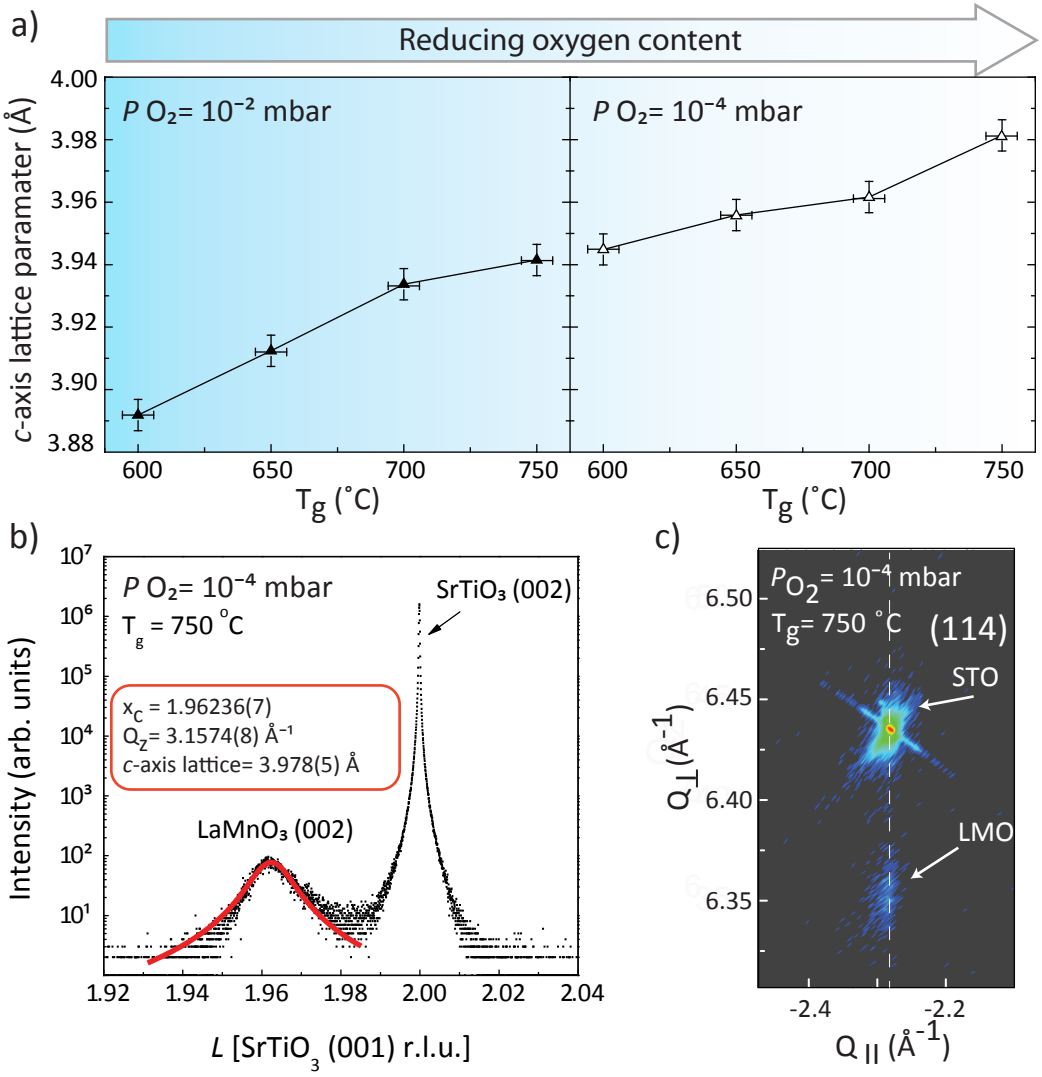

Figure 4.5: a) Variation of c-axis lattice parameter versus T_g. The data is shown for the both oxygen regimes of p_{O_2}. b) As an example the methodology to calculate the c-axis value is shown for the film grown at 750 °C in 10^{-4} mba. Data was fitted by a Voigt function only for the film peak. x_c is the peak position and using its standard error, the error bars for the c-axis were determined to be 0.005 Å c) RSM map (114) of $LaMnO_3$ film grown at 750 °C in 10^{-4} mbar, showing that $LaMnO_3$ film is matched in-plane to the $SrTiO_3$ substrate.

insulating and their resistivity was out of the range that could be measured by the PPMS used in this work. With the exception of the films grown at 600 and 650 °C under high oxygen pressure, which display a resistivity maximum like that of a metal-insulator transition at $T_{IMT} \simeq 201$ °C, the rest of the films show an activated semiconducting

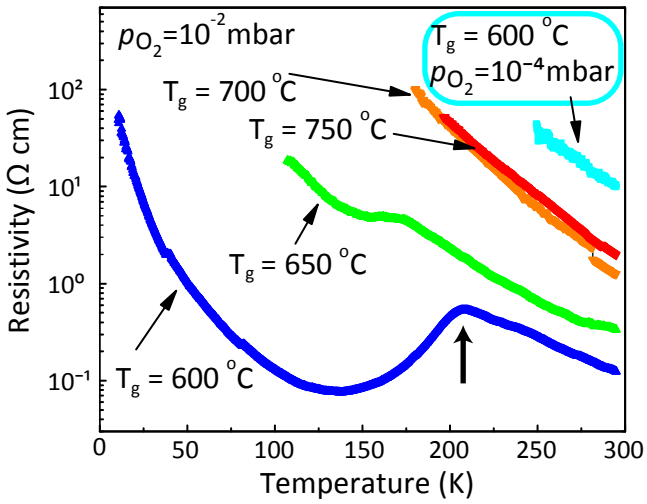

Figure 4.6: Temperature dependence of zero field resistivity of $LaMnO_3$ thin films with varying T_g. A metalinsulator transition (IMT) temperature is shown by the bold arrow in the T=600 °C plot. Appreciable IMT was only found for the film grown at 600 °C and 10^{-2} mbar. The other films grown in low oxygen pressure (10^{-4} mbar) were highly insulating and therefore are not displayed in this figure.

type behaviour over the whole temperature range measured, in agreement with previous studies [35, 157, 187]. The T_{IMT} is shown by a bold arrow in figure 4.6.

Displaying a resistivity maximum has been previously observed for lanthanum deficient thin films [150, 188]. Furthermore, the resistivity maximum shifts towards lower temperature and its magnitude increases when the growth temperature increases until it disappears for the film grown at 700 °C and 10^{-2} mbar. It was observed in XRD data that the films grown at higher temperatures showed a larger c-axis lattice parameter which can be an indication that, when the oxygen content decreases by increasing the T_g, the number of cation vacancies also decreases (i.e. fewer Lanthanum vacancies). Reduction in the Lanthanum deficiency results in a decrease of the Mn^{4+} concentration, causing an increase in the resistivity. Such behaviour has also been observed for $La_{1-x}Ca_xMnO_3$ compounds [189].

Figure 4.6 indicates that unlike typical IMT the resistivity has an upturn at lower temperature ($\simeq$140 K) and again shows insulating behaviour. Similar behaviour was reported in $LaMnO_3$ thin films grown by PLD [35, 150] and also dc magnetron sputtering [188]. Chen *et al.* explained the upturn as a result of charge/orbital ordering (COO) when the ferromagnetic metallic state goes under a transition to COO. It has been suggested that the upturn is an alternative charge and orbital ordering that changes the ferromagnetic metallic phase ($c/a < 1$) into another structural phase that is a

ferromagnetic insulator [190, 191]. In this sense, upon cooling, $LaMnO_3$ films undergo a paramagnetic to ferromagnetic metallic state transition at T_{IMT} and then at low temperatures to a COO phase at T_{COO} [188, 192]. The drop in resistivity can be explained by its correlation with the ferromagnetic transition and should correspond to a higher T_C. In order to verify this correlation, magnetic measurements were obtained.

4.6 Magnetic properties

Magnetisation as a function of temperature with a 2 kOe magnetic field applied along the a-axis is shown in figure 4.7-a and b for a set of films grown in high and low oxygen background pressure when varying the T_g. Figure 4.7-c and d display the hysteresis loops measured at 10 K. Form the hysteresis loops, the values for the saturated magnetic moment of the Mn ion were obtained and plotted against T_g for the both oxygen regimes in figure 4.8.

The saturated magnetic moment of 3.3(1) and 3.3(1) μ_B/Mn were found for the T_g=600 and 650 °C samples respectively. These values can be compared with μ=0.16 μ_B/Mn for pure stoichiometric $LaMnO_3$, 3.8 μ_B/Mn in ferromagnetic insulating compounds and finally to 4 μ_B/Mn for Mn^{3+} [169]. Similar values are reported in the literature for $LaMnO_3$ with characteristic ferromagnetic-like behaviour [157, 187]. It can be seen in both panels a and b of figure 4.7 that, the initial steepness of the temperature dependence decreases as the T_g increases in both oxygen regions. The M(T) curve of the film grown at the lowest temperature and highest oxygen background, (T_g=600 °C and p_{O_2}=10^{-2} mbar) rises sharply as the temperature falls below about 200 K. In contrast, the magnetisation of the film grown in lower p_{O_2} (10^{-2} mbar) and highest T_g (750 °C) exhibits a weak dependence on the temperature reduction with significantly reduced saturated magnetisation of about 0.3 μ_B/Mn. It is clear from figure 4.8-b and c that a similar trend is observed for the remanent magnetisation. However the coercivity increases suddenly for the sample grown at T_g=650 °C and p_{O_2}=10^{-4} mbar. For samples T_g=700 and 750 °C in the both oxygen regimes an anomaly arises at low temperature (∼45 K) which can also be seen in the -dM/d(T) data as a relatively weak peak in figure 4.9. This low temperature transition is attributed to Mn_3O_4 impurities [187] that can be the case in these films as a result of the high growth temperature. Another possible explanation of this transition was suggested by Galdi *et al.* [173] due to the existence of Mn^{2+} that only can be magnetised at low temperatures.

The transition temperature was defined where -dM/dT (figure 4.9) was a maximum. The M(T) was measured when a field of 2 kOe was applied parallel to the substrate and hence, this transition temperature is not the true critical temperature

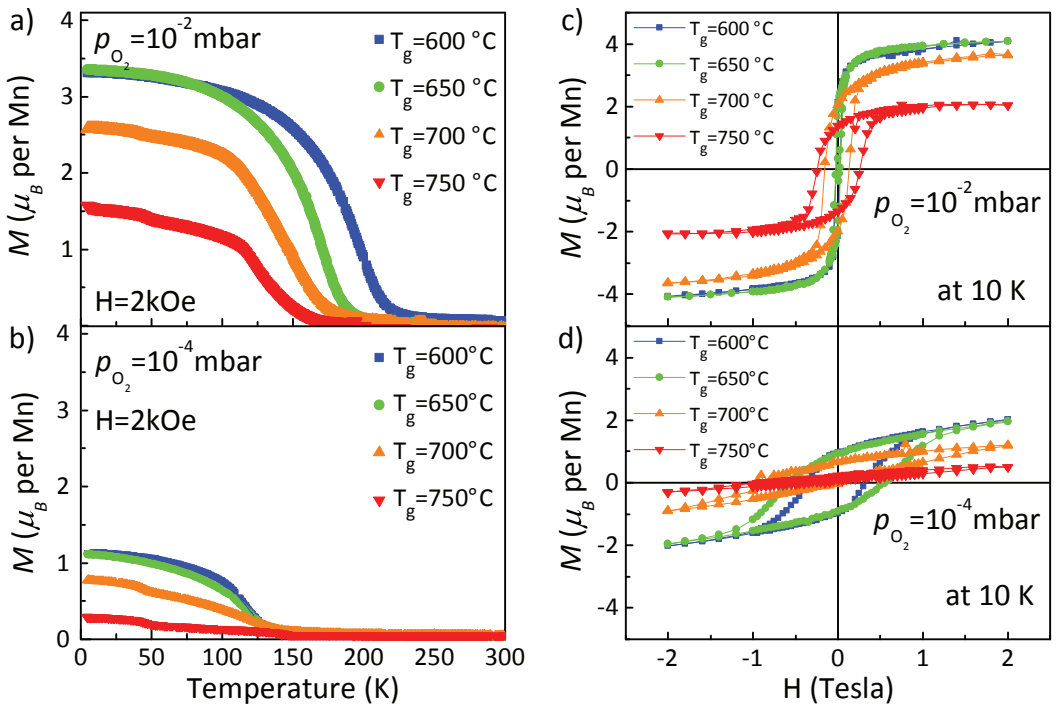

Figure 4.7: a) and b) Magnetisation as a function of temperature when a 2 kOe magnetic field applied upon cooling along the a-axis for p_{O_2}=10^{-2} mbar and 10^{-4} mbar respectively. The magnetic moment is shown after the subtraction of the background contributed from the substrate. Left panels (c) and (d) Hysteresis cycle M(H) at 10 K for $LaMnO_3$ thin films when changing the T_g for p_{O_2}=10^{-2} mbar and 10^{-4} mbar respectively.

(i.e. T_C). Transition temperature is by nature a critical transition, and hence it is required that M(T) be measured in H=0 T. In order to precisely and meaningfully find the critical temperature in these samples, new sets of experiments are required so that hysteresis should be measured at different temperatures then the remnant magnetisation would be extracted from the M(H) for each temperature. For thin films where the spin interaction varies across the sample, this is even truer if M is measured in H$\sim$0. The transition temperature defined from -dM/dT curves is the best estimate considering the measurement condition and is plotted in figure 4.10-a. Magnetic results confirm that the sample that showed a T_{IMT} in resistivity measurements corresponds to the highest T_C observed. It is clear from figure 4.10-a that the transition temperature drops when T_g increases for the films grown under high p_{O_2} (10^{-2} mbar). The trend is not continuous when T_g reaches 700 °C for the films grown under low p_{O_2} (10^{-4} mbar). Cation deficient thin films of $LaMnO_3$ exhibit ferromagnetic properties when the Curie temperature is directly correlated to the delocalisation of e_g orbitals of the manganese ion

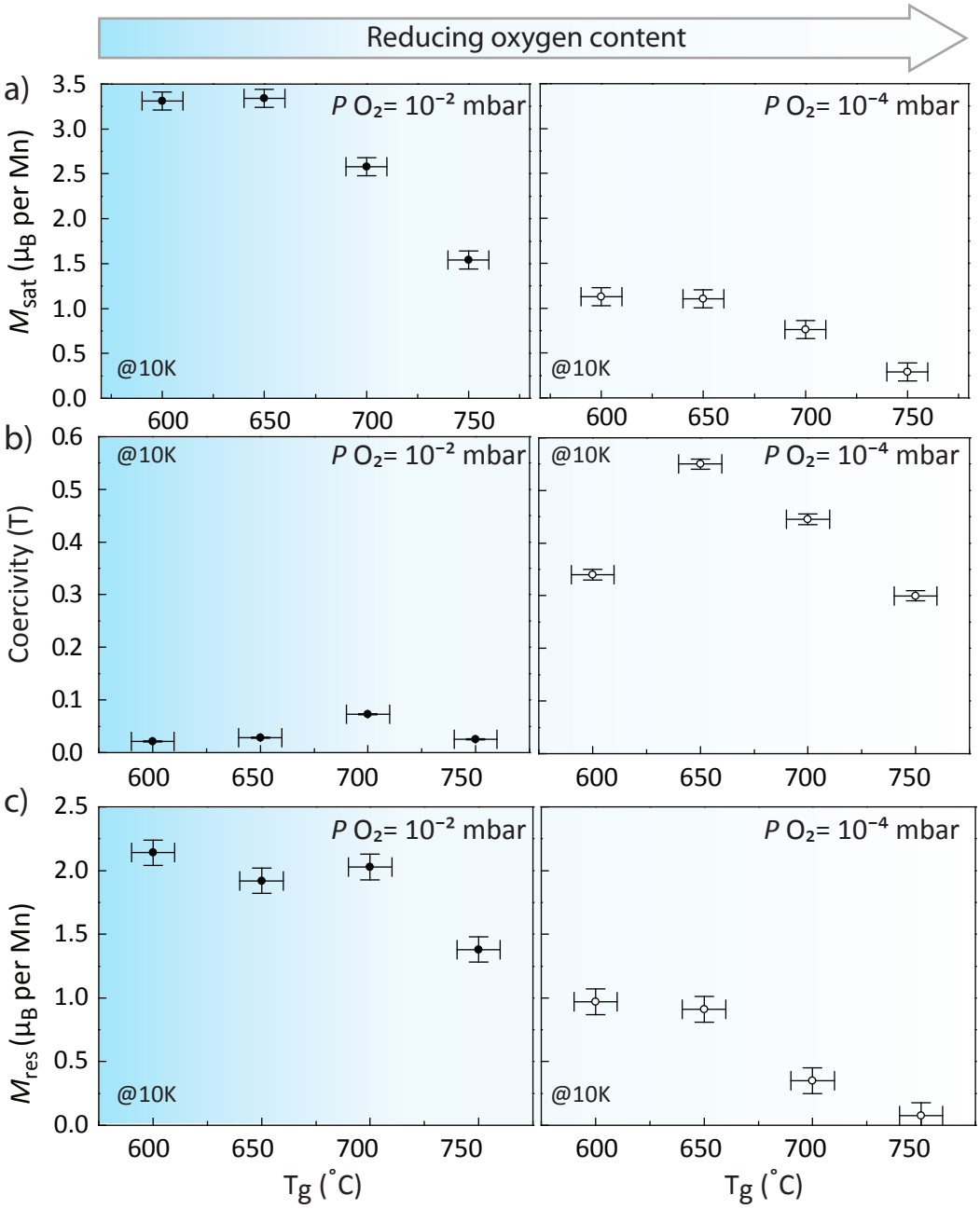

Figure 4.8: a) Saturation magnetisation (M_{sat}, b) coercivity and c) residual magnetisation (M_{res}) as a function of T_g for both p_{O_2}. These values were obtained by the remanent magnetisation and saturation values of the hysteresis loops of $LaMnO_3$ films measured at 10 K.

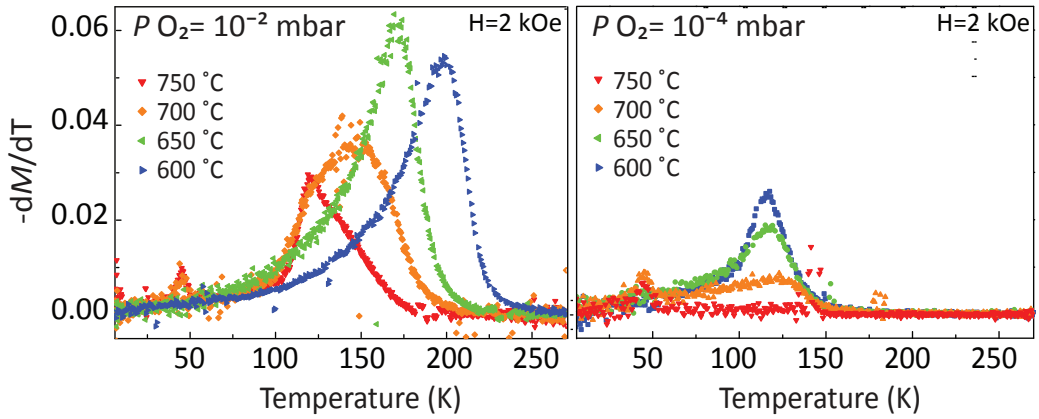

Figure 4.9: -dM/dT versus temperature for the films grown at T_g of 600 to 750 °C for the both p_{O_2} regimes. Critical transition temperature was identified by fitting the curve and obtaining the peak position. At low temperature ∼45 K there is an anomaly for sample gown above 700 °C in both oxygen backgrounds.

(Mn^{3+} or Mn^{4+}). By changing the geometry in which the Mn ion locates, for example, changing the deposition condition, one of the two e_g orbitals ($d_{x^2-y^2}$ or $d_{3z^2-r^2}$) can be selected [153]. If the Jahn-Teller Mn^{3+} ion is in an environment that the energy of the $d_{x^2-y^2}$ orbitals is lower, the in-plane double exchange will be very strong giving a high transition temperature. In contrast, when the $d_{3z^2-r^2}$ orbitals are stabilised, the double exchange will be weak in-plane and has to take place along c-axis. In such a 2D system i.e. thin film, only in-plane interactions are considered and affect the orbital ordering and thus the associated transition temperature [153]. In accordance with this argument stabilisation of the $d_{x^2-y^2}$ over $d_{3z^2-r^2}$ can enhance the magnetic transition temperature and also decrease the tilting of the MnO_6 octahedra that exists in the bulk crystal. The prevention of the octahedra tilt increases the effective exchange integral within the $d_{x^2-y^2}$ in-plane orbitals. In double exchange interactions the Curie temperature is related to the in-plane effective exchange integral between adjacent Mn ions which scales as $J \sim t_{pd}^2 \sim S_{pd}^2$ where t_{pd}^2 is the transfer integral of O2*p*-Mn3*d* and S_{pd}^2 is their overlap. The tilting of the octahedra decreases the overlap between the bridging orbitals of the O2*p* and the in-plane Mn *d* orbitals ($d_{x^2-y^2}$) therefore decreasese the Curie temperature [153, 193]. This scenario is explained schematically in figure 4.10-b. Thus, the thin film grown at T_g=600 °C and p_{O_2}=10^{-2} mbar is the only sample with $c/a < 1$, therefore the $d_{x^2-y^2}$ orbital occupation should be favoured resulting in the high T_C observed. Furthermore, T_C is expected to decrease as a result of elongation of the unit cell, which is in agreement with the data, before growth temperature reaches 700 °C at p_{O_2}=10^{-4} mbar. The observed anomalies in the *M*(T) data at low temperature

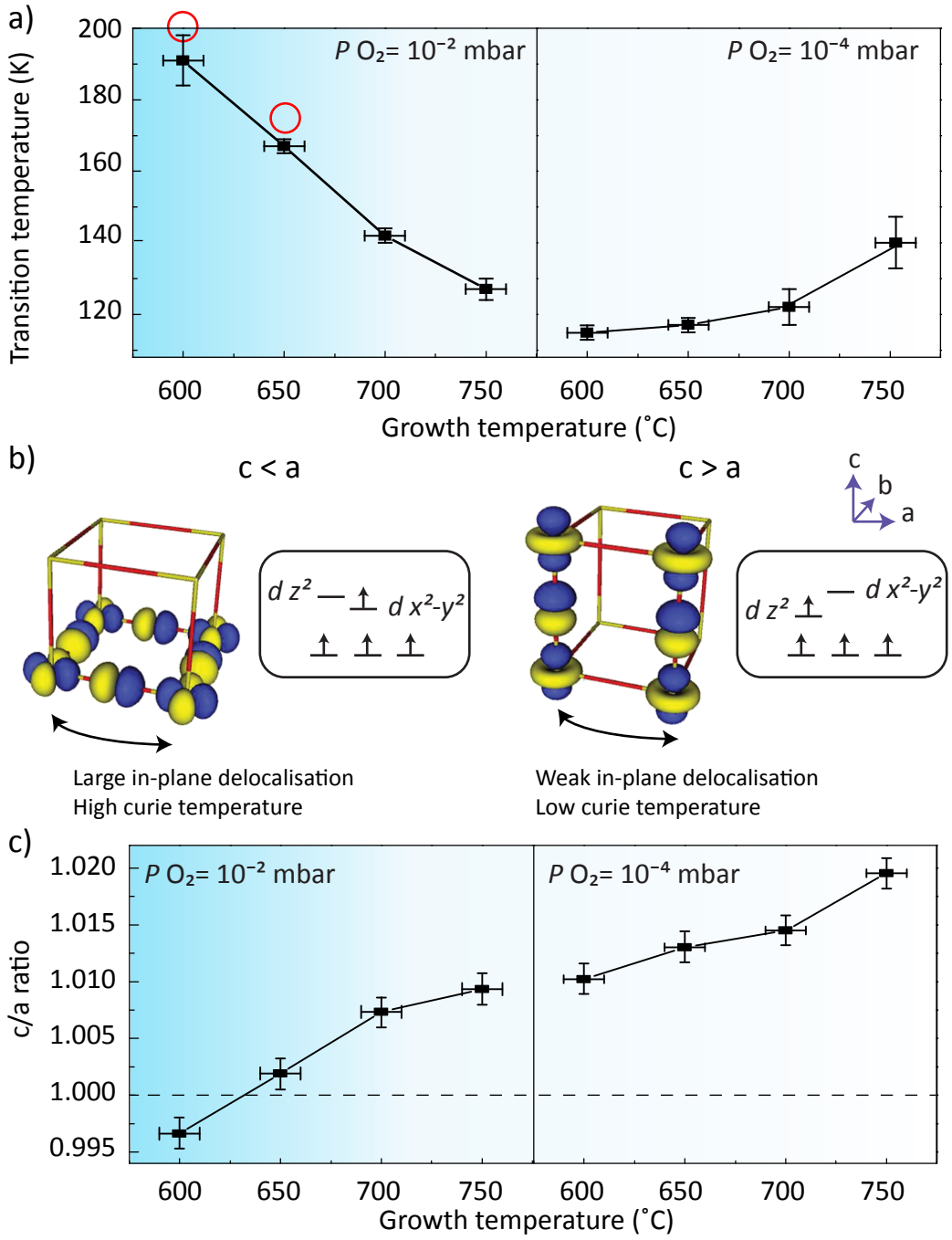

Figure 4.10: a) Transition temperature defined from -dM/dT curves versus T_g. The red circles indicate the T_{IMT} measured from the temperature dependent resistivity data. b) Schematic illustration of orbital ordering due to c-axis lattice elongation and reduction in a 2D system. While $c < a$ is promoting the stabilisation of $d_{x^2-y^2}$ orbitals, in contrary $c > a$ stabilises the z^2-like orbitals (taken from [153]). b) The tetragonal distortion in $LaMnO_3$ films are plotted versus growth temperature for both oxygen pressures.

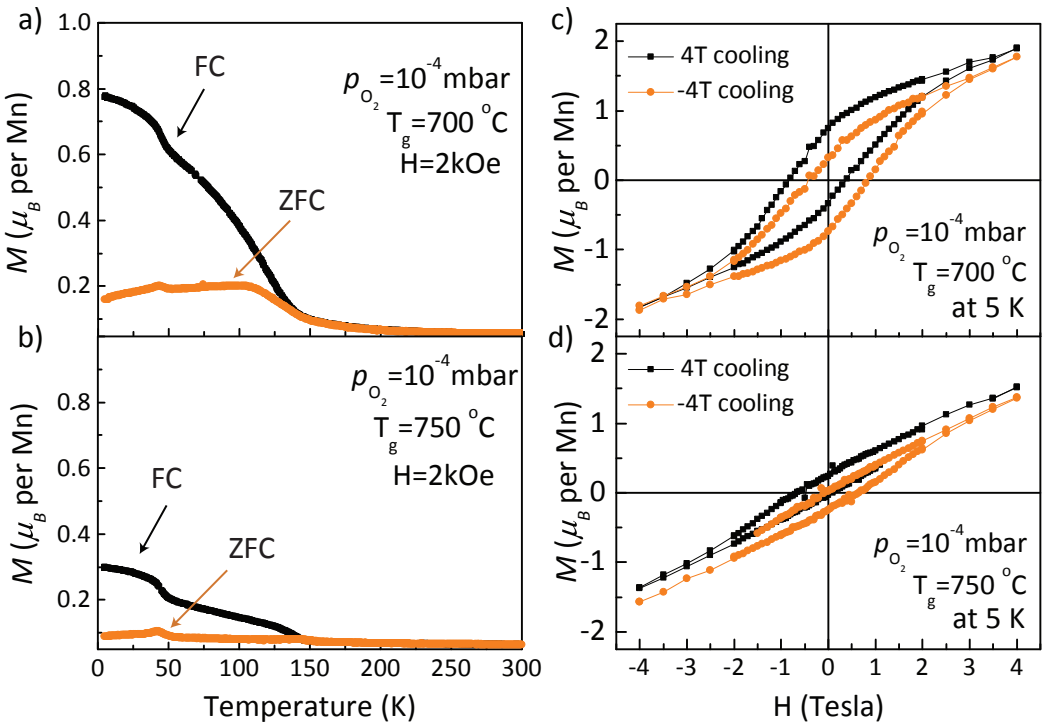

Figure 4.11: Field cooled and zero field cooled magnetisation M(T) in H = 2kOe for $LaMnO_3$ thin films deposited at a) 700 °C b) 750 °C. Arrows show warming vs. cooling curves. The hysteresis loops of the sample grown at high temperature c) 700 °C and d)750 °C shows a shift of the cycle along the magnetic field axis towards negative fields when cooling from room temperature in +4 T field (black line). In contrast when cooling from room temperature in the presence of a -4 T field the hysteresis was biased towards the positive direction (orange line). H_{EB} is defined as $|(H_- + H_+)|/2$, where H_- and H_+ are the positive and negative coercive field respectively (encircled by red lines in panel c).

(∼45 K) can arise from magnetic anisotropy that can result in differences between ZFC and FC measurements.

Figure 4.11-a and b illustrate the temperature dependence of magnetisation on the two selected films measured by SQUID, obtained both by FC in a magnetic field of H=2 kOe oriented parallel to the film plane and by ZFC, applying the same external field at low temperature (T=5 K) and measuring upon heating. There is a clear difference between the two curves typically seen in very lightly doped manganites, as a result of the presence of localised Mn^{4+} giving rise to ferromagnetic contributions surrounded by a canted antiferromagnetic bulk-type $LaMnO_3$ [168]. For the film grown at 700 °C and p_{O_2}=10^{-4} mbar, the two curves merge upon heating at a transition temperature (T_N=140 K) where no ordered moment is present in the antiferromagnetic

background or at localised ferromagnetic Mn^{4+} sites [169]. The measured M_{sat} at 5 K is 0.8(1) μ_B/Mn obtained from FC. This value is higher than that of the pure antiferromagnetic $LaMnO_3$. By comparing the value of M_{sat} with the phase diagram provided in Ref. [168] the films properties matches the magnetically heterogeneous, spin-glass like insulators. Similar behaviour in M(T) is observed for the $LaMnO_3$ films grown at 750 °C and p_{O_2}=10^{-4} mbar. The difference is lower M_{sat}=0.23 μ_B/Mn for FC and 0.01 μ_B/Mn for ZFC. The decrease of oxygen background results in a reduction in the number of Mn-O bonds therefore decreasing the total magnetic moment. T_N is 140(3) K for both samples. The broad range of magnetic transition observed in $LaMnO_3$ thin films can be as a consequence of magnetic frustration occurring near the grain boundary regions leading to a glassy-like state [194]. The unusual magnetic behaviour observed for the films grown at 700 and 750 °C in p_{O_2}=10^{-4} mbar, can be an indication of intrinsically inhomogeneous magnetic states leading to local transitions. There is an important question concerning the origin behind such magnetic inhomogeneity. This can be attributed to the formation of antiferromagnetic correlations with the ferromagnetic phases. Considering the ground state antiferromagnetism in stoichiometric $LaMnO_3$, there is possibility to see AFM interaction even in the oxygen rich thin films. It can be concluded that the unusual magnetic behaviour seen in $LaMnO_3$ films grown at T_g 700 and 750 °C at p_{O_2}=10^{-4} mbar appeared as a result of such antiferromagnetic correlations developing in the ferromagnetic phase.

Panel (c) and (d) in figure 4.11 show the hysteresis loops when the field was applied along the film plane at 5 K of the $LaMnO_3$ films grown at T_g 700 and 750 °C at p_{O_2}=10^{-4} mbar respectively. The hysteresis loops of the sample grown at high temperature (700 °C) shows a shift of the cycle along the magnetic field axis towards negative fields when cooling from room temperature in +4 T field (figure 4.11-c). In contrast when cooling from room temperature in the presence of a -4 T field the hysteresis was biased towards the positive direction. H_{EB} is defined as $|(H_- + H_+)|/2$, where H_- and H_+ are the positive and negative coercive field respectively. Coercivity was defined by $(H_- - H_+)/2$ [195]. As figure 4.11-c displays, an asymmetry can be seen for the highlighted H_- and H_+. This behaviour shows the surprising exchange bias in the single layer of $LaMnO_3$ thin films at low temperatures with biased field of 90(3) Oe. This value was defined as the absolute offset of the hysteresis cycle along the field axis. The EB was also seen for the samples grown at a higher temperature of 750 °C. The EB was reproducible and seen repeatedly for $LaMnO_3$ films grown under similar conditions. Moreover the positively biased loop when negative field was applied during cooling is strong evidence for the presence of EB [196]. The EB effect is indicative of exchange coupling between the phases with different spin orders. Similar results have recently been

reported that showed an EB effect in a single layer of $LaMnO_{3-\delta}$ [184]. In this report, X-ray absorption spectroscopy found a finger print of Mn^{2+} in addition to Mn^{3+} ions. The EB effect was not recognised as a spin-glass-based EB but as a result of a vertical electronic phase separation. It was deduced that the surface region (the upper layer) has a higher concentration of the Mn^{2+} leading to DE ferromagnetism whilst the lower part exhibits a bulk-type SE antiferromagnetism with more Mn^{3+} ions present. In order to know the origin of the EB observed in this work and to distinguish whether it is due to a glassy-like system or vertical phase separation, temperature dependent hysteresis loops and field-dependent FC-ZFC measurement should be performed. The temperature in which the EB and coercivity vanish (the blocking temperature) is characteristic of the origin of exchange coupling. Thickness-dependent hysteresis can also identify if the vertical separation occurs in these films. If the surface of these films are oxygen deficient and Mn^{2+} is present, examining the chemical state of the surface by XPS can aid to further exploit this phenomena.

4.7 Surface properties: the key role of deposition conditions

XPS measurements were performed using an *ex-situ* monochromated Al source XPS and an *in-situ* non-monochromated Mg source XPS. The thin film grown at T_g=700 °C and p_{O_2}=10^{-4} mbar was examined by both of the *in-situ* and *ex-situ* XPS instruments. The full range spectra are shown for both in figure 4.12 to compare the surface state and effect of exposure to air. The peak position for C 1*s* is marked in panel a to see that the as-grown film is contaminant free compared with the *ex-situ* spectra. Figure 4.12-b, c and d compares the *in-situ* and *ex-situ* data for the manganese and oxygen peaks and the difference between them. No significant variation was observed in the Mn 2*p* spectra. The O 2*p* data taken *ex-situ* shows a larger shoulder at a higher binding energy compared with the *in-situ* peak (the FWHM cannot be compared since the non-monochromated XPS has lower resolution). This shoulder can be attributed to the observed carbon (present C 1*s* peak) leading to the formation of CO/CO_2. The oxygen peak at lower binding energy is known as the lattice oxygen while the higher energy position peaks are related to environmental effects (i.e. oxygen vacancies and contaminations).

The surface of the films grown in 10^{-2} mbar was examined using an *ex-situ* XPS shown in figure 4.13. Figure 4.13-a displays the *ex-situ* XPS survey scans of the thin films grown in p_{O_2}=10^{-2} mbar at various T_g. It can be seen that the films grown at higher temperatures show a higher intensity of the C 1*s* peak that is expected since CO/CO_2 can form at those temperatures. Valence band spectra of the films and the

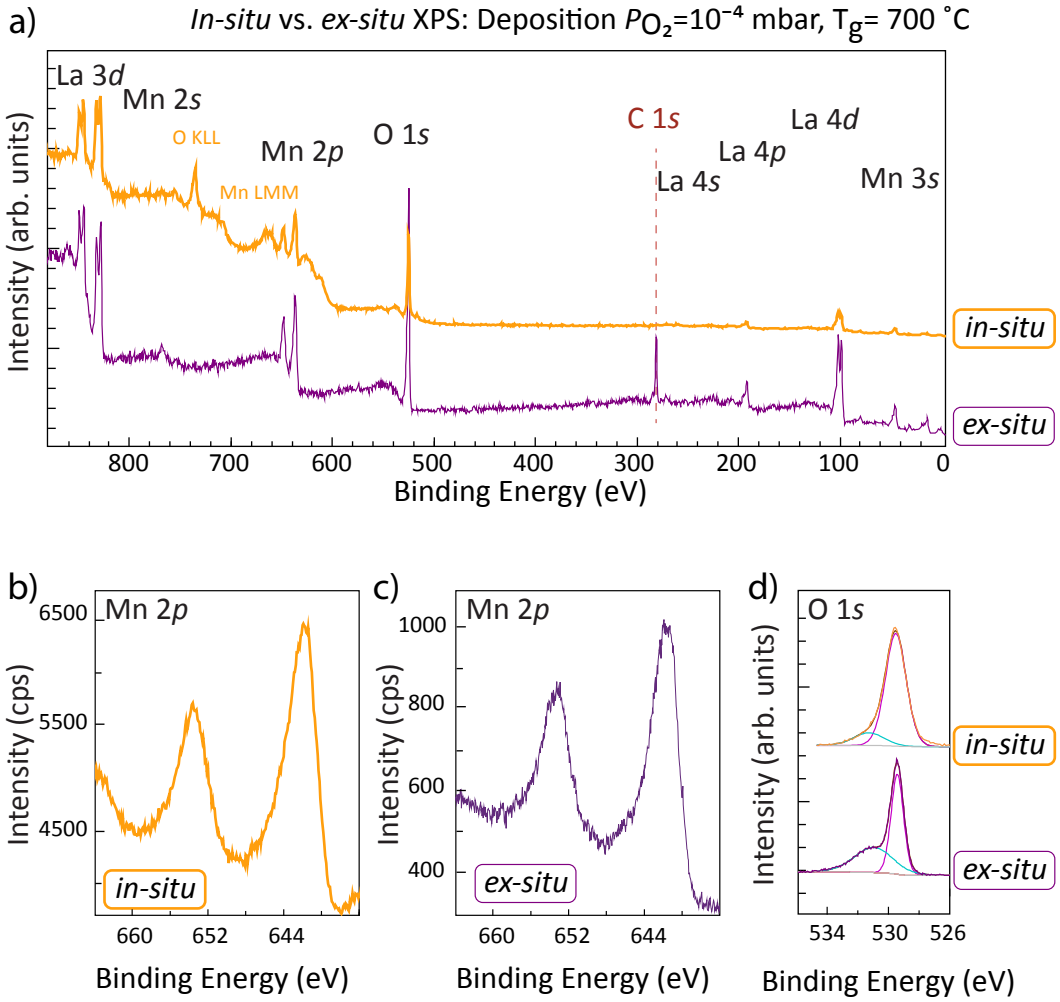

Figure 4.12: a) Survey scans comparing the *in-situ* and *ex-situ* XPS data. The position of the core level binding energy is irrelevant to the energy source however the Auger lines are shifted when the source is changed. b) and c) show the Mn 2*p* areas and d) compares the oxygen peaks and the difference between them for the film grown at 700 °C and p_{O_2}=10^{-4} mbar. No significance change can be observed for the Mn 2*p* spectra; however the shoulder of the oxygen peak at a higher binding energy confirms the presence of carbon on the surface.

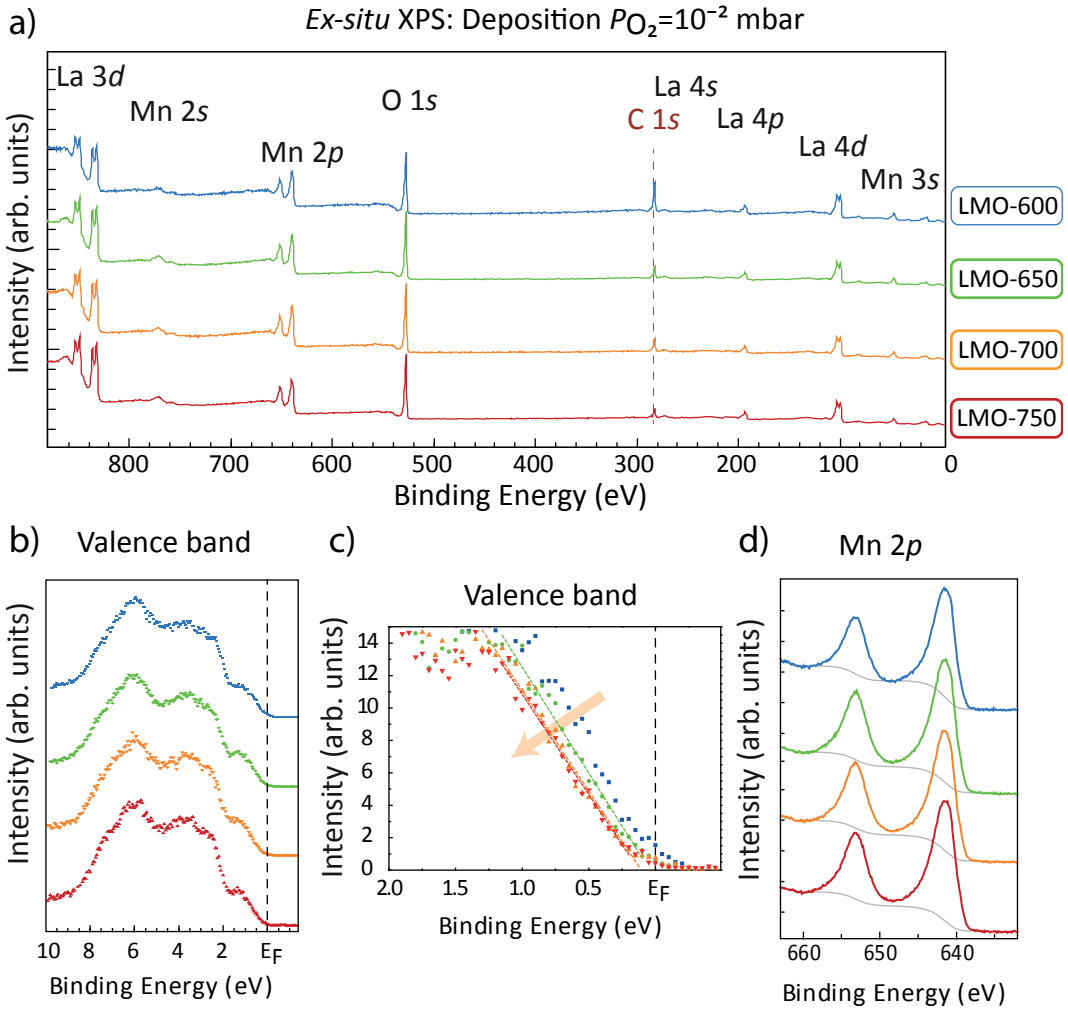

Figure 4.13: *ex-situ* XPS a) survey scans of thin films grown in p_{O_2}=10^{-2} mbar at various T_g reveal that the film grown at highest temperature shows a higher intensity C 1*s* peak that is expected since CO/CO_2 can form at those temperatures. b) Valence band spectra of the films. c) Zoomed in region near the Fermi level spectra show that the film grown at low temperature of 600 °C has slightly higher intensity, an indication of more metallic states near the surface. d) The Mn 2*p* does not change at all with T_g.

zoomed in region near the Fermi level spectra are shown in panels b and c respectively. The film grown at 600 °C has slightly higher intensity, an indication of more metallic states near the surface. Figure 4.13-d shows that the Mn 2*p* shows no change at all with T_g. To see whether the no change in the surface is as a result of the exposure to air, a set of samples grown in p_{O_2}=10^{-4} mbar were measured by the *in-situ* XPS. Similar behaviour was observed for the Mn 2*p* region however the oxygen pressure is 2 orders of magnitude lower than the previous set measured by *ex-situ* (figure 4.14). *In-situ* non-monochromated XPS shows in figure 4.14 that all films expect the one grown at 750 °C are contamination-free at the surface. This sample has the lowest oxygen content, more likely with higher oxygen vacancies at the surface. It has previously been reported that a perovskite with higher oxygen vacancies is more sensitive to contamination and shows hydroxyl bonds at the surface because of the acidity of the surface [172]. Figure 4.14-b compares the La 4*d* region that also shows no dependence on the T_g as does the Mn 2*p* (c). d) The O 2*p* spectra show that only the spectrum of the film grown at T_g= 750 °C has an additional peak on the high binding energy side. This indicates that oxygen is bonded in another environment. With this data the only conclusion that can be made is that samples grown at 750 °C at p_{O_2}=10^{-2} mbar and 10^{-4} mbar show higher contamination at the surface even for the sample measured *in-situ*. XPS composition analysis requires further work to aid to understand the correlation between the growth conditions and the surface electronic properties.

Surface morphology

The surface morphology was examined by RHEED and AFM (figure 4.15). The surface morphology of $LaMnO_3$ films shows a change in roughness with increasing T_g. At higher T_g, surface roughening occurred after cooling in a low oxygen background. Table 4.2 shows the RMS roughness values for the films obtained from 5 μm $\times$ 5 μm size scans. Streaky lines in the RHEED pattern suggest the surface is relatively smooth, however, disorder causes broadening in the streaks compared with that from the substrate. 'Spotty' patterns suggest the presence of crystalline microstructures at the surface of a thickness within the mean free path of the electron beam. Bulk type diffraction occurs as a result of electron transmission through the 3D islands at higher T_g. This effect is more severe at lower p_{O_2}, to the point that no diffraction was observed from the surface. Rougher surface morphology at lower p_{O_2} is in agreement with the hypothesis that oxygen loss occurs after deposition when cooling down at the growth pressure. To avoid this adverse effect on the stoichiometry and also surface morphology future samples in the next chapters were cooled down in a high p_{O_2} of 150 mbar.

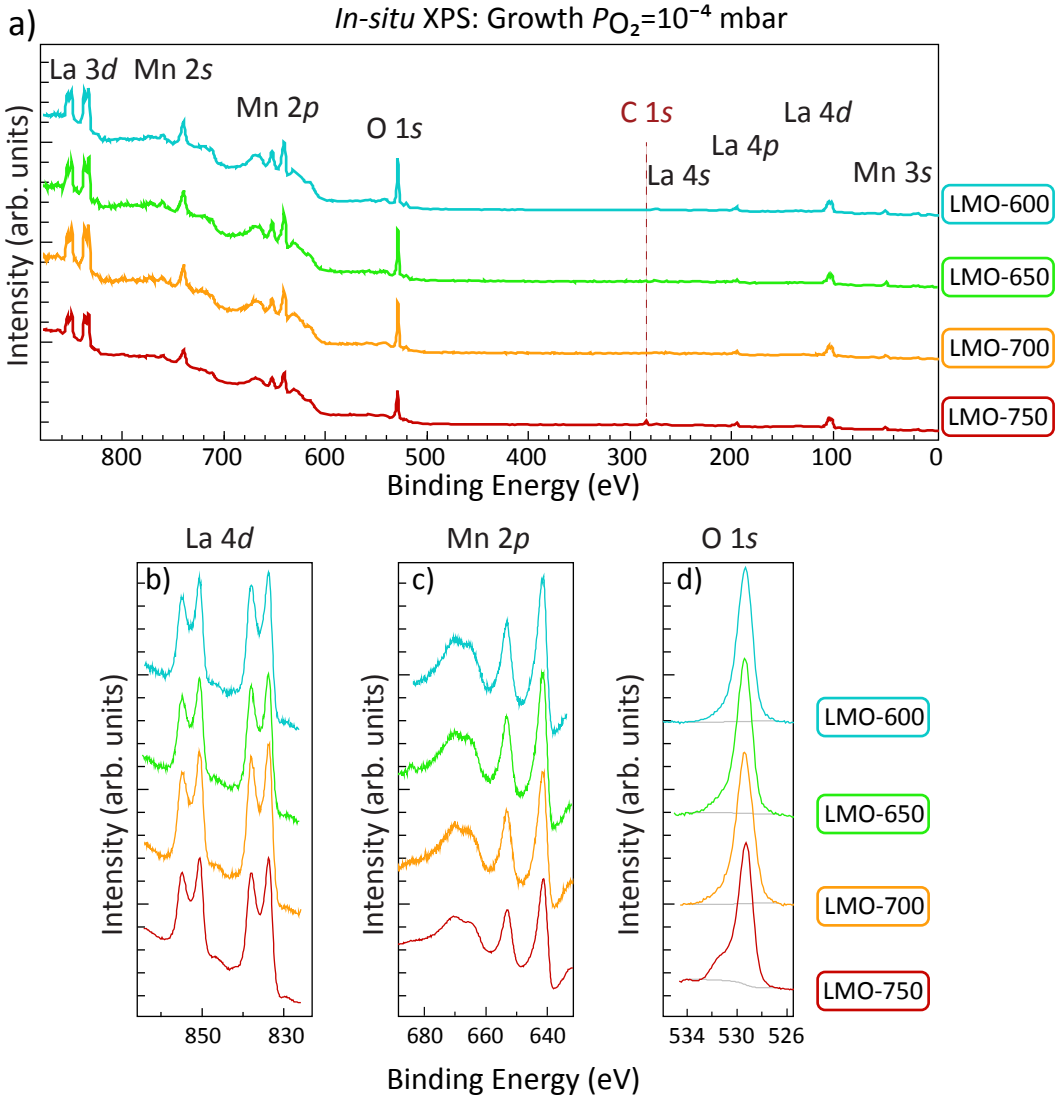

Figure 4.14: *in-situ* non-monochromated XPS a) survey scans of the films grown in p_{O_2}=10^{-4} mbar at different T_g. All films expect the one grown at 750 °C show no contamination at the surface. This can be attributed to a week gap between the growth and the XPS measurement of this sample. b) La 4*d* shows no dependence on the T_g so does the Mn 2*p* (c). d) The O 2*p* spectra show that only the spectrum of the film grown at T_g= 750 °C has an additional peak on the high binding energy side.

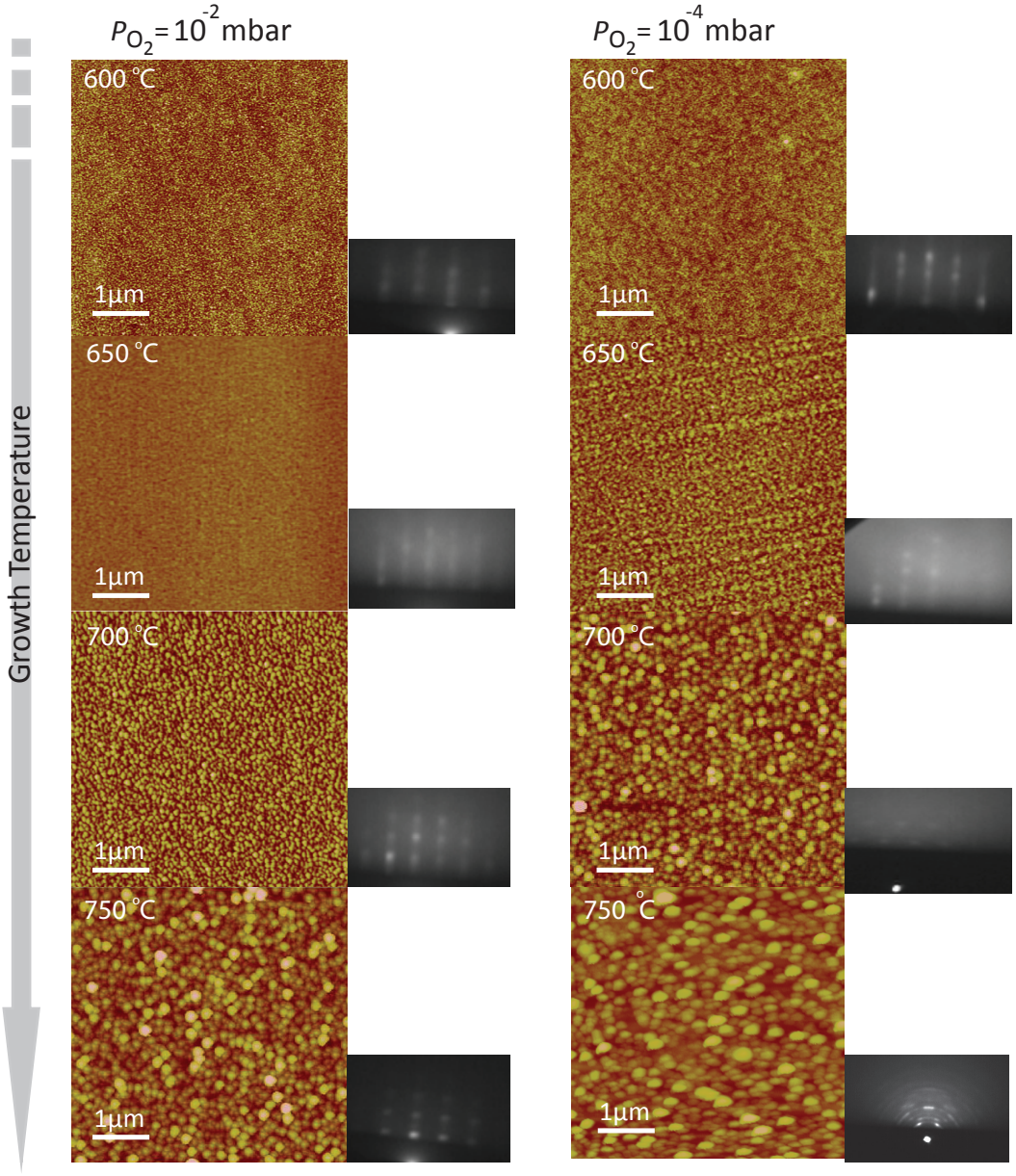

Figure 4.15: RHEED pattern and AFM surface morphology of $LaMnO_3$ films show a change in growth mode from 2D to 3D and island growth as a function of temperature. Streaky lines in the RHEED pattern suggest the smoothness of the film and dots confirms the island growth mode at higher T_g.

Table 4.2: Temperature dependent RMS roughness values of $LaMnO_3$ films grown in two different p_{O_2} of 10^{-2} and 10^{-4} mbar. The roughness RMS values have an error bar of $\pm$0.01 nm.

p_{O_2} mbar	10^{-2}				10^{-4}			
T_g°C	600	650	700	750	600	650	700	750
RMS roughness (nm)	0.37	0.31	2.63	7.52	0.42	0.99	5.05	8.13

4.8 Optimisation of $LaMnO_3$ for superlattice growth

It is essential to achieve strong and defined RHEED intensity oscillations before using $LaMnO_3$ in a heterostructure. This was achieved by increasing the deposition temperature which clearly affects the crystallinity and also the surface morphology as discussed. However in this section growth is optimised purely judged by RHEED intensity oscillations. As can be seen from the figure 4.16, the RHEED intensity exhibits stronger oscillations when the T_g is increased from 600 to 650 °C. However by increasing the temperature to 700 °C no significant improvement was seen. For the $LaMnO_3$ film grown at 750 °C the first oscillations improved compared with the films grown at lower temperatures. However, the RHEED intensity oscillations show strong damping over a few monolayers due to the rapid increase in the surface disorder. As the temperature rises, a transition from a streaky pattern to a spotty pattern is observed due to the electron diffraction arising from the 3D islands on the surface. At 750 °C, $LaMnO_3$ film becomes more textured and the arc-type RHEED pattern where the spots lie on the diffraction rings is observed. This suggests the surface morphology change which is observed in AFM images (figure 4.15). However these conclusions are based purely on RHEED intensity oscillations from the initial growth of $LaMnO_3$. The next parameter to adjust was the laser fluence. It was increased from 1.5 to 2 J/cm^2. It was found that the energy fluence improved the initial oscillations significantly as shown in panel (e) of figure 4.16. The improved RHEED oscillations by increasing temperature can be attributed to an increase in the mobility while the more significant improvement in RHEED intensity oscillations as a result of the increased laser fluence is attributed to an increase in the supersaturation. For example, at low supersaturation, small nucleation on top of a 2D island are less likely to become stable and may decompose to adatoms which finally join the step edges of the lower layer [197]. Therefore, at the early stages of the deposition of a monolayer, deposition conditions such as laser fluence which increases the supersaturation, and hence the surface migration and nucleation of adatoms, are important to achieve strong RHEED oscillations. Marton *et al.* [198] studied the effect of laser fluence on the stoichiometry of $LaMnO_3$ thin films grown by PLD. They found

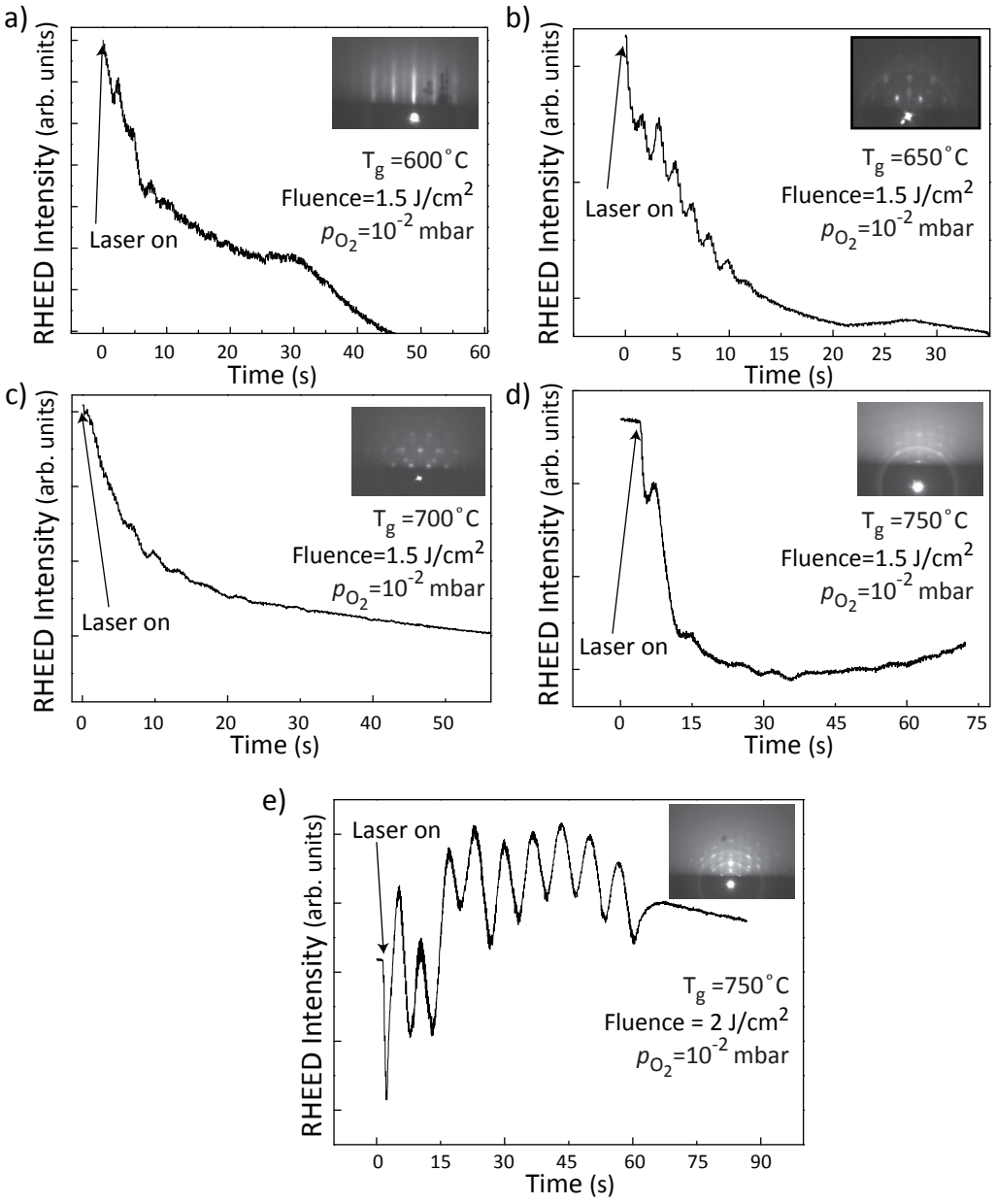

Figure 4.16: RHEED Intensity oscillations of the $LaMnO_3$ films grown at 600 to 750 °C show an improvement in the initial oscillations whilst the strongest oscillations was observed for the film grown at 750 °C with 2 J/cm^2 energy fluence

that using higher laser fluence and lower oxygen background leads to growth of bulk-like stoichiometric $LaMnO_3$ and decreases the oxygen excess (or cation deficiencies). In their report, by changing the laser fluence from 1.5 to 2 2 J/cm^2 no significant change (0.2 % expansion of c-lattice parameter and no change in T_C) was observed, since this energy is above the threshold laser energy ($\sim$0.5 J/cm^2) that results in non-stoichiometric cation transfer. Similar to their results, here no variation in the structural and magnetic properties of $LaMnO_3$ was found as a result of changing the laser fluence.

4.9 Summary

$LaMnO_3$ thin films grown in a partial oxygen pressure of p_{O_2}=10^{-2} mbar showed the ability to self dope by acquiring an oxygen excess resulting in $LaMnO_{3+\delta}$ layers. The structural, transport, and magnetic properties of these $LaMnO_3$ thin films, grown at various substrate temperatures, in both low and high oxygen background pressures were characterised. La vacancies, formed during the growth due to the high oxygen background, lead to an oxidation of Mn ion from Mn^{3+} to Mn^{4+} which favours double exchange interactions, hence, above the critical Mn^{4+} concentration, a metal-insulator-like resistivity maximum appeared. This showed agreement with the exhibited structural properties of $LaMnO_3$ films and reduction in the c-axis lattice parameter when the oxygen content of the film increases (i.e. La deficient films have smaller volume). Films grown in the lower p_{O_2}=10^{-4} mbar and higher temperature (above 700 °C) exhibited rougher surface morphologies due to the formation of oxygen deficiencies during the cooling down cycle (note that films were cooled down in the same p_{O_2} as growth). Increasing the temperature, surface roughening reached a level that no diffraction pattern could be attained from the surface. Rougher surface morphologies at lower p_{O_2} showed agreement with the hypothesis that oxygen loss occurred after deposition when cooling down at low p_{O_2}=10^{-4} mbar (growth pressure). To avoid this adverse effect on the stoichiometry and also surface morphology, samples described in the following chapters were cooled down at a high p_{O_2} of 150 mbar. By increasing the laser fluence from 1.5 to 2 J/cm^2 the initial RHEED intensity oscillations was significantly improved resulting in observation of oscillations up to 10 monolayers, however, no variations in the magnetic properties of the films were observed.

Chapter 5

Optimisation of growth parameters for $LaNiO_3$ thin films

This chapter presents a study of the growth of $LaNiO_3$ on $SrTiO_3$ (001). The effect of substrate temperature on the growth of $LaNiO_3$ thin films has been investigated while the growth was monitored using *in-situ* RHEED. The main aim of this study is to characterise the physical properties of $LaNiO_3$ whilst changing the growth temperature. The growth has been described and surface analysis carried out using RHEED and AFM. The crystallinity of the samples was probed by XRD, which showed (001)-oriented growth. The bulk and surface electronic properties of the layers were investigated using PPMS and XPS respectively. Grazing incidence in-plane XRD and STEM were used to further examine the microstructure of the films.

5.1 Introduction

Recently, artificial layered perovskites, particularly those composed of TMOs, have been an active area of research and have attracted attention owing to their variety of intriguing properties [64, 199]. The family of nickelates, in the form of $RE\mathrm{NiO}_3$ (RE= rare earth), have been considered as a promising platform for these studies due to the charge transfer gap present in their band structure between the unoccupied conduction band of the Ni 3*d* and the occupied O 2*p* valence band [59, 60]. This gap is influenced by the RE radius and also the temperature, hence when they both increase, the gap starts to decrease until it disappears resulting in an insulator-metal transition (IMT) [61]. Bulk $LaNiO_3$ is the only member of this family which remains metallic at all temperatures.

The metallic behaviour of $LaNiO_3$ arises from hybridisation between the Ni 3*d* and the O 2*p* bands, under the influence of NiO_6 octahedra connectivity throughout the

crystal. The resistivity of $LaNiO_3$ is reported to show a T^2 trend which implies a strong influence of electron-electron interaction on the conductivity [62]. It has been reported recently that the metallicity of $LaNiO_3$ can be increased when strong hybridisation of the Ni 3*d* $2t_g$ and O 2*p* states occurs by decreasing the electron-electron interaction in Ni 3*d* e_g states [59]. Therefore, the conductivity of $LaNiO_3$ can be tuned by changing the oxygen octahedra in which the Ni is placed, and this can be achieved by altering the Ni-O bond length or tilting the octahedron. This can be engineered in two ways; changing the growth parameter or using various substrates. The latter changes the type of strain (tensile or compressive strain). As an example, by using $SrTiO_3$ as a substrate under a stable oxygenation condition, $LaNiO_3$ experiences tensile strain. The total resistivity of $LaNiO_3$ thin films also depends on the crystallinity of the layers as defects such as Ni and oxygen vacancies promote charge localisation. Therefore, maintaining stoichiometry in $LaNiO_3$ films becomes a significant growth challenge. This is due to the instability of the thermodynamically unfavourable Ni^{3+} valence state. In $LaNiO_3$ structures, the existence of Ni^{2+} it is often reported [200], and is accompanied by the formation of the oxygen vacancies which are created to maintain the overall charge neutrality of the system [201]. This material is more often referred to as $LaNiO_{3-x}$ where $x \geq 0$. This oxygen deficiency affects both the crystal structure and also the electrical properties of the $LaNiO_3$ [202, 203].

In this chapter the lattice structure of $LaNiO_3$ is explained briefly, then the growth process is described followed by surface analysis of the thin films using RHEED and AFM. The crystallinity of the samples was probed by XRD, which showed (001)-oriented growth. It is shown that the crystallinity of the $LaNiO_3$ thin films is strongly dependent on the growth temperature, and by increasing the growth temperature high quality $LaNiO_3$ films can be grown.

5.2 $LaNiO_3$ structure

$LaNiO_3$ has a rhombohedral crystal structure (symmetry space group $R\bar{3}c$) with lattice parameters of $a = 5.4573$ Å and $c = 13.1462$ Å at room temperature [204, 205]. This rhombohedral structure contains a distorted perovskite pseudo-cubic with lattice parameter $a = 3.838$ Å which is well matched with a number of technologically important substrates such as $SrTiO_3$ and $LaAlO_3$ which is beneficial for its use as a bottom electrode in heterostructure thin film devices [206, 207]. Both rhombohedral and pseudo-cubic $LaNiO_3$ are depicted in figure 5.1, the B-site cation, Ni, is surrounded by 6 oxygen atoms forming an octahedron. Throughout this thesis, only the pseudo-cubic unit-cell of $LaNiO_3$ is discussed and crystallographic orientations labelled in XRD data are defined

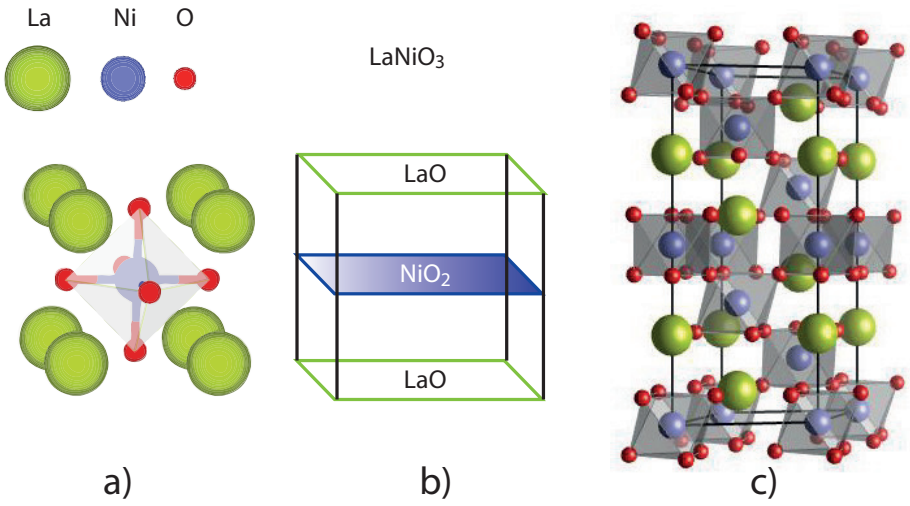

Figure 5.1: Crystal structure of $LaNiO_3$ a) pseudo-cubic perovskite structure, b) different planes of LaO and NiO_2 within the pseudo-cubic lattice, c) rhombohedral structure

in relative pseudo-cubic lattice.

PLD growth of $LaNiO_3$ thin films is explained in the next section to achieve defined RHEED-intensity oscillations which is a strong indication of layer-by-layer growth to control the thickness of $LaNiO_3$.

5.3 Thin film growth

Four thin films of $LaNiO_3$ were deposited onto single crystal $SrTiO_3$ (001) substrates by pulsed laser ablation from a commercially provided bulk $LaNiO_3$ ceramic target. The target was irradiated at low partial pressure of 0.01 mbar at elevated temperatures by a laser beam of 5 Hz frequency. Depositions were carried out at temperatures ranging between 600 to 750 °C in 50 °C increments. The detail process of the deposition was as explained in section 3.2 and the typical deposition parameters of $LaNiO_3$ are summarised in table 5.1. The number of pulses was kept constant at 5000 for each film. After completing the deposition, the chamber was flooded with 150 mbar of pure oxygen and the heater was switched off to minimise oxygen deficiency formation during cooling. XPS measurements and AFM images were both performed *ex-situ* and at room temperature.

Table 5.1: Deposition parameters used for growth of $LaNiO_3$.

Deposition parameters:	Typical values
Compounds	$LaNiO_3$
Background gas	O_2
Background gas pressure (mbar)	0.01
Substrate temperature (°C)	600-750
Spot size (mm^2)	2.16
Shape of spot	rectangular
Target type	sintered pellet
laser fluence (J/cm^2)	1.5

5.3.1 Growth monitoring

By recording the intensity of the RHEED specular spot, growth was monitored during the deposition. The middle panel in figure 5.2 shows the intensity of the RHEED specular reflection as measured during the first 90 s of $LaNiO_3$ growth at various temperatures. The RHEED images on the left side of the main panel represent RHEED patterns of the bare substrates taken at low pressure before heating the substrate. Although substrates were 'as-received' (with no chemical treatment) the Kikuchi lines present are an indication of the smooth surface of the substrates. Images on the right side of the main panel in figure 5.2 show the RHEED patterns of the $LaNiO_3$ films after deposition using 5000 pulses. The thickness of the samples is in the range of 30 to 40 nm, however two dimensional spots have become streaky ovals as a result of electrons scattering from surface disorder. The 3D transmission spots are noticeable in the RHEED patterns of films deposited at elevated temperatures; however they are also accompanied with 2D streaks. This result is in agreement with the AFM images (see figure 5.3) showing crystalline 3D islands on smooth surfaces.

It can be seen from the middle graph of figure 5.2 that the RHEED oscillations damp rather quickly after deposition of less than 10 u.c. for $LaNiO_3$ films. The damping of oscillations can be attributed to the specular spot progressively becoming more streaky as a result of rapidly increasing disorder at the surface due to the growth of islands of various heights creating step edges, and consequently increasing the electron scattering. Kareev *et al.* [102] also reported strong damping after a few u.c. in RHEED specular intensity oscillations in $LaNiO_3$ films. It can be seen in figure 5.2 that the RHEED oscillations become more defined with increasing substrate temperature. This can be attributed to the increased mobility, with a more likely 2D growth. The intensity of the oscillations in figure 5.2 reveals an improved surface order and layer crystallinity with increasing growth temperature. Lower growth temperature appears to give rise to

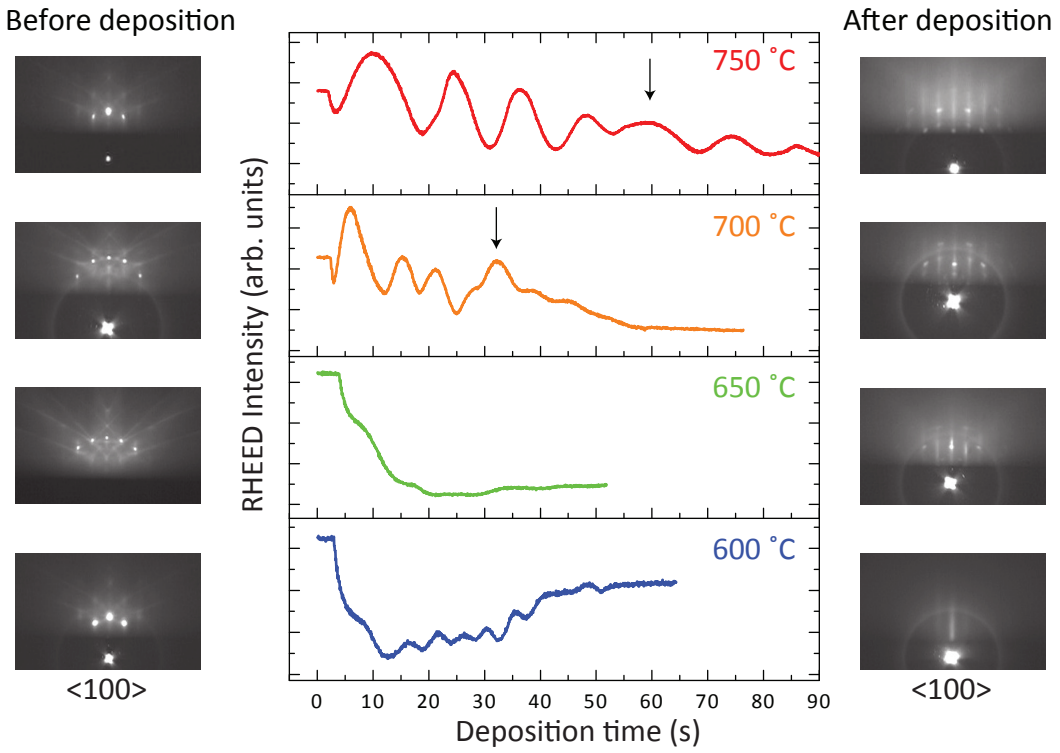

Figure 5.2: RHEED intensity oscillations for $LaNiO_3$ thin films grown at various substrate temperatures on $SrTiO_3$ (001). Middle panel shows the RHEED specular spot intensity oscillations as monitored during the initial 90 s growth. The RHEED images presented on the left hand side are bare substrate at room temperature. The right hand side RHEED images represent the films after deposition of 5000 pulses (after cooling).

3D island formation and this has been investigated with AFM in the next section. By looking at the RHEED and observing bulk transmission, it is expected to see island-like microstructures on the surface, hence AFM was performed to explore this possibility.

5.4 Surface morphology

The surface morphology of the films was investigated using AFM and was compared with the RHEED patterns of the films obtained after deposition. Figure 5.3-a) to -d) shows AFM height images of 1×1 μm^2 area of the films deposited at various temperatures along with line-profiles to compare the height of the islands (lines profiles are shown on the right side of each image). Images on the right side of figure 5.3-e) to -h) are inverted RHEED images of each film and a line profile of the spots are shown under each RHEED pattern for a straightforward comparison of the FWHM of

Table 5.2: Temperature dependent RMS roughness values obtained from 1×1 μm^2. Reported grain sizes are from the islands on the surface of $LaNiO_3$ films.

$T_{Substrate}$	RMS roughness (nm)	Mean grain size (nm)
600	0.45(1)	7(1)
650	0.63(1)	10(1)
700	1.12(1)	83(1)
750	1.56(1)	215(1)

the specular beam peak. The RHEED line profiles were originally in pixels. Using the substrate diffraction spot as a reference (a_{SrTiO_3}= 3.905(1) Å) pixels were converted into a reciprocal streak-spacing ($Å^{-1}$).

As can be seen from the left column of figure 5.3, the film deposited at 600 °C shows a smooth surface without the formation of any distinctive grains. At 650 °C the roughness increases and small islands of average size 10.8(1) nm were observed. Further increases in the temperature lead to a grain size enlargement and surface roughening. The RMS values and average grain size of $LaNiO_3$ films deposited at various temperatures are given in table 5.2. When deposited at 700 and 750 °C, $LaNiO_3$ films show full crystallisation with microstructures oriented along high symmetry directions $\langle 110 \rangle$ (figure 5.3-c)). These microstructures clearly have a preferred growth orientation and their surface is smooth (below 1 nm RMS) as can be seen from the line profiles shown in figure 5.3-c) and -d). These images were taken using *ex-situ* AFM and the RHEED patterns were obtained after the samples were cooled to room temperature, thus there is no way to ascertain whether they were formed during the deposition, or after the growth during cooling to room temperature. Since strong RHEED oscillations at the initial growth of the thin films were observed, suggesting layer-by-layer growth, it can be considered that they are out-growths and so formed after the growth has ended. It is known that off-stoichiometric growth can result in the appearance of precipitates on the surface of perovskite films [208, 209, 210].

The RHEED images showed a transition from streaks to spots indicating a transformation in the morphology of the films. The RHEED pattern of the $LaNiO_3$ film deposited at 600 °C is more diffused indicating poor crystallinity which agrees with the AFM image without distinct grain boundaries. The diffraction spots become sharper with increase growth temperature, correspondingly, the specular spot FWHM will decrease indicating an increase in lateral grain size. RMS roughness of the films are reported in table 5.2 however the roughness of the films under the islands are smooth and their RMS roughness values are below 1 nm. The well-ordered microstructures observed by AFM suggests the films are crystalline, however, to further examine the relation between the

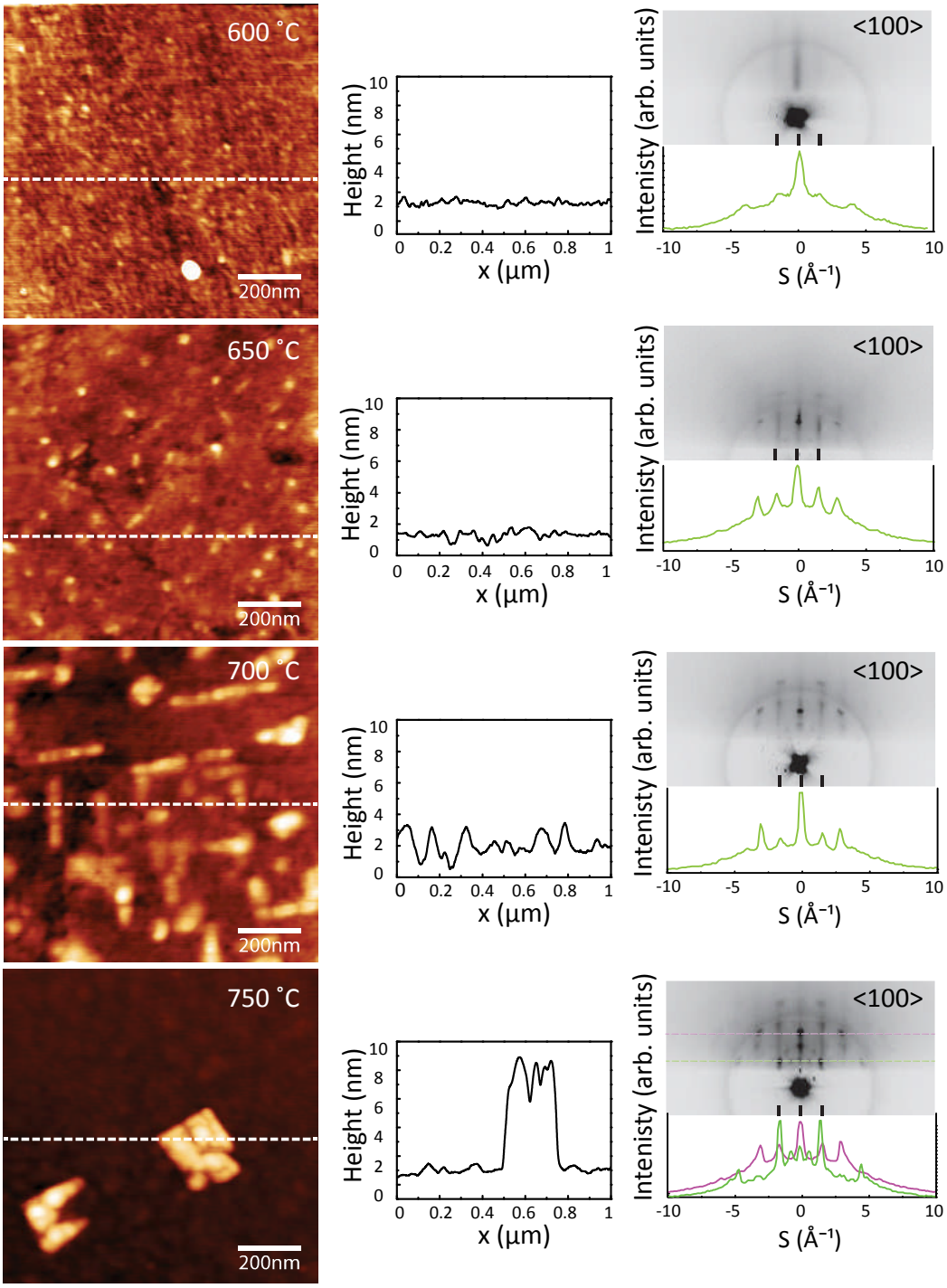

Figure 5.3: Surface morphology and structure dependency of $LaNiO_3$ thin films on substrate temperature. a-d) AFM height images of 1×1 μm area along with line-profile (white dashed line). e-h) Inverted RHEED images of each film with line profile.

Table 5.3: Lattice parameters and crystallite size from Scherrer equation determined from the (002) Bragg peaks shown in figure 5.4

$T_{Substrate}$(°C)	2θ(°)	c lattice parameter(Å)	Crystal size (nm)
600	44.269(1)	4.088(1)	6.6(1)
650	46.731(1)	3.884(1)	21.6(3)
700	46.841(1)	3.875(1)	25.6(1)
750	47.127(1)	3.853(1)	29.9(2)

substrate temperature and growth of $LaNiO_3$ XRD was performed as follows.

5.5 XRD patterns

In order to probe the effect of temperature on the crystallinity of the film quality it was necessary to perform XRD. Figure 5.4 shows XRD $\theta - 2\theta$ patterns of the $LaNiO_3$ films on (001) $SrTiO_3$ substrate deposited at 600, 650, 700, and 750 °C. As revealed from the obtained XRD patterns, for the films grown at 650 °C and above, the indexed peaks in figure 5.4 correspond to the perovskite phase. Furthermore, when increasing deposition temperature, the strength of the (002) peak increases while the non-perovskite phase (indexed by *) disappears. The peak marked by * is indicative of La_2NiO_4 (006). This structural change has been mostly observed at temperatures above 700 °C due to decomposition of the $LaNiO_3$ phase [211, 212, 213]. Upon increasing temperature, uptake of oxygen increased, especially during cooling of the sample when the chamber was flooded with oxygen. It can be assumed that the oxygen incorporated better into the lattice at a higher temperature. In contrast, the films grown at low temperatures were more oxygen deficient. The oxygen deficiency results in the formation of Ni^{2+} and consequently, leads to the formation of La_2NiO_4, which is highly insulating. For films grown with a substrate temperature greater than 700 °C the (003) peak becomes visible indicating increasing crystal quality in the layers. Noticeably, the film grown at 750 °C exhibits only (00l) diffraction peaks, indicating that an entirely (001)-oriented $LaNiO_3$ thin film was grown successfully on the $SrTiO_3$ (001) substrate.

From the $\{001\}$ reflections, the c-axis lattice parameter of $LaNiO_3$ was calculated.

Lattice parameter

As stated earlier, at room temperature $LaNiO_3$ has a rhombohedral crystal structure of space group $R\bar{3}c$ with cell parameters of a = 5.4573 Å and c = 13.1462 Å [204]. This rhombohedral structure contains a distorted perovskite pseudo-cubic structure with a lattice parameter a= 3.838 Å. However, the adjacent NiO_6 octahedra undergo

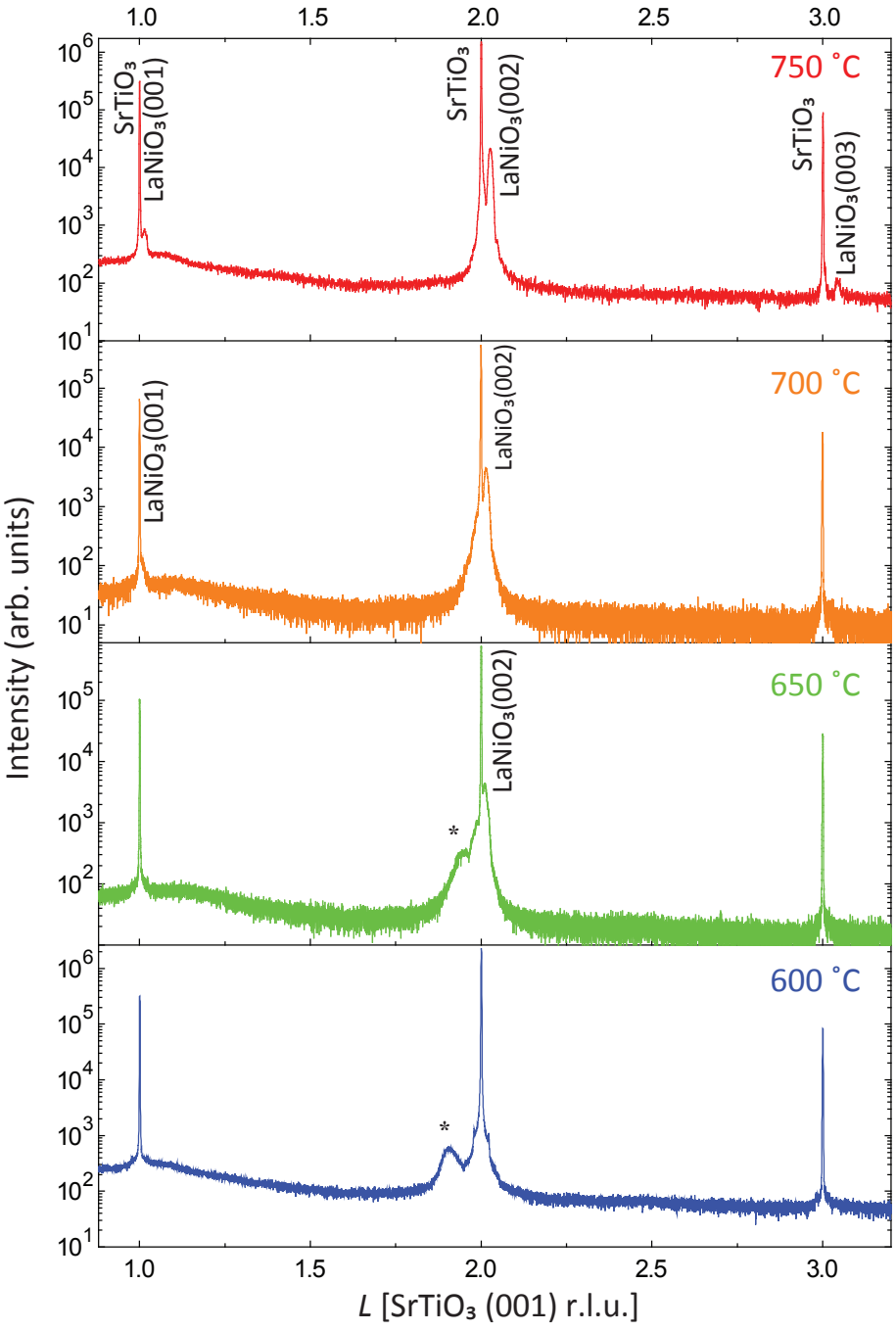

Figure 5.4: XRD $\theta-2\theta$ scans of $LaNiO_3$ thin films grown at various substrate temperatures from 20 to 80 ° shown in r.l.u. relative to the substrate. Peak marked as $*$ corresponds to La_2NiO_4.

an anti-phase rotation about the [111] trigonal axis which is defined by Glazer tilting notation as ($a^-a^-a^-$) [71, 72]. Further lattice distortion can be induced by strain due to lattice mismatch, i.e. the 1.7 % tensile strain when $LaNiO_3$ is grown on $SrTiO_3$ substrate [214]. Figure 5.4 shows that the position of the diffraction peaks shifts to higher angles hence indicating a reduction in the c-axis lattice parameter of the films. The lattice parameter variations of c-axis lattice parameter and crystal size values of the $LaNiO_3$ films deposited at various substrate temperatures are given in figure 5.5 and Table 5.3. The crystallite sizes reported in table 5.3 were calculated from Scherrer's equation and the c-axis lattice parameter was calculated from the d spacing of the (002) planes using Bragg's law. Figure 5.5 illustrates that as the temperature rises, the lattice parameter decreases, i.e. the volume of the unit cell decreases. This reduction in the cell volume is attributed to the decrease in the defect concentration due to the increased uptake of oxygen. When, the temperature rises, the c–axis lattice parameter becomes closer to that of stoichiometric bulk $LaNiO_3$. The lattice parameters determined for the $LaNiO_3$ films is found to agree reasonably with the pseudo-cubic $LaNiO_3$ (3.84 Å) however it is slightly larger. The volume of the u.c. could decrease under tensile strain if the material has a negative Poisson ratio. Considering the strain induced by the lattice mismatch between the $SrTiO_3$ substrate and $LaNiO_3$ under tensile strain, the out-of-plane lattice for the films should be smaller [214] however this is not the case in these films. One suggestion can be that strain is induced not as a result of mismatch, but from the coexistence of a second phase although there was no evidence of such a phase in the out-of-plane XRD pattern.

Considering the presence of a second phase in the films the most thermodynamically favourable secondary phase in $LaNiO_3$ is La_2NiO_4, and its evolution and coexistence in $LaNiO_3$ films grown at temperature above 600 °C has been repeatedly reported [211, 212, 215]. La_2NiO_4 is a layered perovskite in which the layers of $LaNiO_3$ are separated by rock-salt LaO layers. Lattice parameters of tetragonal ($I4/mmm$) La_2NiO_4 at room temperature are a=3.8690(2) Å and c=12.6(2) Å [216]. The in-plane lattice constant of La_2NiO_4 is very similar to that of the pseudo-cubic $LaNiO_3$. If La_2NiO_4 grows in plane, it will be difficult to reliably identify from an out-of-plane $\theta - 2\theta$ scan due to the similarity in the position of the (002) thin film perovskite $LaNiO_3$ and the (200) of the La_2NiO_4 reflection peaks. Moreover, growth of the a-domain La_2NiO_4 has been reported by PLD on $SrTiO_3$ under similar deposition conditions to those used in this work [217].

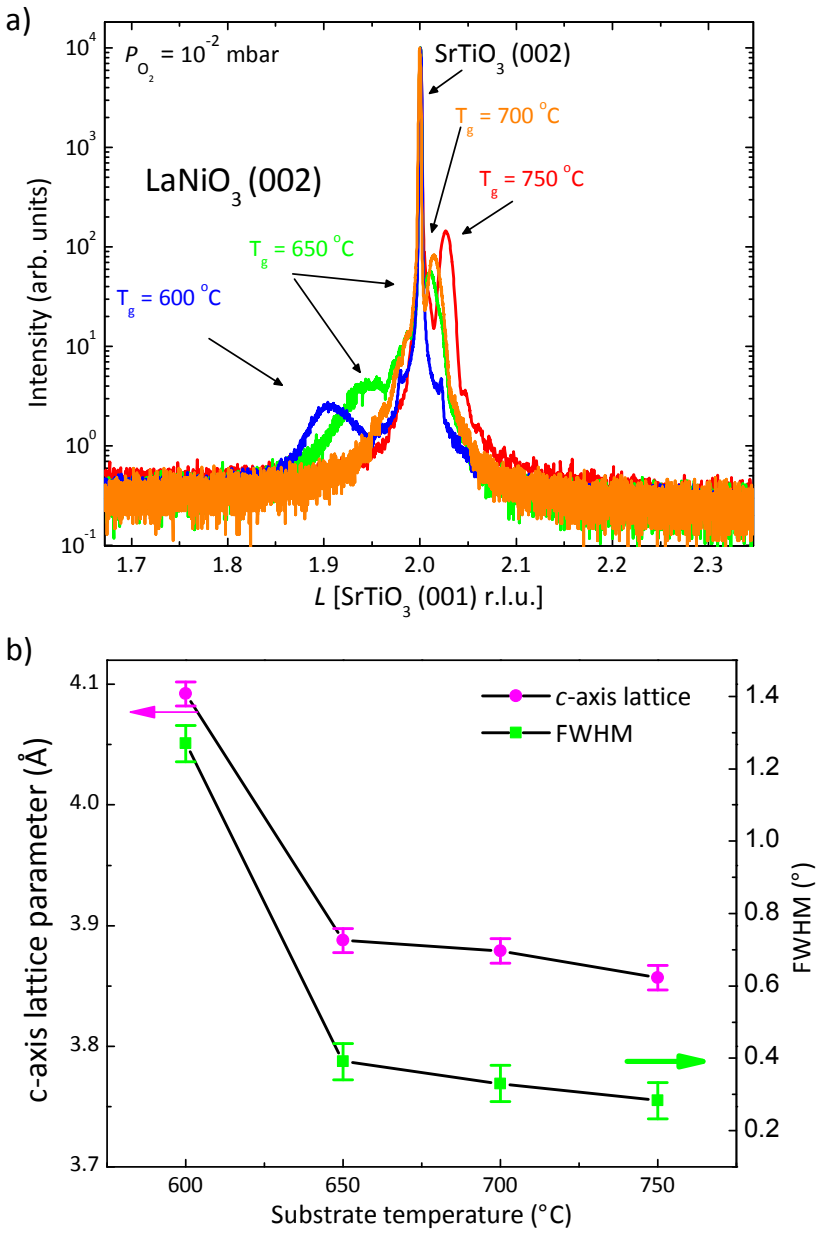

Figure 5.5: a) $\theta - 2\theta$ of the $LaNiO_3$ (002) films shown at smaller range around the (002) peak of $SrTiO_3$ substrate. b) (Right axis) FWHM of the (002) reflection and (left axis) c-axis lattice parameter of $LaNiO_3$ films decrease when substrate temperature rises.

5.6 Transport properties

The temperature-dependent resistivity of $LaNiO_3$ thin films was measured from 300 to 2 K (figure 5.6) using a PPMS-Quantum Design. The room temperature resistivity of $LaNiO_3$ thin films grown at temperatures from 600 to 750 °C is presented in the inset of figure 5.6. Figure 5.6 reveals the effect of substrate temperature on the temperature-dependent resistivity. The resistivity is seen to fall as the substrate temperature increases, while the temperature behaviour also changes. The resistivity dependence on temperature can be conventionally determined as $\rho(T) = \rho_0 + AT^{\alpha}$, where ρ_0 is the temperature independent residual resistivity, α is dependent on the dominant scattering mechanism within the material and A is a constant. Based solely on Coulombic interactions, resistivity has a T^2 dependency in the Fermi liquid model of metals [218, 219]. However, at low

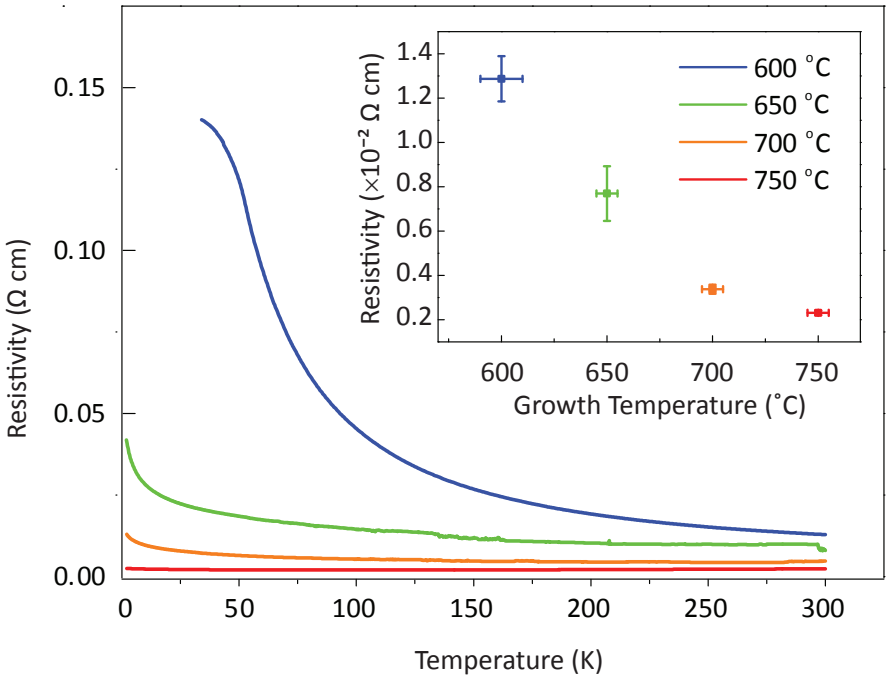

Figure 5.6: Temperature versus resistivity compared for $LaNiO_3$ thin films grown on different substrate temperature. The inset shows the room temperature resistivity of the films and their dependence to the substrate (growth) temperature.

temperatures, in correlated complex oxides, carriers can be localised resulting in a IMT in these marginal metals. Except for the film grown at 750 °C, the films did not show any metallic behaviour. The a-domain La_2NiO_4 phase induces strain in the films and strain has been suggested to be a controlling factor in the relative distribution of localisation,

hence the transport properties. The wide range of resistivity values reported in the literature for thin films of $LaNiO_3$ is another indication of stoichiometry issues during the growth of this material. Room temperature resistivity values reported for $LaNiO_3$ films range between 0.1 to 2 $\times 10^{-3}$ Ωcm [220, 221, 222]. Comparing this range to that of the $LaNiO_3$ film grown at 750 °C ($\approx$2 Ωcm) indicates that the lowest value achieved in this work is at the upper limit of this range. There are several plausible explanations for the formation of defects in the film. First of all, an oxygen background pressure of 0.1 mbar has been widely used for full oxidisation of $LaNiO_3$ films followed by post-annealing in air or pure oxygen. It can be concluded that the oxidisation condition during growth (background oxygen pressure of 0.01 mbar) was not sufficient although the films were cooled down in 150 mbar oxygen pressure to maintain stoichiometry after growth. While post-annealing in air can decrease the resistivity of $LaNiO_3$ films by up to two orders of magnitude, the purpose of this optimisation, which was the synthesis of a layered lanthanum based oxide heterostructure, meaning post annealing was not practical. In conclusion the enhanced resistivity observed in $LaNiO_3$ is ascribed to the non-stoichiometry of $LaNiO_3$ promoted by a low oxidisation environment during growth which leads to the formation of a secondary phase of La_2NiO_4 which further induces strain into the system. This extra strain will then lead to an expansion of the NiO_6 octahedra and a localisation of the Ni-O bond. While bulk-type transport properties were investigated here, XPS can give insight into the surface electronic properties of these films.

5.7 X-Ray Photoelectron Spectroscopy

XPS measurements were performed using monochromated Al K_α X-ray source and the complex XPS system had a typical resolution of 0.4 eV. Figure 5.7-(a) shows a typical XPS survey of a $LaNiO_3$ films (from $LaNiO_3$ deposited at 700 °C) and regions of various chemical states are marked. High resolution scans of valence band spectra for the films grown at 600, 700 and 750 °C are depicted in figure 5.7-(b). These reveal states crossing the Fermi level which confirms the metallic behaviour of the $LaNiO_3$ films grown at 700 °C and above. The observed valence band spectrum is in good agreement with recent theoretical calculations [223]. Valence band spectra features are labelled in figure 5.7-(b) for the film grown at 750 °C. Two features, A and B, near the E_F are assigned to e_g and t_{2g} states of Ni *3d*, respectively. The next two features, named C and D, are associated with O *2p* dominant states [224]. Note that the valence band spectra shown in figure 5.7-(b) are normalised to feature D. It is clear that the $LaNiO_3$ layer grown at 750 °C has more intense features as compared to the films grown at lower temperatures.

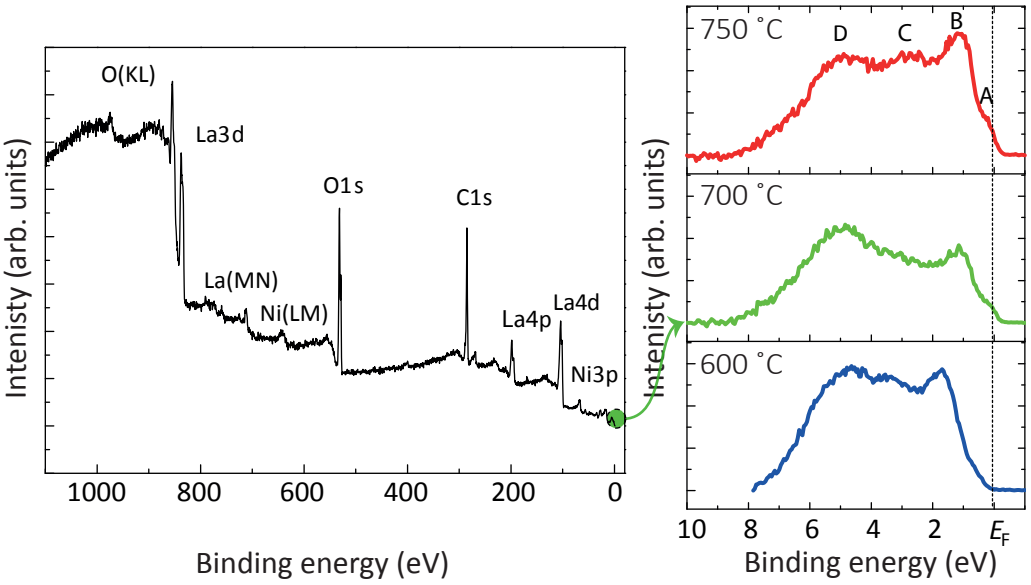

Figure 5.7: XPS spectrum of (right panel) survey wide-scan of $LaNiO_3$ film deposited at 700 °C b) valence band spectra for films deposited 600, 700, 750 °C. Fermi level is shown by the dashed line. A-B and C-D are features of XPS related to Ni *3d* and O *2p* respectively.

Features A and B are very sensitive to the oxygen stoichiometry of the films, and so it is plausible that oxygen vacancies are filled for higher growth temperatures and/or during cooling. The intensity of feature A enhances as growth temperature rises. It is noticeable that feature A crosses the E_F in $LaNiO_3$ grown at 750 °C, an indication of the metallicity of this $LaNiO_3$ film and supporting the transport behaviour of the films based on transport measurements.

5.8 Effect of target on growth

One of the most favourable advantages of PLD is the similarity between the stoichiometry of the target and deposited film, and thus target's stoichiometry should be repeatedly checked, especially if the bulk material is known to be unstable in the desired crystallographic structure. During the pulsed laser irradiation, the target surface is being heated at extremely high rates (10^8 K/s) resulting in congruent evaporation of the target regardless of the evaporation temperatures of each constituent elements in the target. However not only the stoichiometry but also the crystal phase structure of the target should be the same as what is desired in the deposited film, i.e. perovskite

$LaNiO_3$. Earlier, the non-stoichiometry of $LaNiO_3$ was associated with the low oxidisation environment during growth and thus the formation of a secondary unfavourable compound La_2NiO_4. La_2NiO_4 is one of the Ruddlesden-Popper (RP) phases, a homologous series of the form $A_{n+1}B_nO_{3n+1}$ (n=1, 2, and 3) when ABO_3 is the perovskite structure [225]. Attributing the change in stoichiometry to the oxidisation environment is only valid if the target material is stable, and remains stoichiometric throughout the deposition process. If any of the RP phases are present in the target, the formation of $La_{n+1}Ni_nO_{3n+1}$ in the deposited film is expected including La_2NiO_4 (n=1), $La_3Ni_2O_7$ (n=2), $La_4Ni_3O_{10}$ (n=3), and $LaNiO_3$ (n=∞) which are shown schematically in figure 5.8. It has been

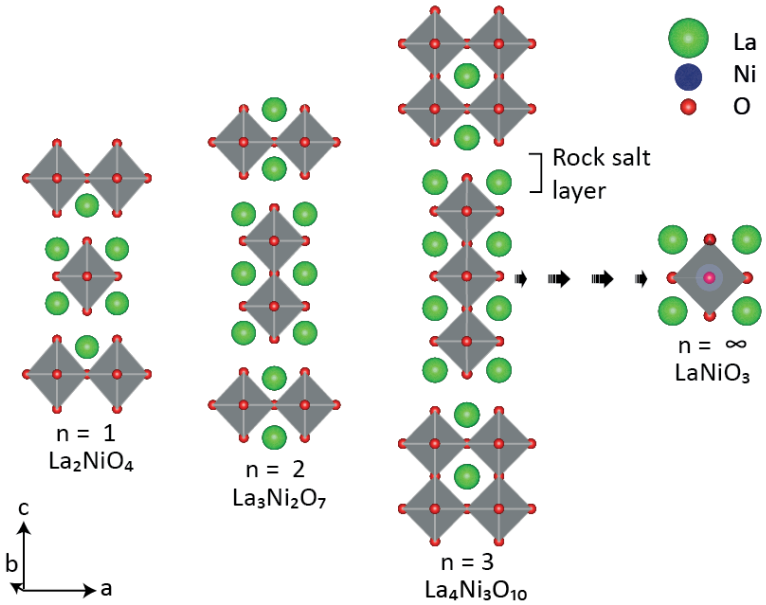

Figure 5.8: Crystal structure $La_{n+1}Ni_nO_{3n+1}$ (n=1, 2, and 3) when $LaNiO_3$ is the perovskite structure (n=∞).

reported previously in the bulk form that the RP family are in equilibrium with NiO and La_2O_3 [226, 227], only $LaNiO_3$ has tie-lines with the gas phase [228]. When increasing temperature or reducing oxygen pressure, whilst the equilibrium with NiO continues, the equilibrium with La_2O_3 is consecutively substituted by that with the gas phase. With further rise in temperature and reduction in oxygen pressure, $LaNiO_3$, $La_3Ni_2O_7$, and $La_4Ni_3O_{10}$, decompose until only the La_2NiO_4 compound coexists with La_2O_3, NiO, Ni and gas. The decomposition process of complex oxide lanthanum nickelate can be

written as;

$$4\ \mathrm{LaNiO_3} \rightarrow \mathrm{La_4Ni_3O_{10}} + \mathrm{NiO} + 1/2\ \mathrm{O_2}, \tag{5.1a}$$

$$3\ \mathrm{La_4Ni_3O_{10}} \rightarrow 4\ \mathrm{La_3Ni_2O_7} + \mathrm{NiO} + 1/2\ \mathrm{O_2}, \tag{5.1b}$$

$$2\ \mathrm{La_3Ni_2O_7} \rightarrow 3\ \mathrm{La_2NiO_4} + \mathrm{NiO} + 1/2\ \mathrm{O_2}. \tag{5.1c}$$

The decomposition temperature of $LaNiO_3$ in air, as reported by Bannikov's group is around 980 °C [229]. The results from various measurements indicated the existence of a second phase in the films and hence higher resistivity than expected for stoichiometric $LaNiO_3$ thin films bought the quality and crystallinity of the target into question. Testing this hypothesis using an energy-dispersive X-ray spectroscopy (EDS) coupled to scanning electron microscopy (SEM) can give misleading results since during the decomposition process no loss of cations occurs. During this project at several points, $LaNiO_3$ target was probed by EDS-SEM. The result showed relatively stoichiometric composition (atomic ratio of La/ Ni ≈ 1) within the errors of the experiment. The ratio of cations (La/Ni) varied between 1 and 1.15 indicating slight Ni deficiency at various parts of the target. The oxygen content cannot be reliably measured using this technique.

To confirm the single phase with the perovskite structure, a XRD powder-type scan was carried out on a sample made of crushed $LaNiO_3$ target and the position and relative intensity of the XRD-pattern were compared with the single phase materials. Figure 5.9 summarises the results including the HighScore Plus Rietveld refinements showing more than 95 % RP phase in the crystalline sample. Only 3% Ni and 1% NiO were detected indicating that target is heavily Ni deficient (La/Ni≈2). It can be assumed that the decomposition has truly occurred in the $LaNiO_3$ ceramic target either during the initial solid-solution of sintering process or later after or during the deposition process. One possible explanation to justify the EDS-SEM results is that there are Ni and NiO precipitations distributed homogenously throughout the pellet, therefore EDS results gave stoichiometric ratio of cations in the target. The true origin of this decomposition is debatable with the existing data.

One experiment that should be performed is to take XRD patterns from a perovskite phase stoichiometric target and repeat the measurements after several thousands laser shots to examine the effect of laser ablation on the stability of perovskite phase. It also should be noted that this target was not continuously kept in vacuum due to technical break downs of the deposition chamber. In this context, the environment in which target is kept might be the reason for this decomposition. However, the temperature reported for the decomposition to take place in the whole target is too high and in none of the stages of the PLD deposition process does the target reaches 900 °C

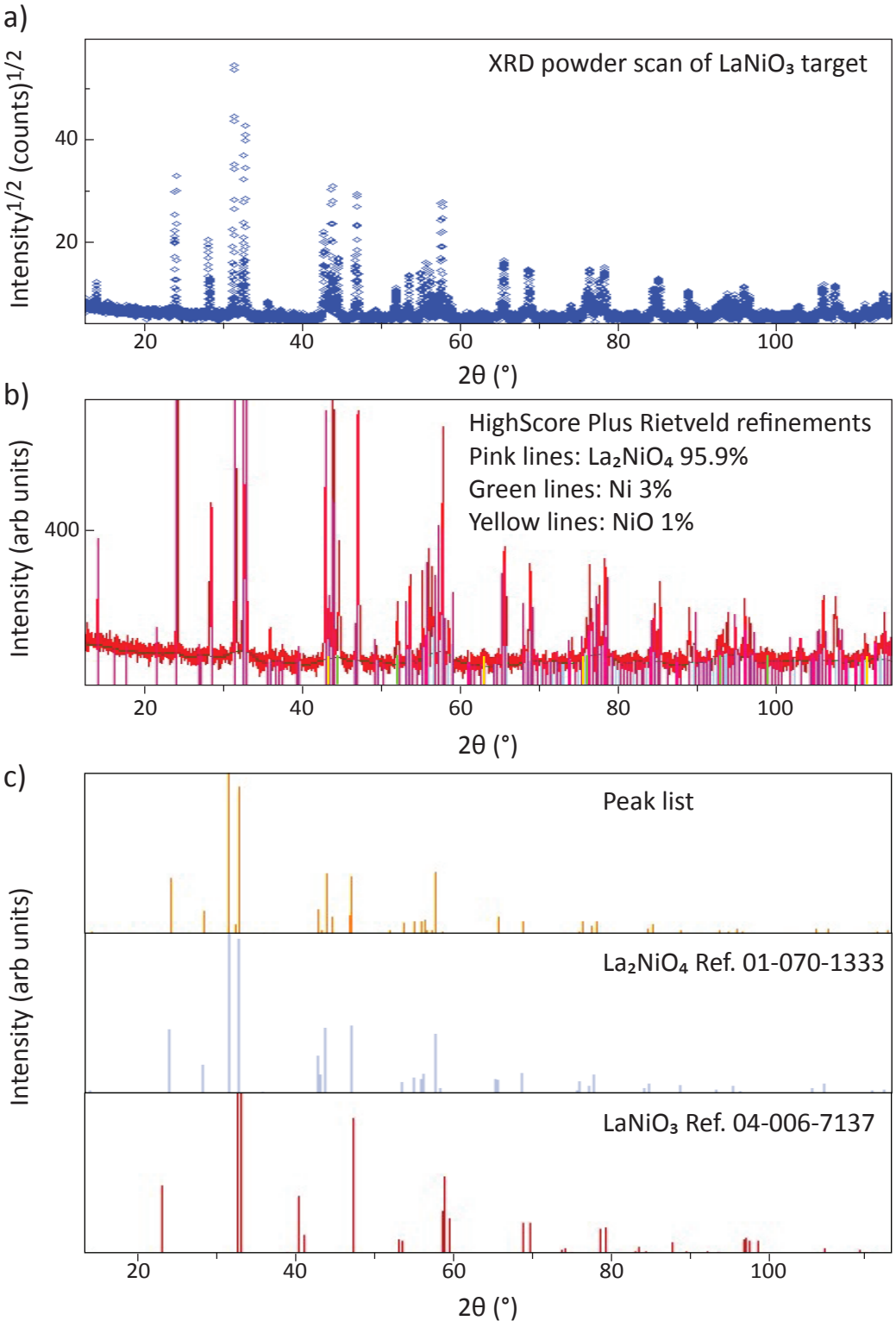

Figure 5.9: a)$\theta - 2\theta$ powder XRD scan of $LaNiO_3$ target b) HighScore Plus Rietveld refinements c) It can be seen by comparing the peak list with the reference compounds that the RP phase is the dominant one.

apart from the very top most surface layer. Knowing this allows us to conclude that the phase of the target was changed during the solid-solution sintering process carried out by the manufacturers. In conclusion, to obtain stoichiometric thin films, not only the composition should be of the required stoichiometry, but also the crystal phase of the ceramic target should be tested and chosen to match because it can drastically change the quality of growth. Regardless of having a RP phase target, films grown at high temperature exhibited similar physical properties to stoichiometric perovskite $LaNiO_3$. To further exploit the microstructure and understand the reason that no RP phase was detected in the out-of-plane XRD $\theta - 2\theta$, the sample with the closest-to-stoichiometry (grown at 750 °C) was prepared for STEM imaging.

5.9 Probing $LaNiO_3$ using STEM

The $LaNiO_3$ thin film grown at 750 °C and 0.01 mbar oxygen exhibited abundant amount of the RP phase as shown in figure 5.10. The profile taken in this image shows the incorporation of an extra LaO plane in the heterostructure and therefore two peaks corresponding to La lie next to each other in the shown HAADF image and are highlighted

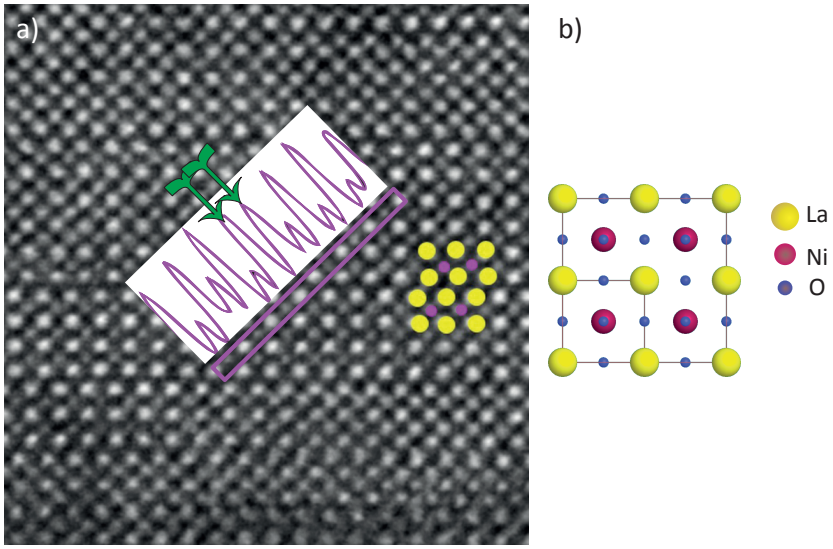

Figure 5.10: a) HAADF image of $LaNiO_3$ thin films showing La_2NiO_4 (RP) planer faults are abundant. Line scan profile shows an extra LaO layer is inserted into the structure. Corresponding two high intensity peaks are shown by green arrows. b) Schematic perovskite $LaNiO_3$ which is also shown in a) to highlight the half u.c. shift and the extra rock-salt LaO plane.

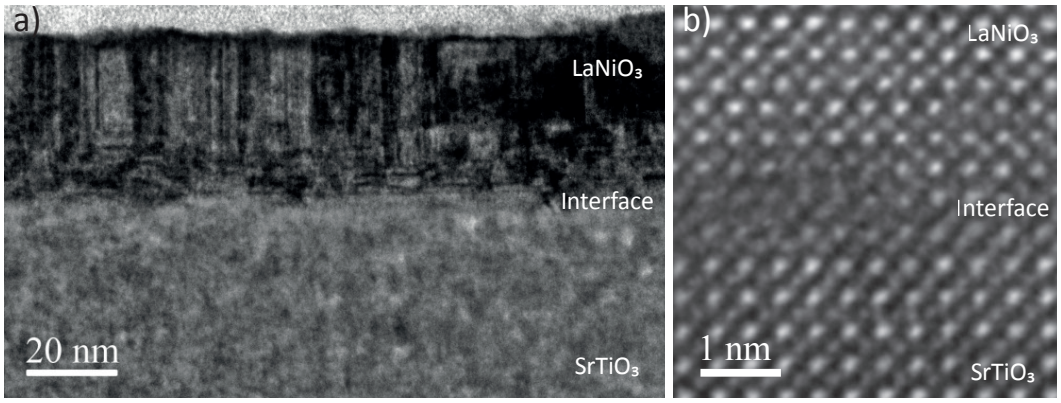

Figure 5.11: a) HAADF image of $LaNiO_3$ thin films showing intermixing at the interface. b) Higher magnification HAADF image shows that the interface is not abrupt and also La_2NiO_4 (RP) phase are grown from the first monolayers of initial growth.

by the green arrows. It is clear from the HAADF images in panel a and b in figure 5.11 that the interface between $LaNiO_3$ and $SrTiO_3$ is not abrupt which can be attributed to using as-received mixed terminated $SrTiO_3$ substrate. To prevent this problem in growth of superlattices, substrate treatment using HF was optimised for $SrTiO_3$ (001). This process is explained in the next chapter. It can be seen in figure 5.11-b that the excess LaO layer is inserted parallel to the interface after 3 monolayers. It seems that the perovskite phase is not energetically favourable and only after deposition of a few monolayers the structure is relaxed by the formation of a rock-salt LaO layer attributed to the RP phase.

Figure 5.12-a shows that both horizontal and vertical RP faults were abundant in the $LaNiO_3$. This was confirmed by electron diffraction patterns (Figure 5.12-b) showing streaking feature predominantly along the $[010]$ direction, an indication of in-plane growth of the a-domain La_2NiO_4. The images seems to infer that the extra La-O planes grow parallel to the interface, and the long vertical RP faults appear later in the growth. This is opposite to the observation carried out during the growth of Sr-excess $SrTiO_3$ homoepitaxial thin films. $LaNiO_3$ has space group $R\bar{3}c$, with the tilt system $a^-a^-a^-$. Figure 5.12-b shows electron diffraction pattern obtained from $LaNiO_3$ thin film grown at 750 °C . This is the same tilt system as $BiFeO_3$ (see figure 7 of reference [74]) as it generates no superstructure reflections when viewed down $[001]$ directions.

According to STEM images RP faults (phases) are abundant, so it is expected that they should be detectable by XRD out-of-plane scan unless their preferred orientations are along the a-axis of the pseudocubic $LaNiO_3$. Considering there was no peak associated with the RP phase, at the expected position in the HR-XRD data, it can be concluded that

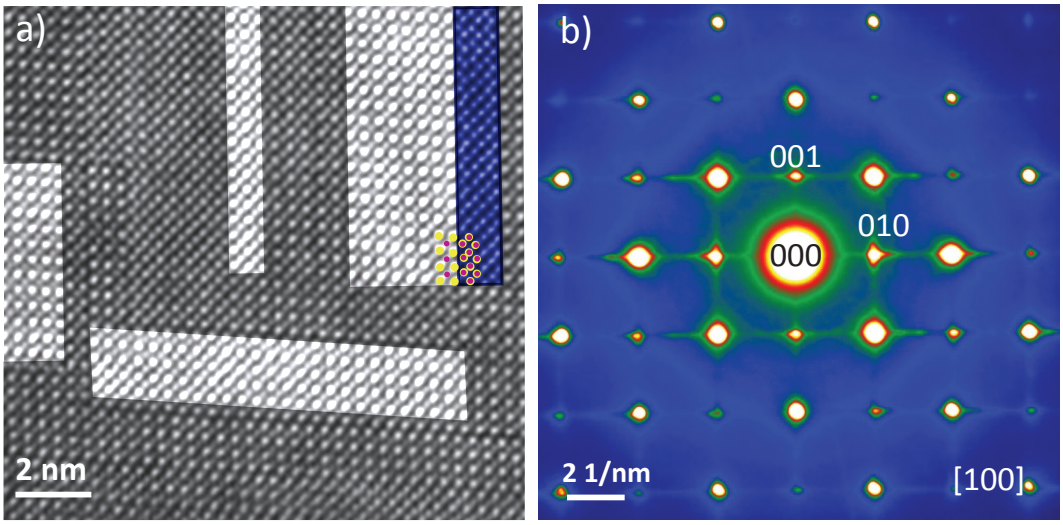

Figure 5.12: a) HAADF image of a $LaNiO_3$ thin film and b) corresponding diffraction pattern. Several perovskite regions are highlighted. It can be seen that there are in a rectangular shape and separated with an extra LaO to the RP phases. One of the region with equal intensity (RP phase) is highlighted with black line next to the perovskite phase. In panel b diffraction spots show streaks dominantly along [010] direction as a result of the a-domain growth of RP phase. There are no superstructure reflections at $1/2$ (odd-odd-even) positions. This pattern is arbitrarily indexed with zone axes [100].

conventional out-of-plane diffraction is not sufficient to characterise the microstructures parallel to the interface. Consequently, the sample grown at 750 °C was taken to the ESRF synchrotron, XMAS beam line for the grazing-incidence X-ray diffraction (GID) measurements.

5.10 Grazing-incidence diffraction of $LaNiO_3$

To examine the in-plane orientation of the microstructures in the films GID was performed at the XMaS beamline of the European Synchrotron Radiation Facility (ESRF)-Grenoble, France. The experimental strategy was to look for the RP phase in the in-plane orientation of the film. The structure of $LaNiO_3$ films along the direction normal and parallel to the surface of the film was evaluated along the $[002]$ and $[200]$ orientations of the $SrTiO_3$ respectively. To complement the in-plane data, an out-of-plane scan was also carried out to investigate the possible c-domain RP phase. Since the growth of the a-domain La_2NiO_4 was reported previously [217], the grazing angle in-plane diffraction was chosen to confirm similar behaviour in these films.

The measurement geometry is shown in figure 5.13. The angles α_i and α_f are the

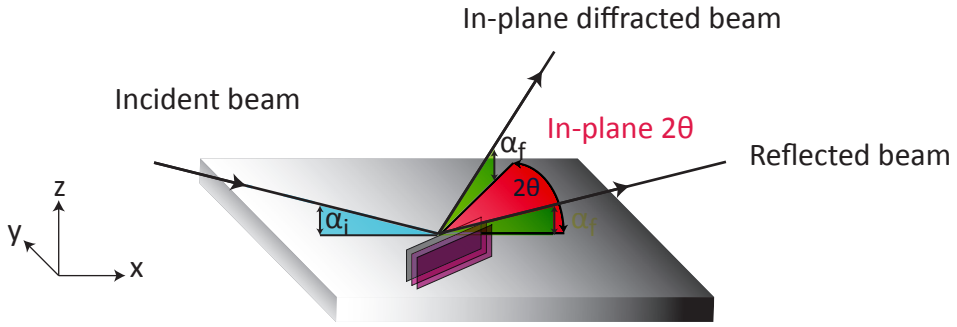

Figure 5.13: Schematic diagram of an in-plane grazing-incidence diffraction geometry. α_i and α_f, incident and final angles, are in the plane perpendicular to the surface of the sample, while $2\theta_{\text{in-plane}}$, the diffracted angle, is in the plane of the sample surface. In this geometry, the sample was oriented such that a lattice plane perpendicular to z is at θ angle with both the detector and the source. The detector was rotated about z to the Bragg angle (2θ). The diffraction is regarded to be entirely in-plane for α_i and $\alpha_f \ll \theta$.

incident and final angles and they lie in the plane perpendicular to the surface of the film, while $2\theta_{\text{in-plane}}$, is the diffracted angle and lies in the film plane (parallel to the sample surface). In this geometry, the sample was oriented such that a lattice plane perpendicular to z is at an angle θ with both the detector and the source, whereas the detector is rotated about z to reach the Bragg angle (2θ). The diffraction is regarded to be entirely in-plane for α_i and $\alpha_f \ll \theta$. Figure 5.14 shows XRD patterns taken using GID at the ESRF. Figure 5.14-a shows a conventional $\theta - 2\theta$ XRD out-of-plane scan. The data was fitted with three peaks including two Gaussian peaks and one Pseudo-Lorentzian peak for the substrate. One of the Gaussian peaks can be attributed to the unstrained-$LaNiO_3$ with smaller FWHM peak at higher angle relative to the $SrTiO_3$ (002). The second broad Gaussian peak is related to the strained-$LaNiO_3$ at lower angle (higher lattice parameters) relative to $SrTiO_3$ (002).

Figure 5.14-b shows the in-plane wide range scan. At position 1.87 r.l.u. in the tail of the substrate in-plane (200) peak, there seems to be a small peak related to the RP phase. Figures 5.14-c and d are the in-plane $\theta - 2\theta$ XRD scan around this area of interest highlighted in panel b. The difference between panel c and d is the phi angle which was rotated 90 degree around the z-axis (normal to the interface). It is clear that there is a weak but clear peak at the expected c-axis value of La_2NiO_4 (006) more dominant in only one of the crystallographic orientations $[100]$ and $[010]$. This arises from the fact that the RP phases are growing in-plane and preferentially only one of the $[h00]$ or $[0k0]$ orientations.

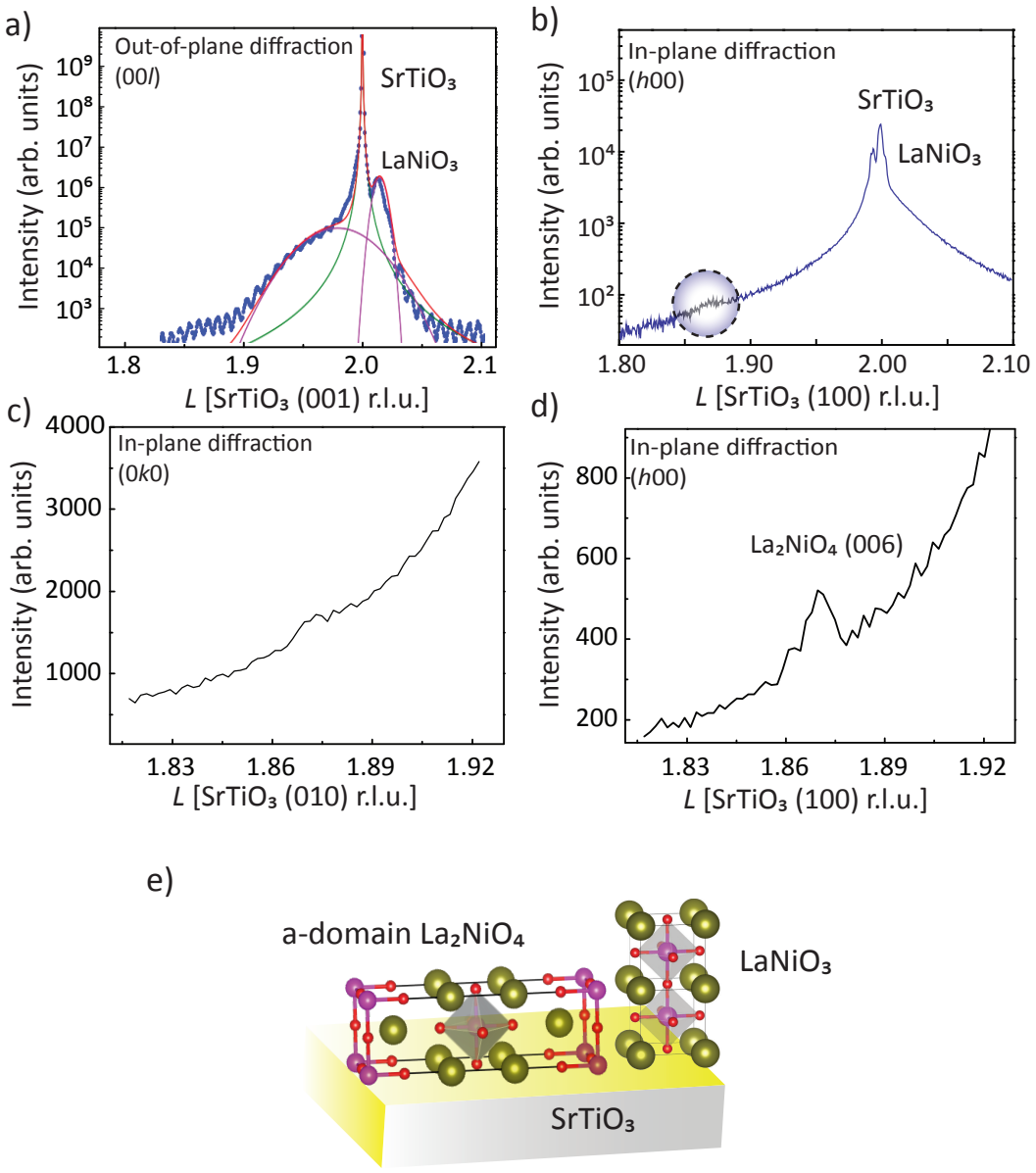

Figure 5.14: a)Out-of-plane $\theta - 2\theta$ XRD scan showed unstrained-$LaNiO_3$ peak at higher angle relative to the $SrTiO_3$ (002) and also a broad Gaussian peak related to the strained-$LaNiO_3$ at lower angle (higher lattice parameters) relative to $SrTiO_3$ (002). b) Very weak but clear peak at the expected c-axis value of RP (006) can be observed. c) and d) more focused scan around 1.87 r.l.u. were performed along either a) $[100]$ or $[010]$ crystallographic orientations. The indexing is arbitrarily. However observed peak is only existed in one of the mentioned orientations. e) a schematic representation of the a-domain RP with the perovskite $LaNiO_3$ on $SrTiO_3$ (001) substrate.

5.11 Summary

Growth of thin $LaNiO_3$ films ($\approx$ 40 nm) has been explored for different growth conditions. It was confirmed that the resistivity falls and crystallinity improves as the substrate temperature rises to 750 °C. The $\{00l\}$ texture of the films continues to increase as the growth temperature is increased. It was also found that at temperatures lower than 700 °C, the RP La_2NiO_4 coexisted in the film affecting the resistivity adversely. The film deposited at 750 °C was found to have the best physical properties, with strong RHEED specular intensity oscillations. XRD patterns of the films indicated the presence of a second phase consisting of La_2NiO_4 at lower growth temperatures. This is in contradiction to what has been reported in the literature that is explained by the structural change due to the decomposition of the $LaNiO_3$ at higher temperatures above 750 °C [211, 213, 214]. Upon increasing the substrate temperature, uptake of oxygen increases during the cooling cycle of the sample when the chamber was filled with oxygen at a pressure of 150 mbar. It suggests that oxygen incorporates better into the lattice when the temperature rises as the films grown at low temperatures are more oxygen deficient. This oxygen deficiency results in the formation of Ni^{2+} and consequently leads to the formation of La_2NiO_4, which is highly insulating. The insulating behaviour of the film grown at 600 °C agreed well with this. The lowest room temperature resistivity value of 2×10^{-3} Ωcm for the film grown at 750 °C is at the upper range of resistivity reported for $LaNiO_3$ previously in the literature. It is plausible to assume that traces of the La_2NiO_4 phase remained in the film grown at 750 °C although it could not be detected by out-of-plane XRD scans. The presence of a second phase is not favourable for strong metallic behaviour of $LaNiO_3$ as defects increase the localisation effect and carriers freeze out at lower temperatures, as shown by the weak IMT in the $LaNiO_3$ film. It can be concluded that regardless of the strong RHEED intensity oscillations, indicating layer-by-layer growth, the $LaNiO_3$ physical properties are strongly dependent on the stoichiometry. Here are two possible explanations for the observed microstructures of the films: Oxidisation conditions during growth was not sufficiently high, therefore higher oxygen background is required to eliminate non-stoichiometry; Decomposition of the target had occurred either during the deposition or it was non-stoichiometric to start with, promoting the growth of the RP La_2NiO_4. Regardless, using a RP La_2NiO_4 target, nearly stoichiometric $LaNiO_3$ films were successfully deposited, owing to the non-equilibrium nature of PLD. This is supported by the EDX composition analysis showing the La:Ni ratio close to unity. A temperature of 750 °C was chosen for the growth of $LaNiO_3$ ultra-thin films to be used later in the superlattices containing $LaNiO_3$. The following chapter deals with the growth of 2.5 and 3 ML ultra-thin films of $LaNiO_3$.

Chapter 6

Ultra-thin $LaNiO_3$ on single terminated $SrTiO_3$

6.1 Introduction

The electronic and magnetic properties of oxide thin films such as RENiO3 alters drastically when changing the system from 3D (i.e. bulk) to 2D (i.e. thin film) [64, 230, 231]. Experimental studies have shown that ultra-thin films of $LaNiO_3$ show a thickness-dependent metal-insulator transition, below the critical thickness these ultra-thin films of $LaNiO_3$ exhibit strong localisation resulting in insulating behaviour [62, 218, 232]. It is essential before embedding a few u.c. of $LaNiO_3$ layers into superlattices to investigate the surface properties of these layers preferably with *in-situ* techniques. In order to fully explore the electronic properties of 2D perovskite systems it is critical that the surface reconstruction and octahedral tilting are fully understood; however, these two phenomena remain relatively unexplored.

In the previous chapter, thick ($\approx$ 40 nm) layers of $LaNiO_3$ were studied in order to investigate the sensitivity of the substrate temperature on the material structure. However, many heterostructure applications require ultra-thin ($<$ few nm) layers. An important prerequisite to the well-controlled growth of heterostructures is an atomically smooth and well-defined crystalline substrate i.e. a single terminated surface [115, 233], therefore the $SrTiO_3$ single crystal substrates used in this chapter were treated prior to growth.

This chapter consists of 2 main sections: optimisation of the $SrTiO_3$ substrate treatment; and the initial growth of $LaNiO_3$ on $SrTiO_3$ in sub-monolayer quantities. Characterisation of the surface properties of $LaNiO_3$ ultra-thin films is a vital step before fabrication of superlattices. Two samples were grown: one fully completed 2D growth (3

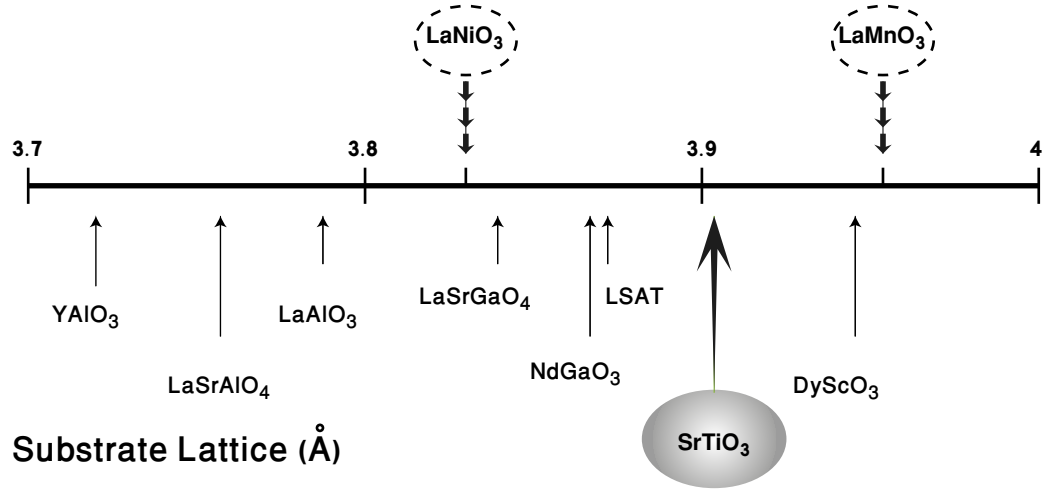

Figure 6.1: The relationship between pseudo cubic lattice parameters of $LaNiO_3$ and $LaMnO_3$ thin films and the $SrTiO_3$ substrate along with some typical substrates used in perovskite thin film growth.

monolayers); and the other interrupted at half coverage (2.5 monolayers). XPS has also been used to provide direct mapping of the core level and valence band electronic states.

6.2 Surface treatment of the $SrTiO_3$ substrate

Among complex oxides with the perovskite structure, $SrTiO_3$ is mostly used as a substrate material because it has the ideal perovskite structure with no octahedral tilts. $SrTiO_3$ (100) has a tolerance factor of ~0.86 with lattice contestant of 3.905 Å [70] and a thermal expansion coefficient $\alpha = 9 \times 10^{-6}$ K^{-1}. Considering the high growth temperature of complex oxides, $SrTiO_3$ is an appealing choice due to its high temperature chemical stability (melting point of 2080 C°). Another reason for the popularity of $SrTiO_3$ is the compatible lattice parameter to the pseudo-cubic lattice of perovskite oxides.

Figure 6.1 shows the relationship between pseudo-cubic lattice parameters of $LaNiO_3$ and $LaMnO_3$ and $SrTiO_3$ the substrate used in this work. Also shown in the figure are other popular substrates for perovskite thin film growth and their lattice parameters. $SrTiO_3$, like other perovskite materials with a crystal structure of ABO_3, is made of alternating planes of SrO (AO) and $SrTiO_2$ (BO_2) (figure 6.2). Depending on the surface energy, the termination planes of a single crystal $SrTiO_3$ substrate can consist of SrO layers, TiO_2 layers or a mixture of both. Regardless of the preferential

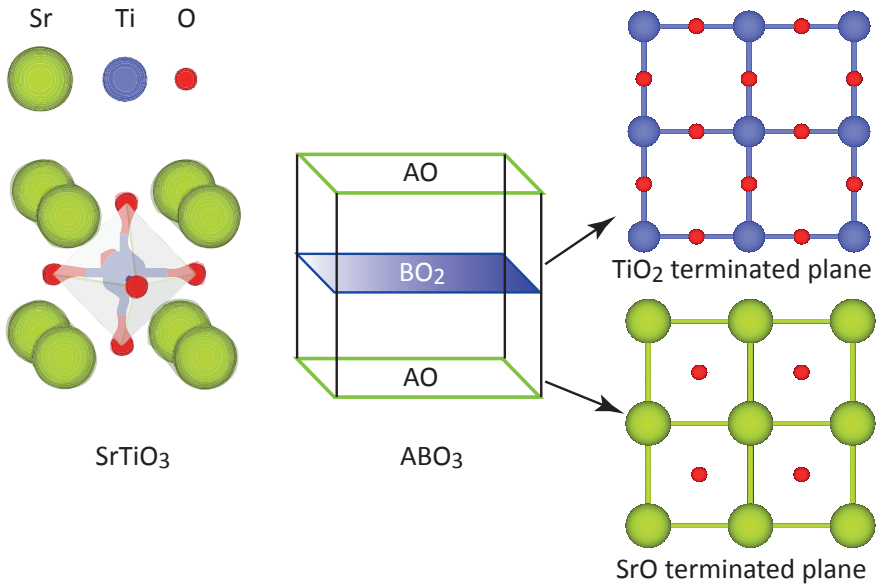

Figure 6.2: Schematic illustration of the $SrTiO_3$ with ABO_3 perovskite crystal structure. Two possible termination planes for $SrTiO_3$.

termination, when substrates are cut or cleaved an equal amount of both SrO and TiO_2 terminated domains are present with half a unit-cell separation step between them [233]. As-received substrates (before any treatment or cleaning) exhibit several kinds of surface defects and contamination as a result of the polishing and handling process.

The critical characteristics of the substrate surface which affect the properties of thin films fall into three categories. First and foremost is the necessity to have a clean and contamination-free surface (e.g. the carbon-base contaminations or H_2O) to start with. On the other hand, surface roughness also plays an important role in the fabrication of complex heterostructures and the average step height of the surface should not be higher than one unit-cell. Moreover, in heterostructure growth, the substrate acts as a template for stacking the subsequent layers and stabilises the crystal structure as a whole. Thus, a well-defined (i.e. single terminated) surface is a prerequisite for reproducible and highly crystalline epitaxial thin film growth. The final criterion is the requirement for a single, unmixed terminating layer. In case of mixed termination there are several possibilities for stacking sequence. Firstly, at the interface, the stacking sequence can be continued (e.g. SrO-TiO_2-AO-BO_2) or shifted by half a unit-cell as the two rock salt layers meet at the interface (e.g. TiO_2-SrO-AO-BO_2).

Surface treatment can not only improve the quality of the growth by minimising any surface electronic defects, but also it can alter the electronic properties of the

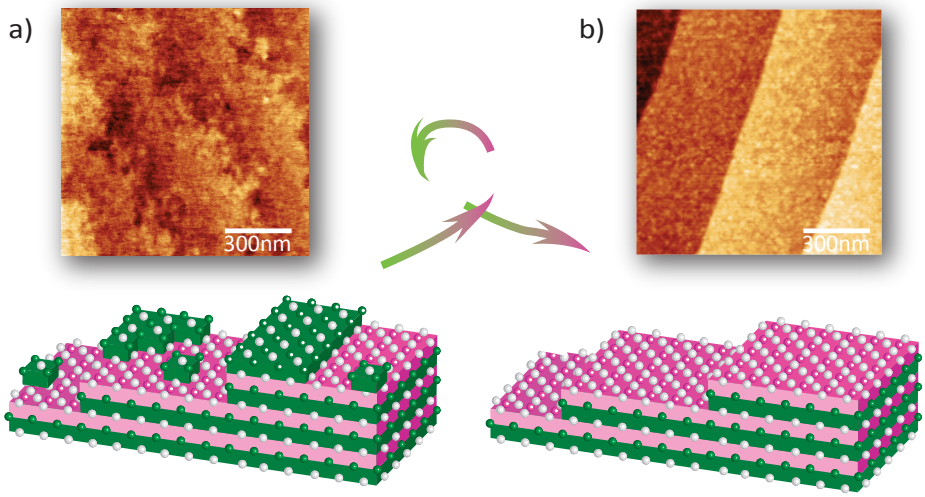

Figure 6.3: Schematic diagram and topography AFM images of the vicinal $SrTiO_3$ substrates a) as-received b) TiO_2 single-terminated after BHF-etching and annealing

interface. This is more enhanced at the interface between a polar and non-polar material. Note only a single-terminated surface can enforce one sequence of stacking, and also prevents various growth kinetics at different terminated domains. A schematic diagram accompanied with AFM images of the as-received and TiO_2 terminated $SrTiO_3$ single crystal substrate are shown in figure 6.3. The next section outlines the methodology for single terminated $SrTiO_3$.

6.2.1 Surface termination control

The effective surface treatments of $SrTiO_3$ have been found recently resulting in highly crystalline, well-defined and clean surfaces, and more importantly single-terminated surface. It was first suggested by Kawasaki *et al.* [115] that a chemical route to treat the $SrTiO_3$ (001) surface prior to thermal treatment would produce a suitable surface. This was regarded as a first step towards achieving fully single-terminated perovskite surfaces. An acidic NH_4F-buffered HF solution (BHF) with controlled pH value was used to etch the surface and obtain TiO_2 terminated $SrTiO_3$, which was then confirmed by ion scattering. However, due to the low pH value of the etchant ($\sim$4.5 pH), a high density of etch pits was reported which was presumed to occur when an underlying crystal defect or polishing damage existed on the surface [115]. Koster *et al.* have since refined the wet-etching method for achieving single-terminated (100) $SrTiO_3$ surfaces [233]. In this revised method, the difference in the reactivity between the top-most SrO and TiO_2

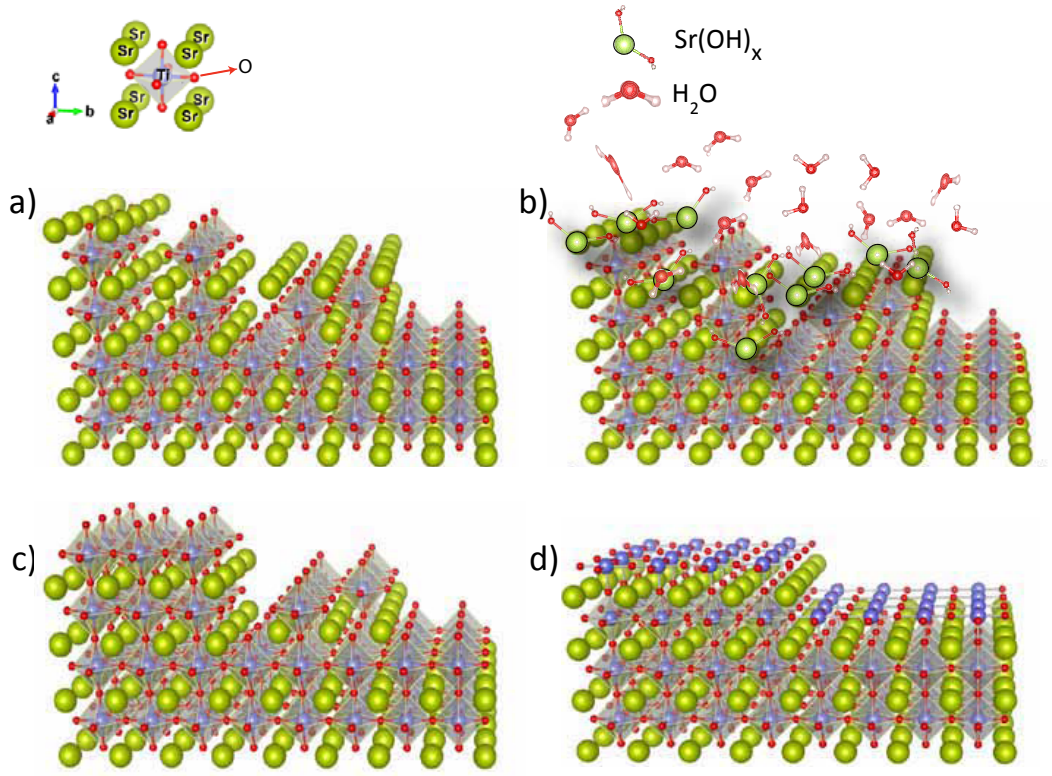

Figure 6.4: Schematic diagram of the preparation for the vicinal single terminated $SrTiO_3$ substrates (a) As received $SrTiO_3$ single crystal substrate (001). The surface shows mixed termination of SrO-layer and TiO_2-layer. (b) Substrate is dipped in deionised water for 10 minutes to allow formation of $Sr(OH)_x$. (c) $SrTiO_3$ (001) after etching by BHF for 30 seconds when strontium hydroxides were dissolved in BHF. (d) Large single terminated terraces have formed after annealing in air in a tube furnace.

layers with water was used for selective etching. In general SrO is known to react with H_2O and CO_2 at room temperature, by immersing $SrTiO_3$ in water, a SrO layer forms a strontium hydroxide complex known to be soluble in acid, unlike TiO_2 layers. In this way, the overall etching rate of SrO was increased significantly. This was followed by a short dip (30 s) in BHF to dissolve the strontium hydroxides. This dissimilarity in solubility in acid decreased the sensitivity of TiO_2-terminated surface treatment to the pH value of BHF and the etching time. Although the procedure to obtain single terminated $SrTiO_3$ is well established, the main obstacle remains to create a complete single termination. A new acid-free framework was recently suggested for 100% TiO_2 termination [234] by water leaching. Fully SrO terminated surfaces were usually achieved by deposition of one unit cell of SrO onto TiO_2 terminated surfaces, however, Bachelet *et al* reported

bulk diffusion of Sr at 1300 °C accompanied by long annealing times for the fully SrO terminated $SrTiO_3$ substrates [235].

The single termination recipe, which was followed in this thesis, consisted of following three steps: 1) first forming Sr-hydroxide by immersing the as-received substrates in deionised water for 10 minutes. $(Sr(OH)_x$ were formed on the surface as illustrated schematically in figure 6.4-b); 2) dissolving the $Sr(OH)_x$ by immersing the substrate in a NH_4F-buffered HF 7:1 solution (BHF) for 30 s (figure 6.4-c). The substrates were then instantly immersed in deionised water repeatedly to prevent the build-up of any residual acid on the surface; 3) the final step consisted of annealing the substrate at atmospheric pressure in a tube furnace for 1.5 hours at 1050 °C (with 10 °C min^{-1} ramping and cooling rates) to improve the surface crystallinity. The substrates were then placed in a round crucible and covered with a lid, both made of alumina, which then were inserted into a dedicated tube furnace to eliminate any contamination during annealing. After recrystallization, large single terminated terraces were formed (figure 6.4-d). The AFM images confirm the formation of large single terminated terraces (figure 6.3-b)). The annealing temperature was optimised for $SrTiO_3$ (001) substrates provided commercially by SurfaceNet GmbH. The following section outlines the results of ex-situ atomic force microscopy (operated in tapping mode) to confirm the surface morphology and chemistry after the treatment.

6.2.2 Surface morphology after substrate treatment

The surface of the as-received substrates consisted of two different step terraces of approximately 1 u.c. and 1/2 u.c. height (0.4 and 0.2 nm respectively), indicating a possible mixed SrO/TiO_2 termination on the surface. Annealing at temperatures higher than 800 °C improved the as-received substrate crystallinity due to the re-growth and re-crystallisation at step edges, although 100% single-termination required chemical treatment as explained above. As an example, two as-received substrates which had different miscut angles were annealed for two 90-min cycles at 950 °C then examined by AFM after each cycle. A combination of SrO and TiO_2 terraces were observed between steps after annealing which could not be removed by further annealing (second cycle). The width of these terraces varied according to the miscut angles of the substrate. Topography, line profile and phase images of the annealed substrates are shown in figure 6.5. Single-termination could not be achieved solely by thermal treatment and terraces of 1 u.c. height were regularly observed alongside half u.c. steps (figures 6.5-c and -h). In mixed terminated substrates, the phase images showed a contrast which can be attributed to chemical differences in the nature of the surface properties (figures 6.5-b and -e). It should be noted that the formation of different terminating layers

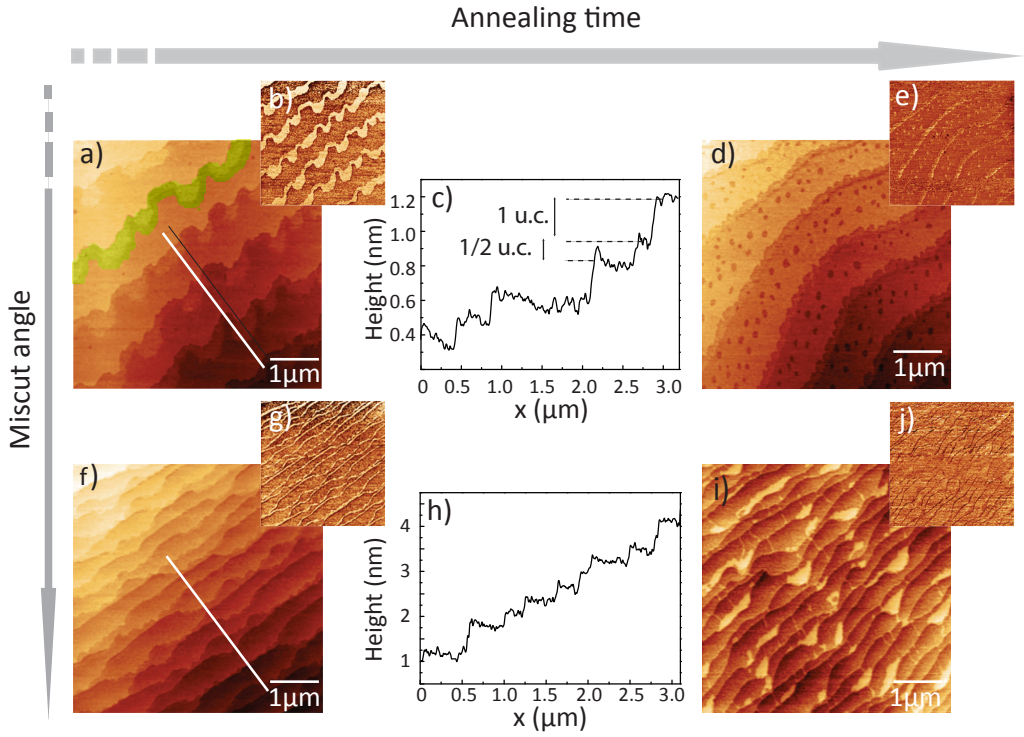

Figure 6.5: AFM micrographs of (a) low and (f) high miscut angle substrate after first cycle of 90 min annealing where (b) and (e) are the phase image, (c) and (h) are the line profile of (a) and (f) and (d) and (i) show the surface morphology after second cycle of 90 min annealing at 950 °C with the phase mode images (e) and (j).

at the surface of annealed $SrTiO_3$ has been reported in both reducing and oxidising environments [236, 237, 238] which could explain the observed phase contrast in this case [239]. In conclusion, comparing topography images in figure 6.5 implies that the surface morphology of the $SrTiO_3$ (100) single crystals depends strongly on the miscut angle and annealing time. While low miscut angles and short annealing time lead to step meandering, higher miscut angles and longer annealing time resulted in step bunching [240]. The effect of annealing temperature should also be considered when discussing the eventual surface morphology. While annealing at moderate temperatures promotes surface diffusion, annealing at higher temperatures results in the bulk diffusion of atoms resulting in a chemical composition alteration of the surface [235, 241].

Remarkable differences were found when the BHF-etched $SrTiO_3$ substrates were annealed in atmospheric pressure at temperatures between 900 to 1200 °C with ramping and cooling rates of about 10 °C min^{-1}. Tapping mode AFM was used to investigate the surface morphology as well as the chemical spatial distribution of different

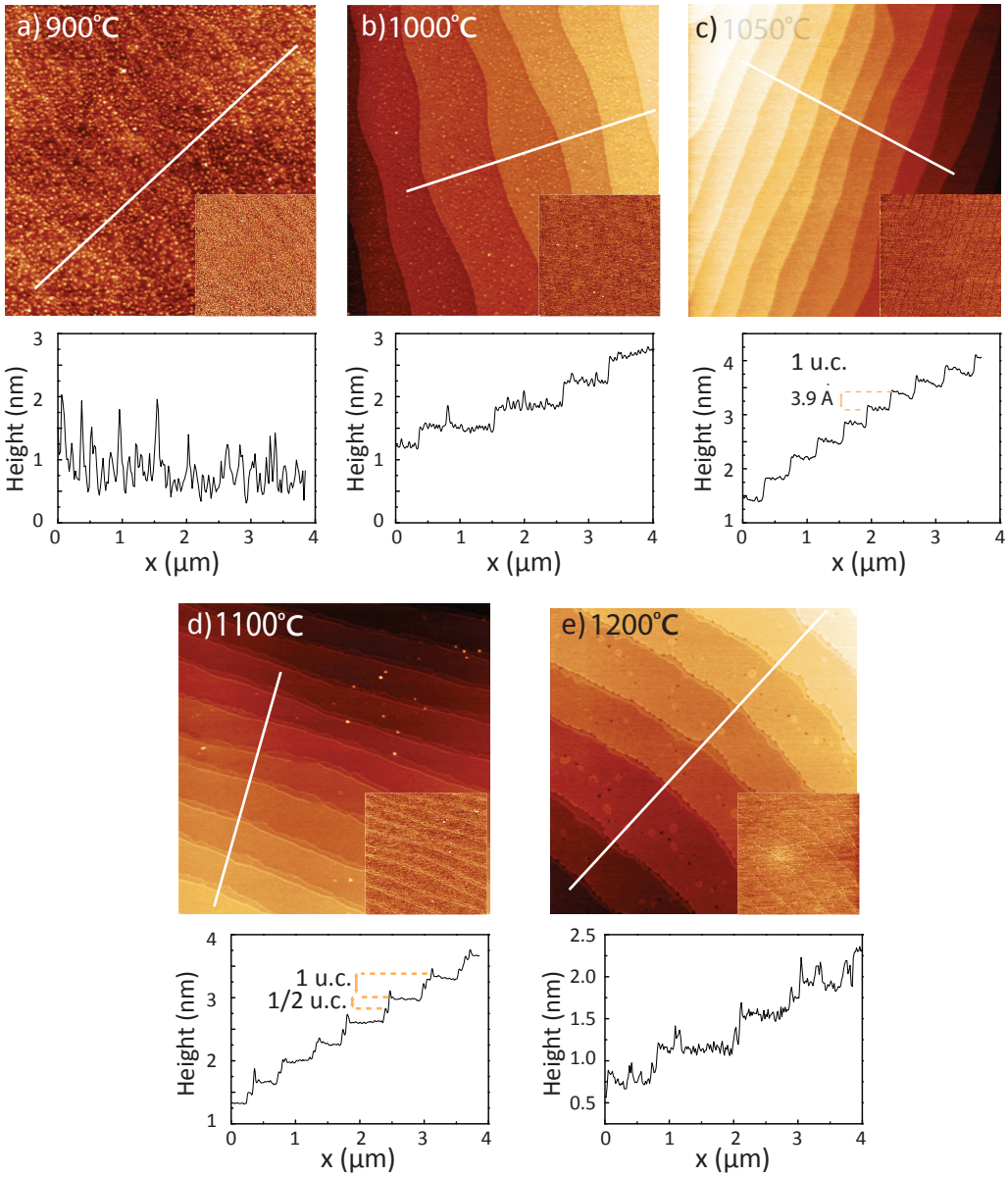

Figure 6.6: The morphological and chemical evolution of BHF-etched $SrTiO_3$ (001) surface with annealing temperature after 30 s BHF-etched substrates. AFM topography images show annealed substrates at (a) 900 °C, (b) 1000 °C, (c) 1050 °C, (d) 1100 °C and (e) 1200 °C for 90 min under air from left to right. The inset shows the phase mode image and line profile of each height image is shown underneath it. The full unit-cell height or half unit-cell height step terraces are shown in line profiles of sample 1050 °C and 1100 °C.

surface termination [242]. Panels a to e in figure 6.6 show the morphological and chemical evolution of BHF-etched $SrTiO_3$ (001) surface with annealing temperature. 30 s BHF-etched substrates taken from the same batch of commercially provided substrate were annealed at 900, 1000, 1050, 1100 and 1200 °C for 90 min under air and their surface morphology was subsequently examined by AFM (figure 6.6). Increasing the annealing temperature from 900 to 1050 °C improved crystallinity and created well-defined atomically flat surfaces. However, as the sample annealed at 1000 °C had a lower miscut angle, it makes the comparison between samples 1000 °C (figure 6.6-b) and 1050 °C (figures 6.6-c) difficult, as longer annealing time could have resulted in fully single termination. The miscut angles of substrates were different even though they were purchased under the same supposed miscut angle below 1 °. At higher annealing temperatures, above 1050 °C, a change in step and terrace nanostructure can be seen. There are no more straight edges and small round islands appeared on the surface. This could be due to Sr diffusion from the bulk resulting in SrO surface enrichment. Bachelet *et al.* observed a similar trend from TiO_2 to SrO termination by increasing the annealing duration [235]. The increased annealing temperature promoted progressive Sr depletion in two forms: 1) as arrays of fairly narrow terraces where regions of TiO_2 termination were separated by steps of half u.c. height of perovskite $SrTiO_3$ (SrO-layers); 2) surface Sr depletion on the terraces. This can be seen more clearly for the substrate annealed at 1200 °C showing round circles with different phase contrast, an indication of further Sr depletion at the surface (figures 6.6-e). The temperature of 1050 °C was found to give the highest quality surface and was used throughout this work. Figure 6.7-a shows straight, well-defined step edges of a fully treated substrate with the height line profile (figure 6.7-c) indicating the disappearance of half u.c. steps.

However, similar treatment of as-received substrates resulted in different surface morphologies. The surface morphology variations due to different miscut angle are exemplified in figures 6.7-b, -e and -f. As was explained earlier for annealed as-received substrates, a combination of miscut angle, duration and temperature of annealing defines the final surface structure [240]. This is also a known phenomenon for other materials [243]. The miscut angle affects the average distance (width of terraces) that atoms require to diffuse and reach the lower energy sites in a given time.

Another typical surface morphology observed for substrates with lower miscut angle were well rounded step edges. Rounded edges were formed, instead of straight lines aligned with low index directions, to minimise the surface energy by decreasing the length (figure 6.7-b). This type of morphology was accompanied with trapped rounded holes on the terraces which tended to move towards the edges over time or with further annealing finally merged with the terrace ledge [239]. The line profile of figure 6.7-b

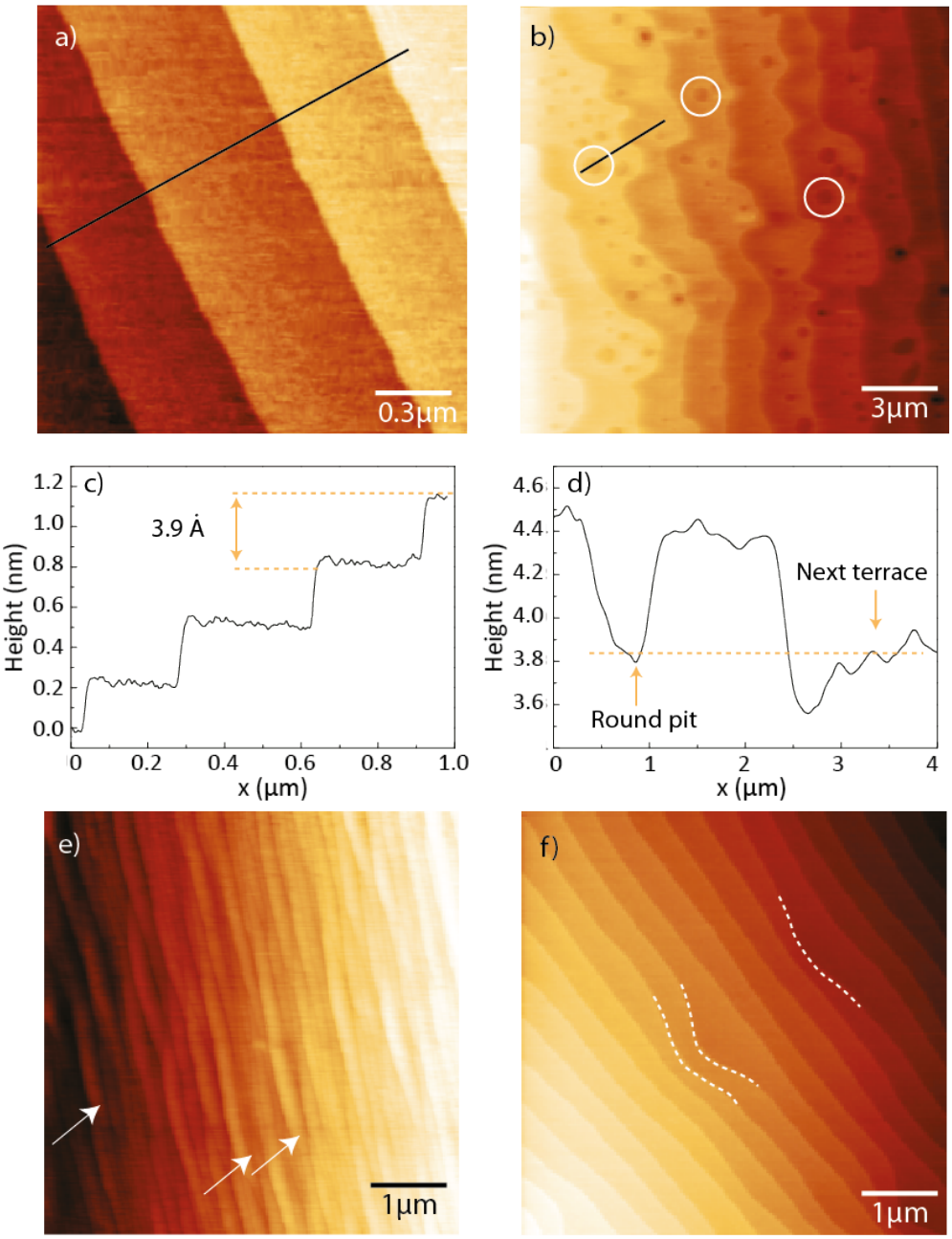

Figure 6.7: a), b), e) and f) AFM height micrograph images of TiO_2-terminated $SrTiO_3$ (001) surface with c) and d) line profiles of a) and b) respectively.

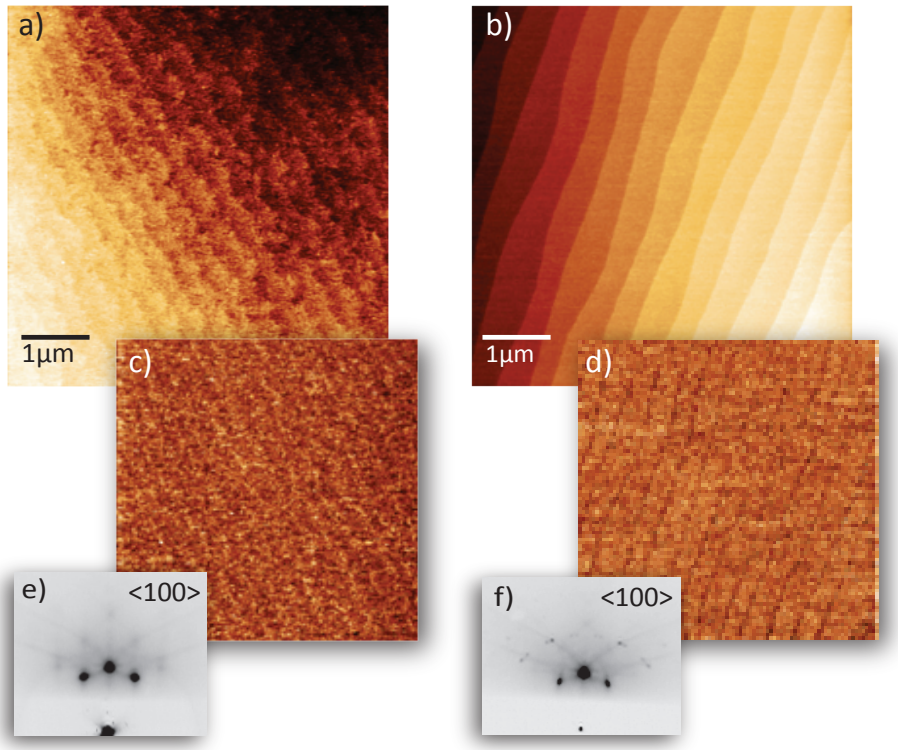

Figure 6.8: AFM micrographs of (a) as-received substrate vs. (b) vicinal single terminated $SrTiO_3$ with the corresponding AFM phase image (c) and (d), plus the <100> RHEED patterns (e) and (f) respectively.

confirms that the trapped circular hole has one u.c. height and did not form as a result of crystal defects. Step bunching is indicated by white arrows for the higher miscut angle substrate in figure 6.7-e, while round holes are encircled on the low miscut angle substrate topography image in figure 6.7-b. The curves marked by the dashed-line on figure 6.7-f should not be mistaken with step bunching and they were routinely seen when underlying crystal defects changed the local isotopy of the surface.

Surface morphologies of an as-received substrate versus fully treated substrate are depicted in figures 6.8-a and -b with the corresponding AFM phase images (c) and (d), in addition to the <100> RHEED patterns (e) and (f) respectively. By comparing an as-received substrate (figure 6.8-a) with a BHF treated one (figure 6.8-b), it is clear that not only did the terraces expand, but also there is no phase contrast arising from different terminations, i.e., the surface is terminated by a single elemental layer. The minimal contrast of the step edges in the phase image and steps with clear 1 u.c. height in the height image indicate, again, a single terminating layer. Finally, it can be concluded

that after 30 s BHF-etching and annealing at the optimised temperature of 1050 °C, the substrate surface was TiO_2 single terminated with high crystallinity showing sharp RHEED diffraction spots indicating a decrease in surface disorder as a result of surface ripening (e.g. lowering defects) by annealing. It was also shown that the substrates with the lower miscut angles require longer annealing time because they have greater distance between stable sites e.g. step edges. The treated substrates were used to grow ultra-thin films of $LaNiO_3$ which is explained below.

6.3 Ultra-thin $LaNiO_3$

$LaNiO_3$ ultra-thin films were grown in a PLD chamber equipped with RHEED, as previously outlined in section 3.2. The sample was loaded into the load-lock chamber and the sequence for RHEED imaging was as explained in section 5.3. RHEED patterns of the substrate did not show any distinctive difference before and after heating (before the deposition) so there was no indication of surface reconstruction at the $SrTiO_3$ (001) $TiO_2$2 terminated surface. As with the thicker layers, the RHEED specular spot was monitored in order to follow the growth at a sub-unit-cell level. After the deposition, the heater was switched off and the chamber filled with 150 mbar oxygen. The deposition conditions for these samples are given in table 6.1.

Table 6.1: Deposition parameters used for growth of ultra-thin $LaNiO_3$ films

Deposition parameters:	Typical values
Compounds	$LaNiO_3$
Background gas	O_2
Background gas pressure (mbar)	0.01
Substrate temperature (°C)	750
Spot size (mm^2)	2.16
Shape of spot	rectangular
Target type	sintered pellet
laser fluence (J/cm^2)	1.5

Figure 6.9 shows the RHEED measurements and these are seen to exhibit strong oscillations. Deposition was started at approximately 3 s (as indicated by the black arrow in figure 6.9) and it was ended for the 3 monolayer film at the purple arrow (labelled 3 ML). For the 2.5 monolayer sample deposition was stopped where there is a RHEED minimum (labelled 2.5 ML). When the growth progressed, by layer-by-layer like growth mode, the RHEED intensity maximum is considered as full coverage of one unit cell. This maximum in intensity occurs owing to the fact that complete layer coverage represents a minimum in the step density and so minimises off-specular scattering. The RHEED

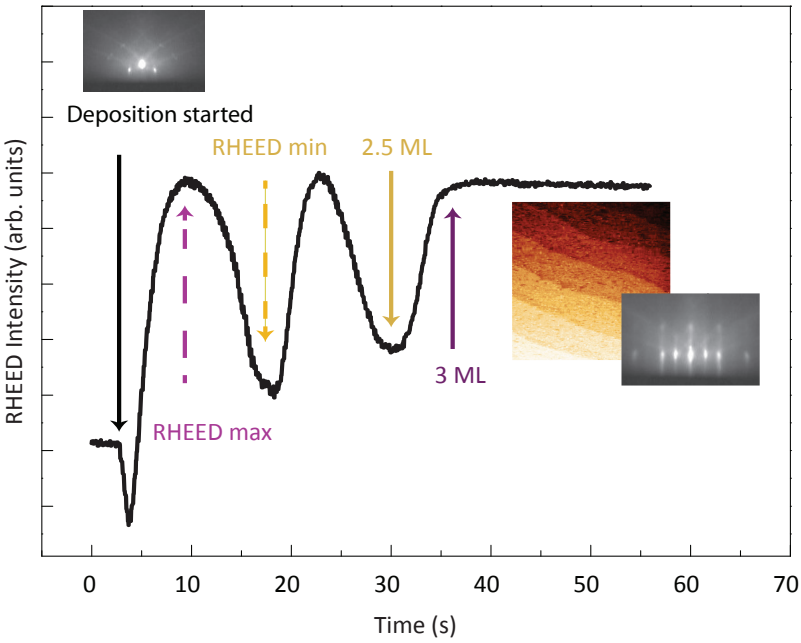

Figure 6.9: RHEED intensity oscillations of heteroepitaxial $LaNiO_3$ growth. The start and stop time of deposition is indicated for 3 ML and 2.5 ML $LaNiO_3$ ultra-thin films. Since the deposition rates were different for each sample, the arrow in this figure is not the time exactly the deposition was stopped for 2.5 ML film.

minimum is then referred to as having the highest atomic roughness at the surface which occurs at half coverage.

6.3.1 Surface analysis

After cooling, RHEED images were taken along the high symmetry $\langle 100 \rangle$ and $\langle 110 \rangle$ directions as presented in figure 6.11. There are no fractional streaks present at the diffraction pattern and the films are fully strained to the substrate, as the measured in-plane lattice parameter matches that of the $SrTiO_3$ substrate. In figure 6.12, RHEED patterns taken along $\langle 100 \rangle$ of the 2.5 ML and 3 ML films are shown and the position of spots are presented schematically and labelled with spacing values given in table 6.2. The values of in-plane lattice spacing are both similar to that of the $SrTiO_3$ showing the films are fully strained. The value names number 4 in figure 6.11-d) can give information on out of plane lattice parameter, however, a more accurate determination would be through XRD measurements which is not achievable due to the ultra-thin layer of the

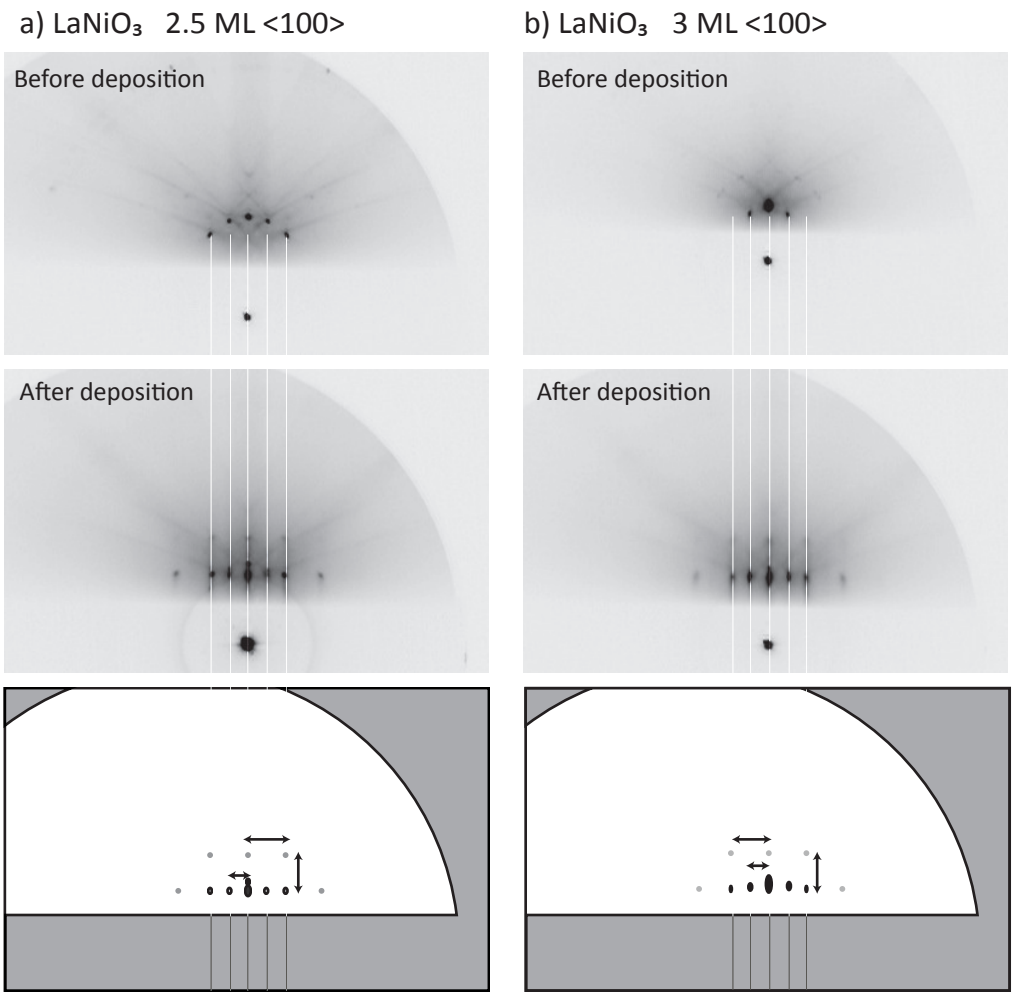

Figure 6.10: RHEED pattern observed before and after the growth of the 2.5 and 3 ML $LaNiO_3$ ultra-thin films on $SrTiO_3$ (001) substrate. The electron beam was oriented along the $SrTiO_3$ $\langle 100 \rangle$ direction. The schematics, presented underneath the RHEED patterns, highlight the streak separations that have *d*-spacing corresponding to the lattice planes of $LaNiO_3$. The solid lines passing through 3 figures of each sample are position of primary observed integer streaks of $SrTiO_3$ showing that the films and substrate are matched in-plane. Extra spots are shown in the schematics when appropriate.

film. It can be seen from figure 6.12 that when comparing the films to the bare substrate, there are two phenomena occurring: 1) a broadening of the streaks and 2) additional spots are observed which are more intense in the half coverage film (2.5 ML), suggesting the presence of 3D-like microstructures at the surface. Kikuchi lines are still present and provide evidence for low surface roughness and high crystal quality. Each RHEED pattern has been analysed and the streak or spot spacing calculated from the line profiles, the pixel separation between features were converted to reciprocal spacing with the same methodology as stated earlier.

The presence of weak transmission spots, indicate the formation of 3D-like islands on the surface. These spots are located at the corners of a square type pattern with the spacing value twice that of the substrate. The extracted values from the RHEED patterns are given in table 6.2 and they can be related to (002) planes of $LaNiO_3$. Considering the structure factor of the perovskite structure, the diffracted intensity from the (002) planes is greater than from the (001) planes and that is why they are not present (or are very weak) in the pattern.

To corroborate the results obtained from RHEED, *ex-situ* AFM imaging of the surface of the full 3 ML and the interrupted half coverage (2.5 ML) samples are shown and have been interpreted by calculating the layer equivalent thickness for the deposition. Large area scan size of 3 μm $\times$ 3 μm are presented for the 2.5 and 3 ML samples in figure 6.12-(a) and -(b) and higher resolution. A plane flattening option cannot be used for processing these films due to the step-terrace structure as it would introduce an artificial tilt. It is common to apply a 3 point flattening which allows illustration of step-terraces with step heights of one unit cell. The 2.5 ML film has pronounced 3D-like islands and figure 6.12-(g) and -h show line profiles of typical 3D microstructures observed on this surface. It is possible that, for the 3 ML film, the deposition was stopped just after completion of one full monolayer and the small islands are then the initial growth of the fourth layer. Such a distinctive transition occurring within only half a monolayer of growth is not easily explainable. If the nature of growth was layer-by-layer as the (strong oscillations in the RHEED intensity of the specular spot suggests) from 2.5 ML to 3 ML, only one u.c. height islands should have been observed. But they are irregularly shaped with 1 to 1.5 nm height variation and basal diameters of 20 to 80 nm. The heights of islands are equivalent of $\sim$ 3 to 4 perovskite u.c.. The 3 ML sample shows smoother morphology with smaller islands with the same height range but basal diameters of 10 to 40 nm. Line profiles across two typical islands for each film are shown in the bottom panel of figure 6.12 and they correspond to the white line marked on the labelled microstructure image above them. From the height topography AFM images, the total island volume can be deduced and used to calculate the volume of the deposited monolayer if the

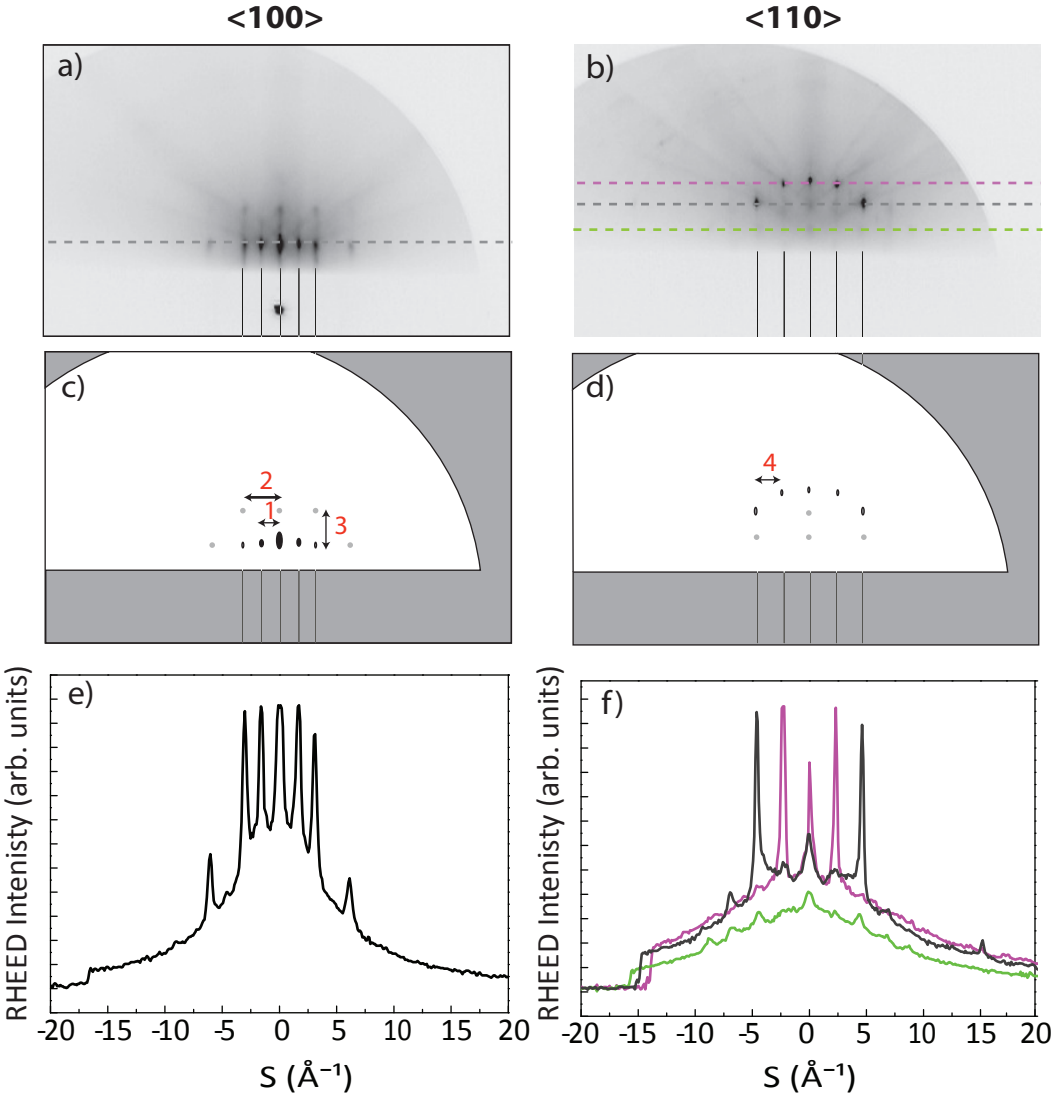

Figure 6.11: RHEED pattern observed during the growth of a 3 ML $LaNiO_3$ ultra-thin film on $SrTiO_3$ (001). The electron beam was oriented along a) the $SrTiO_3$ $\langle 100 \rangle$ and b) $\langle 110 \rangle$ directions. The schematics c) and d) highlighting the streak separations which have the corresponding *d* spacing of planes of $LaNiO_3$. Solid black lines show the primary spacing. For clarity the streak spacings have been numbered and corresponding lattice spacings are given in table 6.2. The values of separations were determined from the peak separations in the line profiles of the RHEED patterns (panels e and f). Panel f shows 3 different line profiles highlighted in panel b crossing 3 various zones to show there is no evidence of fractional streaks relating to the surface reconstruction.

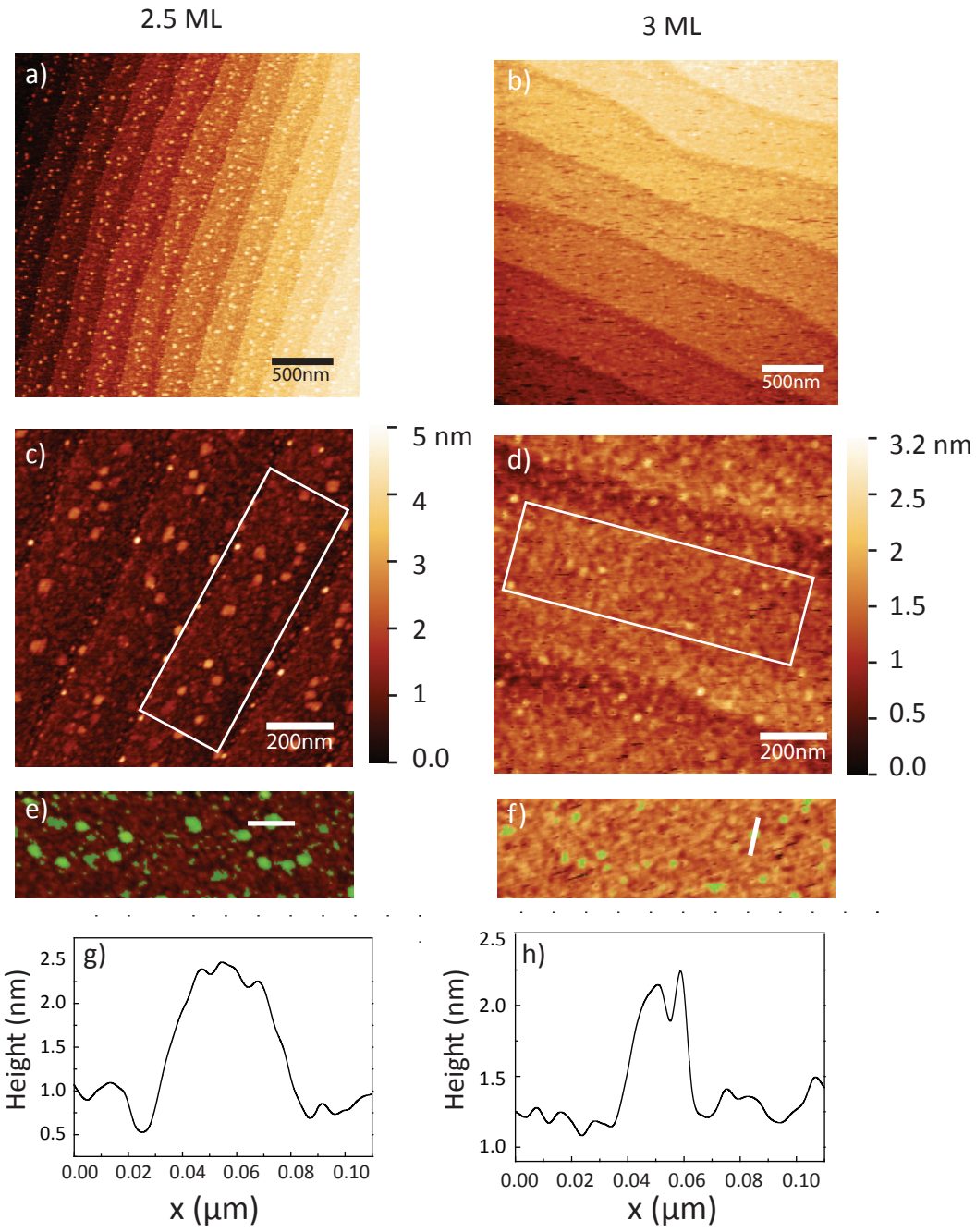

Figure 6.12: Surface morphology of $LaNiO_3$ a) 2.5 ML b) 3 ML ultra-thin films. c) and d) are 1 μm $\times$ 1 μm zoomed in scans and island volumes were extracted from the area shown by white rectangle. g) and h) show line profiles for typical large islands. The island volume was measured by grain statistic and the green areas are the grains, the volumes of which were calculated.

Table 6.2: RHEED streaks spacing calculated for 2.5 and 3 ML $LaNiO_3$ ultra-thin films

Feature spacing label	Electron beam Orientation	Real space separation (Å)
$SrTiO_3$ $d_{(100)}$	100	3.905(1)
$SrTiO_3$ $d_{(110)}$	110	5.522(1)
Figure 6.11(1)-$LaNiO_3$ $d_{(100)}$	100	4.1(2)
Figure 6.11(2)-$LaNiO_3$ $d_{(200)}$	100	2.06(7)
Figure 6.11(3)-$LaNiO_3$ $d_{(002)}$	100	2.08(7)
Figure 6.11(4)-$LaNiO_3$ $d_{(110)}$	110	5.52(2)

growth was performed in a layer-by-layer manner. This is called the 'layer equivalent thickness'. The volumes were obtained using Gwyddion with the built-in grain statistics [147]. One monolayer was considered as a perovskite structure with c-parameter of 0.3846(1) nm. The layer equivalent thickness of the islands on the 2.5 ML surface was found to be (0.48 $\pm$ 0.05 ML) while on the 3 ML surface was (0.09 $\pm$ 0.02 ML) which can be due to stopping the deposition just after one monolayer. This confirms that no surface re-evaporation occurred during the deposition and RHEED can be used reliably to control the number of deposited layers inclusion in heterostructures. To understand the origin of the drastic changes in the nature of the growth by changing only half a monolayer coverage, it should be noted that there are several factors in PLD that requires extra care such as mounting the substrate using the silver paint. The silver paint consists of fine flake silver suspended in methyl isobutyl-ketone. Due to solvent evaporation the consistency of the silver paint gradually changes. By adding solvent, the desired consistency can be achieved; however, it is unlikely to be exactly the same as at the start. The thermal conduction through the silver paint also relies on the method of painting i.e., any trapped air or inhomogeneous dispersion of the paint results in reducing the thermal conductivity. Moreover, to explain the change in the period of oscillations (number of pulses per each layer); it should be considered that the RHEED oscillations are produced by monitoring a small area of the sample depending where the beam is focused on. This adds another uncertainty in which part of the thin film is being monitored. Above all, where the substrate is placed regarding the PLD plume can alter the amount of material deposited. In the next chapter, the deposition rate will be calibrated for each sample at the beginning of the deposition.

It can be summarised that the deposition condition lead to the coherent growth of $LaNiO_3$ ultra-thin films. There was no observation of fractional streaks which is an indication to oxygen octahedral tilt. This can be attributed to the ultra-thin nature of the films. Since $SrTiO_3$ exhibits no octahedral tilt with symmetry group $pm\bar{3}m$ and Glazor $a^0a^0a^0$, the anti-phase tilting of $LaNiO_3$ (Glazor $a^-a^-a^-$) requires a critical thickness

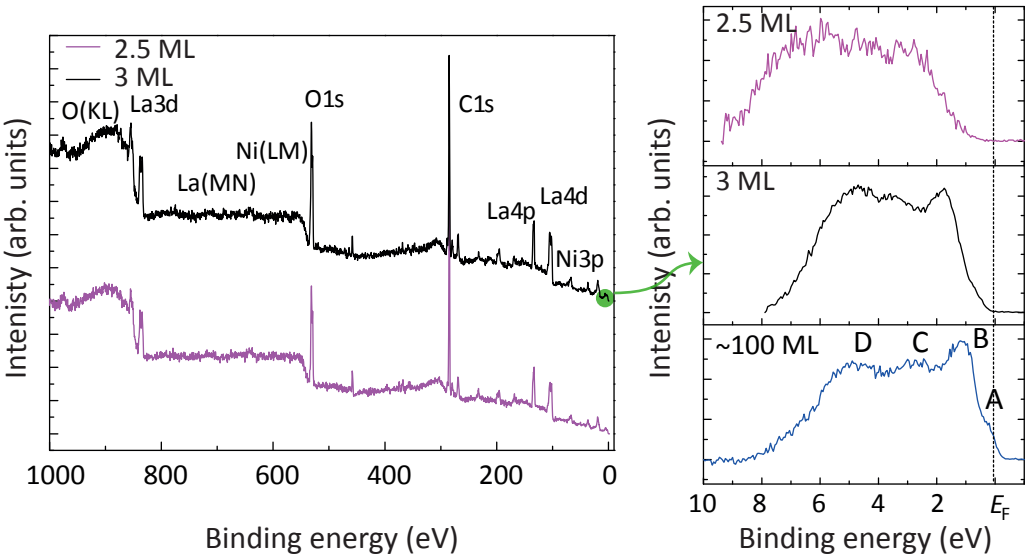

Figure 6.13: XPS spectrum of (left) survey wide-scan of $LaNiO_3$ film deposited of 2.5, 3 ML and (right) valence band spectra for films deposited 2.5, 3 and 100 ML

to overcome the no-tilt condition induced by the substrate.

6.3.2 XPS studies

Previous studies have revealed the evolution from a metallic to localised insulating character as a function of film thickness [62]. This phenomenon was observed from 3 ML to 2 ML thick $LaNiO_3$ films. Here XPS was performed in order to study the region between 2 and 3 ML and gain a better understanding of the origin of the localisation in correlated $LaNiO_3$. Figure 6.13 shows the long range XPS scan for 2.5 and 3 ML $LaNiO_3$. The valence band region is shown in the right hand-side panel of figure 6.13. As a reference a thick sample of $LaNiO_3$ grown at the same deposition condition is presented. Valence band spectra features are labelled in figure 6.13-100 ML for the thick film grown at 750 °C. Two features, A and B, near the E_F are assigned to e_g and t_{2g} states of Ni *3d*, respectively. The next two features, named C and D, are associated with O *2p* dominant states [224]. Note that the valence band spectra shown in figure 6.13 are normalised to feature D. It is clear that the metallic behaviour of $LaNiO_3$ has been affected by the thickness reduction. For the 2.5 ML a band gap has opened and the valence band no longer crosses the Fermi level. The 3 ML sample reveals similar features to the thick $LaNiO_3$ but there are no longer any enhanced intensity features and a shift in the valence band structure is also visible. This indicates that the metallicity of $LaNiO_3$

is related to the thickness and below the critical thickness is insulating. Therefore, if any enhanced conductivity is observed in the superlattices containing $LaNiO_3$ layers below the critical thickness, it must arise from interface effects.

6.4 Summary

Ultra-thin films of $LaNiO_3$ were grown on $SrTiO_3$ terminated substrates. The process of the termination control was optimised to be 30 s BHF etching and 90 minutes annealing at 1050 °C. The effect of termination on the growth quality was clear and layer-by-layer growth with strong RHEED oscillations for 3 ML of $LaNiO_3$ was observed. RHEED patterns obtained from the films suggested that the films were grown coherently on the substrate and fully strained. A soft band gap was opened due to the low dimensionality nature of the growth and enhancement of weak localisations in $LaNiO_3$. The growth of $LaNiO_3$ is optimised as judged by RHEED intensity oscillations and surface morphology of ultra-thin $LaNiO_3$. A layer-by-layer growth mode was observed which is a prerequisite to the synthesis of artificial lattices containing $LaNiO_3$ as will be explained in the next chapter. The integer streak spacings seen in the RHEED, were the same as those of the substrate, showing the film and the substrate are matched in-plane. One u.c. height step-terrace structure of the surface implies that, the growth was in a layer-by-layer fashion. No fractional streaks were observed indicative of the oxygen octahedral tilt or surface reconstruction. It can be suggested that the substrate cubic symmetry is imposed on the film due to the ultra-thin nature of the films. Since $SrTiO_3$ exhibits no octahedral tilt with symmetry group $pm\overline{3}m$ and Glazor $a^0a^0a^0$, the anti-phase tilting of $LaNiO_3$ ($a^-a^-a^-$) requires a critical thickness to overcome the no-tilt condition induced by the substrate. The calculated layer equivalent thickness confirmed that no surface re-evaporation occurred during the deposition and RHEED can be used reliably to control the number of deposited layers of $LaNiO_3$ for inclusion on heterostructures. On the basis of these results, the successful growth of ultrathin $LaNiO_3$ layers has been shown and indicates that they are suitable for use in superlattices. In addition, the growth of ultra-thin films has been studied in order to investigate their suitability for inclusion into heterostructures.

Chapter 7

Superlattice growth of lanthanum-based perovskites ($LaMO_3$ when M=Ni or Mn)

Oxide heterostructures are of great interest as they exhibit a variety of novel properties at the interfaces which are not present in either of the bulk phases of the constituent materials [244]. Recent advances in the fabrication of epitaxial metal-oxide heterostructures have opened new avenues for controlled investigation of the phase dependent behaviour of correlated electron metal oxides [245]. In contrast to perovskite heterostructures of titanates or cuperates, nickelate thin films remain comparably less explored, despite the fact that they have been considered promising as platform for interface studies. $LaNiO_3$ shows paramagnetic metallic behaviour in the bulk at all temperatures, unlike the rest of the rare earth nickelate family which show an antiferromagnetic metal-insulator transition at low temperature [60, 246]. Recent experimental studies have shown unpredicted magnetic behaviour in $LaNiO_3$ heterostructures such as exchange bias in heterostructures of ferromagnetic $LaMnO_3$ and $LaNiO_3$ on (111)-oriented $SrTiO_3$ suggesting an antiferromagnetic or spin glass like behaviour in the $LaNiO_3$ layer [66]. By using first-principles density functional theory calculations, it has been suggested that control of the m/n ratio in $(LaMnO_3)_m/(LaNiO_3)_n$ superlattices with (001) orientation can determine the charge transfer and hence magnetic properties [34]. It was also proposed that 2 monolayers of $LaMnO_3$ separated by one monolayer of $LaNiO_3$ would carry a magnetic moment as high as 8 μ_B [34].

This chapter explains the methodology of growth and preparation of the La_2NiMnO_6 compound by creating superlattices of $LaNiO_3$ and $LaMnO_3$; deposition of each constituent ($LaNiO_3$ and $LaMnO_3$) has been optimised for growth as judged by RHEED

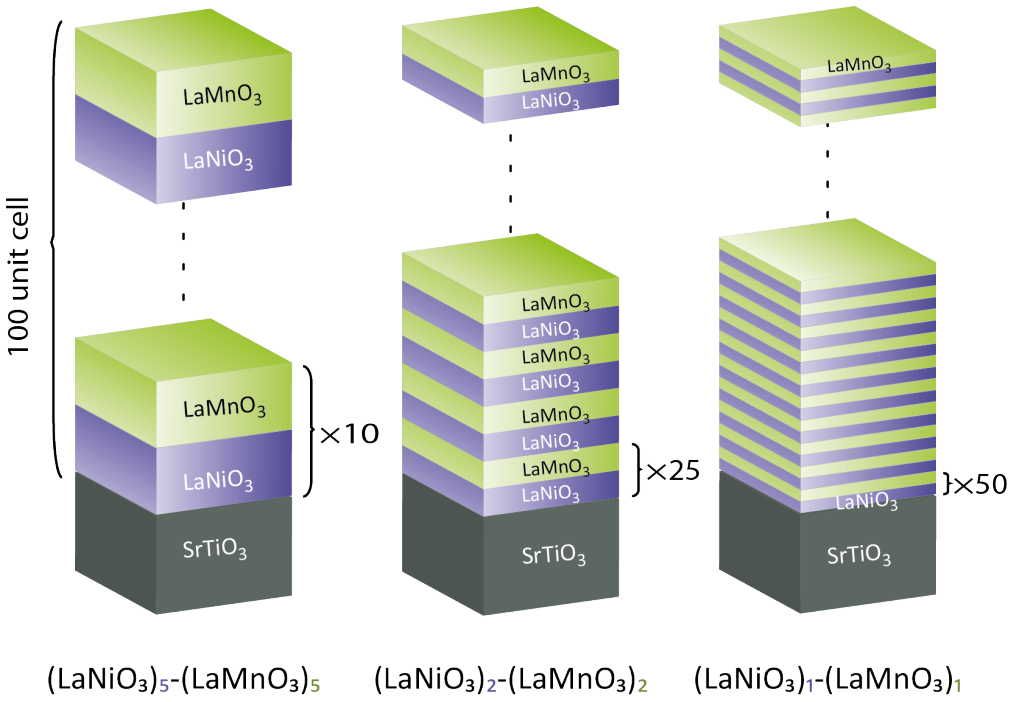

Figure 7.1: Schematic arrangement of artificially layered ($LaNiO_n$-$LaMnO_n)_m$ lattices that were produced during this thesis.

intensity oscillations in the previous chapters. Each oscillation then corresponds to the completion of a u.c. layer and the growth rate of that layer can be calculated from the number of pulses. It will be shown here that a strong RHEED intensity oscillations as an indication of a good growth does not always lead to the best structure due to post-growth effects.

7.1 Superlattices of $(LaNiO_3)_m$-$(LaMnO_3)_m$

All superlattices were deposited by PLD at 750 °C in an oxygen pressure of 0.01 mbar, with a laser fluence of 2 J/cm^2 at 5 Hz. $SrTiO_3$ (001) single crystal substrates were chemically treated to achieve TiO_2-termination using the method of Koster *et al.* [240] (see section 6.2.1 for details). Polycrystalline targets of $LaMnO_3$ and $LaNiO_3$ were pre-ablated prior to deposition to remove any surface contamination. The growth procedure was as stated in chapter 3.2. After completion of the deposition, oxygen pressure was increased to 150 mbar, whilst the temperature of the sample was held at the growth temperature. The sample was then cooled to room temperature in this oxygen environment by switching off the heater power supply. After cooling, RHEED

patterns of the films were taken along the $\langle 100 \rangle$ and $\langle 110 \rangle$ in-plane directions.

AFM was then used to examine the surface topography. Selected films were also prepared by conventional TEM sample preparation (see section 3.3.2.1) along two crystallographic orientations. TEM specimens were additionally cleaned with low pressure oxygen plasma. The JEM-ARM200F STEM microscope with Cs correction was used for imaging with atom-by-atom resolution. In addition, chemical mapping of the superlattices was performed by electron energy-loss spectroscopy (EELS). The microscope was operated with an acceleration voltage of 200 or 80 kV to record the high-angle annular dark field (HAADF) imaging as well as performing chemical mapping.

7.1.1 Growth control

Epitaxial $(n/m)_x$ superlattices consisting n u.c. of $LaNiO_3$ and m u.c. of $LaMnO_3$ were deposited on $SrTiO_3$ (001). The stacking periodicity was repeated to grow a 100 u.c. thick ($\sim$ 400 Å) superlattice. This configuration is depicted in figure 7.1 for the 3 superlattices of $(5/5)_{10}$, $(2/2)_{25}$ and $(1/1)_{50}$. Figure 7.2 shows the recorded RHEED intensity from the specular reflection in 'one-beam' condition of each constituent layer -a) $LaNiO_3$ $\sim$100 u.c. and -b) $LaNiO_3$ $\sim$100 unit cell. The mean number of pulses required for monolayer growth of $LaNiO_3$ and $LaMnO_3$ layers was 32$\pm$1 and 37$\pm$2, respectively, however, prior to each deposition of a superlattice, the exact number of pulses was measured by RHEED, as follows.

Figure 7.3 shows the RHEED intensity oscillations for the $(5/5)_{10}$ superlattice. As the RHEED intensity oscillations damp over time, the number of pulses to grow each individual layer was determined using the mean value for the pulses measured from the first few oscillations (figure 7.3-a). These numbers then were used for subsequent layers of each material in the superlattice (7.3-b). As can be seen from figure 7.3-a, during the initial growth of $LaNiO_3$, the period of oscillations was not equal. Especially, the number of pulses from the first oscillation was small compared to the average number of pulses expected for completion of one u.c. layer of $LaNiO_3$ ($\sim$32). The number of pulses for the first oscillation was 17 pulses, almost half of what was expected. This effect was found to be dependent on the deposition temperature and was more pronounced at high temperatures on mixed terminated substrates. The origin of this change in RHEED intensity is unknown at the moment, but it may be attributed to the termination conversion or a RHEED diffraction phase shift which is more probable as the phase of the diffraction condition is not easy to be determined in one-beam diffraction condition. A self-organised conversion of the atomic layer termination from RuO_2 to SrO was reported by Rijinders *et al.* in ferromagnetic $SrRuO_3$ on TiO_2-terminated $SrTiO_3$ [247].

Regardless of the nature of this variation in the period of RHEED oscillations,

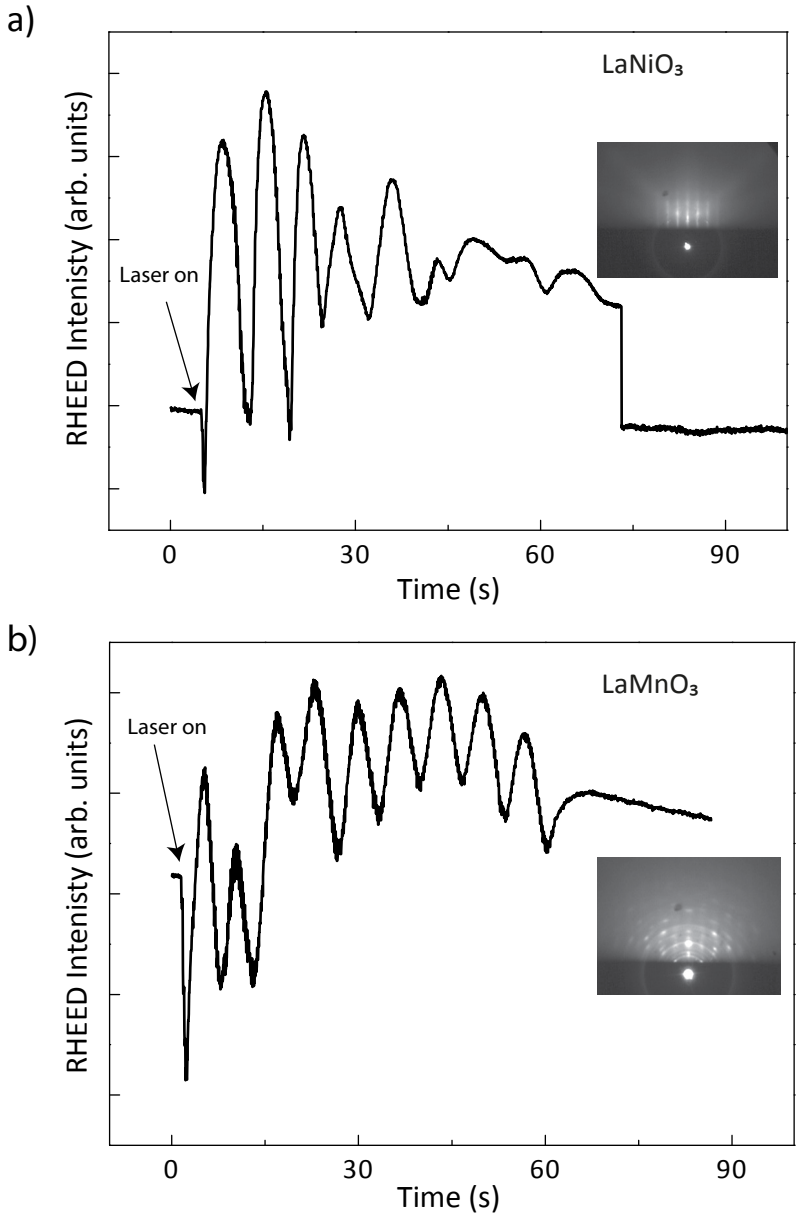

Figure 7.2: RHEED specular beam intensity oscillations for each individual layer of the superlattices a) $LaNiO_3$, b) $LaMnO_3$. The growth was optimised to achieve layer-by-layer growth of each layer for atomic control of artificial layers. It should be noted that the damping in oscillations occurs due to surface roughening which also decreases the intensity. The insets are RHEED images taken from the films at room temperature along the $\langle 100 \rangle$.

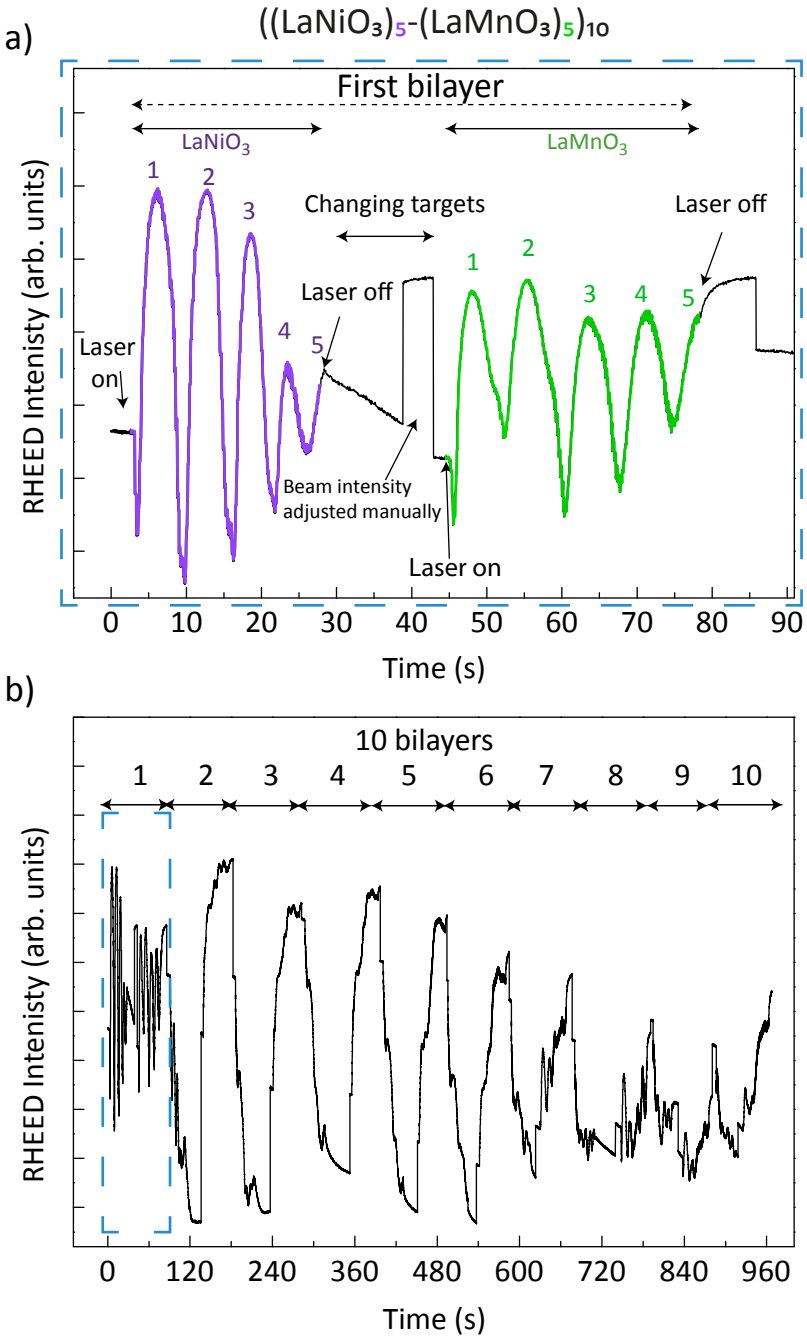

Figure 7.3: The growth was optimised to achieve layer-by-layer growth of each layer for atomic control of artificial layers. a) First 5 monolayers b) full deposition

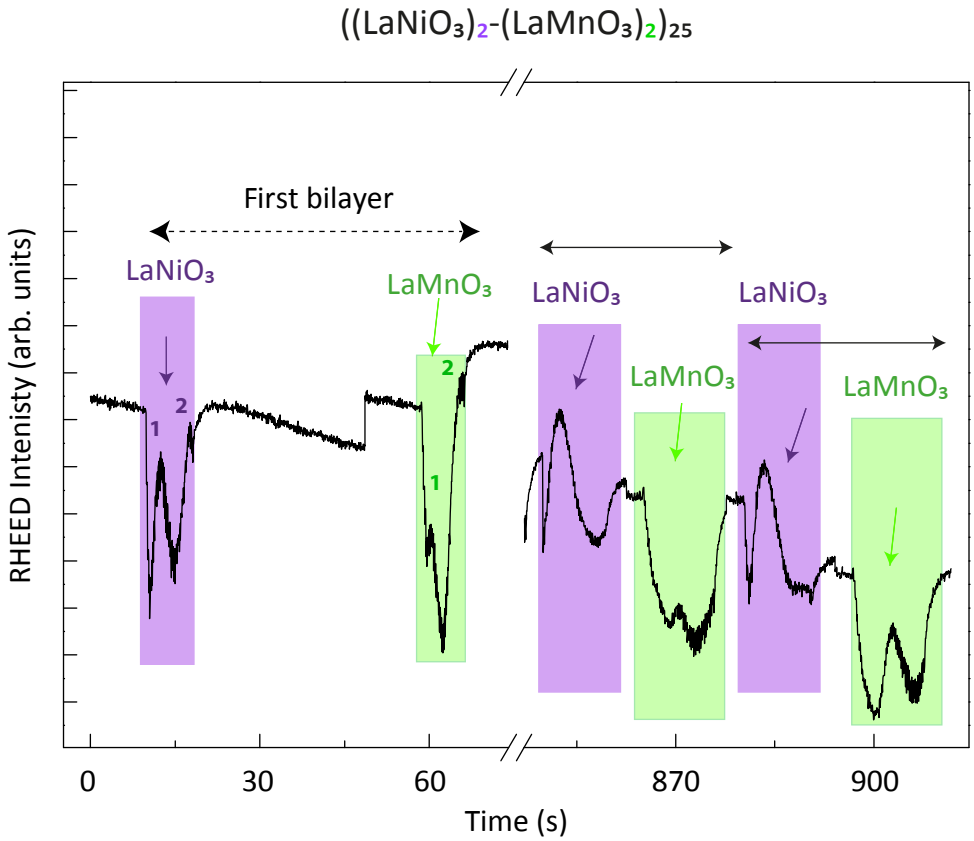

Figure 7.4: RHEED oscillations for the $(2/2)_{25}$ superlattice where the period of second oscillation was used for subsequent layers of each material. After 800 s the oscillations were still strong and corresponded to deposition of 2 monolayer of each material.

clearly it cannot be used as a calibration for the number of pulses required for deposition of 1 u.c. layer and a different approach was used to deposit the $(1/1)_{50}$ superlattice. For the $(5/5)_{10}$ superlattice, where the RHEED period was averaged over 4 cycles after disregarding the first oscillation in each layer as is shown in figure 7.3-a). For the $(2/2)_{25}$ superlattice, the period of the second oscillation was used for subsequent layers of each material as also is depicted in figure 7.4-a). For the $(1/1)_{50}$, the growth control methodology was adjusted and is depicted in figure 7.5. Panel (a) shows, the initial 3 u.c. of $LaNiO_3$ and $LaMnO_3$. This allowed for more accurate number of pulses to be used for deposition of the superlattice to eliminate the error of using the first rather short period of RHEED intensity oscillation obtained from the first u.c. layer. Accordingly, the number of pulses from the second and third oscillations were averaged for each layer and

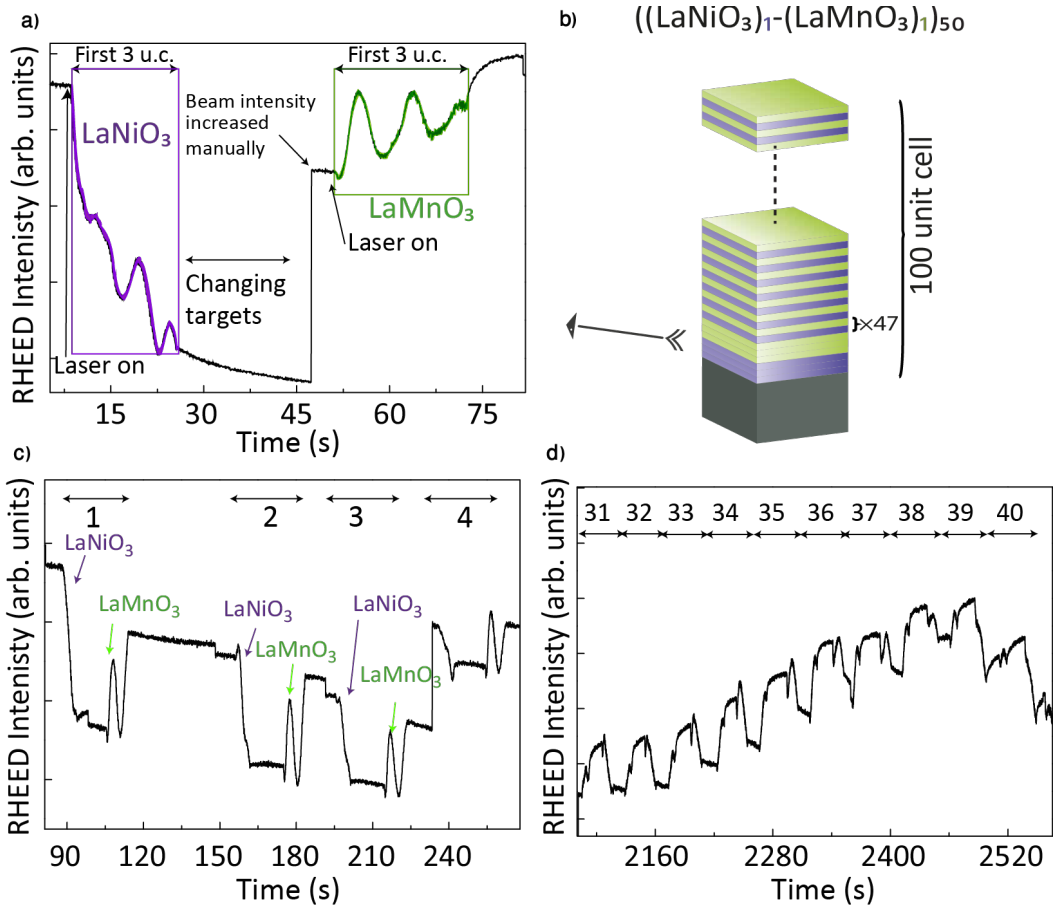

Figure 7.5: RHEED intensity oscillations for the $(1/1)_{50}$ superlattice a) first 3 monolayers b) schematic arrangement of the $(1/1)_{50}$ superlattice c) using the average number of pulses growth of next few bilayers are shown d) after deposition of 40 bilayers the oscillations still continues an indication of high quality interface properties.

used for the following single u.c. layer of each constituent.

The number of pulses required for one u.c. layer growth of the superlattices for each layer is presented in table 7.1. Superlattice $(1/1)_{100}$ was grown with a total thickness equal to 200 unit cell. This sample was grown at thickness similar to that of the $LaMnO_3$ layer grown at the same deposition conditions for comparing the magnetic behaviour Strong RHEED intensity oscillations were observed after deposition up until the end of the deposition of each superlattice as shown in figures 7.3, 7.4, and 7.5. The fact that the oscillations still continued even after deposition of up to 100 u.c. is an indication of high quality interface properties and shows the calculated number of pulses were close to the exact number of pulses required for a full u.c. layer.

Table 7.1: Number of pulses obtained from initial RHEED intensity oscillations which is required for one u.c. layer of each constituent.

superlattice	Number of pulses used for 1 u.c. layer	
	$LaMnO_3$	$LaNiO_3$
$(5/5)_{10}$	30	39
$(2/2)_{25}$	32	35
$(1/1)_{50}$	30	44
$(1/1)_{100}$	52	35

7.1.2 Surface morphology

Defined continuous RHEED intensity oscillations are an indication of layer-by-layer growth. Another indication of this type of growth is observation of a well ordered RHEED pattern and AFM images showing the imprint of the substrate with a step-and-terrace structure. The surfaces of the superlattices were examined by *in-situ* RHEED by analysing the RHEED patterns taken after samples were cooled to room temperature. Then they were examined by AFM as shown in figure 7.6. Figure 7.7 shows the RHEED patterns of the $(5/5)_{10}$, $(2/2)_{25}$ and $(1/1)_{50}$ superlattices along the pseudocubic $\langle 100 \rangle$ (a, b, and c) and $\langle 110 \rangle$ (d, e, and f) orientations respectively. Line profile of the RHEED patterns are shown under each image. The integer and fractional order streaks are marked by long and short white lines on the RHEED patterns respectively. A sharp specular diffracted spot (00) can be seen in all RHEED patterns of the superlattices in both directions with integer streaks separation of the cubic $SrTiO_3$ substrate. Well-defined Kikutchi lines are visible for the $(5/5)_{10}$ and $(2/2)_{25}$ superlattices indicating atomically flat and smooth surfaces. By comparing the RHEED patterns, it is clear that the $(2/2)_{25}$ superlattice shows the least disordered surface as the FWHM of the specular spot is narrower and higher Laue zone diffractions are visible. Red arrows marked on the line profiles of the RHEED images along the $\langle 110 \rangle$ indicate $(\sqrt{2} \times \sqrt{2})\ R45^\circ$ as they were absent in RHEED patterns taken along the $\langle 100 \rangle$ direction.

The surface morphology of the superlattices was investigated with AFM and they also showed smooth surfaces with a step and terrace structure similar to that of the TiO_2 terminated single crystal $SrTiO_3$ substrates (001). AFM images were taken *ex-situ* and after deposition. Figure 7.6(a-d) shows AFM height images of two different scan sizes of $5\ \mu$m$\times\ 5\ \mu$m and $1\ \mu$m$\times\ 1\ \mu$m of the $(5/5)_{10}$ and $(1/1)_{50}$ superlattices. As was suggested from RHEED intensity oscillations and also from the RHEED patterns, true layer-by-layer growth has occurred. It can be seen from the AFM images of the $(5/5)_{10}$ and $(1/1)_{50}$ superlattices in figure 7.6 that even after growth of a 100 u.c., the initial step-terrace morphology of the single-terminated substrate surface remains visible.

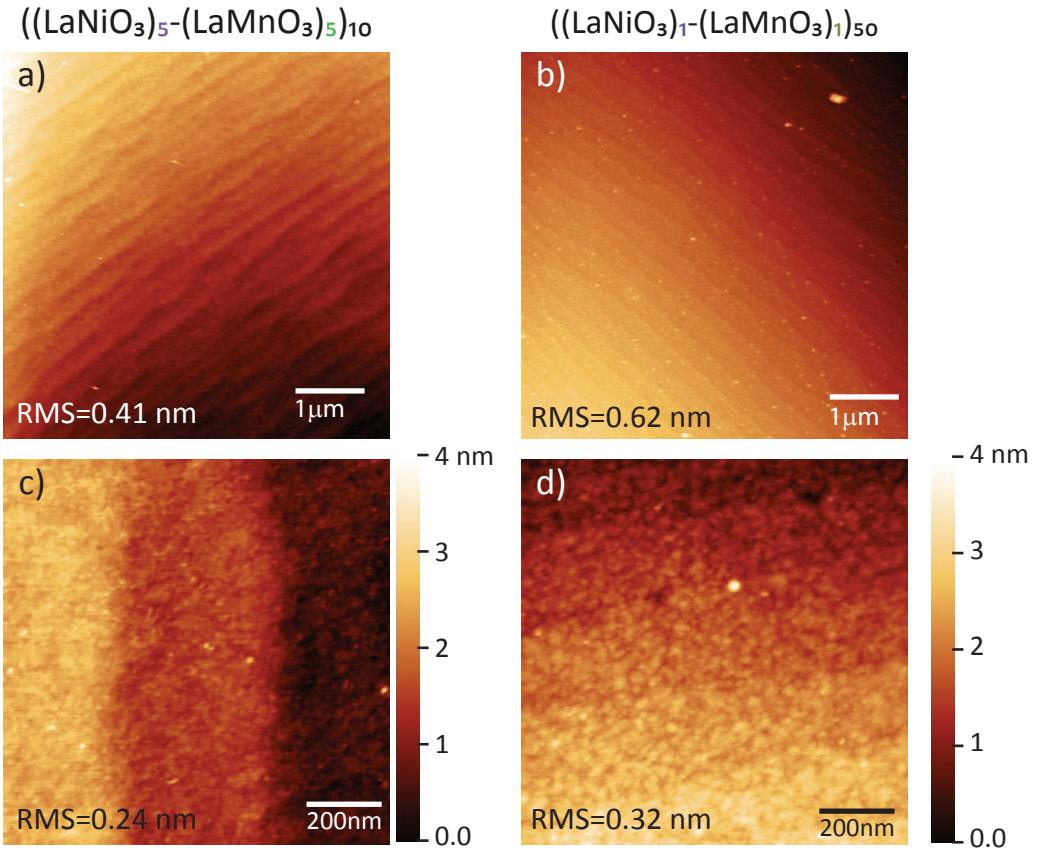

Figure 7.6: AFM topography images show surface morphology of a) and b) 5μm$\times$5μm area scans of $(5/5)_{10}$ and $(1/1)_{50}$ superlattices on single terminated $SrTiO_3$ substrate, respectively. c) and d) are 1μm$\times$1μm area scans.

However, small islands are observed at the terraces in the $(1/1)_{50}$ superlattice. This is likely to be the reason for the relatively large FWHM of the diffraction spots observed in the RHEED pattern. However, these terraces retain the imprint of the underlying substrate indicating, that high quality growth of the $(1/1)_{50}$ superlattice has occurred. Due to the integer nature of the number of pulses, the systematic error in calculations is the required number of pulses for 1 monolayer and remains the main source of error.

7.1.3 Surface octahedral distortions

The AFM and RHEED oscillations both indicated that the perovskite layered structure of $LaNiO_3/LaMnO_3$ has atomically smooth surface, particularly the $(2/2)_{25}$ superlattice. The RHEED pattern of the $(2/2)_{25}$ sample revealed fractional order streaks along the $\langle 110 \rangle$ direction. Figure 7.8 shows patterns of the $(2/2)_{25}$-(001)-$(\sqrt{2}\times\sqrt{2})\ R45^{\circ}$

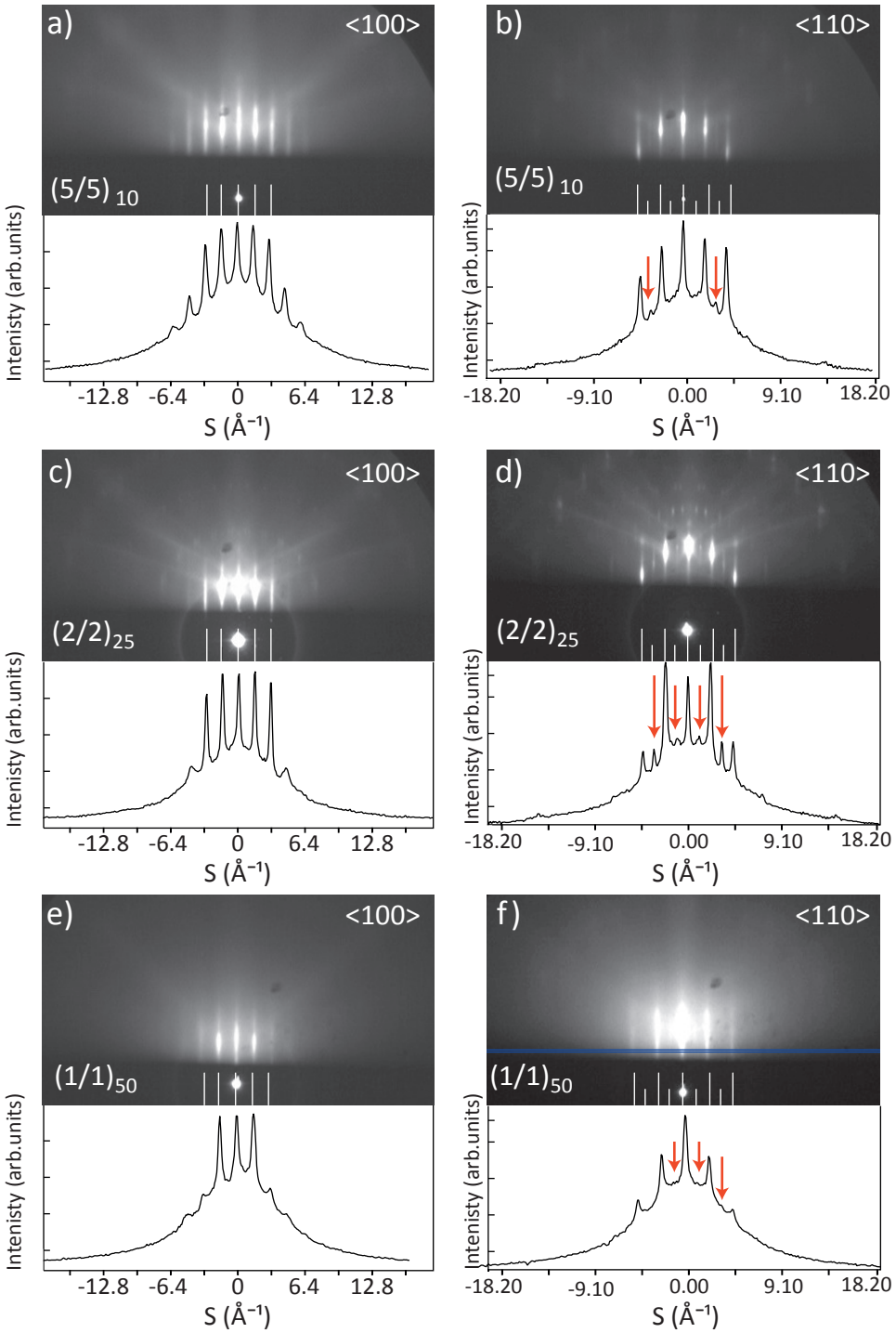

Figure 7.7: RHEED patterns of the $(5/5)_{10}$, $(2/2)_{25}$ and $(1/1)_{50}$ superlattices along pseudocubic $\langle 100 \rangle$ (a, b, and c) and $\langle 110 \rangle$ (d, e, and f) orientations respectively. Line profile of the RHEED patterns are shown under each image. The integer and fractional streaks are marked by long and short white lines on the RHEED patterns respectively.

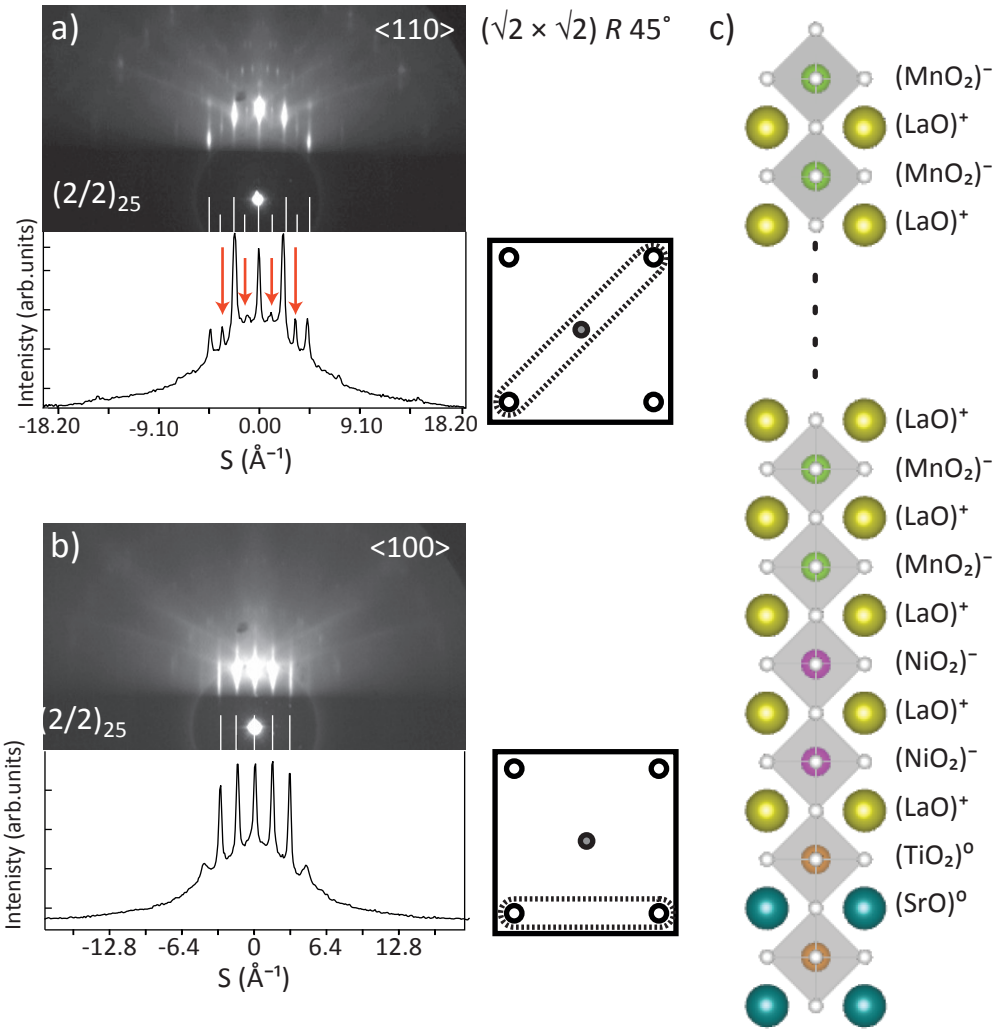

Figure 7.8: RHEED patterns observations along the a) $\langle 110 \rangle$ b) $\langle 100 \rangle$ of the $(2/2)_{25}(001)$ superlattice. The long (short) white lines on the images indicate integer (fractional) streaks. A $(\sqrt{2} \times \sqrt{2})\ R45^{\circ}$ reconstruction or superstructure is observed. In the panel next to the images reciprocal space patterns that are giving rise to the observed features are shown. The dashed lines show the crystallographic orientalising seen in the pattern, the grey (white) indicate fractional (integer) streaks. c) Shows a cross-section of the $(2/2)_{25}$ ideal superlattice.

surface. Panel a) shows the pattern observed with the electron beam aligned along the $\langle 110 \rangle$ direction, while panel b) shows the pattern with the RHEED beam along the $\langle 100 \rangle$ direction. There were no reconstructions observed at the surface of the substrate prior to the deposition. Both the a) and b) images show Kikutchi lines indicating the surface of the superlattice is of high quality and very smooth. In the right hand side of each RHEED pattern, the reciprocal space pattern which gives rise to the observed diffraction feature including the fractional order streaks are shown. The elongated fractional spots observed in figure 7.8-a) are the result of $(\sqrt{2} \times \sqrt{2})\ R45^{\circ}$ reconstructions.

The streaking spacing is half of the integer order streaks in the $\langle 110 \rangle$ direction, while there are no fractional order streaks observed for the $\langle 100 \rangle$ direction. The superstructure or reconstructed structure has a plane spacing twice that of the pseudocubic lattice along the $\langle 110 \rangle$ while the same spacing when the electron beam is along the $\langle 100 \rangle$. This is a characteristic of a 45 degree rotated lattice with in-plane lattice parameter $a{=}\sqrt{2}a_{\text{pseudocubic}}$. To determine the origin of this feature which was observed in the RHEED patterns for all the superlattices, it is beneficial to identify the surface termination of the superlattices assuming the interfaces are atomically sharp with no intermixing. Panel -c) in figure 7.8 illustrates schematically a cross-section of an ideal the $(2/2)_{25}$ superlattice grown on a TiO_2 single-terminated $SrTiO_3$ (001). B-site cations (Ni and Mn) are separated and shifted by half a u.c. out-of-plane by LaO planes.

The oxygen ions are shown in the cubic perovskite structure of $SrTiO_3$. Since the stacking sequence started from the LaO plane as a result of the TiO_2 terminated substrate, the final layer is MnO_2. However, the schematically shown cross-section without any distortion of oxygen octahedra is not what is observed in the deposited heterostructures. This is attributed to the strong spin-charge-lattice coupling in perovskite manganites, giving rise to small distortions of the MnO_6 octahedra [19]. The cubic coordination is distorted by several mechanisms such as the Jahn-Teller effect leading to a reduction in the symmetry and degeneracy of the energy levels or the need to accommodate different cation sizes within the cubic unit cell. This rotation is also sensitive to strain in the lattice, cation vacancies, off-stoichiometry, and oxygen vacancies introduced during the deposition of epitaxial thin films [103]. Since the terminating layer is $LaMnO_3$ in these superlattices regardless of the stacking periodicity, only the MnO_6 octahedral rotation is discussed. The situation is different in the case of the $(1/1)_{50}$ superlattice as the stacking sequence is (LaO)-(NiO_2)-(LaO)-(MnO_2)-(LaO)-(NiO_2), and hence the environment of the MnO_2 differs from the chemical environment to that of bulk $LaMnO_3$. Conversely, the environment of the MnO_2 in the superlattice $(2/2)_{25}$ is chemically symmetric and closer to bulk $LaMnO_3$ [248]. Along the $\langle 110 \rangle$ direction RHEED reveals the orthorhombic symmetry of manganite perovskite when they are strained epitaxially to a cubic substrate

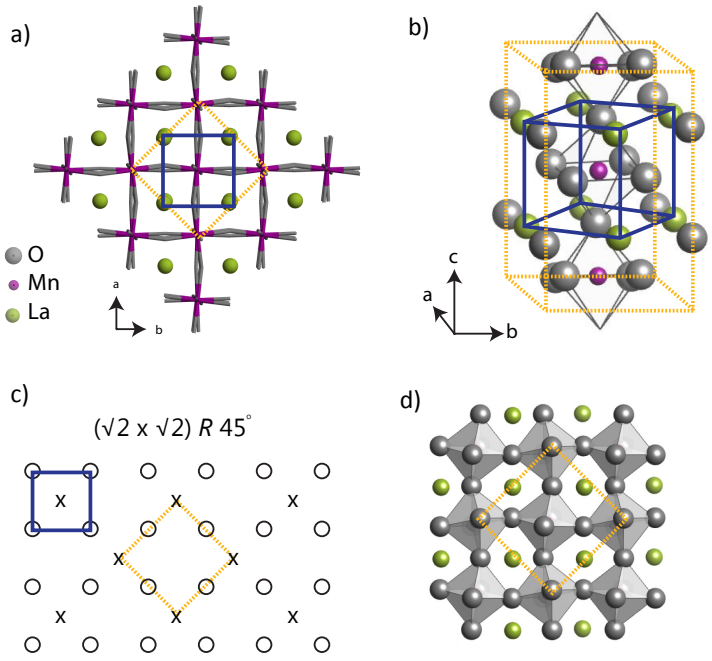

Figure 7.9: a) and c) shows $(\sqrt{2} \times \sqrt{2})\ R45°$ arrangement. b) schematic of $GdFeO_3$-type orthorhombic unit cell (dashed yellow line) with MnO_6 octahedra at the centre together with perovskite pseudocubic unit cell (solid blue line) with Jahn-Teller distortion. d) shows the Jahn-teller distortion in in a and b planes.

such as $SrTiO_3$ [103].

The observation of fractional streaks corresponding to $(\sqrt{2} \times \sqrt{2})\ R45°$ has not been observed previously for $LaNiO_3$-$LaMnO_3$ superlattices. As a matter of fact, the literature on this effect is not extensively explored using RHEED. May *et al.* observed fractional order streaks in the RHEED pattern obtained from the superlattices of $LaNiO_3$-$SrMnO_3$ assuming NiO_2 surface reconstruction has occurred [249]. Matzdorf *et al.* reported in-plane rotation of the RuO_6 in Sr_2RuO_4 leading to the $(\sqrt{2} \times \sqrt{2})\ R45°$ surface reconstruction studied by low energy electron diffraction (LEED) [250]. However, the existence of similar features in RHEED indicating a twofold superstructure along the $\langle 110 \rangle$ electron beam direction was seen in the thin films of La_2NiMnO_6 [251]. It was suggested that the $\sqrt{2}a \times \sqrt{2}a$ was a superstructure originating from the rock-salt type ordering of B site cations in the double-perovskite structure of La_2NiMnO_6. This is unlikely to be the case here as in the $(2/2)_{25}$ superlattice the growth was controlled by RHEED oscillations that did not damp over time indicating that interface mixing did not occur during the deposition. This result is close to the Petrov *et al.* [103]

report on $LaSrMnO_3$ thin films; however, they have reported fractional streaks along the $\langle 100 \rangle$ direction. Figure 7.9 depicts graphically -a) and -b) the ball and stick model of a orthorhombic $GdFeO_3$-type unit cell (dashed yellow line) with MnO_6 octahedra at the centre together with pseudocubic unit cell (solid blue line) with Jahn-Teller distortion taking place in the a and b planes. Panel -c) shows the typical $(\sqrt{2} \times \sqrt{2})\ R45^\circ$ arrangement. Panel d) shows the top view of the in plane Jahn-Teller distortion for $LaMnO_3$ with $Pbnm$ symmetry.

The orthorhombic arrangement is seen in all three superlattices, however, the diffraction spots are sharper in the $(2/2)_{25}$ superlattice with a symmetric MnO_2 environment. The fractional streak intensity can be maximised in deposition optimisation by using real-time monitoring of the RHEED spot which has been previously incorporated to optimise the growth of cuprate films [252]. This can give an insight into the surface termination of manganite because the intensity of fractional spots arise from MnO_6 octahedral rotation and disappear with a change in the surface termination. Further information about crystal structure and periodicity of the superlattices can be gained from XRD measurements.

7.1.4 Structural properties

The typical XRD $\theta - 2\theta$ scans were performed on the $(5/5)_{10}$, $(2/2)_{25}$ and $(1/1)_{50}$ superlattices. The XRD pattern of the (001) reflection of the $(5/5)_{10}$ superlattice is shown in figure 7.10 and clear superlattice satellite peaks ± 1 are marked on the graph. superlattice satellite peaks along with the thickness fringe reflections are as a result of well-defined surface and interfaces of the $(5/5)_{10}$ superlattice. The periodicity of the $(5/5)_{10}$ superlattice was measured using these superlattice satellite peaks and found to be 4.1$\pm$0.1 nm.

The c-axis lattice parameter was obtained for the superlattices from the $\{001\}$ reflections using Bragg's law. An expected total thickness then can be defined by: total expected thickness = No. of layers $\times$ $c_{\text{superlattice}}$. In heterostructures with different stacking periodicity of n layer of $LaNiO_3$ and m layer of $LaMnO_3$ the average c lattice parameter can be obtained from Vegards's law [253] such that

$$c_{\text{average}} = (nc_n + mc_m)/(n+m), \tag{7.1}$$

where n and m are the number of $LaNiO_3$ and $LaMnO_3$ u.c. in the bilayer, and such c_n and c_m correspond to the c-axis lattice parameters of $LaNiO_3$ and $LaMnO_3$ respectively. However, where $n = m$ this is just the simple average of the two c-axis lattice parameters. Comparing the expected thickness to the obtained total thickness (measured by XRD

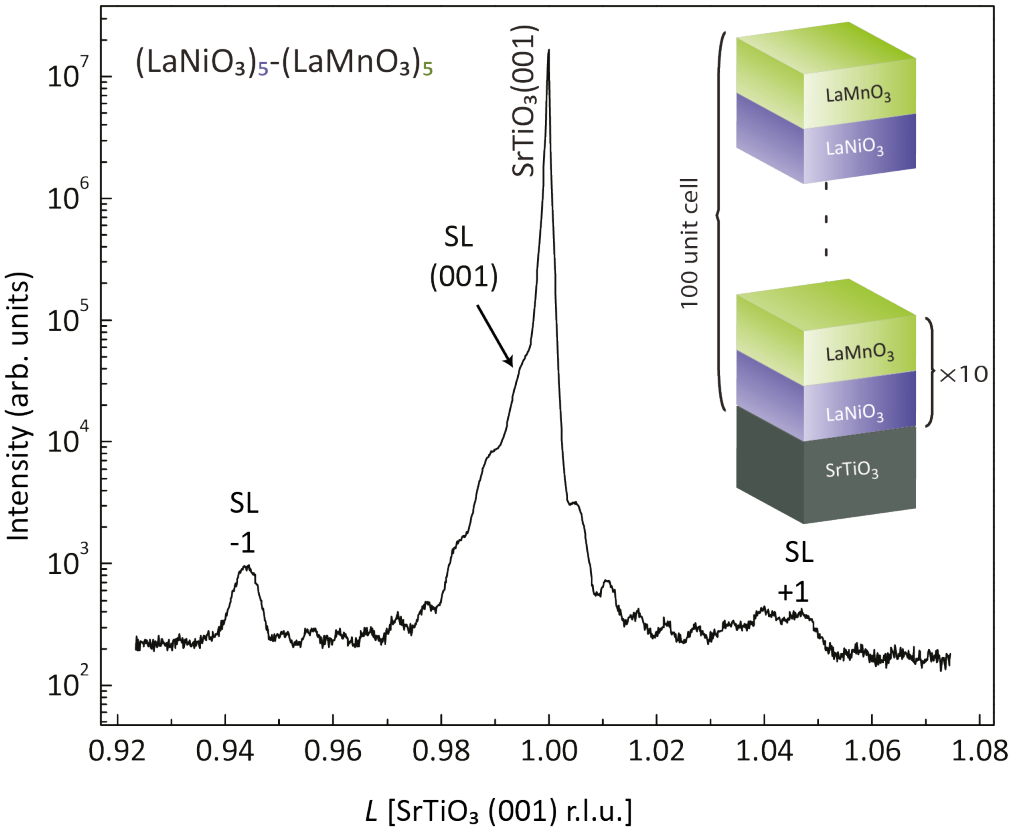

Figure 7.10: X-ray diffraction $\theta - 2\theta$ scan of (001) reflection in the $(5/5)_{10}$ superlattice. The satellite peaks are indicated by green arrows. The total thickness fringes were used for thickness calculations while the superlattice satellite peaks revealed the periodicity of superlattice.

and XRR thickness fringes) can be used as a qualitative tool to know if deposition was stoichiometric and if any re-evaporations occurred during the deposition. The total thickness values were within the range of expected values. In table 7.2 the expected values for the total thickness are compared with the measured ones. It is clear that the $(2/2)_{25}$ superlattice is thinner than expected. Before concluding that the re-evaporation or off-stoichiometric material transfer has occurred, the limitations of RHEED digitally-controlled growth should be considered. By looking at the RHEED intensity oscillations in figure 7.4 and the number of pulses used to grow the $(2/2)_{25}$ superlattice reported in table 7.1, it can be seen that the number of pulses used for deposition of the subsequent $LaMnO_3$ layer is lower than the average and possibly underestimated.

The in-plane lattice parameter was determined from a (103) asymmetric reciprocal space map. It was found that the $(5/5)_{10}$ and $(1/1)_{50}$ superlattices were fully strained to

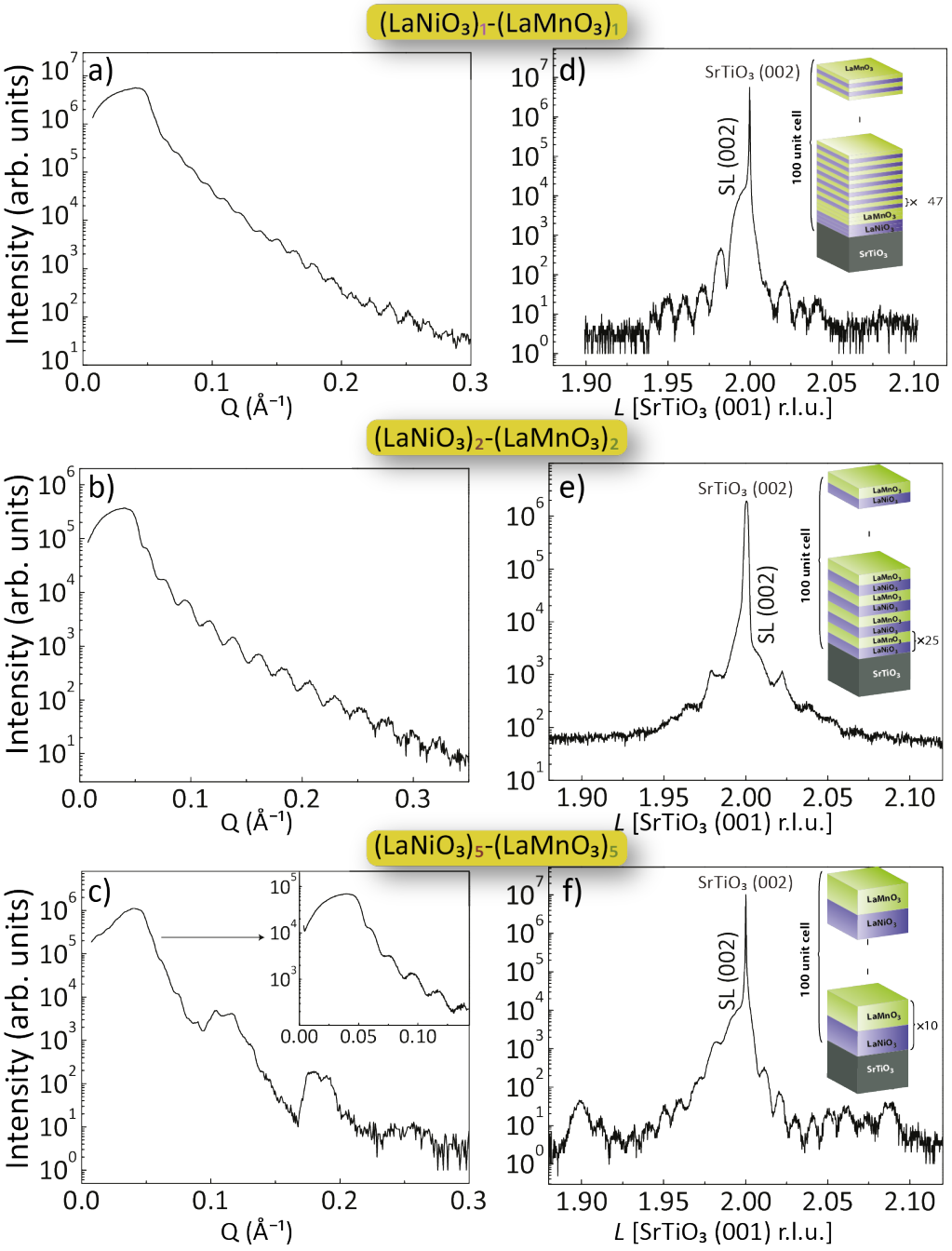

Figure 7.11: X-ray reflectivity measurements a), b) and c) and $\theta - 2\theta$ XRD scan for (002) reflection d), e), and f) of the superlattices $(1/1)_{50}$, $(2/2)_{25}$ and $(5/5)_{10}$, respectively.

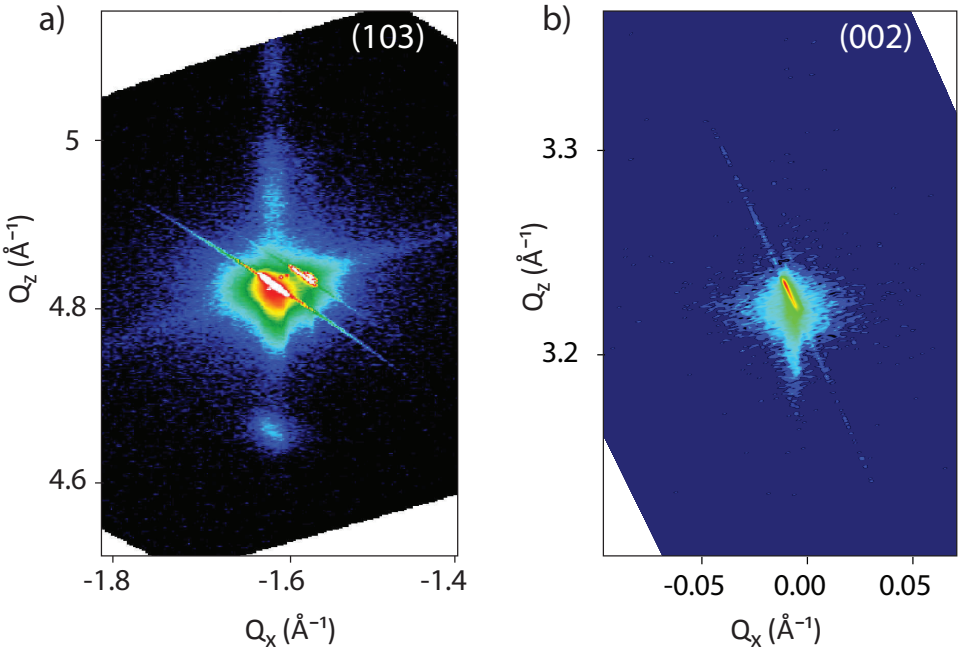

Figure 7.12: X-ray reciprocal space map of the $(5/5)_{10}$ superlattice a) (103) reflection b) (002) reflection. Satellite ± 1 peaks of superlattice are visible in figure a) which are in line with substrate peak in Q_z direction indicating that superlattice is coherently strained to the substrate.

the substrate. Figure 7.12 shows (103) and (002) reflections for the $(5/5)_{10}$ superlattice. The satellite peaks of the superlattice are present, however, the main superlattice peak is too close to the substrate (103) peak to be identified, hence the positions of the satellite peaks were extracted and the midpoint between them was considered as the best estimated position of the $(5/5)_{10}$ superlattice (103) reflection. The spacing between planes with Miller indices $\{$hkl$\}$ can be obtained from vector analysis for perovskite oxides, when the thin film is fully strained to the perovskite cubic substrate. The c-axis lattice is

Table 7.2: Summary of experimentally calculated lattice parameter for superlattices.

superlattice	c-axis parameter (Å)		Total thickness (nm)		
	XRD	expected value	XRD	XRR	expected value
$(5/5)_{10}$	3.917(1)	3.868(1)	41(4)	47(7)	39(1)
$(2/2)_{25}$	3.899(1)	3.868(1)	26(1)	31(5)	39(1)
$(1/1)_{50}$	3.896(1)	3.868(1)	35(2)	42(3)	39(1)
$(1/1)_{100}$	3.886(1)	3.868(1)			78(1)

determined from the value of d which can be found from the tetragonal geometry from the following equation [254]

$$\frac{1}{d^2} = \frac{h^2+k^2}{a^2} + \frac{l^2}{c^2} \,. \tag{7.2}$$

where the substrate has a cubic structure with lattice parameter a.

7.1.5 Theoretical considerations for strain effect in the heteroepitaxial growth

Calculation of critical film thickness is of great importance and is addressed in terms of the onset of the relaxation through the formation of misfit dislocations. Theoretically, the strain can be fully relaxed by introducing misfit dislocations at the interface between the film and the substrate when the thickness of the film exceeds a critical thickness of h_c. The two most widely approached models to predict critical thickness has been Matthews and Blakeslee (MB) [255] and People and Bean (PB) [256]. However, it has been reported that the MB model predicts values that are too low for critical thickness of perovskite oxides [257, 258]. The MB model is also known to predict too low values for semiconductors giving critical thickness of $\approx$ 10 nm for 1% strain in the SiGe/Si system [259]. Similar arguments that explain these low values are also valid for oxides. The PB model is a phenomenological method and can explain semiconductor experimental data better than the MB model. Simple calculations were performed to compare the critical thickness obtained using the MB and PB methods from the equations given by Speck and Pompe *et al.* [260] and Marée *et al.* [261];

$$h_c^{\mathsf{MB}} = \frac{\bar{b}}{8\pi f}\frac{\left(1-\nu\cos^2\alpha\right)}{(1+\nu)\cos\lambda}\left(\ln\beta\frac{h_c}{b}\right), \tag{7.3a}$$

$$h_c^{\mathsf{PB}} = \frac{\bar{b}}{40\pi f^2}\frac{(1-\nu)}{(1+\nu)}\left(\ln\frac{h_c}{b}\right). \tag{7.3b}$$

Here $\bar{b}$ is the Burgers vector of the dislocation, f is the relative misfit, α is the angle between the Burgers vector of the dislocation and its line, λ is defined as the angle between slip direction and the film normal, β is the cut-off parameter employed to explain the continuum energy of the dislocation core (estimated to be $\sim$ 4) and ν is Poisson's ratio. Due to the lack of Poisson's values for $LaNiO_3$ and $LaMnO_3$, ν was assumed equal to 1/3 [258]. For perovskite oxides the main dislocation system is $\langle 110\rangle$ $\{110\}$, b=5.523 Å, α=90° and λ=45° for a film with (001) orientation. Using the above parameters, the critical thickness for the $LaMnO_3$ and $LaNiO_3$ on $SrTiO_3$ (001) substrate is summarised in table 7.3. Lattice parameters used to calculate misfit strain in single layers in table 7.3

Table 7.3: Critical thickness calculated for $LaMnO_3$ and $LaNiO_3$ films grown on $SrTiO_3$ substrate (001).

Film	Substrate	f(%)	h_c^{MB}(nm)	h_c^{PB}(nm)
$LaNiO_3$	$SrTiO_3$	1.67(1)	5(1)	32(1)
$LaMnO_3$	$SrTiO_3$	1.11(1)	8(1)	83(1)
$(LaNiO_3)_n$-$(LaMnO_3)_n$	$SrTiO_3$	1.14(1)	6(1)	52(1)

were those of the bulk pseudocubic. To calculate the misfit strain in the superlattices, the lattice parameter was estimated assuming the multi-layered structure mean lattice parameters which were calculated from the thickness of each constituent layer using equation 7.1 resulting in a mismatch value between those of the single layers.

Comparing these results with what was observed in XRD and TEM studies shows clearly that the MB model underestimates the value of the critical thickness. This can be explained by the difference in the nature of oxides since they are more tolerant to strain compared to semiconductors. Perovskite oxides are slightly less sensitive to the change in the bond due to their partially ionic nature, so the interatomic distances are kept constant because of the dependence of Coulomb interaction on the absolute distance between the charges [262]. The higher tolerance of perovskite to strain can be attributed to their complicated crystal structure since the octahedra can tilt and rotate which gives perovskite oxides extra degrees of freedom to change in their volume. Moreover owing to the peculiarity of having a transition metal in the centre of the octahedra, the stiffness of the oxide can vary by changing the spin state of certain transition metal ions leading to the distortion of the octahedra. Finally the lattice parameter of perovskite oxides can vary significantly by introduction of oxygen vacancies into the crystal [263]. Thus, a higher tolerance to strain is expected when the material can lower its energy because of these internal degrees of freedom [264]. Consequently, pseudomorphic perovskite films can be grown epitaxially with misfit as large as several percent exceeding the theoretically predicted critical thickness [261, 265, 266, 267]. The choice of single crystal substrate and its surface treatment is crucial to coherent epitaxial growth of oxides beyond the expected-strain-relaxed thickness. To further promote coherent growth and prevent formation of misfit dislocations, single-terminated substrates were used. Octahedral tilting can also be one of the reasons that experimental results exceed the theoretical calculation of critical thickness in perovskites with a corner-sharing octahedral network. Calculations of interfaces between two different perovskites cannot easily solve the definite role of the mismatching symmetry at the interface from the other effects such as the lattice mismatch, or change of the valence state. In a system such as $LaNiO_3/LaMnO_3$ on $SrTiO_3$ the symmetry mismatch is one of the most complicated systems. Figure

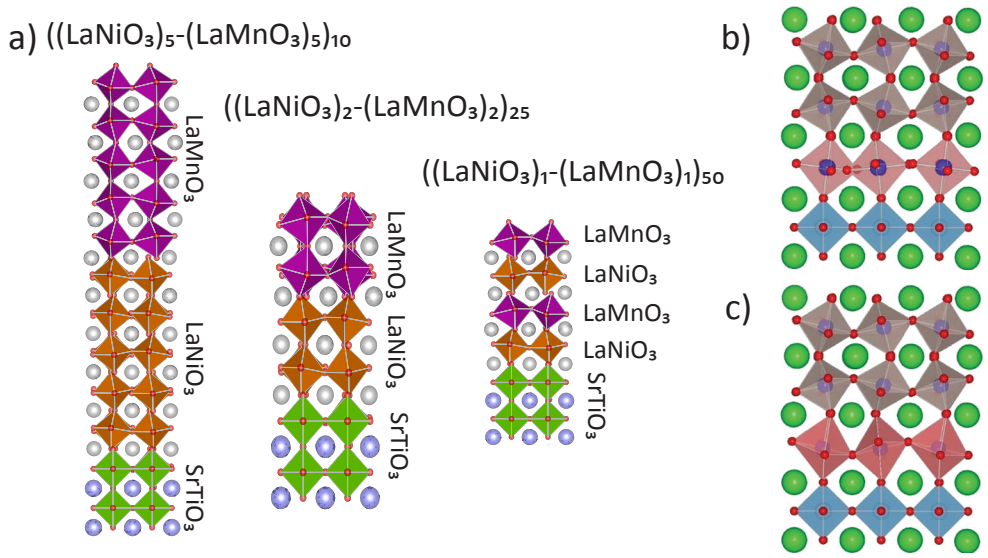

Figure 7.13: Tilted octahedra is shown for bulk-type symmetries of $LaNiO_3$ and $LaMnO_3$ short period superlattices green octahedral with no tilt $SrTiO_3$, Orange octahedral $LaNiO_3$ with anti phase tilting ($a^-a^-a^-$), and purple $LaMnO_3$ with Jahn teller distortion ($a^-b^+a^-$). In this representation the interface effect is not shown and clearly the real octahedral tilt differs from this figure. Right panel: schematic illustration of the oxygen octahedral tilt at the interface between two perovskite oxides where un-tilted octahedral is blue, tilted is beige and the connecting octahedra are shown in pink. In b) the continuity of corner sharing is interrupted; c) showing interface octahedral is distorted to continue the corner sharing. (b and c taken from [268]).

7.13 displays schematically the superlattices grown in this thesis with tilting of their octahedra. Bulk-like symmetries are used in figure 7.13 to show that the corner sharing octahedra will be disrupted (note the disconnected octahedra specifically in the $(1/1)_{50}$ superlattice. Panel b and c of figure 7.13 show that at the interface between two lattice matched but symmetry mismatched perovskites, because of the constraints on the continuously connected octahedral network, the interface layer undergoes additional deformations and distortions not available in their bulk form [268]. Panel b shows the situation without distortion of the octahedral at the interface. Panel c illustrates that the continuity of the octahedral network can be restored if the interface region undergoes octahedral distortions, tilting, or deformations. This includes the Jahn-Teller effect and can involve new rotational modes. The situation is even more complicated for short period superlattices where there is no clear distinction between the substrate and the matching film. When modelling lattice mismatch, the constraint imposed by in-plane lattice of the substrate can be easily applied. In contrast, when considering the symmetry

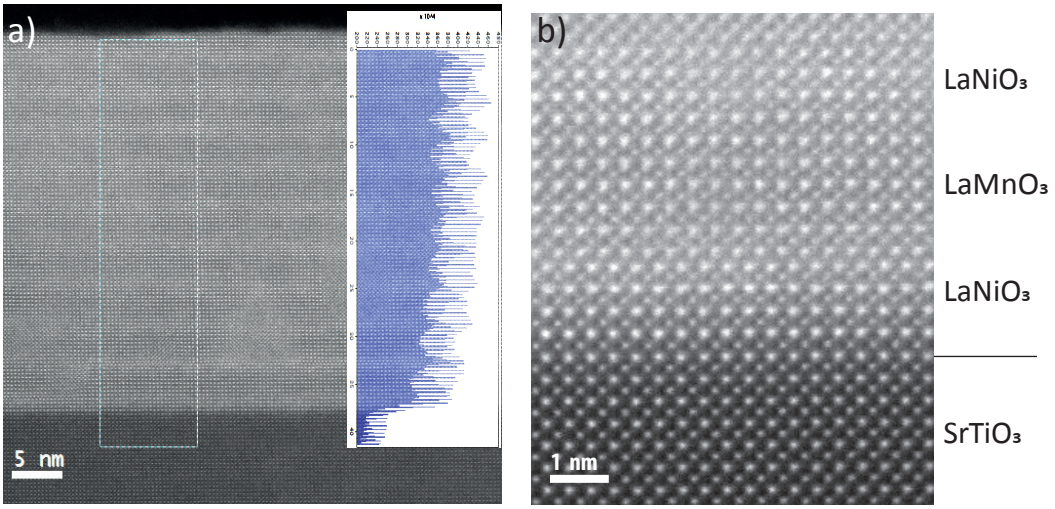

Figure 7.14: An HAADF images of a $(5/5)_{10}$ superlattice: a) an overview of the whole superlattice and b) magnified near the interface region. In this image the brightest points correspond to the Lanthanum and in between are the nickel or even weaker Manganese. The layer structure can be seen from the intensity profile of the HAADF image.

mismatch in superlattice, the symmetries of the constituents are competing against each other.

It should be noted that structural, magnetic and electrical functionalities of perovskite oxides are strongly influenced by the octahedral rotation and deformations through the phonon modes at the zone boundaries [72, 269]. In manganites, the hopping matrix (thus transport properties) is influenced by the octahedral corner sharing network that is defined by the B-O-B bond tilting angle [270]. One of the suggested methods to study the octahedral behaviour is atomic resolution bright field imaging that can reveal the position of oxygen in the lattice using STEM. Thus, STEM and HR-TEM were employed to study the microstructure of the layers at the film-surface interface. The HR-TEM images always indicated the absence of misfit dislocations at the interface of the single layer of $LaMnO_3$ and $LaNiO_3$ up to 70 nm thick films. No misfit dislocations were observed neither in STEM images of the $(1/1)_{50}$, $(2/2)_{25}$ and $(5/5)_{10}$ superlattices, confirming that the interface was matching coherently.

7.1.6 STEM

The $(5/5)_{10}$ and $(1/1)_{50}$ superlattices were examined by scanning transmission electron microscopy. The individual layers of the $(5/5)_{10}$ superlattice can be seen in a HAADF image in figure 7.14 of the complete $(5/5)_{10}$ superlattice. In all the STEM

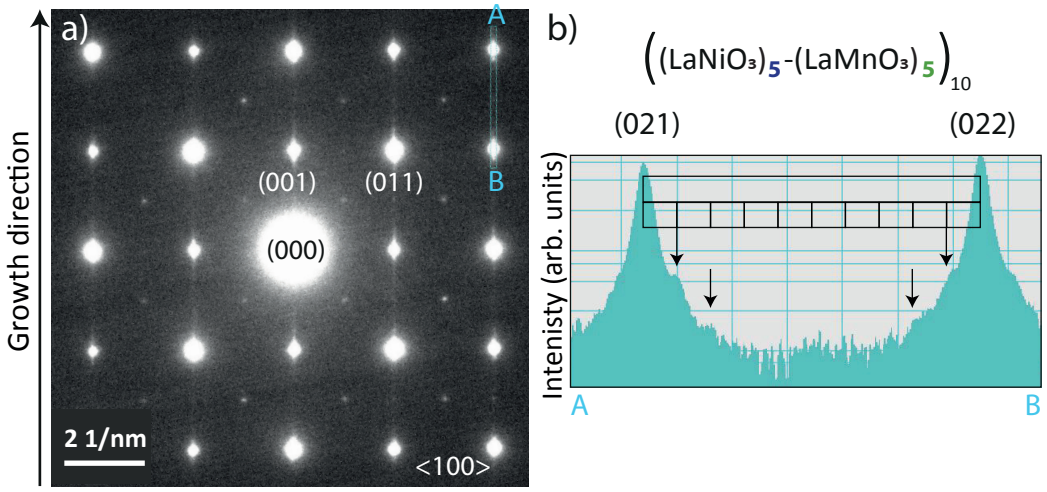

Figure 7.15: $(5/5)_{10}$ superlattice on $SrTiO_3$ (001) a) diffraction pattern. The growth direction of the superlattice is shown by a black arrow on the side. b) Logarithmic-scale intensity profile between A and B, two diffraction reflections shown in panel (a). Black arrows indicate satellite peaks of the $(5/5)_{10}$ superlattice.

images shown, the substrate is located beneath such that, the growth direction of the layer is up. At higher magnification images all atoms (La, Ni, and Mn) are imaged except oxygen. Due to the dependence on the atomic number Z of these HAADF images, the brightest spots correspond to the Lanthanum. The weaker points in between are either nickel and oxygen atoms (average brightness can be seen in $LaNiO_3$ block) or Manganese and oxygen atoms (lowest intensity belongs to $LaMnO_3$ block). In panel (b) of figure 7.14 the lowest part belongs to the substrate $SrTiO_3$ in which the average point intensity is lower than the layer due to the lower atomic number of Sr (Ti) comparing to La (Ni/Mn). In this image of the $(5/5)_{10}$ superlattice, as Mn and Ni do not differ significantly in brightness, the layer structure is not very distinguishable. Moreover, all interfaces are coherent indicating that the strain induced by the $SrTiO_3$ substrate is maintained. This was also confirmed by the XRD reciprocal space map measurements shown in section 7.1.4.

Diffraction pattern along the $\langle 100 \rangle$ zone axis of the $(5/5)_{10}$ superlattice is shown in figure 7.15. The diffraction spots are arranged in a square due to the pseudocubic crystal structure in this orientation. However, there are additional $1/2(000)$ reflections in this patterns arising from octahedral tilting. Moreover, there are additional satellite reflections along the growth direction due to the periodic arrangement of the layers. Considering the diffraction images are recorded over a much larger size range compared to the HAADF images shown previously, observation of satellite superimposed reflections

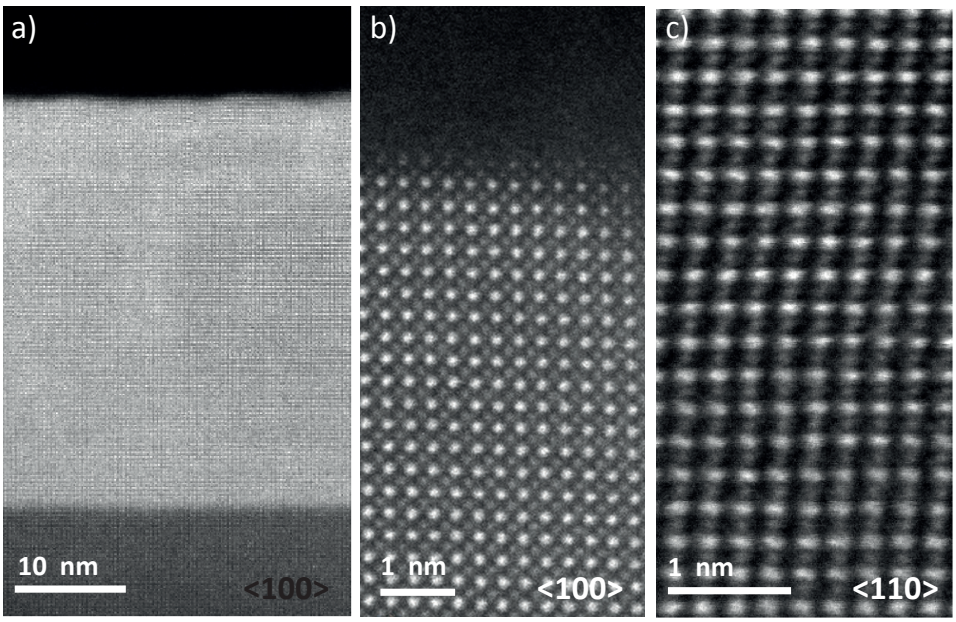

Figure 7.16: HAADF images of the $(1/1)_{50}$ superlattice: a) an overview of the whole superlattice and b) magnified near the top surface. In this image the brightest points correspond to the Lanthanum and in between are the alternating nickel and Manganese. c) The $\langle 110 \rangle$ direction.

indicates a high quality of growth. The position of these satellite reflections are shown in panel (b). The separation is one-tenth of a reciprocal pseudocubic lattice parameter, since the bilayer in the $(5/5)_{10}$ superlattice consists of 10 perovskite unit cells. It can be seen that not all the satellite reflections are present. That can be as a result of the microstructures (Ruddlesden Popper) observed in the layer interrupting the periodicity.

An HAADF image of the $(1/1)_{50}$ superlattice is shown in figure 7.16 in 2 viewing directions of $\langle 100 \rangle$ (panel a and b) and $\langle 110 \rangle$ (panel c). The difference between Mn and Ni is hardly visible so that the alternation of B-site cation is not distinguishable at all. However, the magnified region near the surface of the HAADF image shows the perovskite structure indicating the growth quality was good even up to the last monolayer. Moreover, the total thickness corresponds to that calculated from XRD measurements and anticipated from the RHEED intensity oscillations.

In addition to the HAADF images, the composition of the superlattices can be determined directly by EELS measurements. Following the methodology described in Detemple *et al.* [271] the distribution of Ni and Mn atoms over the superlattices were determined and such EELS composition maps are included within the rectangle highlighted in the HAADF image in figure 7.17.

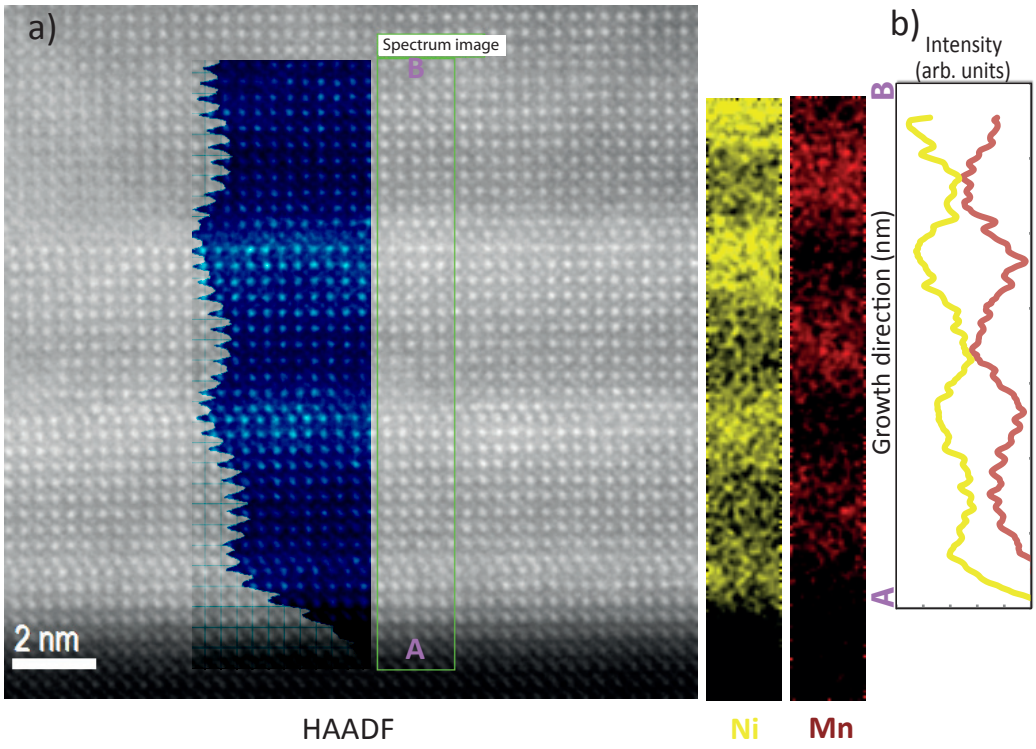

Figure 7.17: $(5/5)_{10}$ superlattice a) HAADF image and the corresponding atomic intensity edge mapping for Ni and Mn atoms b) EELS line scan showing that although Mn intensity goes to zero in $LaNiO_3$ layer, there is a trace of Ni atom in $LaMnO_3$ layer.

The intensity of the Ni-L_2 and Mn-L_2 edges was extracted after background correction (power law fit). These intensity profiles taken from the Mn and Ni maps then show the different layers of alternating Ni and Mn content (Ni is shown with a Yellow colour and Mn with red). It can be observed from figure 7.17 that, unlike the Mn intensity, the Ni intensity does not drop to zero when entering the $LaMnO_3$ layer. There are a few possible phenomena to explain this effect such as insufficient removal of the background noise from EELS spectra and the edges of La and Ni being very close in energy as is shown in table 7.4. The EELS maps, however, should not be used for quantitative analysis since their statistics are not as accurate as the EELS line scan and there are artefacts if the contrast is adjusted unfavourably. However, this is preliminary EELS data and an appropriate de-convolution of the peaks would have been necessary but due to the high noise of the spectra coming from the spectrometer some intensity influenced by La is present in Ni peak. It can be concluded from the HAADF images of the superlattices and the presence of satellite reflections in the diffraction patterns

Element	Energy edge	Energy	Energy edge	Energy
La	M_5	832	M_4	849
Ni	L_3	855	L_2	872

Table 7.4: Energy bands for elemental La and Ni

that there are large areas of homogeneously layered structure which indicates the growth was epitaxial as confirmed also by XRD scans. However, after more exhaustive STEM analysis it was found that anomalies were present in the structure that are discussed in the next section.

7.1.7 Microstructures

Interfaces are often the determining factor in transport properties of oxide heterostructures and their electronic properties sometimes completely differ from the individual constituents. However, the entire heterostructure can be affected by macroscopic properties of the microstructure such as formation of dislocations, planar defects or secondary phases. Their formation alters the transport properties by interfering with the movement of the charge carriers in the layered system. Their presence is unfavourable and more often occurs unintentionally during the growth process. Consequently, in addition to the structural and functional properties measurements, the microstructure of the layers should be characterised on an atomic scale. When tailoring the functional properties of oxide heterostructures by changing the strain, layer thickness etc., it is necessary to study the microstructure to ensure the observed characteristics are solely due to the altered structure of the interface and not caused by microstructures. In this way it is valid to correlate the sample design and the properties of heterostructure.

Although the superlattices show interference fringes in the XRD corresponding to the expected nominal total thickness which is also in agreement with the electron diffraction observations, the presence of excess LaO layers is observed in the $(5/5)_{10}$, $(1/1)_{50}$ and $(1/1)_{100}$ superlattices when investigated by STEM. The presence of such faults has been reported previously in perovskite heterostructures [271, 272, 273]. The following images are examples of the observed faults. Figure 7.18-a) is a HAADF image representative of these faults in the $(1/1)_{50}$ superlattice. In panel (b) two regions 1 and 2 can be clearly observed. In region 2 the peaks corresponding to the different cations A and B in the ABO_3 compound have very different intensities. On the other hand, the difference in the intensity of the respective atomic columns becomes significantly less in region 1. This is likely due to extra LaO planes in this region [272]. The growth direction of the excess LaO layer in the $(1/1)_{50}$ superlattice changed from normal to parallel to the substrate surface, however, it was rarely seen in the 45 $^\circ$ to the substrate normal.

The mechanism to explain the intensity change between regions 1 and 2 in figure 7.18 is schematically shown in panel (c). In the $(1/1)_{50}$ superlattice extra LaO planes, are partially included in the region on the left and therefore the crystal shifts by 1/2 u.c. in the [011] direction relative to the other region. On the right, there is a rearrangement of the atomic columns in the $\langle 100 \rangle$ direction and the La columns of the shifted region overlap the Mn-O or Ni-O columns of the defect free region. It is relatively difficult to identify the Mn and Ni atoms due to the lack of Z contrast between them. As a result of this rearrangement the intensity difference between the two atomic columns decreases in region 2. This half a unit cell shift is a result of excess LaO occurs in both the (100) and (110) directions which is shown in figure 7.19 for the $(5/5)_{10}$ superlattice.

The microstructure observed in these superlattices ($(1/1)_{50}$ and $(5/5)_{10}$) represents the structure of a Ruddlesden-Popper (RP) phase. It was concluded from the previous chapter that the presence of a small amount of the RP phase could be the reason for a decrease in the resistivity of $LaNiO_3$ thin films. Consequently, the formation of $La_{n+1}Ni_nO_{3n+1}$ (with n=1) in the superlattices might be expected. The La_2NiO_4 is a natural superlattice consisting of alternating stacks of n layers of perovskite $LaNiO_3$ and a monolayer of rocksalt LaO both orientated along (001). In this case, the RP-type planar faults are a result of in-plane RP phases. There were observed both horizontally and vertically in the $(1/1)_{50}$ and $(5/5)_{10}$ superlattices. Figure 7.19-b shows a HAADF image with an extra LaO plane initially parallel to the interface. Two arrows in the profile indicate La atoms next to each other. An intensity variation spectra is shown for a region in the $(5/5)_{10}$ superlattice in figure 7.17. It clearly shows an extra layer of LaO has been inserted to the superlattice, the STEM image is also magnified to show the atomic position of the excess LaO layer clearly.

However, figure 7.19-a and -b show that extra LaO planes can be observed both parallel (green arrows) and perpendicular (red arrows) to the interface in the $(1/1)_{50}$ superlattice. The difference in the intensity distribution between area 1 and 2 is because of the RP phase. While the HAADF images of this heterostructure show a mosaic of RP phase. Although both horizontal and vertical Ruddlesden-Popper phases were abundant in the heterostructure, different features (figure 7.19-c and -d inside the blue ovals) were also observed. Nevertheless it is noticeable in panels -c and -d of figure 7.19 that not all the boundaries are parallel or perpendicular to the interface, but there are boundaries which lie at 45° which would correspond to (110) planes in the pseudocubic structure. By comparing the intensity an atomic distribution inside and outside the oval area can be found and this is seen to be very similar to the previously shown figures. The area inside the blue oval contains extra LaO plane partially inserted into the film. This has not been previously reported for this material system and it would be interesting to study

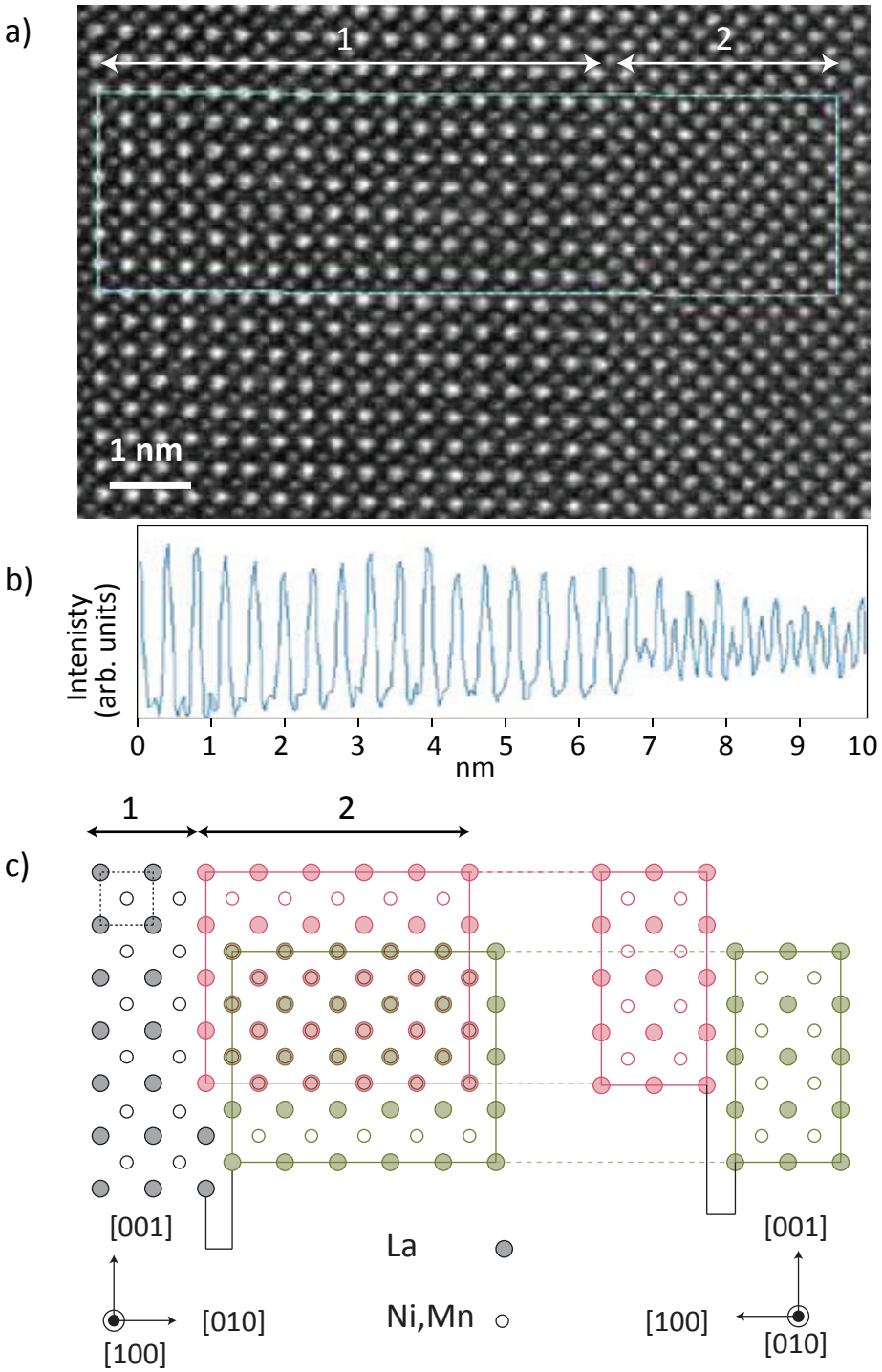

Figure 7.18: HAADF-STEM image of the $(1/1)_{50}$ superlattice b) intensity profile, and c) schematic representation of the fault explaining the decrease in intensity in region 2.

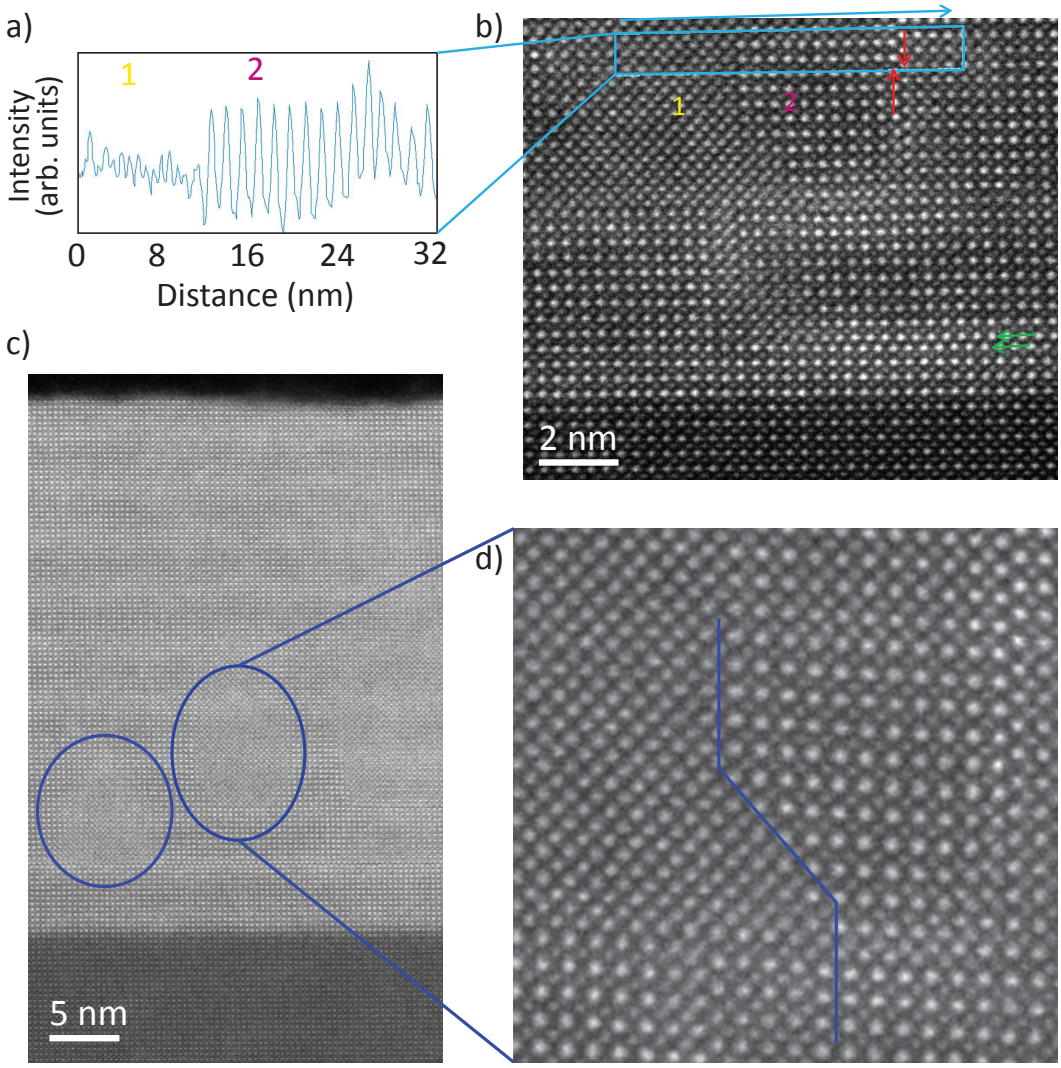

Figure 7.19: HAADF image of the $(5/5)_{10}$ superlattice. a) Showing the intensity variation measure for the blue box marked on b) which shows the mosaic RP phase. Extra LaO planes are included in the region 1. Extra LaO planes can be observed both parallel (green arrows) and perpendicular (red arrows) to the interface. c) HAADF image of the $(5/5)_{10}$ superlattice showing the 45° boundaries. d) is magnified area inside the blue oval that contains extra LaO plane partially inserted into the film, and a shift is produced, so the shifted region overlaps with the pristine one b) higher magnification image of thee 45° extra LaO layer

further and obtain information on the (110) plane boundaries within the pseudocubic perovskite structure or relate it to the RP phase formation. To determine the true origin of the faults caused by the RP phase, cross-sectional STEM of the superlattices along the $\langle 110 \rangle$ direction were performed.

$\langle 110 \rangle$ cross-sectional STEM

Interpretation of atomic resolution STEM for phase identification can be misleading as it is a 2D projection and to relate the observed images to the crystal structure requires changing the viewing point (i.e. Rotating the sample and studying different planes of the sample). This rotation is limited in the microscope and requires a cross-section specifically prepared for imaging the plane of interest. In perovskites the $\langle 100 \rangle$ planes are of interest due to increasing the possibility of identifying oxygen atoms and thus octahedral rotation. The $\langle 110 \rangle$ cross-section samples were prepared by conventional TEM preparation (section 3.3.2.1). Figure 7.20 shows the HAADF images taken along the $\langle 110 \rangle$ pseudocubic direction. No more straight and defined boundaries were observed similar to those seen along the $\langle 100 \rangle$ direction. As suggested by XRD the RP phase are preferably grown in-plane, a $LaNiO_3$ perovskite (a= 3.84 Å) structure was modelled which contained the RP structure. The viewing direction was rotated by 45° and is shown in panel c). However, the model does not match the HAADF images accurately, and further work is required. It has been shown that the coexistence of the RP phase can affect the stacking periodicity of the superlattices adversely. However, the effect of these microstructures on the functionality of superlattices is currently ambiguous. Preliminary magnetic measurements indicate an interesting effect of low dimensionality related to the superlattice on the total magnetic moment.

7.1.8 Bulk octahedral distortions

Diffraction patterns along the $\langle 100 \rangle$ zone axis of the $(5/5)_{10}$ superlattice are shown in figure 7.21. The diffraction spots are arranged in a square due to the pseudocubic crystal structure in this orientation. However, there are additional reflections in these 2 diffraction patterns taken from the same specimen ($(5/5)_{10}$), which are caused by the octahedral tilting. Considering the diffraction images are recorded over a much larger size range indicates that there is evidence for the existence of the octahedral tilting over a wide range. In figure 7.21, it can be seen clearly that the extra reflections are present in panel a) and b). To identify distortions or rotations of the octahedra from these diffraction patterns, it is necessary to determine the symmetry of the superlattice.

From Glazer [71, 72] tilting classification, $SrTiO_3$ substrate ($Pm\bar{3}m$) shows no

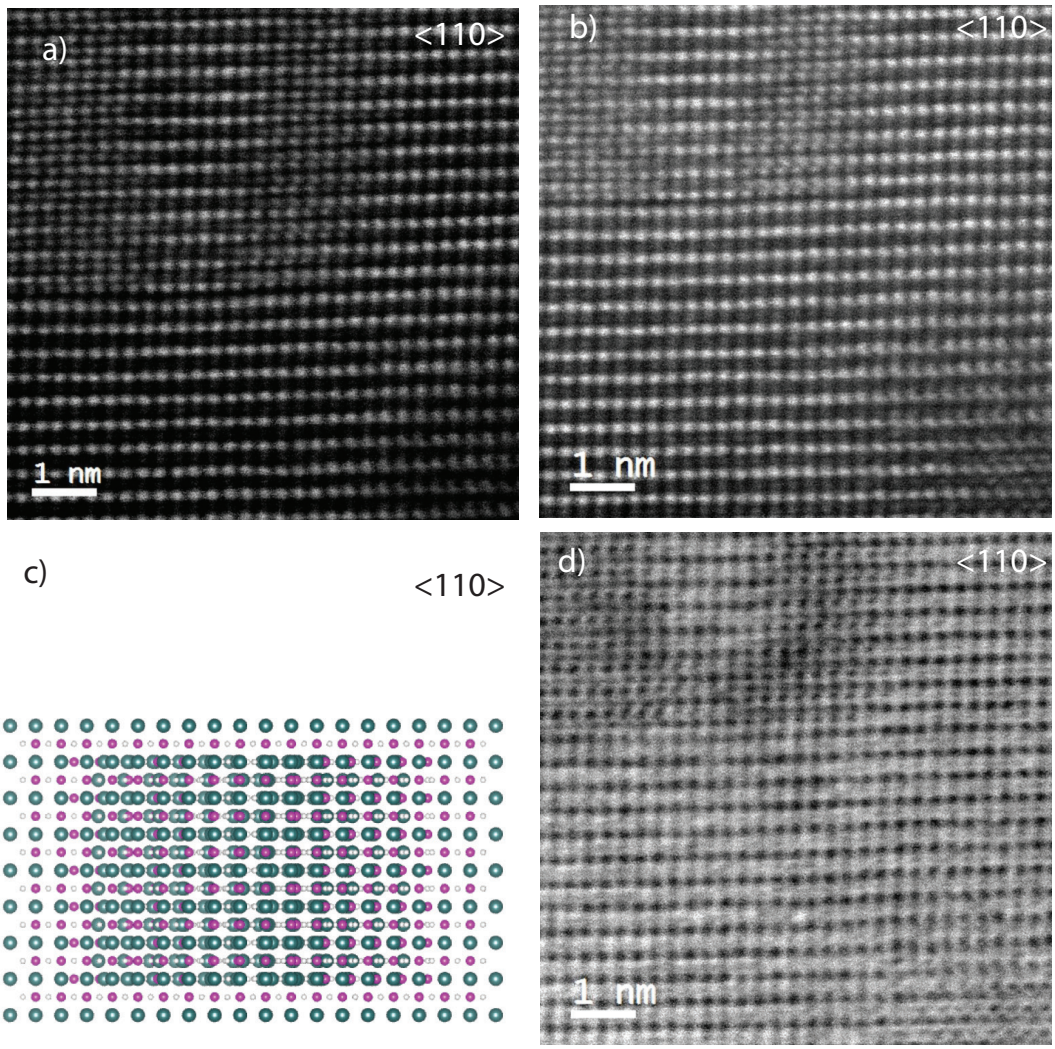

Figure 7.20: Ruddlesden-Popper faults imaged along the ⟨110⟩ direction a)) and b) annular dark field and d) bright field conditions respectively c) shows a 3d model structure of a perovskite lattice with RP grown in plane inside.

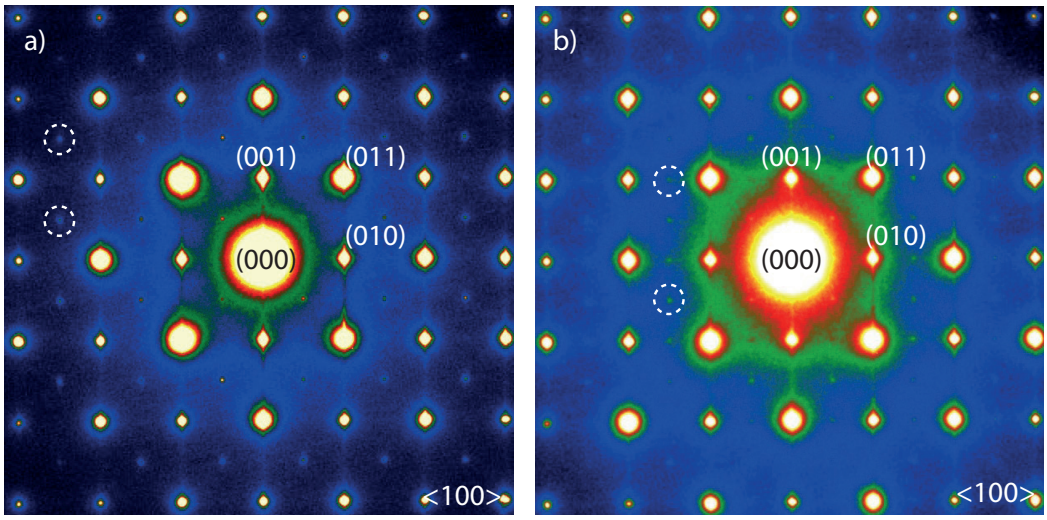

Figure 7.21: Diffraction patterns along the $\langle 100 \rangle$ zone axis of the $(5/5)_{10}$ superlattice a) and b) were diffraction patterns taken from different parts of the same specimen showing different tilting system exist in various domains of the structure. a) Superstructure reflections at $1/2\{\text{odd odd even}\}$ positions are present due to the in-phase tilting of octahedral along the viewing axis. b) The weak reflections are present at $1/2\{\text{odd even even}\}$ positions as a result of a combination of in-phase and anti-phase tilting within the $LaMnO_3$ unit cell.

tilting of the octahedra shown by $a^0a^0a^0$, $LaNiO_3$ has a $R\bar{3}c$ group symmetry with distinct tilt system of $(a^-a^-a^-)$. The $LaMnO_3$ undergoes a Jahn-Teller distortion and has a space-group symmetry of $Pnma$ with $a^+b^-b^-$. Woodward *et al.* [74] simulated the diffraction patterns for each of the perovskite tilts and compared them to the selected-area diffraction patterns. The extra reflections arising from the octahedral tilt were compared to their simulated data and the extra reflections appeared in panel a) in figure 7.21 is similar to data presented in their work. They concluded that, the $\frac{1}{2}\{odd\ even\ even\}$ reflections are not observed in exclusively anti-phase or in-phase tilt systems, therefore it can be concluded that TEM diffraction patterns of the superlattices are predominantly influenced by the $Pnma$ symmetry of the $LaMnO_3$ tilt system unlike the solely anti-phase tilt system in $LaNiO_3$. Whereas, The $\frac{1}{2}\{odd\ even\ even\}$ reflections can be used as a helpful indication of mixed tilting system, it should be noted cautiously that the displacement of cations in an anti-parallel manner can also lead to a doubling along $\langle 100 \rangle$ directions [74]. In section 7.1.3 it was discussed that the top layers showed surface reconstruction due to the tilting of oxygen octahedra in a $Pnma$ orthorhombic structure. This is in agreement with the diffraction pattern shown in panel (a) of figure 7.21. However, panel (b) shows extra spots in $\frac{1}{2}(0\ k\ l)$ when $k \neq l$ an indication of a

phase change in the tilting of octahedra. The $a^+b^-b^-$ tilt system can be identified as a result of cooperative Jahn-Teller distortion giving rise to the superposition reflections in TEM diffraction patterns (see figure 6 of ref. [74]). b) Weak reflections at $1/2\{$odd even even$\}$ positions arise from combination of in-phase and anti-phase tilting within the unit-cell of $LaMnO_3$ [274]. Extra reflections show that there are tilted domains superimposed in the film. The extra spots cannot be related to $LaNiO_3$ layer since $a^-a^-a^-$ anti-phase titling gives no superstructure reflections (figure 7 of ref. [74]). From the diffraction patterns shown in figure 7.21, it can be concluded that none of the reflections arise from the $LaNiO_3$, and $LaMnO_3$ is more likely to be the origin of the observed reflection spots. A further experiment to investigate this would be rotating to a different zone axis such as [110] or growing the superlattices on different crystal planes of the substrate, eg [110] or [111].

7.1.9 Magnetic properties

M(H) and M(T) magnetic measurements were performed on the $(1/1)_{50}$, $(2/2)_{25}$, and $(5/5)_{10}$ superlattices. All 3 superlattices showed weak ferromagnetism with a magnetisation comparable to that of the 70 nm $LaMnO_3$ thin film grown under the same deposition conditions. Figure 7.22 shows ZFC temperature dependent magnetisation measurements for the superlattices. As a reference the 70 nm thin film of $LaMnO_3$ is also shown. The diamagnetic signal of the substrate was subtracted by measuring the bare substrate over the same temperatures and magnetic field range as the superlattices and then subtracted using the SQUID built-in software. It can be seen that the $(2/2)_{25}$

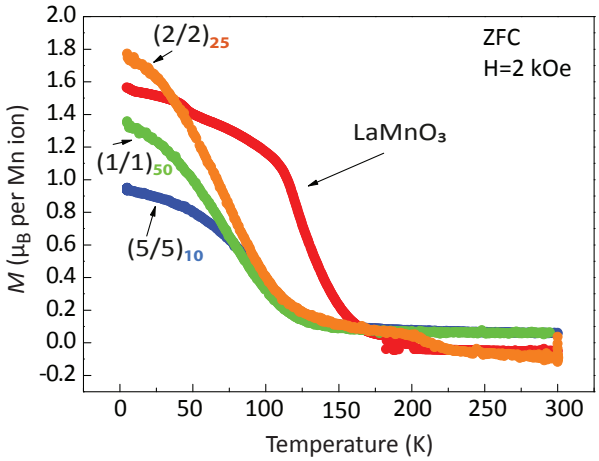

Figure 7.22: Magnetisation as a function of temperature with 2 kOe magnetic field applied along the axis M(T) curves for superlattices grown with various periodicity.

superlattice shows higher magnetisation at low temperature when compared to both the $(5/5)_{10}$ and $(1/1)_{50}$ superlattices. It also shows higher magnetisation per Mn ion than thick $LaMnO_3$ films. This suggests a weak enhancement in the net magnetisation of the Ni site in the $(2/2)_{25}$ superlattice. In the ideal case, B-site cations (Ni and Mn) are separated and shifted half a u.c. out-of-plane by the LaO planes. The magnetic behaviour of superlattice containing an even number of $LaMnO_3$ layers can be discussed form the chemical environment of MnO_2. The situation is different for odd-stacking numbers of $LaMnO_3$ layers, particularly in the case of the $(1/1)_{50}$ superlattice as the stacking sequence is (LaO)-(NiO_2)-(LaO)-(MnO_2)-(LaO)-(NiO_2), and hence the environment of MnO_2 differs from the chemical environment found in bulk $LaMnO_3$. Conversely, the environment of MnO_2 in the $(2/2)_{25}$ superlattice is chemically symmetric resulting in magnetic behaviour closer to that of the bulk $LaMnO_3$ [248].

7.2 Summary

Detailed surface analysis of the superlattices revealed a $(\sqrt{2} \times \sqrt{2})\ R45^\circ$ orthorhombic arrangement due to the distortion of the MnO_6. The RHEED data suggests that the growth of these materials is optimised with purely 2D layer-by-layer growth mode. Strong intensity oscillations were observed and streaky patterns were seen in the RHEED suggesting a layer-by-layer growth mode. This does indeed occur in agreement with the out-of-plane XRD data obtained on the superlattices. It is unlikely that a truly 2D growth mode would be observed by RHEED if the precipitation of these RP phases was occurring simultaneously with growth. Therefore, it is suggested that the kinetics of this process are slower and, as a result of the non-stoichiometry combined with elevated temperature at low oxidisation conditions and RP phase forms. It is clear from this data that detailed *ex-situ* analysis of these superlattices is essential to truly understand the nature of the material properties required for devices.

Chapter 8

Conclusions and future work

8.1 Conclusions

In this thesis a wide range of techniques have been used to study the preparation of thin films of artificially layered lanthanum based oxides. Structural, chemical, electrical, and magnetic properties of lanthanum-based oxides have been studied systematically. State-of-the-art fabrication by UHV-PLD was used to take advantage of such controlled thin film deposition to engineer novel predesigned, layered materials. By varying the growth parameters, one can tune the structural and magnetic properties of lanthanum manganite thin films. If chosen carefully, thin films of specific crystal structures can be fabricated which would not otherwise be stable. Each constituent layer was carefully optimised to achieve high crystallinity and smooth interfaces. The observation of RHEED intensity oscillations during the growth allows precise growth rate control and the ability to design artificial lattices on the atomic level. This approach makes fabrication of exceptionally rare metastable superstructures possible. It has been shown that to achieve atomically sharp interfaces, surface treatment of the substrate was crucial. The conventional HF treatment [240] followed by annealing in a tube furnace was used to start the growth from single terminated surface of $SrTiO_3$ crystal to achieve atomically controlled fabrication of thin films and superlattices. The substrates used in this work were closely matched to the pseudocubic in-plane lattice parameter of the chosen layers. The orientation of the substrate crystal was (001) without any observed surface reconstruction. The structure and surface morphology of the treated substrates were examined by atomic force microscopy and x-ray diffraction, respectively, and the annealing temperature was optimised accordingly. The temperature of 1050 °C and an etching time of 30 s were determined to be appropriate for the purpose of single termination and also surface roughness within one unit cell of the perovskite $SrTiO_3$

crystal. Pulsed laser deposition was used to grow $LaMnO_3$ thin films on $SrTiO_3$ (001) substrates. Layers were successfully deposited, demonstrating the ability of self doping using an oxygen excess resulting in $LaMnO_{3+\delta}$ layers. The structural, transport, and magnetic properties of these $LaMnO_3$ thin films, grown at various substrate temperatures, were characterised in both low and high oxygen background pressures. The unusual magnetic properties, such as spin glass-like behaviour and an exchange bias, observed for the films grown at high temperatures in lower oxygen pressure is an indication of an intrinsically inhomogeneous magnetic state in the locality of the transition. There is an important question concerning the origin of such magnetic inhomogeneity. This can be attributed to the formation of antiferromagnetic correlation with the ferromagnetic phases. Considering the ground state antiferromagnetism in stoichiometric $LaMnO_3$, there is the possibility that such antiferromagnetic interactions can occur, even in oxygen rich thin films [275]. It can be concluded that, the unusual magnetic behaviour seen in the $LaMnO_3$ films grown at T_g=700 and 750 °C in p_{O_2}=10^{-4} mbar, appeared as a result of the antiferromagnetic correlation developing in the ferromagnetic phase. The effect of deposition conditions on the surface morphology suggested that films tend to lose more oxygen during the cooling cycle, as this effect is more severe in lower oxygen pressure for higher temperature of growth. Surface roughening occurred to the point where no diffraction pattern could be attained from the surface, suggesting oxygen loss occurred after deposition when cooling in low oxygen pressures. To avoid this adverse effect on the stoichiometry and also at the surface morphology, later samples were cooled in a high oxygen pressure of 150 mbar. It would be of interest to run these experiments in an oxygen filled chamber during cooling and investigate the effect on the magnetic properties and also stoichiometry of the films.

It has also been established that for the $LaNiO_3$ thin films the resistivity falls and crystallinity improves as the growth temperature rises from 600 °C to 750 °C. The intensity of the (00l) reflections continues to increase as the temperature is increased. It was also found that at temperatures lower than 700 °C, a Ruddlesden-Popper (RP) family of nickelates (La_2NiO_4) coexists adversely affecting the resistivity. The films deposited at 750 °C found to have the best physical properties with strong RHEED specular intensity oscillations. XRD patterns of the films indicate the presence of a La_2NiO_4 second phase at lower growth temperatures. This contradicts what has been reported in the literature and explains the structural change by decomposition of $LaNiO_3$ at temperatures above 750 °C [211, 213, 214]. Increasing the growth temperature increases the uptake of oxygen during the cooling. Since it remains at a high temperature for longer oxygen better incorporates into the lattice. By contrast, the films grown at low temperatures are more oxygen deficient due to the shorter exposure to a high oxygen pressure. Oxygen

deficiency results in the formation of Ni^{2+} and the subsequent nucleation of La_2NiO_4 which is highly insulating. This was also confirmed by the highly insulating behaviour of the film grown at 600 °C. The lowest room temperature resistivity value of 2 mΩcm for the film grown at 750 °C is at the upper range of resistivity reported previously for $LaNiO_3$. The existence of an RP phase was confirmed using an in-plane grazing incidence XRD and also an atomic resolution STEM. There were traces of La_2NiO_4 remained in the film grown at 750 °C, although it could not be detected by out-of-plane XRD scans. It can therefore be concluded that, regardless of strong RHEED intensity oscillations, indicating a layer-by-layer growth mode, the physical properties of $LaNiO_3$ are strongly dependent on the oxidisation conditions. Hence, a higher oxygen background pressure is required to eliminate non-stoichiometric growth. Considering that the $LaNiO_3$ target contains 95 % RP phase, it can be concluded that the role of the target is more dominant than that of the growth conditions. Moreover, the existence of the RP phase has been reported previously for $LaNiO_3$ superlattices where the authors claimed the target was stoichiometric [271]. Ultra-thin films of $LaNiO_3$ were grown on TiO_2 single terminated $SrTiO_3$ substrates. The effect of surface termination on the growth quality was clear and layer-by-layer growth with strong oscillation for 3 ML of $LaNiO_3$ was observed. RHEED patterns obtained from the films suggested that the films were coherently grown on the substrate and fully strained.

Using RHEED and XRD the growth was optimised for each layer of $LaMnO_3$ and $LaNiO_3$. Epitaxial $(n/m)_x$ superlattices consisting n unit cells of $LaNiO_3$ and m unit cells of $LaMnO_3$ were deposited on $SrTiO_3$ (001) using real-time monitoring of RHEED intensity oscillations. The stacking periodicity was repeated x times to grow a 100 unit cell. However, the instability of $LaNiO_3$ leads to a secondary phase of the RP La_2NiO_4 within the superlattices. Only within a small PLD growth window, such as target, laser, substrate temperature and oxygen pressure, can (cation) stoichiometric $LaNiO_3$ and $LaMnO_3$ thin films be synthesised from a stoichiometric target. It has been shown in this work that regardless of the non-stoichiometric transfer of the cations during ablation, strong RHEED intensity oscillations and layer-by-layer (2D) growth mode can be observed. Although the structural properties of $LaNiO_3$, $LaMnO_3$ and the superlattice containing them stay intact for large stoichiometric deviations, even small percentage deviations can lead to changes in the transport and magnetic properties of them. The RP phase was detected in the $LaNiO_3$ single layer film and also the superlattice containing $LaNiO_3$ using STEM microstructure analysis. It is unlikely that a truly 2D growth mode would be observed by RHEED if the precipitation of the RP phases was occurring simultaneously with growth. It is clear from this data that detailed *ex-situ* analysis of these superlattices is essential to truly understand the nature of the materials properties required for devices.

8.2 Future work

The unusual magnetic transition observed in $LaMnO_3$ thin films grown in low oxygen background pressure and temperatures above 700 °C could be a consequence of magnetic frustration occurring near the grain boundary regions leading to a glassy-like state. By performing temperature dependant AC-susceptibility measurements in an applied field at various frequencies, this point can be clarified. If the position of the real AC-susceptibility peak does not show any dependence on frequency, the presence of glassy-like state could be ruled out. There remain several questions to be answered for the existence of the secondary phase of RP in the superlattice samples. The initial investigation suggested the non-stoichiometry target material of $LaNiO_3$ to be the main reason and this was further investigated using EDX and XRD. While the EDX results showed a La:Mn ratio of 1:1, the XRD results were surprisingly different and showed no perovskite phase at all. Further work should be done to investigate the origin of this phase transformation. At 900 °C, decomposition of the perovskite $LaNiO_3$ to the RP phase occurs. It is unlikely that the whole target reaches such a temperature as a result of the laser irradiation, although it can be tested by performing XRD after a couple of thousands laser pulses at the energy density that was used during this work. The present results are not sufficient on their own to draw a final conclusion, since there is no information on the target phase purity and stoichiometry prior to deposition. The way forward should be to fabricate new stoichiometric targets, then deposit $LaNiO_3$ films with the exact deposition conditions used in this work. If the RP phase is seen again then the growth dynamics should be investigated. TEM microstructure studies along with grazing angle in-plane XRD proved to be the right tools to verify the stoichiometry. Temperature dependant Hall-effect measurements can be used to monitor the electrical properties of $LaNiO_3$ films since stoichiometric $LaNiO_3$ films show metallic behaviour at all temperatures.

HAADF images revealed the existence of both horizontal and vertical RP planer faults in the $(1/1)_{50}$ and $(5/5)_{10}$ heterostructures. However, not all the boundaries were parallel or perpendicular to the interface, as there were also boundaries which lie at 45 ° to the interface that could corresponding to (110) planes in a pseudocubic structure. This has not been previously reported for this material system and excessive data analysis is required for truly understanding the formation of the RP phase in $LaNiO_3$ thin films and also in the nickelate based superlattices. For example, digital-large angle convergent beam electron diffraction (D-LACBED) is a new approach that can be used to characterise several types of defects such as stalking faults, anti-phase boundaries, and dislocations. By digitally controlling the movement of the aperture in a TEM, a series of

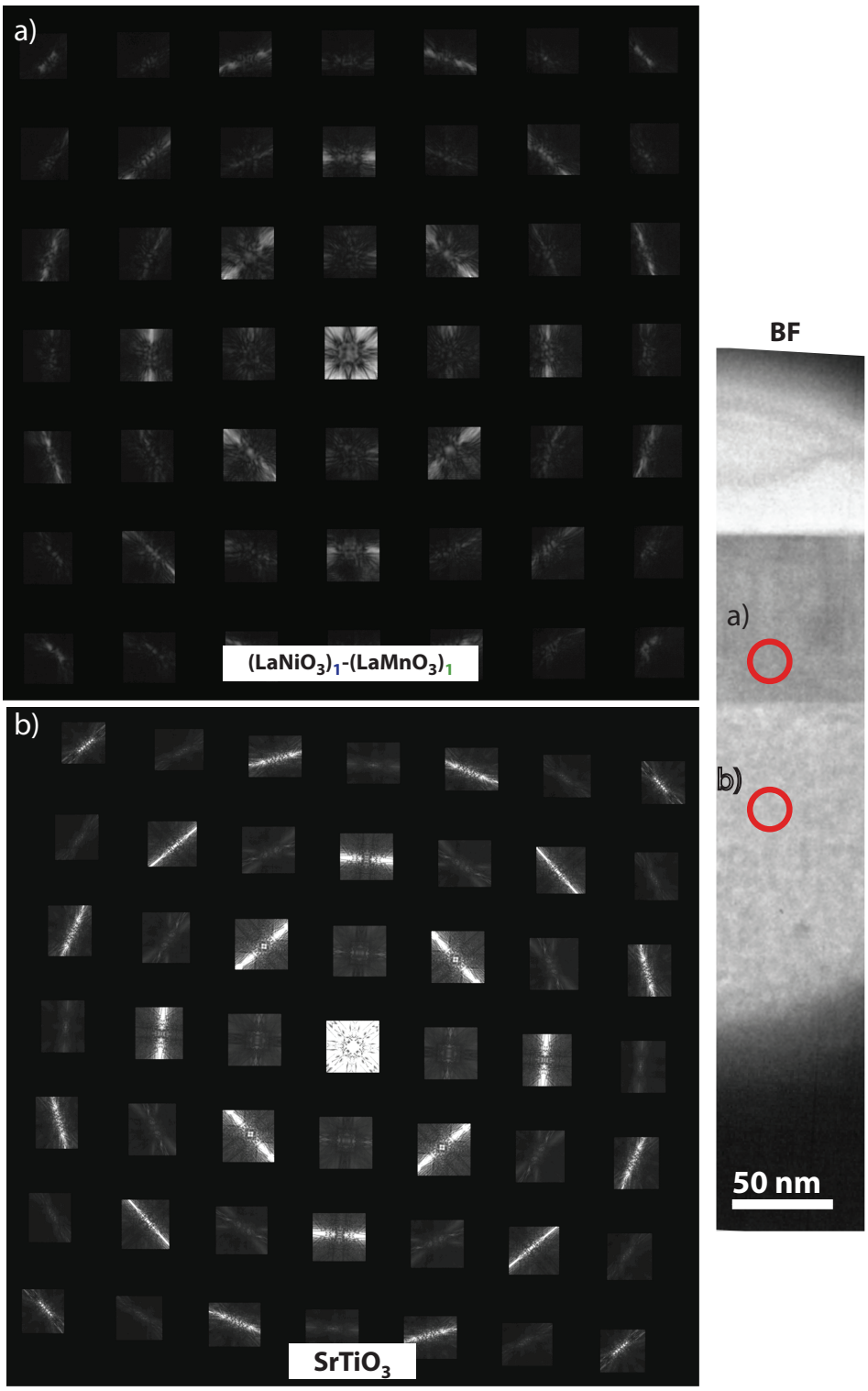

Figure 8.1: D-LACBED pattern produced by recombining the (000) beam (a) the $(1/1)_{100}$ superlattice and (b) $SrTiO_3$ substrate with $Pm\bar{3}m$ symmetry. The film has clearly lost the 3 fold mirror symmetry of the substrate.

convergent beam electron diffraction (CBED) patterns can be collected and reconstructed to from a large angle convergent beam electron diffraction (LACBED) pattern. This was performed on the $(1/1)_{100}$ superlattice where the RP faults were abundant and on the fault-free perovskite substrate. The BF HR-TEM and the corresponding place where the LACBED was measured are encircled (see panel (a) in figure 8.1 the $(1/1)_{100}$ superlattice and panel (b) the $SrTiO_3$ substrate). In contrast to panel (b) (the cubic $SrTiO_3$ with perfect perovskite structure), the D-LACBED pattern of the $(1/1)_{100}$ superlattice in panel (a) shows lower symmetry. In this manner the centre of the pattern is the (000) disc which always shows at least two-fold symmetry. It is clear from the panel (b) of figure 8.1 that the mirror symmetries corresponding to a cubic material are not present in this pattern. For the future work the D-LACBED images can be quantitatively compared to the simulated patterns for the $[000]$ straight through beam. This is a novel technique to resolve structure and space group of the perovskite thin films and superlattices.

The observed $(\sqrt{2} \times \sqrt{2})\ R45^\circ$ surface reconstruction seen for the $LaNiO_3$-$LaMnO_3$ superlattices gives rise to fractional streaks when the electron beam is aligned along the $< 110 >$ crystallographic orientation of the $SrTiO_3$ substrate. Their origin was associated with the oxygen octahedral tilting during the growth. By real-time monitoring of these spots, deposition can be stopped at the desired termination. Surface X-ray diffraction can give valuable information on the in-plane coherence length of the orthorhombic unit cell at the surface formed as a result of the distortion of the MnO_6 octahedra. The effect of the periodicity of the superlattice on the long range order of the orthorhombic surface unit-cell can be studied quantitatively using the structural refinement of SXRD data. The effect of the non Jahn-Teller Ni^{3+} ion on the scale of the Jahn-Teller component and rotations about the pseudocubic axis of MnO_6 in $(1/1)_{50}$ superlattice can also be investigated using this method.

The content of this thesis has attempted to demonstrate the huge strides that have been made in the crystalline growth of perovskite oxide thin films using PLD. It has, however, only scratched the surface with an investigation of $LaNiO_3$ and $LaMnO_3$ thin films and superlattices. It was illustrated an experimental route by which the rotation and tilting of the functional BO_6 octahedral units can be detected. There remains a number of potential directions for future work, in particular, the opportunity to use epitaxial constrains in targeted perovskites to possibly achieve new ground-states inaccessible in their bulk. Full exploration of these exciting opportunities can be achieved not only by epitaxial strain thorough the lattice mismatch but also via the symmetry mismatch resulting in a unique octahedral tilting system, therefore, different properties. Consequently, *in-situ* surface analysis during the growth could provide a structural-driven control method of the desired functional properties in perovskite heterostructures.

Bibliography

[1] R. Federico. Nanostructured surfaces: challenges and frontiers in nanotechnology. *Journal of Physics: Condensed Matter*, **16**(17):S1373, 2004.

[2] Feynman R. P. There's plenty of room at the bottom, Eng. Sci. J. (http://www.its.caltech.edu/feynman/plenty.html), 1959.

[3] Project on Emerging Nanotechnologies. Consumer products inventory (http://www.nanotechproject.org/cpi/), 2014.

[4] CAMP Technical Adventure Equipment. Corsa nanotech, (http://www.camp-usa.com/products/ice-axes/corsa-nanotech.asp), 2014.

[5] Project on Emerging Nanotechnologies. Iogear germ free wireless laser mouse, consumer products inventory (http://www.nanotechproject.org/cpi/products/iogear-r-germ-free-wireless-laser-mouse/), 2014.

[6] D. M. Eigler and E. K. Schweizer. Positioning single atoms with a scanning tunnelling microscope. *Nature*, **344**(6266):524–526, 1990.

[7] A. J. Heinrich, C. P. Lutz, J. A. Gupta, and D. M. Eigler. Molecule cascades. *Science*, **298**(5597):1381–1387, 2002.

[8] M. Brust, D. J. Schiffrin, D. Bethell, and C. J. Kiely. Novel gold-dithiol nano-networks with non-metallic electronic properties. *Advanced Materials*, **7**(9):795–797, 1995.

[9] M. Schulz. The end of the road for silicon? *Nature*, **399**(6738):729–730, 1999.

[10] B. E. Kane. A silicon-based nuclear spin quantum computer. *Nature*, **393**(6681):133–137, 1998.

[11] J. M. D. Coey. *Magnetism and Magnetic Materials*. Cambridge University Press, Cambridge, UK, 2010.

[12] M. Gajek, M. Bibes, S. Fusil, K. Bouzehouane, J. Fontcuberta, A. Barthelemy, and A. Fert. Tunnel junctions with multiferroic barriers. *Nat Mater*, **6**(4):296–302, 2007.

[13] A. Ruotolo, F. Miletto Granozio, A. Oropallo, G. P. Pepe, P. Perna, U. Scotti di Uccio, D. Pullini, G. Innocenti, and P. Perlo. Novel low-field magnetoresistive devices based on manganites. *Journal of Magnetism and Magnetic Materials*, **310**(2, Part 3):e684–e686, 2007.

[14] W. Eerenstein, M. Wiora, J. L. Prieto, J. F. Scott, and N. D. Mathur. Giant sharp and persistent converse magnetoelectric effects in multiferroic epitaxial heterostructures. *Nat Mater*, **6**(5):348–351, 2007.

[15] H. Yamada, Y. Ogawa, Y. Ishii, H. Sato, Masashi Kawasaki, H. Akoh, and Y. Tokura. Engineered interface of magnetic oxides. *Science*, **305**(5684):646–648, 2004.

[16] J. Chakhalian, J. W. Freeland, H.-U. Habermeier, G. Cristiani, G. Khaliullin, M. van Veenendaal, and B. Keimer. Orbital reconstruction and covalent bonding at an oxide interface. *Science*, **318**(5853):1114–1117, 2007.

[17] J. Chakhalian, A. J. Millis, and J. Rondinelli. Whither the oxide interface. *Nature Materials*, **11**(2):92–94, 2012.

[18] J. De Teresa, A. Barthlmy, A. Fert, Jean P. Contour, F. Montaigne, and P. Seneor. Role of metal-oxide interface in determining the spin polarization of magnetic tunnel junctions. *Science*, **286**(5439):507–509, 1999.

[19] E. Dagotto. Complexity in strongly correlated electronic systems. *Science*, **309**(5732):257–262, 2005.

[20] Y. Tokura and Y. Tomioka. Colossal magnetoresistive manganites. *Journal of Magnetism and Magnetic Materials*, **200**(13):1–23, 1999.

[21] J. G. Bednorz and K. A. Mller. Possible hight c superconductivity in the BaLaCuO system. *Zeitschrift fr Physik B Condensed Matter*, **64**(2):189–193, 1986.

[22] A. P. Ramirez. Colossal magnetoresistance. *Journal of Physics-Condensed Matter*, **9**(39):8171–8199, 1997.

[23] R. von Helmolt, J. Wecker, B. Holzapfel, L. Schultz, and K. Samwer. Giant negative magnetoresistance in perovskitelike LaBaMnO$_x$ ferromagnetic films. *Phys. Rev. Lett.*, **71**(14):2331–2333, 1993.

[24] K. Chahara, T. Ohno, M. Kasai, and Y. Kozono. Magnetoresistance in magnetic manganese oxide with intrinsic antiferromagnetic spin structure. *Applied Physics Letters*, **63**(14):1990–1992, 1993.

[25] S. Jin, T. H. Tiefel, M. McCormack, R. A. Fastnacht, R. Ramesh, and L. H. Chen. Thousandfold change in resistivity in magnetoresistive La-Ca-Mn-o films. *Science*, **264**(5157):413–415, 1994.

[26] P. Orgiani, A. Galdi, C. Aruta, V. Cataudella, G. De Filippis, C. A. Perroni, V. Marigliano Ramaglia, R. Ciancio, N. B. Brookes, M. Moretti Sala, G. Ghiringhelli, and L. Maritato. Multiple double-exchange mechanism by Mn^{2+} doping in manganite compounds. *Phys. Rev. B*, **82**:205122, 2010.

[27] J. Park, G. Park, I. Song, J. Bae, J. Lee, J. Yoo, Y. Murakami, and D. Shindo. Analysis of magnetic microstructure in mram bits by electron holography and lorentz microscopy. *Journal of Electron Microscopy*, **55**(1):17–21, 2006.

[28] L. Balcells, E. Calvo, and J. Fontcuberta. Room-temperature anisotropic magnetoresistive sensor based on manganese perovskite thick films. *Journal of Magnetism and Magnetic Materials*, **242245, Part 2**(0):1166–1168, 2002.

[29] G. J. H. M. Rijnders, G. Koster, D. H. A. Blank, and H. Rogalla. In situ monitoring during pulsed laser deposition of complex oxides using reflection high energy electron diffraction under high oxygen pressure. *Applied Physics Letters*, **70**(14):1888–1890, 1997.

[30] A. Ohtomo and H. Y. Hwang. A high-mobility electron gas at the $LaAlO_3/SrTiO_3$ heterointerface. *Nature*, **427**(6973):423–426, 2004.

[31] L. W. Martin, Y. H. Chu, and R. Ramesh. Advances in the growth and characterization of magnetic, ferroelectric, and multiferroic oxide thin films. *Materials Science and Engineering: R: Reports*, **68**(4-6):89–133, 2010.

[32] P. Zubko, S. Gariglio, M. Gabay, P. Ghosez, and J. Triscone. Interface physics in complex oxide heterostructures. *Annual Review of Condensed Matter Physics*, **2**(1):141–165, 2011.

[33] S. Dong and E. Dagotto. Quantum confinement induced magnetism in $LaNiO_3$ superlattices. *Physical Review B*, **87**(19):195116, 2013.

[34] A. T. Lee and M. J. Han. Charge transfer, confinement, and ferromagnetism in $LaMnO_3$ (001) superlattices. *Physical Review B*, **88**(3):035126, 2013.

[35] H. S. Kim and H. M. Christen. Controlling the magnetic properties of $LaMnO_3$ thin films on srtio 3 (100) by deposition in a O_2/Ar gas mixture. *Journal of Physics: Condensed Matter*, **22**(14):146007, 2010.

[36] J. Hubbard. Electron correlations in narrow energy bands. *Proceedings of the Royal Society of London. Series A. Mathematical and Physical Sciences*, **276**(1365):238–257, 1963.

[37] N. F. Mott. The basis of the electron theory of metals, with special reference to the transition metals. *Proceedings of the Physical Society. Section A*, **62**(7):416, 1949.

[38] Mark T. Greiner and Zheng-Hong Lu. Thin-film metal oxides in organic semiconductor devices: their electronic structures, work functions and interfaces. *NPG Asia Mater*, **5**:e55, 2013.

[39] F. J. Morin. Oxides of the 3d transition metals. *Bell System Technical Journal*, **37**(4):1047–1084, 1958.

[40] S. Blundell. *Magnetism in condensed matter*. Oxford University Press, Oxford, 2001.

[41] B. Jeroen van den. Orbital-only models: ordering and excitations. *New Journal of Physics*, **6**(1):201, 2004.

[42] J. Kanamori. Crystal distortion in magnetic compounds. *Journal of Applied Physics*, **31**(5):S14–S23, 1960.

[43] K.I. Kugel and D.I. Khomskii. Crystal structure and magnetic properties of substances with orbital degenracy. *Sov. Phys. JETP*, **37**:725, 1973.

[44] J. M. D. Coey, M. Viret, and S. von Molnr. Mixed-valence manganites. *Advances in Physics*, **48**(2):167–293, 1999.

[45] F. Moussa, M. Hennion, J. Rodriguez-Carvajal, H. Moudden, L. Pinsard, and A. Revcolevschi. Spin waves in the antiferromagnet perovskite $Lamno_3$: A neutron-scattering study. *Physical Review B*, **54**(21):15149–15155, 1996.

[46] Y. Murakami, J. P. Hill, D. Gibbs, M. Blume, I. Koyama, M. Tanaka, H. Kawata, T. Arima, Y. Tokura, K. Hirota, and Y. Endoh. Resonant x-ray scattering from orbital ordering in $LaMnO_3$. *Physical Review Letters*, **81**(3):582–585, 1998.

[47] J. B. Goodenough and J. S. Zhou. Orbital ordering in orthorhombic perovskites. *Journal of Materials Chemistry*, **17**(23):2394–2405, 2007.

[48] J. B. Goodenough. An interpretation of the magnetic properties of the perovskite-type mixed crystals $La_{1-x}Sr_xCoO_{3-\lambda}$. *Journal of Physics and Chemistry of Solids*, **6**(23):287–297, 1958.

[49] J. Kanamori. Superexchange interaction and symmetry properties of electron orbitals. *Journal of Physics and Chemistry of Solids*, **10**(23):87–98, 1959.

[50] P. W. Anderson. Antiferromagnetism. theory of superexchange interaction. *Physical Review*, **79**(2):350–356, 1950.

[51] E. O. Wollan and W. C. Koehler. Neutron diffraction study of the magnetic properties of the series of perovskite-type compounds. *Physical Review*, **100**(2):545–563, 1955.

[52] J. B. Goodenough. Theory of the role of covalence in the perovskite-type manganites [La, M(II)]MnO_3. *Phys. Rev.*, **100**:564–573, Oct 1955.

[53] C. Zener. Interaction between the d-shells in the transition metals. ii. ferromagnetic compounds of manganese with perovskite structure. *Physical Review*, **82**(3):403–405, 1951.

[54] M. Fiebig. Revival of the magnetoelectric effect. *Journal of Physics D-Applied Physics*, **38**(8):R123–R152, 2005.

[55] Masatoshi Imada, Atsushi Fujimori, and Yoshinori Tokura. Metal-insulator transitions. *Reviews of Modern Physics*, **70**(4):1039–1263, 1998.

[56] S. Cheong and M. Mostovoy. Multiferroics: a magnetic twist for ferroelectricity. *Nature Materials*, **6**(1):13–20, 2007.

[57] E. Dagotto, T. Hotta, and A. Moreo. Colossal magnetoresistant materials: The key role of phase separation. *Physics Reports-Review Section of Physics Letters*, **344**(1-3):1–153, 2001.

[58] M. B. Salamon and M. Jaime. The physics of manganites: Structure and transport. *Reviews of Modern Physics*, **73**(3):583–628, 2001.

[59] R. D. Snchez, M. T. Causa, A. Caneiro, A. Butera, M. Vallet-Reg, M. J. Sayagus, J. Gonzlez-Calbet, F. Garca-Sanz, and J. Rivas. Metal-insulator transition in oxygen-deficient $LaNiO_{3-x}$ perovskites. *Physical Review B*, **54**(23):16574–16578, 1996.

[60] G. Catalan. Progress in perovskite nickelate research. *Phase Transitions*, **81**(7-8):729–749, 2008.

[61] J. B. Torrance, P. Lacorre, A. I. Nazzal, E. J. Ansaldo, and Ch Niedermayer. Systematic study of insulator-metal transitions in perovskites $RNiO_3$ (R=Pr,Nd,Sm,Eu) due to closing of charge-transfer gap. *Physical Review B*, **45**(14):8209–8212, 1992.

[62] R. Scherwitzl, S. Gariglio, M. Gabay, P. Zubko, M. Gibert, and J. M. Triscone. Metal-insulator transition in ultrathin $LaNiO_3$ films. *Physical Review Letters*, **106**(24):246403, 2011.

[63] J. W. Freeland, Jian Liu, M. Kareev, B. Gray, J. W. Kim, P. Ryan, R. Pentcheva, and J. Chakhalian. Orbital control in strained ultra-thin $LaNiO_3$-$LaAlO_3$ superlattices. *Epl*, **96**(5), 2011.

[64] J. Son, J. M. LeBeau, S. J. Allen, and S. Stemmer. Conductivity enhancement of ultrathin $LaNiO_3$ films in superlattices. *Applied Physics Letters*, **97**(20):202109, 2010.

[65] J. Chaloupka and G. Khaliullin. Orbital order and possible superconductivity in $LaNiO_3/LaMo_3$ superlattices. *Physical Review Letters*, **100**(1):016404, 2008.

[66] M. Gibert, P. Zubko, R. Scherwitzl, J Iniguez, and J. Triscone. Exchange bias in $LaNiO_3$-$LaMnO_3$ superlattices. *Nature Materials*, **11**(3):195–198, 2012.

[67] J. Hoffman, I. C. Tung, B. B. Nelson-Cheeseman, M. Liu, J. W. Freeland, and A. Bhattacharya. Charge transfer and interfacial magnetism in $LaNiO_3$-$LaMnO_3$ superlattices. *Physical Review B*, **88**(14):144411, 2013.

[68] V. M. Goldschmidt. Die gesetze der krystallochemie. *Naturwissenschaften*, **14**(21):477–485, 1926.

[69] R. Beanland. Structure of planar defects in tilted perovskites. *Acta Crystallographica Section A*, **67**:191–199, 2011.

[70] K. M. Rabe, C. H. Ahn, and J. Triscone. *Physics of Ferroelectrics, A Modern Perspective*. Springer, USA, 2007.

[71] A. Glazer. The classification of tilted octahedra in perovskites. *Acta Crystallographica Section B*, **28**(11):3384–3392, 1972.

[72] A. Glazer. Simple ways of determining perovskite structures. *Acta Crystallographica Section A*, **31**(6):756–762, 1975.

[73] C. J. Howard and H. T. Stokes. Group-theoretical analysis of octahedral tilting in perovskites. *Acta Crystallographica Section B*, **54**(6):782–789, 1998.

[74] D. I. Woodward and I. M. Reaney. Electron diffraction of tilted perovskites. *Acta Crystallographica Section B*, **61**(4):387–399, 2005.

[75] J. M. Rondinelli, S. J. May, and J. W. Freeland. Control of octahedral connectivity in perovskite oxide heterostructures: An emerging route to multifunctional materials discovery. *MRS Bulletin*, **37**(03):261–270, 2012.

[76] G. K. Hubler D. B. Chrisey. *Pulsed Laser Deposition of Thin Films*. Wiley-Blackwell, 1994.

[77] P. R. Willmott and J. R. Huber. Pulsed laser vaporization and deposition. *Reviews of Modern Physics*, **72**(1):315–328, 2000.

[78] R. Eason. *Pulsed Laser Deposition of Thin Films: Applications-Led Growth of Functional Materials*. John Wiley and Sons, Inc., 2006.

[79] H. Krebs, M. Weisheit, J. Faupel, E. Saske, T. Scharf, C. Fuhse, M. Starmer, K. Sturm, M. Seibt, H. Kijewski, D. Nelke, E. Panchenko, and M. Buback. *Pulsed Laser Deposition (PLD) – A Versatile Thin Film Technique*, volume 43 of *Advances in Solid State Physics*, chapter 36, pages 505–518. Springer Berlin Heidelberg, 2003.

[80] Rijnders G. and Blank D. H. A. *Real-Time Growth Monitoring by High-Pressure RHEED During Pulsed Laser Deposition*, pages 355–384. Springer, USA, 2005.

[81] D. Basting. *Excimer Laser Technology: laser sources, optics, systems and applications*. Lambda Physik AG, Goettingen, Germany, 2001.

[82] M. N. R. Ashfold, F. Claeyssens, G. M. Fuge, and S. J. Henley. Pulsed laser ablation and deposition of thin films. *Chemical Society Reviews*, **33**(1):23–31, 2004.

[83] F. Bechstedt. *Principles of Surface Physics*. Springer-Verlag, Germany, 2003.

[84] M. Ohring. *Materials Science of Thin Films (Second Edition)*. Academic Press, San Diego, 2002.

[85] B. W. Wessels. Morphological stability of strained-layer semiconductors. In *Morphological stability of strained-layer semiconductors*, volume 15, pages 1056–1058. AVS.

[86] D. A. King Woodruff and D. P. *The Chemical Physics of Solid Surfaces*, volume 5. Elsevier, Amsterdam, 1988.

[87] R. A. McKee, F. J. Walker, and M. F. Chisholm. Crystalline oxides on silicon: The first five monolayers. *Physical Review Letters*, **81**(14):3014–3017, 1998.

[88] S. Wicklein, A. Sambri, S. Amoruso, X. Wang, R. Bruzzese, A. Koehl, and R. Dittmann. Pulsed laser ablation of complex oxides: The role of congruent ablation and preferential scattering for the film stoichiometry. *Applied Physics Letters*, **101**(13):131601, 2012.

[89] D. B Geohegan. Physics and diagnostics of laser ablation plume propagation for high-Tc superconductor film growth. *Thin Solid Films*, **220**(1-2):138–145, November 1992.

[90] S. Amoruso, A. Sambri, and X. Wang. Propagation dynamics of a $LaMnO_3$ laser ablation plume in an oxygen atmosphere. *Journal of Applied Physics*, **100**(1):13302, 2006.

[91] M. Strikovski and J. H Miller. Pulsed laser deposition of oxides: Why the optimum rate is about 1 Å per pulse. *Applied Physics Letters*, **73**(12):1733, 1998.

[92] J. Gonzalo, C. N. Afonso, J. Perrire, and R. Gmez San Roman. The importance of gas scattering processes on the stoichiometry deviations of laser deposited films. *Applied Surface Science*, **9698**(0):693–696, 1996.

[93] B. Dam, J. H. Rector, J. Johansson, S. Kars, and R. Griessen. Stoichiometric transfer of complex oxides by pulsed laser deposition. *Applied Surface Science*, **9698**(0):679–684, 1996.

[94] B. Dam, J. Rector, M. F. Chang, S. Kars, D. G. de Groot, and R. Griessen. The laser ablation threshold of yba2cu3o6+x as revealed by using projection optics. *Applied Surface Science*, **86**(14):13–17, 1995.

[95] R. K. Singh, O. W. Holland, and J. Narayan. Theoretical model for deposition of superconducting thin films using pulsed laser evaporation technique. *Journal of Applied Physics*, **68**(1):233–247, 1990.

[96] A. Sambri, S. Amoruso, X. Wang, F. Miletto Granozio, and R. Bruzzese. Plume propagation dynamics of complex oxides in oxygen. *Journal of Applied Physics*, **104**(5):053304, 2008.

[97] P. R. Willmott and J. R. Huber. Pulsed laser vaporization and deposition. *Rev. Mod. Phys.*, **72**:315–328, 2000.

[98] G. J. H. M. Rijnders. *The initial growth of complex oxides: Study and manipulation*. PhD thesis, 2001.

[99] M. Lippmaa, N. Nakagawa, M. Kawasaki, S. Ohashi, and H. Koinuma. Growth mode mapping of $SrTiO_3$ epitaxy. *Applied Physics Letters*, **76**(17):2439–2441, 2000.

[100] T. Okada, Y. Nakata, M. Maeda, and W. K. A. Kumuduni. Ultraviolet laser light scattering diagnostics of the plume in pulsed-laser deposition process. *Journal of Applied Physics*, **82**(7):3543–3547, 1997.

[101] M. Ohring. *Material science of thin films*. Academic Press, 2nd edition, 2002.

[102] M. Kareev, S. Prosandeev, B. Gray, Jian Liu, P. Ryan, A. Kareev, Eun Ju Moon, and J. Chakhalian. Sub-monolayer nucleation and growth of complex oxides at high supersaturation and rapid flux modulation. *Journal of Applied Physics*, **109**(11):114303, 2011.

[103] A. Yu Petrov, X. Torrelles, A. Verna, H. Xu, A. Cossaro, M. Pedio, J. Garcia-Barriocanal, G. R. Castro, and B. A. Davidson. Surface octahedral distortions and atomic design of perovskite interfaces. *Advanced Materials*, **25**(29):4043–4048, 2013.

[104] A. Ohtomo and H. Y. Hwang. Growth mode control of the free carrier density in $SrTiO_3$ films. *Journal of Applied Physics*, **102**(8):083704, 2007.

[105] T. Ohnishi, K. Shibuya, T. Yamamoto, and M. Lippmaa. Defects and transport in complex oxide thin films. *Journal of Applied Physics*, **103**(10):103703, 2008.

[106] C. M. Brooks, L. Fitting Kourkoutis, T. Heeg, J. Schubert, D. A. Muller, and D. G. Schlom. Growth of homoepitaxial $SrTiO_3$ thin films by molecular-beam epitaxy. *Applied Physics Letters*, **94**(16):162905, 2009.

[107] Masatoshi Imada, Atsushi Fujimori, and Yoshinori Tokura. Metal-insulator transitions. *Rev. Mod. Phys.*, **70**:1039–1263, 1998.

[108] J. Garcia-Barriocanal, J. C. Cezar, F. Y. Bruno, P. Thakur, N. B. Brookes, C. Utfeld, A. Rivera-Calzada, S. R. Giblin, J. W. Taylor, J. A. Duffy, S. B. Dugdale, T. Nakamura, K. Kodama, C. Leon, S. Okamoto, and J. Santamaria. Spin and orbital ti magnetism at $LaMnO_3/SrTiO_3$ interfaces. *Nat Commun*, **1**:82, 2010.

[109] T. M. Shaw, A. Gupta, M. Y. Chern, P. E. Batson, R. B. Laibowitz, and B. A. Scott. Atomic-scale oxide superlattices grown by rheed controlled pulsed-laser deposition. *Journal of Materials Research*, **9**(10):2566–2573, 1994.

[110] A. Ichimiya and P. I. Cohen. *Reflection High Energy Electron Diffraction*. Cambridge University Press, 2004.

[111] N. W. Ashcroft and N. D. Mermin. *Solid State Physics*. Brooks/Cole, Belmont, CA USA, 1976.

[112] D. P. Woodruff and T. A. Delchar. *Modern Techniques of Surface Science*. Cambridge University Press, Cambridge UK, 2nd edition, 1994.

[113] G. Attard and C. Barnes. *Surfaces*. Oxford University Press, 2003.

[114] J. G. Mavroides, J. A. Kafalas, and D. F. Kolesar. Photoelectrolysis of water in cells with $srtio_3$ anodes. *Applied Physics Letters*, **28**(5):241–243, 1976.

[115] Masashi Kawasaki, Kazuhiro Takahashi, Tatsuro Maeda, Ryuta Tsuchiya, Makoto Shinohara, Osamu Ishiyama, Takuzo Yonezawa, Mamoru Yoshimoto, and Hideomi Koinuma. Atomic control of the $SrTiO_3$ crystal surface. *Science*, **266**(5190):1540–1542, 1994.

[116] Y. Lin, A. E. Becerra-Toledo, F. Silly, K. R. Poeppelmeier, M. R. Castell, and L. D. Marks. The (2 x 2) reconstructions on the $SrTiO_3$ (001) surface: A combined scanning tunneling microscopy and density functional theory study. *Surface Science*, **605**(17-18):L51–L55, 2011.

[117] S. Nishikawa and S. Kikuchi. Diffraction of cathode rays by mica. *Nature*, **121**:1019–1020, 1928.

[118] P. Goodhew, F. J. Humphreys, and R. Beanland. *Electron Microscopy and Analysis*. Taylor and Francis, London and New York, third edition, 2001.

[119] O. Auciello and A.R. Krauss. *In Situ Process Diagnostics and Intelligent Materials Processing*. Wiley Science, 2000.

[120] G. J. H. M. Rijnders. *The Initial Growth of Complex Oxides: Study and Manipulation*. PhD thesis, Faculty of Science and Technology, 2001.

[121] C. W. Burrows. *Growth and characterisation of MnSb thin-films and interfaces*. PhD thesis, Physics, 2012.

[122] Staib Instrumente GmbH. RHEED vision.

[123] S. R. C. McMitchell. Reflection high energy electron diffraction and growth control in pld. 2011.

[124] J. M. Van Hove, P. R. Pukite, and P. I. Cohen. The dependence of RHEED oscillations on MBE growth parameters. *Journal of Vacuum Science and Technology B: Microelectronics and Nanometer Structures*, **3**(2):563–567, 1985.

[125] J. M. Van Hove, P. Pukite, P. I. Cohen, and C. S. Lent. RHEED streaks and instrument response. *Journal of Vacuum Science and Technology A: Vacuum, Surfaces, and Films*, **1**(2):609–613, 1983.

[126] S. Tanuma, C. J. Powell, and D. R. Penn. Calculations of electron inelastic mean free paths. V. Data for 14 organic compounds over the 50-2000 eV range. *Surface and Interface Analysis*, **21**(3):165–176, 1994.

[127] W. Umrath. *Fundamentals of Vacuum Technology*. Oerlikon, Leybold Vacuum GmbH, Cologne, Germany, 2007.

[128] J. O'Hanlon. *A User's Guide to Vacuum Technology*. Wiley-Interscience, 2003.

[129] R. Delmdahl and R. Pätzel. Pulsed laser deposition with excimer lasers. *physica status solidi (c)*, **5**(10):3276–3279, 2008.

[130] T. J. Jackson, S. B. Palmer, H. J. Blythe, and A. S. Halim. Giant magnetoresistance in granular cobalt copper thin films prepared by pulsed laser ablation deposition. *Journal of Magnetism and Magnetic Materials*, **159**(1-2):269–281, 1996.

[131] G. Rijnders and D.H.A. Blank. *In Situ Diagnostics by High-Pressure RHEED During PLD*. John Wiley and Sons, Inc., New Jersey, 2006.

[132] U. Pietsch, V. Holy, and T. Baumbach. *High-Resolution X-Ray Scattering, From Thin Films to Lateral Nanostructures*. Springer, 2nd edition, 2004.

[133] P. E. Batson, N. Dellby, and O. L. Krivanek. Sub-angstrom resolution using aberration corrected electron optics. *Nature*, **418**(6898):617–620, 2002.

[134] E. J. Kirkland. On the optimum probe in aberration corrected ADF-STEM. *Ultramicroscopy*, **111**(11):1523–1530, 2011.

[135] M. Haider, S. Uhlemann, E. Schwan, H. Rose, B. Kabius, and K. Urban. Electron microscopy image enhanced. *Nature*, **392**(6678):768–769, 1998.

[136] M. Ohtsuka, T. Yamazaki, Y. Kotaka, I. Hashimoto, and K. Watanabe. Imaging of light and heavy atomic columns by spherical aberration corrected middle-angle bright-field STEM. *Ultramicroscopy*, **120**(0):48–55, 2012.

[137] http://barrett-group.mcgill.ca/tutorials/nanotechnology/nano02.htm.

[138] R. Beanland. Cross-sectional specimens for transmission electron microscopy. *Microscopy today*, **11**(1):29–31, 2003.

[139] A. Einstein. Über einen die Erzeugung und Verwandlung des Lichtes betreffenden heuristischen Gesichtspunkt. *Annalen Der Physik*, **322**:132–148, 1905.

[140] F. Reinert and S. Hufner. Photoemission spectroscopy from early days to recent applications. *New Journal of Physics*, **7**(1):97, 2005.

[141] C. N. Berglund and W. E. Spicer. Photoemission studies of copper and silver: Theory. *Phys. Rev.*, **136**:A1030–A1044, 1964.

[142] K. W. Kolasinski. *Surface Science, foundation of catalysis and nanoscience*. John Wiley and Sons, Ltd, Queen Mary, University of London, UK, 2002.

[143] J. Vickerman Gilmore and I. S. *Surface analysis, the principal techniques*. John Wiley and sons, Ltd, UK, 2nd edition, 2009.

[144] Casa Software Ltd. Casaxps, 2009.

[145] K. Kalantar-zadeh and B. Fry. *Nanotechnology-Enabled Sensor*. Springer, 1st edition, 2007).

[146] Y. Martin, C. C. Williams, and H. K. Wickramasinghe. Atomic force microscope–force mapping and profiling on a sub 100-[a-ring] scale. *Journal of Applied Physics*, **61**(10):4723–4729, 1987.

[147] D. Necas and P. Klapetek. Gwyddion: an open-source software for SPM data analysis. *Central European Journal of Physics*, **10**:181–188, 2012.

[148] Quantum Design. (www.qdusa.com), MPMS Application note 1014-213, Subtracting the sample holder background from dilute samples, 2002.

[149] T Hotta, M. Moraghebi, A. Feiguin, A. Moreo, S. Yunoki, and E. Dagotto. Unveiling new magnetic phases of undoped and doped manganites. *Phys. Rev. Lett.*, **90**:247203, 2003.

[150] A. Gupta, T. R. McGuire, P. R. Duncombe, M. Rupp, J. Z. Sun, W. J. Gallagher, and Gang Xiao. Growth and giant magnetoresistance properties of La deficient $La_xMnO_{3-\delta}(0.67 \leq x \leq 1)$ films. *Applied Physics Letters*, **67**(23):3494–3496, 1995.

[151] A. P. Ramirez. Colossal magnetoresistance. *Journal of Physics: Condensed Matter*, **9**(39):8171, 1997.

[152] C. Adamo, X. Ke, P. Schiffer, A. Soukiassian, M. Warusawithana, L. Maritato, and D. G. Schlom. Electrical and magnetic properties of $(SrMnO_3)_n(LaMnO_3)_{2n}$ superlattices. *Applied Physics Letters*, **92**(11):112508, 2008.

[153] A. Sadoc, B. Mercey, C. Simon, D. Grebille, W. Prellier, and M. Lepetit. Large increase of the curie temperature by orbital ordering control. *Phys. Rev. Lett.*, **104**:046804, 2010.

[154] S. Dong, R. Yu, S. Yunoki, G. Alvarez, J.-M. Liu, and E. Dagotto. Magnetism, conductivity, and orbital order in $(LaMnO_3)_{2n}/(SrMnO_3)_n$ superlattices. *Phys. Rev. B*, **78**:201102, 2008.

[155] P. A. Salvador, A.-M. Haghiri-Gosnet, B. Mercey, M. Hervieu, and B. Raveau. Growth and magnetoresistive properties of $(LaMnO_3)_m(SrMnO_3)_n$ superlattices. *Applied Physics Letters*, **75**(17):2638–2640, 1999.

[156] T. Koida, M. Lippmaa, T. Fukumura, K. Itaka, Y. Matsumoto, M. Kawasaki, and H. Koinuma. Effect of A-site cation ordering on the magnetoelectric properties in $[(LaMnO_3)_m/(SrMnO_3)_m]_n$ artificial superlattices. *Phys. Rev. B*, **66**:144418, Oct 2002.

[157] W. S. Choi, Z. Marton, S. Y. Jang, S. J. Moon, B. C. Jeon, J. H. Shin, S. S. A. Seo, T. W. Noh, K. Myung-Whun, H. N. Lee, and Y. S. Lee. Effects of oxygen-reducing atmosphere annealing on $LaMnO_3$ epitaxial thin films. *Journal of Physics D: Applied Physics*, **42**(16):165401, 2009.

[158] B. Jeroen van den. Orbital-only models: ordering and excitations. *New Journal of Physics*, **6**(1):201, 2004.

[159] J. B. A. A. Elemans, B. Van Laar, K. R. Van Der Veen, and B. O. Loopstra. The crystallographic and magnetic structures of $La_{1-x}Ba_xMn_{1-x}Me_xO_3$ (Me = Mn or Ti). *Journal of Solid State Chemistry*, **3**(2):238–242, 1971.

[160] N. Sakai, H. Fjellvag, and B. Lebech. Effect of non-stoichiometry on properties of $La_{1-t}MnO_{3+\delta}$. crystal structure. *Acta Chemica Scandinavica*, **51**(9):904–909, 1997.

[161] Q. Huang, A. Santoro, J. W. Lynn, R. W. Erwin, J. A. Borchers, J. L. Peng, and R. L. Greene. Structure and magnetic order in undoped lanthanum manganite. *Phys. Rev. B*, **55**:14987–14999, 1997.

[162] H. A. Jahn and E. Teller. Stability of polyatomic molecules in degenerate electronic states. i. orbital degeneracy. *Proc. R. Soc. Lond. A*, **161**(905):220–235, 1937.

[163] J. B. Goodenough. Electronic and ionic transport properties and other physical aspects of perovskites. *Reports on Progress in Physics*, **67**(11):1915, 2004.

[164] M. Wolcyrz, R. Hory, F. Bourée, and E. Bukowska. Structural defects in $LaMnO_3$ phase studied by neutron diffraction. *Journal of Alloys and Compounds*, **353**(12):170–174, 2003.

[165] J. A. M. Van Roosmalen, E. H. P. Cordfunke, R. B. Helmholdt, and H. W. Zandbergen. The defect chemistry of $LaMnO_{3\pm\delta}$: 2. structural aspects of $LaMnO_{3+\delta}$. *Journal of Solid State Chemistry*, **110**(1):100–105, 1994.

[166] M. Hervieu, R. Mahesh, N. Rangavittal, and C. N. R. Rao. Defect structure of $LaMnO_3$. *Eur. J. Solid State Inorg. Chem*, **32**(2):79–94, 1995.

[167] Q. Huang, A. Santoro, J. W. Lynn, R. W. Erwin, J. A. Borchers, J. L. Peng, and R. L. Greene. Structure and magnetic order in undoped lanthanum manganite. *Physical Review B*, **55**(22):14987–14999, 1997.

[168] J. Töpfer and J. B. Goodenough. Transport and magnetic properties of the perovskites $La_{1-y}MnO_3$ and lamn1-zo3. *Chemistry of Materials*, **9**(6):1467–1474, 1997.

[169] C. Aruta, M. Angeloni, G. Balestrino, N. G. Boggio, P. G. Medaglia, A. Tebano, B. Davidson, M. Baldini, D. Di Castro, P. Postorino, P. Dore, A. Sidorenko, G. Allodi, and R. De Renzi. Preparation and characterization of $LaMno_3$ thin films grown by pulsed laser deposition. *Journal of Applied Physics*, **100**(2):023910, 2006.

[170] R. Cortés-Gil, A. Arroyo, L. Ruiz-Gonzàlez, J. M. Alonso, A. Hernando, J. M. Gonzlez-Calbet, and M. Vallet-Reg. Evolution of magnetic behaviour in oxygen deficient $LaMnO_{3-\delta}$. *J. Phys. Chem. Solids*, **67**(13):579–582, 2006.

[171] L. Ruiz-Gonzlez, R. Corts-Gil, J. M. Alonso, J. M. Gonzlez-Calbet, and M. Vallet-Reg. Revisiting the role of vacancies in manganese related perovskites. *Open Inorg. Chem. J.*, **1**:37–46, 2007.

[172] J. T. Mefford, W. G. Hardin, S. Dai, K. P. Johnston, and K. J. Stevenson. Anion charge storage through oxygen intercalation in $LaMnO_3$ perovskite pseudocapacitor electrodes. *Nat Mater*, **13**(7):726–732, 2014.

[173] A. Galdi, C. Aruta, P. Orgiani, N. B. Brookes, G. Ghiringhelli, M. Moretti Sala, R. V. K. Mangalam, W. Prellier, U. Lüders, and L. Maritato. Magnetic properties and orbital anisotropy driven by Mn^{2+} in nonstoichiometric $La_xMnO_{3-\delta}$ thin films. *Phys. Rev. B*, **83**:064418, 2011.

[174] P. A. Joy, C. Raj Sankar, and S. K. Date. The limiting value of x in the ferromagnetic compositions $La_{1-x}MnO_3$. *Journal of Physics: Condensed Matter*, **14**(39):L663, 2002.

[175] R. Hory, A. Sikora, and E. Bukowska. Polymorphic forms and defect structure formation within homogeneity domain of $LaMnO_3$ phase. *J. Alloys Comp.*, **353**(12):153–169, 2003.

[176] A. Galdi. *Magnetic orbital and transport properties in $LaMnO_3$ based based heterostructures*. Thesis, Universita degli studi di Salerno, 2011.

[177] M. Lepetit, B. Mercey, and C. Simon. Interface effects in perovskite thin films. *Phys. Rev. Lett.*, **108**:087202, 2012.

[178] C. Adamo, X. Ke, H. Q. Wang, H. L. Xin, T. Heeg, M. E. Hawley, W. Zander, J. Schubert, P. Schiffer, D. A. Muller, L. Maritato, and D. G. Schlom. Effect of biaxial strain on the electrical and magnetic properties of (001) $La_{0.7}Sr_{0.3}MnO_3$ thin films. *Applied Physics Letters*, **95**(11):112504, 2009.

[179] I. C. Infante, F. Sanchez, J. Fontcuberta, M. Wojcik, E. Jedryka, S. Estradé, F. Peiró, J. Arbiol, V. Laukhin, and J. P. Espinós. Elastic and orbital effects on thickness-dependent properties of manganite thin films. *Phys. Rev. B*, **76**:224415, 2007.

[180] M. Bibes, Ll. Balcells, S. Valencia, J. Fontcuberta, M. Wojcik, E. Jedryka, and S. Nadolski. Nanoscale multiphase separation at $LaCaMnO_3$-$SrTiO_3$ interfaces. *Phys. Rev. Lett.*, **87**:067210, 2001.

[181] A. Tebano, C. Aruta, S. Sanna, P. G. Medaglia, G. Balestrino, A. A. Sidorenko, R. De Renzi, G. Ghiringhelli, L. Braicovich, V. Bisogni, and N. B. Brookes. Evidence of orbital reconstruction at interfaces in ultrathin $La_{0.67}Sr_{0.33}MnO_3$ films. *Phys. Rev. Lett.*, **100**:137401, 2008.

[182] M. V. Abrashev, A. P. Litvinchuk, M. N. Iliev, R. L. Meng, V. N. Popov, V. G. Ivanov, R. A. Chakalov, and C. Thomsen. Comparative study of optical phonons in the rhombohedrally distorted perovskites $LaAlO_3$ and $LaMnO_3$. *Phys. Rev. B*, **59**:4146–4153, 1999.

[183] B. Cui, C. Song, G. Y. Wang, H. J. Mao, F. Zeng, and F. Pan. Strain engineering induced interfacial self-assembly and intrinsic exchange bias in a manganite perovskite film. *Sci. Rep.*, **3**, 2013.

[184] J. J. Peng, C. Song, B. Cui, F. Li, H. J. Mao, Y. Y. Wang, G. Y. Wang, and F. Pan. Exchange bias in a single $LaMnO_3$ film induced by vertical electronic phase separation. *Physical Review B*, **89**(16):165129, 2014.

[185] A. N. Ulyanov, D. S. Yang, N. Chau, S. C. Yu, and S. I. Yoo. Divalent manganese in a-position of perovskite cell: X-ray absorption finite structure study of $La_{0.6}Sr_{0.4-x}MnTi_xO_3$ manganites. *Journal of Applied Physics*, **103**(7):07F722, 2008.

[186] R. Zhao, K. Jin, Z. Xu, H. Guo, L. Wang, C. Ge, H. Lu, and G. Yang. The oxygen vacancy effect on the magnetic property of the $LaMnO_{3-\delta}$ thin films. *Applied Physics Letters*, **102**(12):122402, 2013.

[187] C. Ritter, M. R. Ibarra, J. M. De Teresa, P. A. Algarabel, C. Marquina, J. Blasco, J. Garcia, S. Oseroff, and S-W. Cheong. Influence of oxygen content on the structural, magnetotransport, and magnetic properties of $LaMnO_{3+\delta}$. *Phys. Rev. B*, **56**:8902–8911, 1997.

[188] J. Chen, L. Hu, W. J. Lu, B. Yuan, K. J. Zhang, J. M. Dai, and Y. P. Sun. Tuning of transport and magnetic properties in epitaxial $LaMnO_{3+\delta}$; thin films. *Advances in Condensed Matter Physics*, **2014**:5, 2014.

[189] R. Mahendiran, R. Mahesh, A. K. Raychaudhuri, and C. N. R. Rao. Composition dependence of giant magnetoresistance in $La_{1-x}Ca_xMnO_3$ (0.1-x-0.9). *Solid State Communications*, **94**(7):515–518, 1995.

[190] G. L. Liu, J. S. Zhou, and J. B. Goodenough. Interplay between charge, orbital, and magnetic ordering in $La_{1-x}Sr_xMnO_3$. *Phys. Rev. B*, **64**:144414, 2001.

[191] B. B. Van Aken, O. D. Jurchescu, A. Meetsma, Y. Tomioka, Y. Tokura, and Thomas T. M. Palstra. Orbital-order-induced metal-insulator transition in $La_{1-x}Ca_xMnO_3$. *Phys. Rev. Lett.*, **90**:066403, Feb 2003.

[192] G.-L. Liu, J.-S. Zhou, and J. B. Goodenough. Competing magnetic phases in mixed-valent manganese oxide perovskites. *Phys. Rev. B*, **70**:224421, 2004.

[193] G. Venkataiah, V. Prasad, and P. Venugopal Reddy. Influence of a-site cation mismatch on structural, magnetic and electrical properties of lanthanum manganites. *Journal of Alloys and Compounds*, **429**(12):1–9, 2007.

[194] M. S. Kim, J. G. Park, K. H. Kim, T. W. Noh, and H. C. Ri. Evidence of spin frustration in $LaMnO_{3+\delta}$ with $\delta=$ 0.0 and 0.025. *Journal of the Korean Physical Society*, **37**(5):561–564, 2000.

[195] J. F. Ding, O. I. Lebedev, S. Turner, Y. F. Tian, W. J. Hu, J. W. Seo, C. Panagopoulos, W. Prellier, G. Van Tendeloo, and T. Wu. Interfacial spin glass state and exchange bias in manganite bilayers with competing magnetic orders. *Phys. Rev. B*, **87**:054428, 2013.

[196] X. H. Huang, J. F. Ding, G. Q. Zhang, Y. Hou, Y. P. Yao, and X. G. Li. Size-dependent exchange bias in $La_{0.25}Ca_{0.75}MnO_3$ nanoparticles. *Phys. Rev. B*, **78**:224408, 2008.

[197] H. Guo, D. Sun, W. Wang, Z. Gai, I. Kravchenko, J. Shao, L. Jiang, T. Z. Ward, P. C. Snijders, L. Yin, J. Shen, and X. Xu. Growth diagram of $La_{0.7}Sr_{0.3}MnO_3$ thin films using pulsed laser deposition. *Journal of Applied Physics*, **113**(23):234301, 2013.

[198] Z. Marton, S. S. A. Seo, T. Egami, and H. N. Lee. Growth control of stoichiometry in $LaMnO_3$ epitaxial thin films by pulsed laser deposition. *Journal of Crystal Growth*, **312**(20):2923–2927, 2010.

[199] J. Mannhart and D. G. Schlom. Oxide interfaces-an opportunity for electronics. *Science*, **327**(5973):1607–1611, 2010.

[200] Q. Liang and B. Xiaofang. Direct observation of Ni^{3+} and Ni^{2+} in correlated $LaNiO_3$ films. *EPL (Europhysics Letters)*, **93**(5):57002, 2011.

[201] Tiwari Ashutosh and K. P. Rajeev. Electrical transport in $LaNiO_3$. *Journal of Physics: Condensed Matter*, **11**(16):3291, 1999.

[202] N. Gayathri, A. K. Raychaudhuri, X. Q. Xu, J. L. Peng, and R. L. Greene. Electronic conduction in $LaNiO_3$: the dependence on the oxygen stoichiometry. *Journal of Physics: Condensed Matter*, **10**(6):1323, 1998.

[203] M. J. Sayagus, M. Vallet-Reg, A. Caneiro, and J. M. Gonzlez-Calbet. Microstructural characterization of the $LaNiO_3$-y system. *Journal of Solid State Chemistry*, **110**(2):295–304, 1994.

[204] J. L. Garca-Muoz, J. Rodrguez-Carvajal, P. Lacorre, and J. B. Torrance. Neutron-diffraction study of $RNiO_3$ (R=La,Pr,Nd,Sm): Electronically induced structural changes across the metal-insulator transition. *Physical Review B*, **46**(8):4414–4425, 1992.

[205] A. Wold, B. Post, and E. Banks. Rare earth nickel oxides. *Journal of the American Chemical Society*, **79**(18):4911–4913, 1957.

[206] M. Chen, T. Wu, and J. Wu. Effect of textured $LaNiO_3$ electrode on the fatigue improvement of $Pb(Zr_{0.53}Ti_{0.47})O_3$ thin films. *Applied Physics Letters*, **68**(10):1430–1432, 1996.

[207] A. Li, C. Ge, P. L, and N. Ming. Preparation of perovskite conductive $LaNiO_3$ films by metalorganic decomposition. *Applied Physics Letters*, **68**(10):1347–1349, 1996.

[208] L. Fitting Kourkoutis, J. H. Song, H. Y. Hwang, and D. A. Muller. Microscopic origins for stabilizing room-temperature ferromagnetism in ultrathin manganite layers. *Proceedings of the National Academy of Sciences*, **107**(26):11682–11685, 2010.

[209] T. Higuchi, T. Yajima, L. Fitting Kourkoutis, Y. Hikita, N. Nakagawa, D. A. Muller, and H. Y. Hwang. Mn_3O_4 precipitates in laser-ablated manganite films. *Applied Physics Letters*, **95**(4):043112, 2009.

[210] E. Detemple, Q. M. Ramasse, W. Sigle, G. Cristiani, H.-U. Habermeier, E. Benckiser, A. V. Boris, A. Frano, P. Wochner, M. Wu, B. Keimer, and P. A. van Aken. Polarity-driven nickel oxide precipitation in $LaNiO_3$-$LaAlO_3$ superlattices. *Applied Physics Letters*, **99**(21):211903, 2011.

[211] N. Wakiya, T. Azuma, K. Shinozaki, and N. Mizutani. Low-temperature epitaxial growth of conductive $LaNiO_3$ thin films by rf magnetron sputtering. *Thin Solid Films*, **410**(12):114–120, 2002.

[212] S. Liu, B. Ma, M. Narayanan, S. Tong, R. Koritala, and U. Balachandran. Microstructure and electrical properties of $LaNiO_3$ thin films by rf sputtering for the growth of (Pb,La)(Zr,Ti)O_3 films on silicon and nickel substrates. *Journal of Vacuum Science amp; Technology A*, **30**(6):061505, 2012.

[213] L. Qiao and X. Bi. Effect of substrate temperature on the microstructure and transport properties of highly (100)-oriented $LaNiO_3$ films by pure argon sputtering. *Journal of Crystal Growth*, **310**(15):3653–3658, 2008.

[214] M. Zhu, P. Komissinskiy, A. Radetinac, M. Vafaee, Z. Wang, and L. Alff. Effect of composition and strain on the electrical properties of $LaNiO_3$ thin films. *Applied Physics Letters*, **103**(14):141902, 2013.

[215] C. C. Yang, M. S. Chen, T. Hong, C. M. Wu, J. Wu, and T. Wu. Preparation of (100)-oriented metallic $LaNiO_3$ thin films on si substrates by radio frequency magnetron sputtering for the growth of textured Pb($Zr_{0.53}Ti_{0.47}$)O_3. *Applied Physics Letters*, **66**(20):2643–2645, 1995.

[216] Y. Takeda, R. Kanno, M. Sakano, O. Yamamoto, M. Takano, Y. Bando, H. Akinaga, K. Takita, and J. B. Goodenough. Crystal chemistry and physical properties of La_2SrNiO_4. *Materials Research Bulletin*, **25**(3):293–306, 1990.

[217] D. Telesca, B. O. Wells, and B. Sinkovic. Structural reorientation of pld grown La_2NiO_4 thin films. *Surface Science*, **606**(910):865–871, 2012.

[218] E. J. Moon, B. A. Gray, M. Kareev, J. Liu, S. G. Altendorf, F. Strigari, L. H. Tjeng, J. W. Freeland, and J. Chakhalian. Strain-dependent transport properties of the ultra-thin correlated metal, $LaNiO_3$. *New Journal of Physics*, **13**(7):073037, 2011.

[219] F. Rivadulla, J. S. Zhou, and J. B. Goodenough. Electron scattering near an itinerant to localized electronic transition. *Physical Review B*, **67**(16):165110, 2003.

[220] A. Yu Dobin, K. R. Nikolaev, I. N. Krivorotov, R. M. Wentzcovitch, E. Dan Dahlberg, and A. M. Goldman. Electronic and crystal structure of fully strained $LaNiO_3$ films. *Physical Review B*, **68**(11):113408, 2003.

[221] K. M. Satyalakshmi, R. M. Mallya, K. V. Ramanathan, X. D. Wu, B. Brainard, D. C. Gautier, N. Y. Vasanthacharya, and M. S. Hegde. Epitaxial metallic $LaNiO_3$ thin films grown by pulsed laser deposition. *Applied Physics Letters*, **62**(11):1233–1235, 1993.

[222] C. Hsiao and X. Qi. Substrate-dependant chemical stability and conductivity of $LaNiO_{3-x}$ thin films. *Thin Solid Films*, **529**(0):356–359, 2013.

[223] J. Chakhalian, J. M. Rondinelli, Jian Liu, B. A. Gray, M. Kareev, E. J. Moon, N. Prasai, J. L. Cohn, M. Varela, I. C. Tung, M. J. Bedzyk, S. G. Altendorf, F. Strigari, B. Dabrowski, L. H. Tjeng, P. J. Ryan, and J. W. Freeland. Asymmetric orbital-lattice interactions in ultrathin correlated oxide films. *Phys. Rev. Lett.*, **107**:116805, 2011.

[224] K. Horiba, R. Eguchi, M. Taguchi, A. Chainani, A. Kikkawa, Y. Senba, H. Ohashi, and S. Shin. In situ photoemission study of $LaNiO_3$ thin films grown by pulsed laser deposition. *Journal of Electron Spectroscopy and Related Phenomena*, **156158**(0):107–110, 2007.

[225] S. N. Ruddlesden and P. Popper. The compound $Sr_3Ti_2O_7$ and its structure. *Acta Crystallographica*, **11**(1):54–55, 1958.

[226] C. Brisi, M. Vallino, and F. Abbattista. Composition and structure of two hitherto unidentified phases in the system La_2O_3-NiO-O. *Journal of the Less Common Metals*, **79**(2):215–219, 1981.

[227] P. Odier, Y. Nigara, J. Coutures, and M. Sayer. Phase relations in the La-Ni-O system: Influence of temperature and stoichiometry on the structure of La_2NiO_4. *Journal of Solid State Chemistry*, **56**(1):32–40, 1985.

[228] M. Zinkevich and F. Aldinger. Thermodynamic analysis of the ternary La−NiO system. *Journal of Alloys and Compounds*, **375**(12):147–161, 2004.

[229] D. O. Bannikov and V. A. Cherepanov. Thermodynamic properties of complex oxides in the LaNiO system. *Journal of Solid State Chemistry*, **179**(8):2721–2727, 2006.

[230] J. Chakhalian, J. M. Rondinelli, Jian Liu, B. A. Gray, M. Kareev, E. J. Moon, N. Prasai, J. L. Cohn, M. Varela, I. C. Tung, M. J. Bedzyk, S. G. Altendorf, F. Strigari, B. Dabrowski, L. H. Tjeng, P. J. Ryan, and J. W. Freeland. Asymmetric orbital-lattice interactions in ultrathin correlated oxide films. *Physical Review Letters*, **107**(11):116805, 2011.

[231] S. D. Ha, G. H. Aydogdu, and S. Ramanathan. Examination of insulator regime conduction mechanisms in epitaxial and polycrystalline smnio3 thin films. *Journal of Applied Physics*, **110**(9), 2011.

[232] A. V. Boris, Y. Matiks, E. Benckiser, A. Frano, P. Popovich, V. Hinkov, P. Wochner, M. Castro-Colin, E. Detemple, V. K. Malik, C. Bernhard, T. Prokscha, A. Suter, Z. Salman, E. Morenzoni, G. Cristiani, H.-U. Habermeier, and B. Keimer. Dimensionality control of electronic phase transitions in nickel-oxide superlattices. *Science*, **332**(6032):937–940, 2011.

[233] Gertjan Koster, Boike L. Kropman, Guus J. H. M. Rijnders, Dave H. A. Blank, and Horst Rogalla. Quasi-ideal strontium titanate crystal surfaces through formation of strontium hydroxide. *Applied Physics Letters*, **73**(20):2920–2f922, 1998.

[234] J. G. Connell, B. J. Isaac, G. B. Ekanayake, D. R. Strachan, and S. S. A. Seo. Preparation of atomically flat $SrTiO_3$ surfaces using a deionized-water leaching and thermal annealing procedure. *Applied Physics Letters*, **101**(25):251607, 2012.

[235] R. Bachelet, F. Sanchez, F. J. Palomares, C. Ocal, and J. Fontcuberta. Atomically flat SrO-terminated $SrTiO_3$ (001) substrate. *Applied Physics Letters*, **95**(14):141915, 2009.

[236] M. R. Castell. Nanostructures on the $SrTiO_3$ (001) surface studied by stm. *Surface Science*, **516**(1-2):33–42, 2002.

[237] Y. Liang and D. A. Bonnell. Structures and chemistry of the annealed $SrTiO_3$ (001) surface. *Surface Science*, **310**(1-3):128–134, 1994.

[238] Y. Liang and D. A. Bonnell. Atomic structures of reduced $SrTiO_3$ (001) surfaces. *Surface Science*, **285**(3):L510–L516, 1993.

[239] Koster G. *Artificial Layered Oxides by Pulsed Laser Depostion*. Thesis, 1999.

[240] G. Koster, B. L. Kropman, Gjhm Rijnders, D. H. A. Blank, and H. Rogalla. Influence of the surface treatment on the homoepitaxial growth of $SrTiO_3$. *Materials Science and Engineering B-Solid State Materials for Advanced Technology*, **56**(2-3):209–212, 1998.

[241] T. Ohnishi, K. Shibuya, M. Lippmaa, D. Kobayashi, H. Kumigashira, M. Oshima, and H. Koinuma. Preparation of thermally stable tio2-terminated $SrTiO_3$(100) substrate surfaces. *Applied Physics Letters*, **85**(2):272–274, 2004.

[242] Ricardo Garcia, Robert Magerle, and Ruben Perez. Nanoscale compositional mapping with gentle forces. *Nat Mater*, **6**(6):405–411, 2007.

[243] P. Muller and A. Saul. Elastic effects on surface physics. *Surface Science Reports*, **54**(5-8):157–258, 2004.

[244] H. Y. Hwang, Y. Iwasa, M. Kawasaki, B. Keimer, N. Nagaosa, and Y. Tokura. Emergent phenomena at oxide interfaces. *Nature Materials*, **11**(2):103–113, 2012.

[245] E. Benckiser, M. W. Haverkort, S. Brueck, E. Goering, S. Macke, A. Frano, X. Yang, O. K. Andersen, G. Cristiani, H. Habermeier, A. V. Boris, I. Zegkinoglou, P. Wochner, V. Kim, H.and Hinkov, and B. Keimer. Orbital reflectometry of oxide heterostructures. *Nature Materials*, **10**(3):189–193, 2011.

[246] M. Mara Luisa. Structural, magnetic and electronic properties of $RNiO_3$ perovskites (R = rare earth). *Journal of Physics: Condensed Matter*, **9**(8):1679, 1997.

[247] G. Rijnders, D. H. A. Blank, J. Choi, and C. Eom. Enhanced surface diffusion through termination conversion during epitaxial $SrRuO_3$ growth. *Applied Physics Letters*, **84**(4):505–507, 2004.

[248] W. S. Choi, D. W. Jeong, S. S. A. Seo, Y. S. Lee, T. H. Kim, S. Y. Jang, H. N. Lee, and K. Myung-Whun. Charge states and magnetic ordering in $LaMnO_3$ superlattices. *Physical Review B*, **83**(19):195113, 2011.

[249] S. J. May, T. S. Santos, and A. Bhattacharya. Onset of metallic behavior in strained $(LaNiO_3)_n/(SrMnO_3)_2$ superlattices. *Physical Review B*, **79**(11):115127, 2009.

[250] R. Matzdorf, Z. Fang, Ismail, Jiandi Zhang, T. Kimura, Y. Tokura, K. Terakura, and E. W. Plummer. Ferromagnetism stabilized by lattice distortion at the surface of the p-wave superconductor S_2RuO_4. *Science*, **289**(5480):746–748, 2000.

[251] M. Hashisaka, D. Kan, A. Masuno, M. Takano, Y. Shimakawa, T. Terashima, and K. Mibu. Epitaxial growth of ferromagnetic La_2NiMnO_6 with ordered double-perovskite structure. *Applied Physics Letters*, **89**(3):032504, 2006.

[252] Bruce A. Davidson, Revaz Ramazashvili, Simon Kos, and James N. Eckstein. Broken particle-hole symmetry at atomically flat interfaces. *Physical Review Letters*, **93**(10):107004, 2004.

[253] L. Vegard. Die konstitution der mischkristalle und die raumfllung der atome. *Zeitschrift fr Physik*, **5**(1):17–26, 1921.

[254] B.D. Cullity and S.R. Stock. *Elements of X-ray Diffraction*. Pearson, 3rd edition, 2003.

[255] J. W. Matthews and A. E. Blakeslee. Defects in epitaxial multilayers: I. misfit dislocations. *Journal of Crystal Growth*, **27**(0):118–125, 1974.

[256] R. People and J. C. Bean. Erratum: Calculation of critical layer thickness versus lattice mismatch for Ge_xSi_{1-x}/Si strained-layer heterostructures [appl. phys. lett. 47, 322 (1985)]. *Applied Physics Letters*, **49**(4):229–229, 1986.

[257] L. Qiao, T. C. Droubay, T. Varga, M. E. Bowden, V. Shutthanandan, Z. Zhu, T. C. Kaspar, and S. A. Chambers. Epitaxial growth, structure, and intermixing at the $LaAlO_3/SrTiO_3$ interface as the film stoichiometry is varied. *Phys. Rev. B*, **83**:085408, 2011.

[258] S. Venkatesan, A. Vlooswijk, B. J. Kooi, A. Morelli, G. Palasantzas, Jeff T. M. De H., and B. Noheda. Monodomain strained ferroelectric $PbTiO_3$ thin films: Phase transition and critical thickness study. *Physical Review B*, **78**(10):104112, 2008.

[259] T. E. Whall and E. H. C. Parker. Sige heterostructures for fet applications. *Journal of Physics D: Applied Physics*, **32**(10):1187, 1999.

[260] J. S. Speck and W. Pompe. Domain configurations due to multiple misfit relaxation mechanisms in epitaxial ferroelectric thin films. i. theory. *Journal of Applied Physics*, **76**(1):466–476, 1994.

[261] P. M. J. Maree, J. C. Barbour, J. F. Vanderveen, K. L. Kavanagh, C. W. T. Bullelieuwma, and M. P. A. Viegers. Generation of misfit dislocations in semiconductors. *Journal of Applied Physics*, **62**(11):4413–4420, 1987.

[262] A. A. Demkov, , , and A. B. Posadas. *Integration of Functional Oxides with Semiconductors*. Springer, New York, 2014.

[263] S. B. Adler. Chemical expansivity of electrochemical ceramics. *Journal of the American Ceramic Society*, **84**(9):2117–2119, 2001.

[264] H. Seo, A. Posadas, and A. A. Demkov. Strain-driven spin-state transition and superexchange interaction in $lacoo_3$ study. *Physical Review B*, **86**(1):014430, 2012.

[265] L. Qiao, T. C. Droubay, T. Varga, M. E. Bowden, V. Shutthanandan, Z. Zhu, T. C. Kaspar, and S. A. Chambers. Epitaxial growth, structure, and intermixing

at the laalo$_3$-srtio$_3$ interface as the film stoichiometry is varied. *Physical Review B*, **83**(8):085408, 2011.

[266] V. Mehta, M. Liberati, F. J. Wong, R. V.s Chopdekar, E. Arenholz, and Y. Suzuki. Ferromagnetism in tetragonally distorted $LaCoO_3$ thin films. *Journal of Applied Physics*, **105**(7):07E503, 2009.

[267] R. People and J. C. Bean. Calculation of critical layer thickness versus lattice mismatch for Ge $_x$ Si_{1-x} /Si strained-layer heterostructures. *Applied Physics Letters*, **47**(3):322–324, 1985.

[268] J. He, A. Borisevich, S. V. Kalinin, S. J. Pennycook, and S. T. Pantelides. Control of octahedral tilts and magnetic properties of perovskite oxide heterostructures by substrate symmetry. *Phys. Rev. Lett.*, **105**:227203, 2010.

[269] P. Woodward. Octahedral tilting in perovskites. I. geometrical considerations. *Acta Crystallographica Section B*, **53**(1):32–43, 1997.

[270] A. J. Millis. Lattice effects in magnetoresistive manganese perovskites. *Nature*, **392**(6672):147–150, 1998.

[271] E. Detemple, Q. M. Ramasse, W. Sigle, G. Cristiani, H. U. Habermeier, B. Keimer, and P. A. van Aken. Ruddlesden-popper faults in $LaNiO_3/LaAlO_3$ superlattices. *Journal of Applied Physics*, **112**(1), 2012.

[272] Y. Tokuda, S. Kobayashi, T. Ohnishi, T. Mizoguchi, N. Shibata, Y. Ikuhara, and T. Yamamoto. Growth of ruddlesden-popper type faults in sr-excess $SrTiO_3$ homoepitaxial thin films by pulsed laser deposition. *Applied Physics Letters*, **99**(17), 2011.

[273] R. J. D. Tilley. An electron microscope study of perovskite-related oxides in the srtio system. *Journal of Solid State Chemistry*, **21**(4):293–301, 1977.

[274] David I. Woodward. Private communactions on effects of octahedra tilting on electron diffraction patterns of perovskites., 2014.

[275] C. Sayan, B. Anis, D. Subarna, G. Barnali, V. Siruguri, A. K. Raychaudhuri, M. H. Phan, and H. Srikanth. Evidence of a canted magnetic state in self-doped $LaMnO_{3+\delta}$ (δ=0.04): a magnetocaloric study. *Journal of Physics: Condensed Matter*, **24**(36):366004, 2012.